Interaction of mammalian cells with ZnO nanowire arrays: Towards a piconewton force sensor.

Brown, Richard A

Prifysgol Abertawe
Swansea University

Interaction of mammalian cells with ZnO nanowire arrays:
Towards a piconewton force sensor

A dissertation submitted in partial fulfilment of the

requirements for the degree of

Doctor of Philosophy

In

Nanotechnology

By

Richard A Brown

2014

Thesis Supervisor: Dr Thierry Maffeis

DEDICATION

This thesis is dedicated to my amazing wife, **Michelle** and my adorable Sons, **Charlie** and **Harry**, without whom I would not have made it this far; as it is their love, patience and support that have kept me going these past four years.

"If writing your Master's thesis was an uphill struggle,
then obtaining your Doctorate must be like climbing Mt. Everest!"
- Michelle Brown

DECLARATION

This work has not previously been accepted in subst ance for any degree and is not being concurrently submitted in candidature for any degree.

Signed ..... (candidate)

Date .....04/06/2014.....

STATEMENT 1

This thesis is the result of my own investigations, except where otherwise stated. Where correction services have been used, the exten t and nature of the correction is clearly marked in a footnote(s). Othe r sources are acknowledged by citation notes giving explicit references, and a bi bliography is appended to the end of each chapter.

Signed ..... (candidate)

Date .....04/06/2014.....

STATEMENT 2

I hereby give consent for my thesis, if accepted, t o be available for photocopying and for inter-library loan, and for the title and s ummary to be made available to outside organisations.

Signed ..... (candidate)

Date .....04/06/2014.....

AKNOWLEDGEMENTS

I would like to thank my beautiful wife, Michelle who has stayed with me throughout my doctorate providing the support, love and encouragement needed to get this monstrosity finished; even though I've been the grumpiest husband for 4 years.

I want to thank my boys, Charlie and Harry who have at every convenience provided acoustic accompaniment while writing my thesis, the screams, the tears, the whining and the hysterical laughter followed by 'Weewee Mummy!'

To the three of you I promise to be a better husband and father over the coming years, we have sacrificed a lot of fun occasions for this thesis and career, so I can only give the three of you my deepest apologies for how bad things have been up till now! ☹

To Thierry, without you I would never have made it this far, I feel that you have shaped me, moulded me, encouraged me to work my hardest, to put in the hours, to get the publications to make something of myself. Thank you so much for giving me this opportunity, I hope that we may stay in touch and explore the vast quantity of data I've accumulated over 4 years. After all this thesis contains only 14.87 % of the experiments I conducted so you may not be rid of me just yet....

To Mark, thank you so much for all the guidance these last 5 years, I'll CC you in to proof the publications I'm planning over the next year for some sneaky 2nd authors! ☺

To my old chums from 108, I'm finally free! Without our little chats and Friday night gaming sessions I think I would have died of boredom by now... Charlie can't wait to see Uncle Jay, Malc and Tim again soon! Roll on Christmas LAN!!!

Finally a quick thank you to my new manager and colleagues at QQ, for letting me improve the thesis whenever I had spare time – thanks' guys I owe you all a pint!

THESIS SUMMARY

This summary sheet should be completed after you have read the accompanying notes. The completed sheet should be submitted by you to your Head of School at the time of submission of your work and the supporting documentation.

Candidate's Surname / Family Name ..... BROWN .....

Candidate's Forenames ..... RICHARD, ALAN .....

Candidate for the Degree of ..... DOCTOR OF PHILOSOPHY ..... (PhD, MPhil etc.)

Full title of thesis ..... INTERACTION OF MAMMALIAN CELLS WITH ZnO NANOWIRE ARRAYS: TOWARDS A PICONEWTON FORCE SENSOR .....

Summary:

In this work Zinc Oxide (ZnO) Nanowires were fabrication using the Hydrothermal Growth method. All the major variables were explored, solution temperature, concentration, growth time, seed layer thickness and method, substrate position, ratio of precursors, yet initially reproducible crystal growth could not be obtained. Tolerances were too high when comparing the morphology results from nanowire arrays using the same recipe; a significant variable was clearly being overlooked. By collating all the quantitative data and compiling it against all recorded variables it was promptly determined how the solution was stirred and for how long had an astonishingly high impact on the final morphology and optical properties of the obtained ZnO nanowires.

Once ZnO nanowire reproducibility was obtained the thesis then examines biocompatibility. Where this work shows that ZnO nanowires are stable in media for 7 days, that U-2 OS cells adhere and proliferation as normal for 3 days. Promega's MTS assay results showed that at 3 days both 2:1 nanowires and the glass control had 88 % the number of cells of a no substrate (well only) control. It was also shown with Invitrogen's LIVE DEAD assay that 2:1 nanowires obtained results similar to the glass control, with the results at low seeding after 3 days being 59, 65 and 62 % live cells for glass control, 2:1 and 1:1 nanowires, respectively. It was therefore found in this work that hydrothermally grown ZnO nanowires are biocompatible with U-2 OS cells for up to 3 days.

Contents

Chapter 1. Introduction

1.1. Preamble

It is becoming increasing apparent that the field of cellular mechanics which focuses on observing the minute forces exerted by cells on the extra cellular matrix and substrate is of key importance in further understanding of both physiological and pathological processes such as inflammation, wound healing and the growth and spread of disease (angiogenesis and metastasis) [1]. It has recently been shown in the literature that both cell form and function can be manipulated via mechanical tension of the cytoskeleton, and that associated changes in cell shape affect cell behaviour altering functions such as growth, differentiation, apoptosis, motility, signal transduction, gene expression, and chromosome movement just to name a few [2]. These forces when applied to the cytoskeleton are also transmitted across the cell surface and have been shown in the literature to influence tissue development, with even formation of complex organs, vertebrate and the brain being guided by mechanical forces [3]. However measurements of these forces on living cells currently lack the sensitivity required to gain a significant insight into cell mechanics, being limited to intrusive external probes such as the atomic force microscope (AFM). Intra-cellular reporters capable of delivering in-situ monitoring of cellular forces for insight into cell behaviour on material surfaces as they proliferate would represent a paradigm shift in the field of biomaterials science. Obtaining this information is crucial for the development of long-term implantable materials as a better understanding of cell-substrate interaction could improve the biocompatibility and success rate of implants.

The subject of this Doctorate is to develop a method to successfully integrate ZnO nanowires with mammalian cells, so that the many wonderful properties of ZnO (covered in the next chapter) can be exploited to yield information on cell-substrate interaction. Of particular interest is the application of ZnO nanowire arrays as novel optical force sensors, sensitive enough to detect the tractional forces induced by cell motion as mammalian cells proliferate and migrate. However, this is only one of many directions this research can take once the ground-work for both reproducible ZnO nanowire array production and biocompatibility has been covered. Nanowires could be

bound with drugs and shape optimised for phagocytosis for rapid drug delivery. Surface properties could be tailored to promote changes in phenotype, or arrays coated in cytokines to investigate chemo-taxis. They could even be developed as coatings for implants to promote cell differentiation to relevant lineages. However, all these ideas and directions cannot be achieved without obtaining reproducible production and biocompatibility. These will be the focus of this work.

Because ZnO is an optically non-linear material, this work originally wished to exploit the nonlinear optical process of Second Harmonic Generation (SHG), to observe in the traction forces exerted by the cells on the nanowires as they proliferate leading to strain induced band gap change. These changes in band gap position or size affect the intensity of the SHG signal [4] resulting in a method to monitor the proliferation of cells across the ZnO array, where intensity will be used as contrast to create an optical map of forces. An example can be found from the work of Butet et al. [5], (in Fig. 1.1.) where they use a Ti:Sapphire laser tuned to a wavelength of 794 nm with 180 fs pulses at 76 MHz to image the SHG intensity of 150 nm diameter Au colloids in gelatin. The image presents good spatial resolution and contrast allowing distinction between the colloidal clusters and the gelatin background. The cells used in this work are typically 50 - 60 μm in diameter and the wires 80 - 150 nm in diameter, thus it can be understood how similar preliminary results should certainly be achievable.

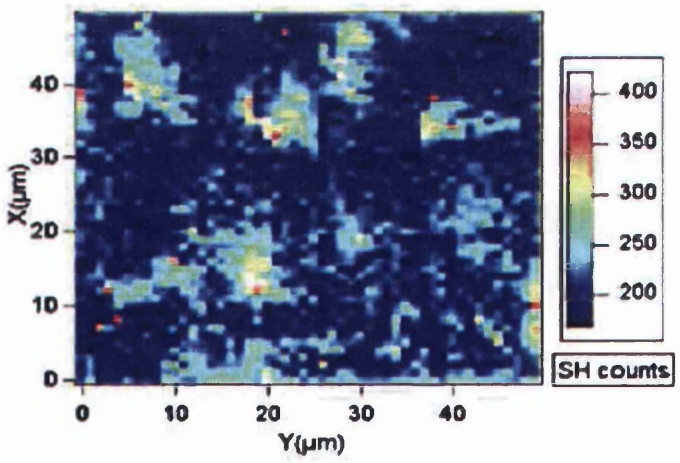

Figure 1.1. Shows a map of second harmonic intensity at 397nm of a 50x50μm area of gelatin where embedded Au nanoparticles are seen as higher contrast than the background, from [5].This work forms the basis of using SHG as a tool to track Au colloid tagged antibodies which can be programmed to target almost any protein.

One of the key advantages of using SHG is that because the photons are frequency doubled then they are of higher energy and are less likely to inflict cell damage due to less perturbation of the cells. Also due to these reduced peak power requirements of SHG, required power density only occurs at the focal point resulting in intrinsic 3D sectioning without the traditional use of a confocal aperture [6]. This greatly reduces out of focal plane photo-bleaching and photo-toxicity, which are unwanted processes that typically break down dyes and form reactive oxygen ion species in other optical based life sciences techniques; as limiting of interaction to only the focal plane allows data acquisition with SHG over much longer timescales. Also, Agopov et al [7] have reported that imaging through a medium is possible with SHG, where Phosphate Buffered Saline (PBS) was used to wash and suspend bio-materials for imaging and reported to yield better signal to noise ratio (SNR) due to less scattering. This is because the obtained image always comprises of both direct backward components as well as some forward components that have been backscattered towards the objective lens due to mean free path length propagation and scattering in the sample [8]. Although SHG inherently will have SNR far better than other optical techniques due to the excitation source being twice the wavelength of the emission, care must be taken to ensure that phase mismatch between the interacting waves is close to zero.

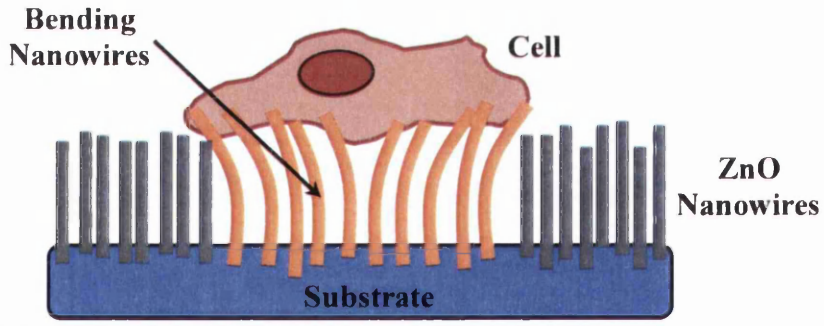

Figure 1.2. Concept of final device to be completed by phase 3 of the work, where cells are grown on the nanowires bending the nanowires (shown in orange) causing a change ZnO's optical properties.

The proposed sensor will consist of a vertical array of ZnO nanowires onto which cells will be allowed to proliferate for up to 72 hours, as illustrated by Fig.1.2. The tangential forces exerted by the cells as they migrate and proliferate will bend the nanowires (orange in Fig.1.2.) with the resulting strain altering crystal quality and hence altering the intensity of the SHG signal. Therefore it will be possible to use SHG to

image the nanowires underneath the cells, yielding a map of the forces exerted by the cells leading edge with a spatial resolution of a few hundred nanometres. However it should be noted that spatial resolution will be determined by altering the dimensions of the nanowires, allowing manipulation of device sensitivity for specific force regimes. The concept of using the structural deformation of ZnO nanowires and the ensuing non-symmetry of the crystal lattice to provide non-linear optical sensing of force presents a challenge. Whilst deformation of crystal symmetry in nanowires is being explored for electrical sensors, through piezoelectric properties [9], its use in fluorescence sensors producing second harmonic generation is wholly novel (at the time of writing) and presents a true paradigm shift in the way microbiologists may study cell mechanics.

The scope of work in this thesis is large comprising of multiple disciplines throughout each of the 9 chapters; and may be broken down into three main phases:

1. Fabrication of ZnO Nanowires
2. Biocompatibility of ZnO Nanowires
3. Refinement of Optical and Mechanical Properties

1.2. References

[1] S. Kumar and V. M. Weaver, "Mechanics, malignancy, and metastasis: the force journey of a tumor cell.," *Cancer Metastasis Rev.*, vol. 28, no. 1–2, pp. 113–27, Jun. 2009.

[2] M. E. Chicurel, C. S. Chen, and D. E. Ingber, "Cellular control lies in the balance of forces.," *Curr. Opin. Cell Biol.*, vol. 10, no. 2, pp. 232–9, Apr. 1998.

[3] D. C. Van Essen, "A tension-based theory of morphogenesis and compact wiring in the central nervous system.," *Nature*, vol. 385, no. 6614, pp. 313–8, Jan. 1997.

[4] J. Si, "Band-gap dependence of optically encoded second-harmonic generation in Bi2O3–B2O3–SiO2 glasses," *Opt. Commun.*, vol. 180, no. 1–3, pp. 179–182, Jun. 2000.

[5] J. Butet, J. Duboisset, G. Bachelier, I. Russier-Antoine, E. Benichou, C. Jonin, and P.-F. Brevet, "Optical second harmonic generation of single metallic nanoparticles embedded in a homogeneous medium.," *Nano Lett.*, vol. 10, no. 5, pp. 1717–21, May 2010.

[6] W. Denk, J. H. Strickler, W. W. Webb, and D. Winfried, "Two-Photon Laser Scanning fluorescence Microscopy," *Science (80-.).*, vol. 248, no. 4951, pp. 73–76, Oct. 1990.

[7] M. Agopov, L. Lomb, O. La Schiazza, and J. F. Bille, "Second harmonic generation imaging of the pig lamina cribrosa using a scanning laser ophthalmoscope-based microscope.," *Lasers Med. Sci.*, vol. 24, no. 5, pp. 787–92, Sep. 2009.

[8] F. Légaré, C. Pfeffer, and B. R. Olsen, "The role of backscattering in SHG tissue imaging.," *Biophys. J.*, vol. 93, no. 4, pp. 1312–20, Aug. 2007.

[9] J. Zhou, P. Fei, Y. Gao, Y. Gu, J. Liu, G. Bao, and Z. L. Wang, "Mechanical-electrical triggers and sensors using piezoelectric micowires/nanowires.," *Nano Lett.*, vol. 8, no. 9, pp. 2725–30, Sep. 2008.

Chapter 2. Optical and Mechanical Properties of Zinc Oxide

2.1. Introduction

Zinc Oxide (ZnO) has obtained renewed attention due to the synthesis of p-type ZnO by several groups [1-3]. ZnO's semiconducting and piezoelectric properties, as well as its direct wide band gap of 3.37 eV and exciton binding energy of 60 meV [4,5], show that the material system has many applications in optoelectronics. Recently ZnO research has intensely focused on fabrication and operation of one-dimensional (1D) ZnO nanomaterials, typically centered on nanowires, nanorods, nanotubes, and nanobelts due to their mechanical and electrical properties [6,7]. Due to these properties ZnO nanomaterials have been reported to have abundant potential for applications in electronic and optoelectronic devices, such as ultraviolet lasers [8], photo sensors [9], gas sensors [10], and nanogenerators [11]. Additionally its high isoelectric point (9.5), biocompatibility and fast electron transfer kinetics make it promising for biosensing applications [12]. ZnO has also been used in non-linear optical techniques such as multiphoton fluorescence [13] and second harmonic generation to image live tumour (KB) cells [14]; with both applications making ZnO an ideal material system for application as a live cell force sensor.

As discussed in chapter 1, the deformation of crystal symmetry in nanowires is being explored for mechanical sensors via piezoelectric effects [15], its use in fluorescence based sensors producing second harmonic generation is novel and yet to be fully explored. Yet the concept of using the structural deformation of ZnO nanowires and their non-symmetry of the crystal lattice to exploit non-linear optical sensing of force could cause a flurry interest in field of force sensing. It is the periodicity of atomic nuclei that determine the separation of the energy levels into bands, then an introduction of defects in the crystal lattice could result in a breakdown of symmetry, having implications on the optical properties of the material. Therefore to fully understand the

concepts explored later in the thesis this chapter will explain the basic properties, crystallography and optical property dependence on lattice homogeneity.

2.2. Crystal structure of ZnO

Due to ZnO's non-centrosymmetric hexagonal wurtzite crystal structure yielding both piezoelectric *(electric field created when mechanical strain applied)* and pyroelectric *(voltage generated with when temperature change)* properties then there has been much interest in application of ZnO in devices in the literature for energy harvesting [15] and temperature sensing [16]. Therefore it is best to first understand the crystal structure of ZnO.

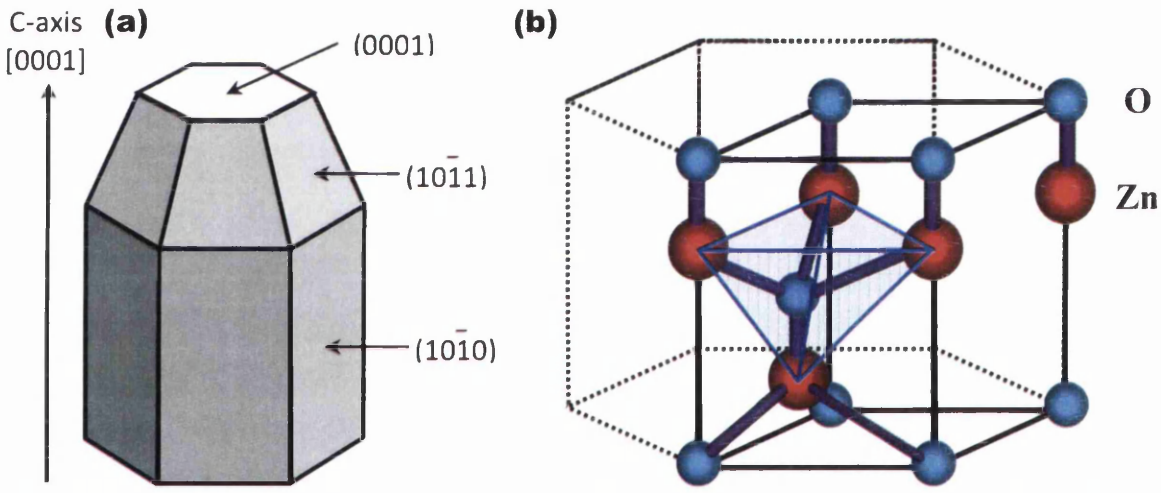

Figure 2.1. Diagram a) represents the common morphology of ZnO nanowires grown using the hydrothermal method with 3 facets labeled with Miller-Bravais indices, adapted from [17]. Diagram b) shows a the wurtzite unit cell of ZnO, adapted from [18]. Full explanation of Miller-Bravais indices and lattice constants given in Appendix I.

Fig. 2.1. shows the hexagonal wurtzite structure of the semiconductor ZnO, that consists of group II Zn^{2+} ions and group VI O^{2-} ions that tetrahedrally arranged and are alternatively stacked along the c-axis. Meaning that each Zinc ion has 4 Oxygen ions neighbouring in a tetrahedral arrangement and the same is also true for an Oxygen ion. The crystal structure of adjacent tetrahedrons causes the formation of bi-layers of zinc and oxygen, where typically the (0001) and (000$\bar{1}$) facets would be Zinc and Oxygen terminated, respectively. However this leads to differences in charge distributions and a

reduction is often witnessed at the polar (0001) surface because the Zinc and Oxygen surface atoms have only 3 neighbours instead of 4. Therefore hexagonal unit cell contains a negatively charged polar $(000\bar{1})$ facet and a positively charged polar (0001) facet, this has an effect on biocompatibility and is discussed in chapter 8. The lattice constants are a_0 = 0.325 nm and c_0 = 0.521 nm and belong to the point group C_{6v} and space group C^4_{6v} using Schoenflies notation [19]; yielding a c/a ratio of 1.602 which is close to the ideal value of 1.633 for a hexagonal cell [20]. This is not quite ideal due to ZnO's u value of 0.345 that is a measure of the amount by which atoms are displaced along the c-axis; known as inter-atomic spacing. This is because u affects the following relationship uc/a=(3/8)1/2, where c/a=(8/3)1/2 and u=3/8 for an ideal wurtzite crystal [21].

2.3. Properties of ZnO

Semiconductors are formed (in our case) when group II and VI (*2 and 6 electrons available respectively*) elements coalesce forming a neutral compound; however elements from other groups can often be incorporated changing the properties of the material system. This is called doping and is often used as a method of changing ZnO optical properties [22]. Typically semiconductors are (poor conductors) at room temperature as thermal equilibrium conditions prevail so that all electrons occupy the valence band states; however if the material is excited via optical pumping or temperature elevation then electrons can obtain sufficient energy to be excited into the conduction band. Adjacent vacant conduction band states allow charge to travel and the material becomes a conductor [23]. This process can be altered significantly with the inclusion of dopants [24] as well as defects within the lattice [25]; both these with be discussed in further detail. Table 2.1 shows bulk ZnO properties as nanowires have been confirmed by both X-ray diffraction and TEM to share the same wurzite lattice structure as the bulk [26].

It should be noted that the properties listed in Table 2.1. are for bulk ZnO and that when this material becomes nanoscale in one or more dimensions its properties tend to alter slightly. However it has been shown in the literature that the exciton Bohr radius for ZnO is 2.34 nm [27] and therefore the optical properties of the nanowires fabricated in this work will not be affected by their dimensions due to their large 50 – 150 nm

diameter widths. The properties are more likely to be affected by the change in surface area to volume ratio which often leads to enhancement of surface states for nanostructures.

Table 2.1. Properties of wurtzite ZnO at 300 K, from [28].

Property		Value
Molecular Weight		81.408 g/mol
Lattice parameters at 300K:	a_0	0.325 nm
	c_0	0.521 nm
	a_0 / c_0	1.602 (1.633 ideal)
	u	0.345
Density		5.606 g/cm^3
Melting Point		1975 °C
Thermal Conductivity		25 W/mK at 20 °C
Linear expansion coeff. (/°C):	a_0	6.5×10^{-6}
	c_0	3.0×10^{-6}
Static dielectric constant		8.656
Refractive index		2.008
Band gap		3.37eV
Carrier concentration:	Intrinsic	$< 10^6$ cm^{-3}
	max n-type doping	10^{20} cm^{-3} electrons
	max p-type doping	10^{17} cm^{-3} holes
Exciton binding energy		60 meV
Effective mass of:	Electron (m_e^*)	0.24
	Hole (m_h^*)	0.59
Hall mobility at 300 K:	n-type conductivity	200 cm^2/Vs
	p-type conductivity	5-50 cm^2/Vs

To better understand the electronic and optical properties of ZnO discussed in the following sections it is ideal to understand band diagrams, as they can be used to explain the spectral changes witnessed in photoluminescence data [29] (explained in chapter 4). In semiconductors a region exists between the valence and conduction bands containing forbidden energy levels between that determine the behaviour of the semiconductor. Semiconductors require an external energy source to excite their electrons to traverse the forbidden region (band gap) up an energy level; such as optical excitation. However when the electron transitions back to the valence band to combine with a hole it looses this energy by emitting a single photon. This process is called recombination and is shown in Fig. 2.2. The conduction and valence bands are not flat but parabolic curves, or for some materials even more complex curves that are different for each material. There exist multiple methods for electrons and holes to recombine. Direct recombination occurs when the conduction band minimum aligns with the valence band maximum, and indirect recombination occurs when the conduction band minimum and valence band maximum do not align.

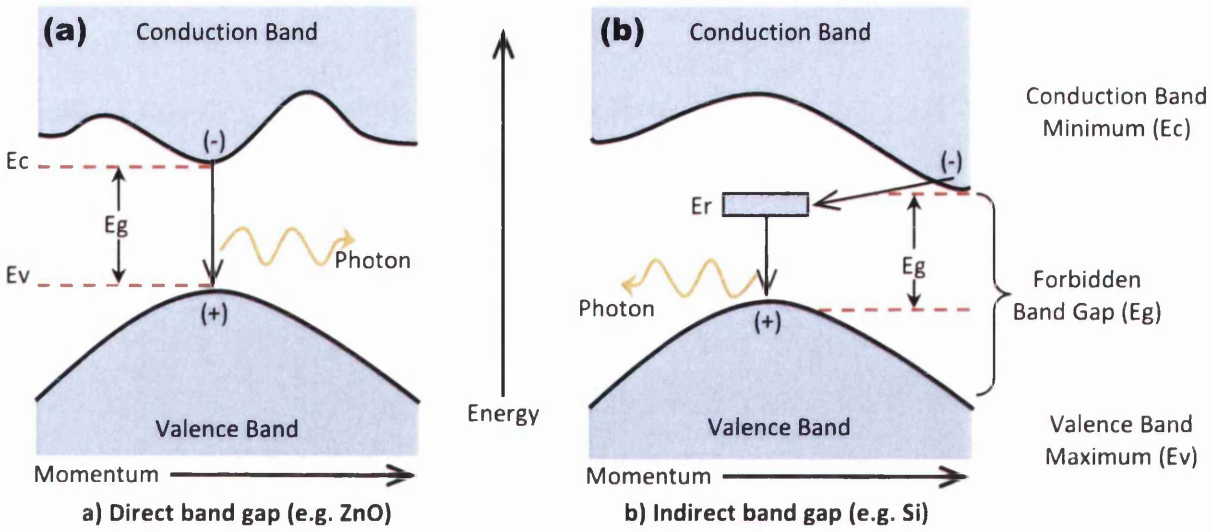

Figure 2.2. Band diagram of the two major recombination processes, direct and indirect recombination. (a) Electron-hole pair recombination in ZnO, a direct band gap semiconductor. (b) Electron-hole pair recombination in Si an indirect band gap semiconductor, via a recombination centre [30].

Fig. 2.2. shows if an electron is given sufficient energy then it may traverse the band gap, in doing so a positively charged hole will be left behind and recombining these two carriers will result in emission of a photon to conserve energy. This process can happen either directly or indirectly depending on the material system and the amount of defects present within the lattice as defect provide energy levels within the bandgap. In Fig. 2.2a an electron is shown making the transition from conduction to valence band via the direct recombination process giving up its energy by emitting a photon in the process; this is called spontaneous emission and is a radiative recombination process. In Fig. 2.2b the valence band maximum and conduction band minimum are not aligned due to being located at different k-values, therefore the electron is required to make the transition via a double-step process including a phonon (*a vibrational lattice quasi-particle*) absorption or emission. Thus, energy and momentum conservation require that the phonon be accounted for producing a photon of lower energy and larger wavelength. Because the indirect recombination process involves a phonon as well as a photon and electron, the probability of a collision between all three particles is much lower than a direct band gap photon-electron interaction [31]; therefore the emission intensity is often lower compared to a direct bandgap transition due to equation 2.1 [30].

$$\hbar\omega = E_c - E_v \pm \hbar\omega_{ph} \quad (2.1)$$

Where $\hbar\omega$ is the photon energy, and $\hbar\omega_{ph}$ the phonon energy with plus and minus indicating emission or absorption, respectively. It is for this reason that semiconductor based optoelectronic devices tend to use direct band gap materials, and why ZnO has great potential in the field of optoelectronics. Additionally the use of nanostructures will provide an increase of electron-hole interaction by several orders of magnitude [32] due to their density of states being disparate forming discontinuous spikes called van Hove singularities that form at the conduction band minimum and valence band maximum. The formation of defects in these materials creates inhomogeneities leading to indirect recombination's yielding a non-radiative recombination process heating the semiconductor due to phonon interaction; this is problematic and can lead to increased defect growth and eventually failure of the device. More importantly for this work such defects in ZnO could lead to unwanted spectral changes in emission wavelength and intensity [33] leading the device to fail to function as a force sensor.

2.4. Mechanical Properties

Typically the average contact pressure hardness (H) and Young's modulus (E, a measure of the elasticity) are obtained as a function of the forces applied and penetration of a plastic indenter; and these properties would be used to describe the mechanical properties of a material system. However in the nanoscale regime these values obtained from bulk have no significant meaning and so they're omitted from Table 2.1. This is quite evident from the discrepancies within the literature with values of E ranging from 10 - 100 GPa. This is usually due to the various methods and strain types (i.e. compressive or tensile) applied to the material system to yield Young's modulus. Ozgur et al. [34] state that for bulk ZnO for a plastic penetration depth of 300 nm the hardness value is measured to be 5.0 ± 0.1 GPa, while the Young's modulus remains constant over the indenter penetration depth at 111.2 ± 4.7 GPa.

These values are completely contrasted by those reported in the literature for a single nanowire. Since application of an indenter at the nanoscale is unrealistic (due to surface effects), a popular technique used to evaluate E is by monitoring the oscillatory

response of a single nanowire subjected to an alternating electrostatic field of known frequency under a transmission electron microscope (TEM). The amplitude of the response is used to calculate E, and has been reported by Chen et al. [35] to increase from 140 to 220 GPa for ZnO nanowires of diameter 120 and 17 nm respectively. Other work focuses on atomic force microscopy (AFM, see chapter 6), where Song et al. [36] observe a Young's modulus of 29 ± 8 GPa by compressing a single nanowire between an AFM cantilever tip and substrate. Ni et al. [37] use an AFM tip to conduct a three point bending of a single nanobelt yielding a Young's modulus of 38.2 ±1.8 GPa for a nanobelt of thickness 50 - 140 nm. Stan et al. [38] use a contact resonance AFM technique similar to Chen et al, observing 104 - 198 GPa for nanowires ranging from 25.5 to 134.4 nm in diameter. Several of these methods yield elastic modulus values lower than reported for the bulk; which is ~140 GPa in the [0001] direction [35].

2.5. Optical properties of ZnO

The optical properties of the nanowires may change depending on the growth conditions used (see chapter 3) before any form of strain has even been applied, therefore it is crucial to understand how the optical properties of ZnO can be observed and the data utilised to determine the force exerted on the nanowire array. Photoluminescence (see chapter 4) will be the preliminary technique used to assess the optical properties of the ZnO nanowires. Photoluminescence can be used to yield much data about the nanowires, such as band gap determination, impurity levels and defect detection and the overall quality of the material system. It has often been shown that altering the stoichiometry of the ZnO lattice, for example by growing the nanowires with an Oxygen rich environment leads to additional recombination sites within the band gap observed as a strong deep-level green emission [39].

It has been reported by Reynolds et al. [40] that this 2.4 eV (~516.60 nm) centered green emission is likely derived from a transition from two separate shallow donors to a deep acceptor. However for this work the strong UV emission peak shown in Fig. 2.3a-c will be investigated as it is the near band edge (NBE) emission peak and represents the band gap of the material. The visible broadband emission peak informs to the number of defects within the lattice and can be used to determine crystal quality; however the literature has shown that for a radius less than 30 nm the luminescent

properties of ZnO nanowires are entirely dominated by surface properties [41]; this will be discussed further in chapter 4. See Appendix I for a detailed explanation of the effect of point defects or acceptor / donor levels within the band-gap on optical properties.

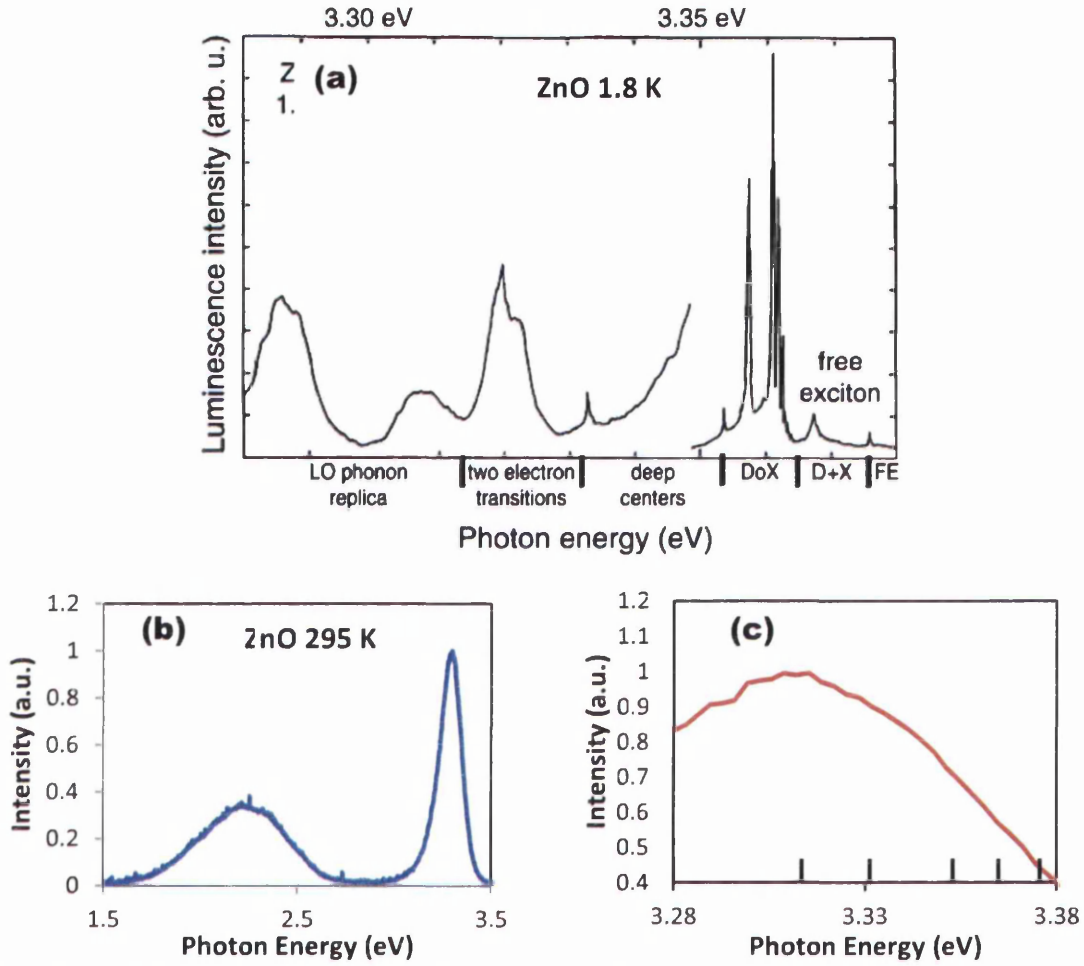

Figure 2.3. Shows a) UV luminescence spectrum of thin film ZnO at 1.8K (-271°C) with all contributions to spectra labeled, from[42], b) a typical photoluminescence spectra taken from a ZnO nanowire array created in this work using a 325nm HeCd excitation source and c) an enlargement of the NBE from b) matching the scale from a) with UV spectrum component dividers for comparison to a). See how although the exciton to bound to neutral donors (3.35 - 3.37 eV) dominates at reduced temperature when conducted at room temperature there is significant contribution from longitudinal-optical phonon interactions.

Fig. 2.3a. shows the luminescence spectra of thin film ZnO samples from [39] acquired at 1.8 K in liquid helium, where it can be observed that at 3.35 - 3.37 eV (~367.91 - 370.10 nm) multiple intense lines dominate from exciton bound to neutral donor bound (D^0X) transitions. However in the present work all optical experiments were conducted at room temperature (295 K) where it has been shown in the literature these lower energy longitudinal-optical (LO) phonon (free exciton replica) interactions

dominate [42]; as confirmed by the photoluminescence spectra in Fig. 2.3b,c. However work by Park et al [43] observing the temperature dependence of photoluminescence spectra of ZnO nanorods from 10 - 300 K suggest that the main contribution to UV emission at room temperature is from decomposition of bound excitons to free excitons due to increased thermal energy. In our spectra the longitudinal-optical-phonon replicas of these free excitons (FX-1LO) will constitute the majority of our observed near band edge UV emission peak. This is very promising when coupled with work by Yan et al. [44] who explain that the LO photon is very sensitive to both strain and defect formation.

Yan et al. [44] find that by subjecting a ZnO nanowire to compressive and tensile stresses results in a shift of the phonon peak to a higher and lower wavenumber, respectively. As room temperature photoluminescence is dominated by FX-1LO then any changes in the lattice such as defects or strain will directly correlate to a change in peak position that can be easily observed. It should however be noted that Ahn et al. [45] reported that discrepancies in the behaviour of UV emission peak can be related to surface defects causing different strengths of exciton-phonon coupling. This hypothesis was supported with an observed 52 meV redshift of UV emission peak position when ZnO nanowire diameter was reduced from 230 - 340 nm to 35 - 55 nm. Sub-section 2.5.2 shall explain crystallographic defects and examine their effect on optical properties on ZnO. Teklemichael and McCluskey [46] have reported that contributions from surface states have significant effect on the optical properties of ZnO nanowires, where they propose two major surface state level that exist just within the donor and acceptor levels, yielding a transition of approximately 1.84 eV (673.77 nm). For more information and diagrams see Appendix I. This section has discussed some on the origins of several emission wavelengths observed with photoluminescence, and will be built up on in section 4.4.

2.5.1. The effect of strain

The force applied by a cell as it proliferates around the substrate is intended to bend the nanowires significantly enough to provide the previously discussed spectral shifts in peak position. This section shall further explain the mechanisms that cause strain to affect photoluminescence peak position as well investigate whether the major cause of the observed peak shift is due to a change in band gap or as previously

discussed the inclusion of more levels within the band gap. Han et al. [47] use the electron beam of a HRTEM to bend and pin a single ZnO nanowire to a carbon coated TEM grid, allowing control of the strain applied by careful manipulation of the radius of curvature. By using cathodoluminescence they observed a significant broadening and red shift of the near band edge UV emission peak compared to an unbent nanowire. Reynolds et al. [48] use photoluminescence to observe that band gap increases due to compressive strain can be relieved by annealing the sample between 700 – 800° C. Zhang et al. [49] calculate that under uniaxial compressive strain ultra-thin ZnO nanowires undergo a band gap transition from direct to indirect due to a change in crystal structure from regular wurtzite to a more closely-packed hexagonal. This transition has also been investigated by Li et al. [50] who used density function theory to simulate the transition from direct to indirect, also observing a band gap increase with increasing compressive strain. Thus, further supporting that a compressive strain results in a blue shift of wavelength of photoluminescence shown in equation 2.2:

$$Eg = hc/\lambda \tag{2.2}$$

Xue et al. [51] use cathodoluminescence and HRTEM on a bent ZnO nanowire to report that the band edge UV emission will blue shift under compressive strain (on the inside of the nanowire) and red shift with tensile strain (on the outside of the nanowire). They observed the blue and red shift by profiling the cross-section of each side of the nanowire independently, obtaining a 40 meV (~1.63 nm) difference between compressive and tensile sides. Therefore it could be argued that the observed peak shifts would likely just be observed as a broadening of FWHM of near band edge emission peak when looking at the whole nanowire with a less spatially accurate system. However their nanowires have a diameter of 100 - 200 nm, and it has been reported by Xiang et al. [1] that strain will relax along the radial direction of a nanowire where the amount of relaxation increases with decreasing nanowire diameter. Therefore larger diameter nanowires will see an increased peak shift, but at the cost of additional force/mass required to bend/compress the nanowire.

2.5.2. Crystallographic defects

It has been explain how defects can affect the emission wavelength of photons that could drastically impair any devices ability to function correctly for the brief of this work (chapter 1). It is believed it is also fundamental to have an understanding of what defects are and how they can be created intentionally via doping to tune the optical properties of this works ZnO nanowires. Fig. 2.4 shows the Zn-O lattice with several different types of point defects; however large lattice defects such as edge, screw and threading dislocations are not covered here but an explanation of donor / acceptor levels due to defects and their affect on the band diagram of ZnO is covered in Appendix I.

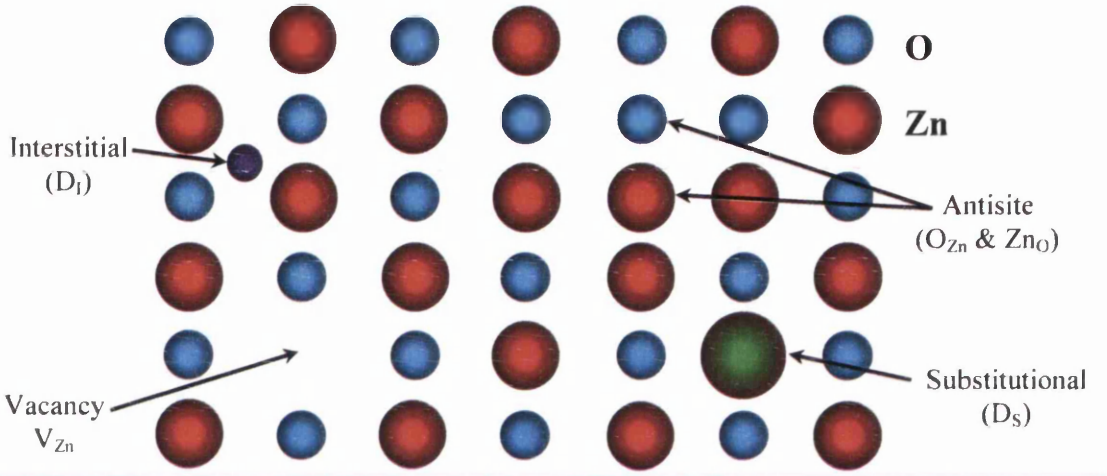

Figure 2.4. Diagram of point defects in ZnO, where uppercase letters represent the current atom or vacancy on the lattice site and subscript represent the normal occupation of the lattice site in a perfect crystal, adapted from [52, 53]. Where V_{Zn} is a missing Zn atom, O_{Zn} and Zn_O are an oxygen antisite atom on a zinc site and zinc antisite atom on a oxygen site respectively. D_S is a dopant atom on a subtitutional site and D_I on an interstitial site.

Fig. 2.4. shows a simple 2D example of a periodic arrangement of our zinc and oxygen atoms with some of the more common point defects that can occur within the crystal lattice labelled using Kroger-Vink notation. Point defects are where an atom is either missing or in an irregular place such as to break the periodicity of a perfect lattice. An atom may often be located between lattice sites and is referred to as an interstitial and schematically shown in the top left of the figure as a small purple atom. Interstitials are typically small foreign atoms from outside the lattice (as shown) or they can come from similar atoms within the lattice. Bottom left of Fig. 2.4. shows an atom missing from its lattice site and is referred to as a vacancy. Vacancy and interstitial defects can have a subtle effect on the electrical and optical properties of the material

system as they disturb not only the perfect geometric arrangement of atoms but also the chemical bonds between the atoms resulting in fluctuations of charge [52]. When interstitial and vacancy defects are in close proximity they are called a Frenkel defect because a single non impurity atom creates the interstitial and vacancy. Because there is no alteration to the total number of atoms a change of charge balance doesn't have to be considered. However the presence of a small quantity of Frenkel defects within the lattice does affect the Gibbs energy of the crystal [54], which can affect the Young's modulus of the material.

Top right of the image shows an antisite defect, which is when the atoms exchange position. It has been reported by Lin et al. [55] that antisite defects are one of the major contributors to the green band emission seen in the photoluminescence spectrum of ZnO, due to creating local recombination sites for indirect transition across the band gap. Bottom right shows the case where a foreign atom (or impurity) has been incorporated into a regular atomic site in the lattice, and is called a substitutional. As an impurity atom will be of a different valancy and have either more of less electrons then a charge discrepancy is introduced to the lattice resulting in a charge compensation mechanism occurring where by either one of the elements is oxidized, reduced or ion vacancies created [56]. Other more complex defects (dislocations) may also occur in the crystal lattice, however this introductory section is here only to show that a crystal lattice is never perfect and explain some of the basic types of point defects. The effect these imperfections have on the optical properties of ZnO will be discussed in further detail in chapter 4.

2.6. Summary

We have covered the majority of the most crucial fundamental ZnO nanowire theory, its basic properties and proceeded to go into further detail for optical and mechanical properties for a better understanding of the results and discussion chapters to follow. There has been heavy emphasis on using research results from the literature to help explain the properties of ZnO as they represent the scientific community's most recent understandings of the ZnO material system. Any sections that slowed the pace of this chapter can be found in Appendix I.

2.7. References

[1] B. Xiang, P. Wang, X. Zhang, S. a Dayeh, D. P. R. Aplin, C. Soci, D. Yu, and D. Wang, "Rational synthesis of p-type zinc oxide nanowire arrays using simple chemical vapor deposition.," *Nano Lett.*, vol. 7, no. 2, pp. 323–8, Feb. 2007.

[2] Y. F. Hsu, Y. Y. Xi, K. H. Tam, A. B. Djurišić, J. Luo, C. C. Ling, C. K. Cheung, A. M. C. Ng, W. K. Chan, X. Deng, C. D. Beling, S. Fung, K. W. Cheah, P. W. K. Fong, and C. C. Surya, "Undoped p-Type ZnO Nanorods Synthesized by a Hydrothermal Method," *Adv. Funct. Mater.*, vol. 18, no. 7, pp. 1020–1030, Apr. 2008.

[3] G. D. Yuan, W. J. Zhang, J. S. Jie, X. Fan, J. a Zapien, Y. H. Leung, L. B. Luo, P. F. Wang, C. S. Lee, and S. T. Lee, "p-Type ZnO nanowire arrays.," *Nano Lett.*, vol. 8, no. 8, pp. 2591–7, Aug. 2008.

[4] G. Substrates, M. Kadota, and M. Minakata, "Piezoelectric Properties of Zinc Oxide Films on," *IEEE Trans. Ultrason. Ferroelectr. Freq. Control*, vol. 42, no. 3, pp. 345–350, 1995.

[5] K. Takahashi, A. Yoshikawa, and A. Sandhu, *Wide bandgap semiconductors: fundametal properties and modern photonic and electronic devices*. Springer, 2007, p. 460.

[6] F. Xu, Q. Qin, A. Mishra, Y. Gu, and Y. Zhu, "Mechanical properties of ZnO nanowires under different loading modes," *Nano Res.*, vol. 3, no. 4, pp. 271–280, Mar. 2010.

[7] M. Sakurai, Y. G. Wang, T. Uemura, and M. Aono, "Electrical properties of individual ZnO nanowires.," *Nanotechnology*, vol. 20, no. 15, p. 155203, Apr. 2009.

[8] J.-H. Choy, E.-S. Jang, J.-H. Won, J.-H. Chung, D.-J. Jang, and Y.-W. Kim, "Soft Solution Route to Directionally Grown ZnO Nanorod Arrays on Si Wafer; Room-Temperature Ultraviolet Laser," *Adv. Mater.*, vol. 15, no. 22, pp. 1911–1914, Nov. 2003.

[9] S.-M. Peng, Y.-K. Su, L.-W. Ji, S.-J. Young, C.-N. Tsai, J.-H. Hong, Z.-S. Chen, and C.-Z. Wu, "Transparent ZnO Nanowire-Network Ultraviolet Photosensor," *IEEE Trans. Electron Devices*, vol. 58, no. 7, pp. 2036–2040, Jul. 2011.

[10] A. Tarat, R. Majithia, R. A. Brown, M. W. Penny, K. E. Meissner, and T. G. G. Maffeis, "Surface Science Synthesis of nanocrystalline ZnO nanobelts via pyrolytic decomposition of zinc acetate nanobelts and their gas sensing behavior," *Surf. Sci.*, vol. 606, no. 7–8, pp. 715–721, 2012.

[11] C. Chen, J. Huang, J. Song, Y. Zhou, L. Lin, P. Huang, and C. E. T. Al, "Anisotropic Outputs of a Nanogenerator from Oblique-Aligned ZnO Nanowire Arrays," *ACS Nano*, vol. 5, no. 8, pp. 6707–6713, 2011.

[12] J. Liu, C. Guo, C. M. Li, Y. Li, Q. Chi, X. Huang, L. Liao, and T. Yu, "Carbon-decorated ZnO nanowire array: A novel platform for direct electrochemistry of enzymes and biosensing applications," *Electrochem. commun.*, vol. 11, no. 1, pp. 202–205, Jan. 2009.

[13] T. Voss, I. Kudyk, L. Wischmeier, and J. Gutowski, "Nonlinear optics with ZnO nanowires," *Phys. Status Solidi*, vol. 246, no. 2, pp. 311–314, Feb. 2009.

[14] A. V. Kachynski, A. N. Kuzmin, M. Nyk, I. Roy, and P. N. Prasad, "Zinc Oxide Nanocrystals for Non-resonant Nonlinear Optical Microscopy in Biology and Medicine," *J. Phys. Chem. C*, vol. 112, no. 29, pp. 10721–10724, 2008.

[15] Y. Qin, X. Wang, and Z. L. Wang, "Microfibre-nanowire hybrid structure for energy scavenging.," *Nature*, vol. 451, no. 7180, pp. 809–13, Feb. 2008.

[16] C.-C. Hsiao, K.-Y. Huang, and Y.-C. Hu, "Fabrication of a ZnO Pyroelectric Sensor," *Sensors*, vol. 8, no. 1, pp. 185–192, Jan. 2008.

[17] R. A. Laudise and A. A. Ballman, "Hydrothermal synthesis of Zinc Oxide and Zinc Sulfide," *J. Phys. Chem.*, vol. 64, no. 5, pp. 688–691, 1960.

[18] S. Baruah and J. Dutta, "Hydrothermal growth of ZnO nanostructures," *Sci. Technol. Adv. Mater.*, vol. 10, no. 1, p. 013001, Jan. 2009.

[19] C. F. Klingshirn, *Zinc Oxide: from Fundamental Properties Towards Novel Applications*. Springer, 2010, p. 359.

[20] U. Rossler and D. Strauch, "Group IV Elelments and Compoints - Lattice Properties," in in *Semiconductors*, Springer-Verlag, 2001.

[21] V. A. Coleman and C. Jagadish, "Basic Properties and Applications of ZnO," in in *Zinc Oxide Bulk, Thin Films and Nanostructures*, C. Jagadish and S. Pearton, Eds. Elsevier, 2006, p. 600.

[22] J. H. He, C. S. Lao, L. J. Chen, D. Davidovic, and Z. L. Wang, "Large-scale Ni-doped ZnO nanowire arrays and electrical and optical properties.," *J. Am. Chem. Soc.*, vol. 127, no. 47, pp. 16376–7, Nov. 2005.

[23] K. J. Pascoe, *Chemical and Physical Properties of Materials for Electrical Engineers*. Wiley-Blackwell, 1973, p. 324.

[24] J. Chen, J. Wang, R. Zhuo, D. Yan, J. Feng, F. Zhang, and P. Yan, "The effect of Al doping on the morphology and optical property of ZnO nanostructures prepared by hydrothermal process," *Appl. Surf. Sci.*, vol. 255, no. 7, pp. 3959–3964, Jan. 2009.

[25] P. Xu, "The electronic structure and spectral properties of ZnO and its defects," *Nucl. Instruments Methods Phys. Res. Sect. B Beam Interact. with Mater. Atoms*, vol. 199, pp. 286–290, Jan. 2003.

[26] R. B. M. Cross, M. M. De Souza, and E. M. Sankara Narayanan, "A low temperature combination method for the production of ZnO nanowires.," *Nanotechnology*, vol. 16, no. 10, pp. 2188–92, Oct. 2005.

[27] Y. Gu, I. L. Kuskovsky, M. Yin, S. O'Brien, and G. F. Neumark, "Quantum confinement in ZnO nanorods," *Appl. Phys. Lett.*, vol. 85, no. 17, p. 3833, 2004.

[28] S. Pearton, "Recent progress in processing and properties of ZnO," *Prog. Mater. Sci.*, vol. 50, no. 3, pp. 293–340, Mar. 2005.

[29] S. Xu, W. Guo, S. Du, M. M. T. Loy, and N. Wang, "Piezotronic Effects on the Optical Properties of ZnO Nanowires.," *Nano Lett.*, vol. 12, no. 11, pp. 5802–7, Nov. 2012.

[30] O. Manasreh, *Semiconductor Heterojunctions and Nanostructures*. McGraw Hill, 2005, p. 556.

[31] A. Karoui and A. Kechiantz, "Quantum Mechanics Design of Two Photon Processes Based Solar Cells," in in *Some Applications of Quantum Mechanics*, M. R. Pahlavani, Ed. InTech, 2012, p. 424.

[32] S. Brovelli, R. D. Schaller, S. A. Crooker, F. García-Santamaría, Y. Chen, R. Viswanatha, J. A. Hollingsworth, H. Htoon, and V. I. Klimov, "Nano-engineered electron-hole exchange interaction controls exciton dynamics in core-shell semiconductor nanocrystals.," *Nat. Commun.*, vol. 2, p. 280, Jan. 2011.

[33] V. Nikitenko, "Optics and Spectroscopy of Point Defects in ZnO," in in *Zinc Oxide — A Material for Micro- and Optoelectronic Applications*, N. H. Nickel and E. Terukov, Eds. Netherlands: Springer Netherlands, 2005, pp. 69–81.

[34] U. O□zgu□r, Y. I. Alivov, C. Liu, A. Teke, M. a. Reshchikov, S. Dog□an, V. Avrutin, S.-J. Cho, and H. Morkoc□, "A comprehensive review of ZnO materials and devices," *J. Appl. Phys.*, vol. 98, no. 041301, pp. 1–103, 2005.

[35] C. Q. Chen, Y. Shi, Y. S. Zhang, J. Zhu, and Y. J. Yan, "Size Dependence of Young's Modulus in ZnO Nanowires," *Phys. Rev. Lett.*, vol. 96, p. 075505, 2006.

[36] J. Song, X. Wang, E. Riedo, and Z. L. Wang, "Elastic property of vertically aligned nanowires.," *Nano Lett.*, vol. 5, no. 10, pp. 1954–8, Oct. 2005.

[37] H. Ni and X. Li, "Young's modulus of ZnO nanobelts measured using atomic force microscopy and nanoindentation techniques.," *Nanotechnology*, vol. 17, no. 14, pp. 3591–7, Jul. 2006.

[38] G. Stan, C. V. Ciobanu, P. M. Parthangal, and R. F. Cook, "Diameter-Dependent Radial and Tangential Elastic Moduli of ZnO Nanowires," *Nano Lett.*, vol. 7, no. 12, pp. 3691–3697, Dec. 2007.

[39] E. S. Jung, J. Y. Lee, and H. S. Kim, "Structural and Optical Characteristics of ZnO Films with Oxygen Content," *J. Korean Phys. Soc.*, vol. 47, no. November, pp. 480–484, 2005.

[40] D. C. Reynolds, D. C. Look, and B. Jogai, "Fine structure on the green band in ZnO," *J. Appl. Phys.*, vol. 89, no. 11, p. 6189, 2001.

[41] I. Shalish, H. Temkin, and V. Narayanamurti, "Size-dependent surface luminescence in ZnO nanowires," *Phys. Rev. B*, vol. 69, no. 24, pp. 1–4, Jun. 2004.

[42] C. Klingshirn, R. Hauschild, H. Priller, M. Decker, J. Zeller, and H. Kalt, "ZnO rediscovered — once again!?," *Superlattices Microstruct.*, vol. 38, no. 4–6, pp. 209–222, Oct. 2005.

[43] W. I. Park, Y. H. Jun, S. W. Jung, and G.-C. Yi, "Excitonic emissions observed in ZnO single crystal nanorods," *Appl. Phys. Lett.*, vol. 82, no. 6, p. 964, 2003.

[44] B. Yan, R. Chen, W. Zhou, J. Zhang, H. Sun, H. Gong, and T. Yu, "Localized suppression of longitudinal-optical-phonon-exciton coupling in bent ZnO nanowires.," *Nanotechnology*, vol. 21, no. 44, p. 445706, Nov. 2010.

[45] C. H. Ahn, S. K. Mohanta, N. E. Lee, and H. K. Cho, "Enhanced exciton-phonon interactions in photoluminescence of ZnO nanopencils," *Appl. Phys. Lett.*, vol. 94, no. 26, p. 261904, 2009.

[46] S. T. Teklemichael and M. D. McCluskey, "Acceptor and surface states of ZnO nanocrystals: a unified model.," *Nanotechnology*, vol. 22, no. 47, p. 475703, Nov. 2011.

[47] X. Han, L. Kou, X. Lang, J. Xia, N. Wang, R. Qin, J. Lu, J. Xu, Z. Liao, X. Zhang, X. Shan, X. Song, J. Gao, W. Guo, and D. Yu, "Electronic and Mechanical Coupling in Bent ZnO Nanowires," *Adv. Mater.*, vol. 21, no. 48, pp. 4937–4941, Dec. 2009.

[48] D. Reynolds, "Optical properties of ZnO crystals containing internal strains," *J. Lumin.*, vol. 82, no. 2, pp. 173–176, Aug. 1999.

[49] Y. Zhang, Y.-H. Wen, J.-C. Zheng, and Z. Zhu, "Direct to indirect band gap transition in ultrathin ZnO nanowires under uniaxial compression," *Appl. Phys. Lett.*, vol. 94, no. 11, p. 113114, 2009.

[50] S. Li, Q. Jiang, and G. W. Yang, "Uniaxial strain modulated band gap of ZnO nanostructures," *Appl. Phys. Lett.*, vol. 96, no. 21, p. 213101, 2010.

[51] H. Xue, N. Pan, M. Li, Y. Wu, X. Wang, and J. G. Hou, "Probing the strain effect on near band edge emission of a curved ZnO nanowire via spatially resolved cathodoluminescence.," *Nanotechnology*, vol. 21, no. 21, p. 215701, May 2010.

[52] D. A. Neamen, *Semiconductor Physics and Devices: Basic Principles*, 3rd ed. McGraw Hill, 2003, p. 729.

[53] R. J. D. Tilley, *Defects in Solids*. John Wiley & Sons Ltd, 2008, p. 400.

[54] R. J. D. Tilley, *Understanding Solids: The Science of Materials*. John Wiley & Sons Ltd, 2005, p. 616.

[55] B. Lin, Z. Fu, and Y. Jia, "Green luminescent center in undoped zinc oxide films deposited on silicon substrates," *Appl. Phys. Lett.*, vol. 79, no. 7, p. 943, 2001.

[56] A. R. West, *Basic Solid State Chemistry*. Scotland, Great Britain: Joh Wiley & Sons Ltd., 1988, p. 415.

Chapter 3. Fabrication Methods for Zinc Oxide Nanowires

3.1. Introduction

The flurry of recent research in ZnO materials and devices over the last few years has been mainly due to the introduction of new low temperature hydrothermal fabrication methods that yield reproducible results. The following chapter will review and explore the most recent advances in methods and recipes to fabrication of ZnO nanowires using solution based low temperature techniques, such as chemical, sol-gel and hydrothermal synthesis, electro-spinning etc... Early on in the project it was decided that in order to combine the intended second harmonic generation optical bench with a typical life sciences inverted optical microscope with an incubation chamber (to maintain 5 % CO_2 and 37 °C – see chapter 5) setup then all images would have to be captured in transmission. Initially research began using furnaces with GaN and Si substrates as these were traditionally used to obtain aligned nanowire arrays. However, glass cover slips would ideally be required for seamless integration into the protocols, equipment and environment of a life sciences laboratory as neither quartz nor sapphire (both optically transparent in the wavelengths of interest) could be easily be cut to sufficient size to allow at the very least 48-well plates to be used. However, Qin et al. [1] reported that the hydrothermal technique could be used to fabricate ZnO nanowires on any substrate due to the low temperature (< 90 °C) of the technique; and so work soon began to introduce this technique to Swansea's laboratory. This chapter will therefore concentrate on the hydrothermal synthesis method exploring the effect of the variables on obtained ZnO nanowires as the knowledge will be needed for chapter 7.

3.2. High temperature chemical vapour deposition

At the start of the project much expertise and equipment for use of the Au catalyst based high temperature (>1000 °C) Vapour Liquid Solid (VLS) Chemical

Vapour Deposition (CVD) technique to fabricate arrays of zinc oxide nanowires existed within the department. Therefore this was the method used initially until it was decided to use glass substrates and the hydrothermal method was adopted. However before that decision substantial time and effort was invested refining recipes to fabricate highly ordered arrays of ZnO nanowires on GaN substrates (see Fig. 3.1) using a recipe similar to work by Maffeis et al. [2]. The following method was used to obtain the well aligned ZnO nanowire array in Fig. 3.1. GaN substrates were acetone cleaned then sputter coated with a 3 - 5 nm thick Au layer and placed 6 - 8 cm from the middle of the furnace towards the exhaust. A ceramic boat containing 1:1 weight mixture of ZnO and graphite (source) powders was placed in the middle of the furnace, upstream from the substrates. The furnace was set to 1050 °C yielding temperatures of around 1030 °C and 960 °C for source and substrate respectively, and the temperature was maintained for up to 1 hour under a 50 sccm Ar flow with 2 % O_2.

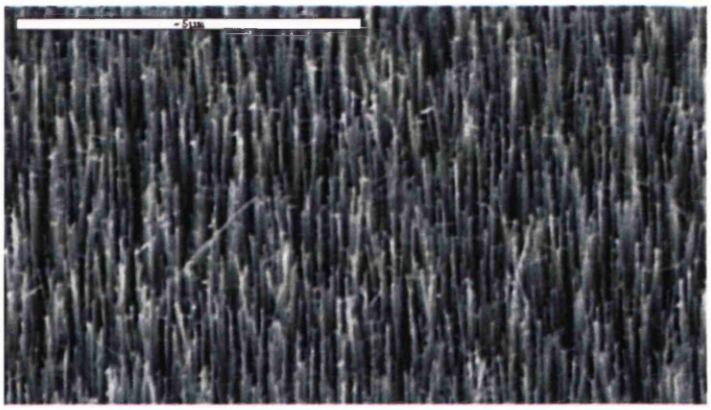

Figure 3.1. ZnO nanowire array fabricated using the Au catalyst VLS-CVD technique. Scale bar is 5µm.

The VLS method occurs in 3 stages. Firstly the sputtered Au colloids melt forming liquid droplets on the substrate surface and the source is vaporised above 907 °C [3] due to the inclusion of the graphite that thermally decomposes ZnO forming CO and Zn. The vapour is carried on the 2 % O_2 flow towards the substrates and is absorbed, diffusing into the liquid Au droplets until super-saturation of ZnO occurs whereby nucleation at the phase transition between liquid/solid (droplet/substrate) interfaces leads to growth of ZnO crystal. The VLS method has a substantial growth rate, yielding nanowires of 5 – 10 µm within the hour in this work; and also allows control of nanowire diameter by altering the Au thickness on the substrate, with greater control obtained by using mono-disperse Au colloids.

While this technique has been shown in the literature [4] to create extremely well aligned and high aspect ratio ZnO nanowires, it could however no longer be used when it was concluded that optically transparent substrates would be required for confocal microscopy. And thus the project was redirected into application of the hydrothermal method to fabricate arrays of ZnO nanowires on the No. 0 (90 - 130 μm) glass cover slips required for subsequent optical and biological phases of the project.

3.3. Low temperature hydrothermal growth methods

The recent renewed interest in ZnO nanomaterials synthesis has stemmed from the recent advances in production of p-type ZnO, as reported by Xiang et al. [5] using a modified CVD method. However continued research and improvement of low temperature growth methods such as electrodeposition, sol-gel, polymer assisted growth, and hydrothermal has begun to yield several attempts to produce p-type ZnO [6]. The increased research activity into low temperature methods is certainly due such advances in production of p-type material, and additionally it is becoming more beneficial to avoid high temperature based techniques which can be costly and offer no support for several lithography based techniques now that low temperature based techniques can fabricate p-type material. Patterning for device fabrication is extremely difficult using traditional vapour transport standard lithography techniques due to the high temperature required to melt Zn and the low melting temperature of resist. However, recently Wei et al. [7] reported that two lasers could be used to create an interference pattern to selectively etch a layer of resist to fabricate a mask/template allowing control of where ZnO nanostructure formation occurs using the hydrothermal method. A similar method by Xu et al. [8] used e-beam lithography to pattern a resist layer that sits above the seed layer controlling the position of the nanowires.

The method described by this work as the 'hydrothermal' method is more accurately known as the thermal decomposition of hydroxide precursors and was first demonstrated by Verges et al. [9] in 1990. There are several growth procedures that fall under the hydrothermal tag, which simply explains the field of solution based growth rather than the technique, as 'hydrothermal' can be ascribed to production via hot water; where the main mechanism is simply supersaturation to drive crystal precipitation, typically achieved at high pressure and temperature. The generally accepted growth

mechanism for the majority of aqueous solution routes is the precipitation of ZnO by the hydrolysis of Zn salts in a basic solution. For each wet chemical technique it is the abundance of Zn^{2+} and the intermediate complexes contained within that determines the fate of the precipitate. It is by controlling the environment of the solution containing the Zn^{2+} that one may control the intermediates formed; where ZnO is obtained by dehydration of these intermediates. For example it has been reported by Baruah and Dutta [10] that by changing the pH of the growth solution by titrating the solution with either HCl or NaOH that the morphology of the obtained nanostructures can be controlled. The reactions governing the growth of nanostructures in aqueous systems are generally considered to be in a reversible equilibrium, whereby the precipitation of ZnO is the systems method to minimise free energy [11].

As discussed in chapter 2, wurtzite ZnO is grown with polar c-axis direction (0001) facets that comprise of alternating Zn^{2+} terminated and O^{2-} terminated surfaces [12]. To achieve one-dimensional growth, the surface chemistry between the polar (0001) and non polar $(10\bar{1}0)$ $(01\bar{1}0)$, $(\bar{1}100)$, $(\bar{1}010)$, $(0\bar{1}10)$. $(1\bar{1}00)$ prism planes (see appendix I) needs to be exploited such that the growth rate of these facets may be promoted or suppressed to control nanowire morphology. The reason for one-dimensional preferred growth has been attributed to the different in growth rates of the crystal facets by Baomei et al. [13], where they report that the velocities hkil for the hydrothermal growth method are such that (0001) > (0110) > (1000). To better understand this let's first explain the growth mechanism. When a ZnO nucleus is first formed (or found in the case of seeded substrates) then due to the high energy (caused by atomic layer arrangement) of the polar facets, precursor molecules in the solution are preferentially adsorbed onto a polar facet; likely due to the electrostatics of the facets in solution [14]. The reason for this preferential attachment of new precursor ions is simple, energy. Denianets et al. [15] have reported the activation energies of the (0001), $(000\bar{1})$, and $(10\bar{1}0)$ faces equal to 59 ±3, 66 ±3 and 68 ±3 kJ/mol respectively; indicating that the (0001) faces can also grow at somewhat lower critical supersaturation than the $\{10\bar{1}0\}$ and $(000\bar{1})$ faces. This however leads to a polarity change as once the layer is completely filled the facet will have inverted polarity due to a Zn^{2+} terminated surface becoming a O^{2-} terminated one. Again this, provides a high energy surface for the other precursor molecules to adsorb to, with the process repeating yielding an accelerated c-axis [0001] direction growth rate [16]. This process is repeated until the non-polar facets are revealed. Therefore the key to control of this process is to control

the supply of precursors within the solution. Although the mechanism of nucleation and crystal growth within a supersaturated solution is not yet fully understood, it is generally believed that high precursor super saturation of the solution yields improved nucleation, whereas low super saturation favour crystal growth [17].

This is because a precipitate forms when a solute exceeds its solubility in an aqueous solution [18]. The formation of a precipitate involves supersaturation of the solution, nucleation, and then finally growth. Where a supersaturated solution contains more dissolved solute than would be possible under equilibrium conditions. The supersaturation level of the solution is important in hydrothermal growth as it can determine if the majority of growth is heterogeneous (i.e. grown on a surface, such as the nanowire arrays) or homogenous (i.e. grown in solution, such as colloids). Supersaturation is commonly defined as the ratio between the solute concentration in a supersaturated solution (C) and a solution at equilibrium conditions (C_{eq}), and therefore can be simply be written as [19].

$$S = C/C_{eq} \tag{3.1}$$

It has been reported by Govender et al. [20] that homogenous nucleation dominates in supersaturated solutions. This can be explained using equation 3.1, as for salts (C_{eq} typically of 0.1 to 1 kmol m^{-3}), precipitation (i.e. homogenous nucleation) requires a much higher degree of supersaturation (S ~ 1000) [21] compared with only 0.01 to 0.20 for crystallisation. However, a supersaturated solution will not spontaneously convert to form a solid, unless the solution is highly supersaturated and crystal nuclei are needed to begin crystal formation. Homogeneous nucleation can occur because ions present in the solution interact and collide due to constant motion resulting in formation of clusters that become a crystal nucleus; however precipitation can only proceed if S > 1. Therefore it becomes beneficial to provide nucleation sites, typically by coating a substrate with crystals of the same element(s) that are to be grown, to seed the growth providing a template from which to grow.

3.4. Importance of ZnO thin film 'Seed Layers'

It is well supported in the literature that ZnO seed layer properties affect the subsequent growth of ZnO nanowires using the hydrothermal growth technique, whether due to seed layer thickness [22], grain size [23] or surface roughness [24]. It was even shown in this work that ZnO nanowire growth rate was significantly affected by ZnO seed layers with different roughness and grain size; with the growth rate decreasing with increasing roughness [25]. As with all chemical deposition via aqueous solution based techniques the growth of wurtzite ZnO on any substrate requires the initial step of heterogeneous nucleation. Therefore a seed layer is required to be coated onto the substrate to provide a point of nucleation to start deposition of ZnO, and it is the properties of this layer that can affect the final morphology of the ZnO nanowires.

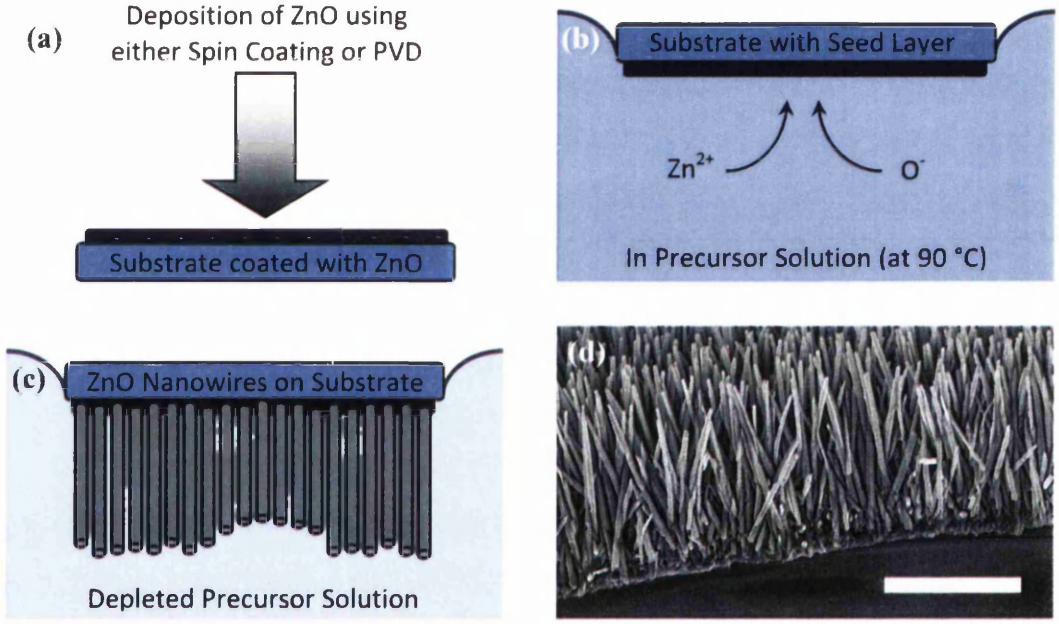

Figure 3.2. Diagram showing the steps of the hydrothermal growth process, where a) the substrate is coated in ZnO grains using spin coating or a ZnO film using PVD, b) ZnO coated substrate is flipped upside down and floated on surface of precursor solution, c) ZnO nanowires have been created as well as colloids due to homogenous nucleation which led to depletion of precursors and d) SEM of final product. Scale bar 2 µm.

It is well accepted that careful fabrication of the seed layer is key to obtaining reproducible growth. Many groups have created a seed layer by applying a solution of ZnO nano-particles to the substrate and allowing them to air dry [26], [27]. Greene et al. [28] use thermogravimetry (TG) and differential thermal analysis (DTA) to observe that at temperatures exceeding 337 °C zinc acetate dihydrate will have fully thermally

decomposed into ZnO; providing an easier route to ZnO nanoparticle derived seed layers than using the older Bahenmen et al. method to fabricate colloidal ZnO [29]. Cross et al. [30] deposit their seed layer using an RF magnetron sputtering system, this technique has the advantage creating uniform thin films without requiring the substrate to be heated. In this work two methods were used, spin coating and physical vapour deposition to create a coating of ZnO grains on the surface of the substrate, used as the template for growth and initiation of heterogeneous nucleation in the solution. The seed particles are nucleation centres for the nanowires and they undergo Ostwald ripening during the initial stages of growth. This accounts for the fact that the nanowires are much wider than the seed crystals. The solubility of small crystals as a function of size is given by the Ostwald– Freundlich equation:

$$c(r) = c_0 e^{\frac{\gamma V}{rkT}} \tag{3.2}$$

where c is the solubility, c_0 the bulk solubility, r is the crystal size, γ is the surface free energy, V the molecular volume, k the Boltzmann constant and T the absolute temperature. Equation 3.2 shows that the solubility increases with decreasing size, therefore, the smaller seed crystals tend to dissolve and deposit on larger particles. Where they combine together to reduce interfacial free energy [31]. It follows that larger seed layer grains have a higher supersaturation and a higher initial growth rate, giving them a greater likelihood of developing into nanowires [23]. According to C. Xu et al. [23] this is the main mechanism controlling nanowire density and therefore seed layer properties and their effect on nanowire morphology will be extensively investigated in section 7.5. The seed layer is vitally important as it lowers the interfacial energy and therefore the nucleation barrier between ZnO nuclei and the substrate. Also it has been reported by Qui et al. [32] that the inclusion of a seed layer can promote oriented growth of the nanowires on the substrate via an epitaxial growth mechanism, provided that the seed layer itself is of good quality.

Given the importance of the ZnO seed layer for hydrothermal growth as the starting point of heterogeneous nucleation, the following is a selection of current hypotheses of the seed layers involvement in final nanowire morphology. Ji et al. [22] report that the morphology of ZnO nanowires strongly depends on the thickness of their

RF magnetron sputtered ZnO seed layers. They observe an increase in nanowire diameter from 50 to 130 nm as well as a decrease in density from 110 to 60 μm^{-2} while the seed layer thickness is varied from 20 to 1000 nm. Similar to the results observed in Fig. 7.20. (p.149) C. Xu et al. [23] suggest that larger seed layer grains would have a higher supersaturation and a higher initial growth rate, giving them a greater likelihood of developing into nanowires, therefore directly controlling final nanowire array density. Also, Y. Lee et al. [24] report that vertical alignment appears most prominent on thicker seed layers due to the increased density. This literature ties in well to work by G. Kenanakis et al. [33] who observe that seed layer grain size increases with increasing film thickness; likely due to the additional time atoms have to coalesce. Therefore it could be rashly concluded that thicker seed layer lead to better alignment due to grain size controlling initial nanowire morphology mechanism.

It should be noted that the time between making the precursor solution and adding the seed layer covered substrate in Fig. 3.2 b. has a significant effect on the final morphology of the nanowires. It has been reported by Govender et al. [20] that the size of the crystallites comprising films depends largely on when the ZnO seed layer covered substrate is immersed in the water bath. If the substrate is added before the solution reaches set temperature the seed layer will dissolve and no nanowires will form. If it is added when the solution reaches set point (90 °C) then no homogeneous precipitation occurs and a dense array of long nanowires is obtained. However, if the sample is placed in the solution > 30 minutes after 90 °C is reached then a sparsely populated array of short nanowires is obtained as homogeneous precipitation of ZnO colloids has exhausted the solution. Therefore in this work care was always taken to preheat 90 % of the de-ionised water while the other 10 % was used to dissolve the chemicals, this way the solution (after a quick 1 – 2 minute stir) and substrate were added to the bath together; allowing every experiment to have the worked precursor concentration rather than an exhausted one. However even the 1 – 2 minutes given to stir 100 % of the solution at the derived 81.3 °C temperature after mixture would have been sufficient enough time for formation of ZnO crystal nuclei before the substrate is added [32] yielding faster crystal growth. The specifics of each seed layer coating method will be discussed next.

3.4.1. Spin Coating Seed Layers

The 0.1 M seed solution was created by dissolving 2.195 g of zinc acetate dihydrate [$C_4H_6O_4Zn{\cdot}2(H_2O)$] (zinc acetate) in 100 ml of ethanol at room temperature and stirring for 30 minutes (at 60 °C) followed by 30 minutes in sonic bath. The substrates were sonicated in acetone, ethanol, isopropanol and de-ionised water for 10 minutes each, and subsequently nitrogen dried and placed on a hotplate in air at 165 °C for 10 minutes to remove absorbed moisture. Solvent cleaned substrates were further cleaned by oxygen plasma (Emitech K1050X Plasma Asher) at 80 Watts with 30 mm^3/s oxygen flow rate for 15 minutes to remove any remaining hydrocarbons from the substrates, then placed on a hotplate in air at 165 °C to maintain temperature. Hot substrates were individually placed on the spin coater (GME PRS14e) and 10 µl of seed solution added with a (Gilson) micro pipette to the substrate before subsequent spinning at 3000 rpm for 30 seconds. Once finished the substrate is immediately put back on the hotplate to maintain temperature, as the process is repeated again. This can be done multiple times, but only twice per substrate in this work. When the final spin coat is completed the substrates with zinc acetate films were annealed on a hotplate in ambient air at 360 °C for 15 minutes to form ZnO crystals with preferential crystallographic orientation to (002) as reported by Ohyama et al. [34].

However, due to the spinning of the substrate and the solution being forced away from the centre the layer was heterogeneous in nature, yielding a non monodisperse distribution of nanowire morphology across the substrate as the hydrothermal growth method is seed layer sensitive [28]. This 'crowning effect' can be minimised by careful investigation of substrate surface hydrophobicity and choosing solvents of different viscosity. More importantly the spin coating method is very sensitive and can be quite difficult to reproduce, even subtle changes in the environment can affect seed layer formation. For example, Lee et al. [24] report significant changes in nanowire morphology using seed layers spin coated at different relative humidity. Also Yamabi et al. [35] have observed changes in ZnO nanowire array density grown on different substrates. Greene et al. report that the texture of acetate derived seed layers is likely not due to ZnO-substrate interaction. It could therefore be concluded that the driving force behind the observed differences between substrates of different materials is likely due to hydrophobicity determining the thickness of the seed layer. It is well established that seed layer thickness plays an important role in determining final ZnO nanowire morphology [33], and has been observed in this work also, see sub-section 7.5.2. Use of

non-solution based seed layer deposition techniques would avoid such issues with substrate properties, and therefore Physical Vapour Deposition (PVD) was an investigated replacement.

3.4.2. PVD Seed Layers

The literature shows that sputter deposition has received much interest for fabrication of ZnO thin films in recent years due to its advantages over other techniques, such as low substrate temperatures (down to ambient), good film adhesion (spin coating would often peel if substrates were not cleaned correctly, see Fig. 7.18.), and good uniformity of thickness and density. Sputter deposition is a PVD technique whereby plasma is formed and used to bombard a target ejecting material towards a substrate. Modern PVD systems use magnetrons that create strong electro-magnetic fields that are used to confine plasma ions to the immediate area around the target, improving deposition rate as more target material is ejected. The chamber gas(es) are typically inert but can be carefully selected to react with sputtered material. Investigation of the gas pressure is crucial to fabrication of high quality ZnO thin films using any PVD system. This is because at higher gas pressures the increased concentration of gas atoms reduces the mean free path of the sputtered ions, reducing their energy and therefore altering the way they interact with the substrate. This has been shown in the literature, where Zhu et al. [36] have reported that a reduction of chamber pressure yields improved crystalline quality due to increased kinetic energy of particles resulting in high surface mobility.

Fig. 3.3. shows the working principle of the sputtering method adopted in this work to create ZnO thin films of uniform thickness. PVD is essentially the formation of an inert plasma which is used to bombard our target ejecting atoms to be deposited. The plasma is formed from the argon gas introduced to the chamber by use of an electric field applied between the target and substrate. The field ionises the argon atoms creating cations (positively charged ions) that are subsequently accelerated towards the cathode (negatively charged target), ejecting target atoms and electrons. The ejected atoms often adhere to the substrate and if conditions are favourable they will coalesce to form a thin film. Meanwhile the ejected electrons are restrained by the magnetic field created by the magnetron, increasing the ionisation rate of argon due to the reduced mean free path within the field; therefore increasing the ejection/deposition rate.

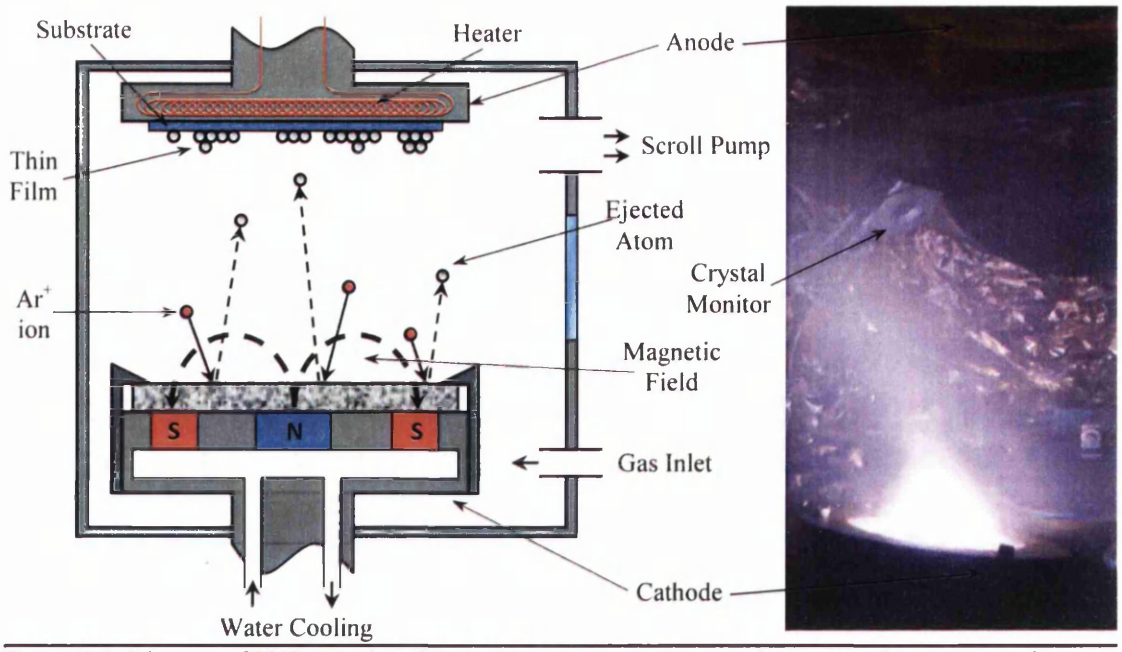

Figure 3.3. Diagram of PVD chamber showing the many components of the sputtering process, with photograph showing inside deposition chamber of Kurt Lesker 75 during operation for comparison.

It is well established that the alignment of the nanowires greatly depends on the crystalline quality and preferred orientation of the ZnO thin film they grow upon, where subtle changes in sputtering parameters can greatly influence final morphology and alignment of both the seed layer and nanowires. The Thornton model [37] (see Fig. 3.4.) is a well established method to determine the microstructure of sputtered thin films based on argon pressure and substrate temperature. In this work it was decided not to heat the substrate to avoid softening of the 80 - 130 µm thick glass cover slip substrates. Given our inability to heat the substrates then by consulting the Thornton model using the values below would suggest our films to be of porous nature with unorganized crystallites yielding rough surfaces [38]. This is likely due to energy being insufficient for deposited atoms to coalesce before the next layer has been deposited meaning that any slight morphology on the substrate would be highly influential on the resulting seed layer.

However work by Bin et al. [39] has shown that addition of oxygen to the chamber can compensate for the lack of substrate heating, dropping growth rate but improving c-axis orientation of the thin film deposited. Interestingly it has been shown by Lee et al. [40] that the ZnO thin film preferred crystallographic orientation and grain size is dependent on film thickness; this is supported in sub section 7.5.1. They report that generally films with thicknesses less than 0.5 µm have a columnar structures where

the c-axis is well orientated normal to the substrate surface; however, as thickness was increased the intensity of (002) decreased compared to other peaks. The c-axis orientation is often observed in sputtered polycrystalline films even on a glass substrate, and it is often the preferred orientation, likely due to the c-plane of ZnO crystallites being the most densely packed (see Fig. 7.48a. p.185).

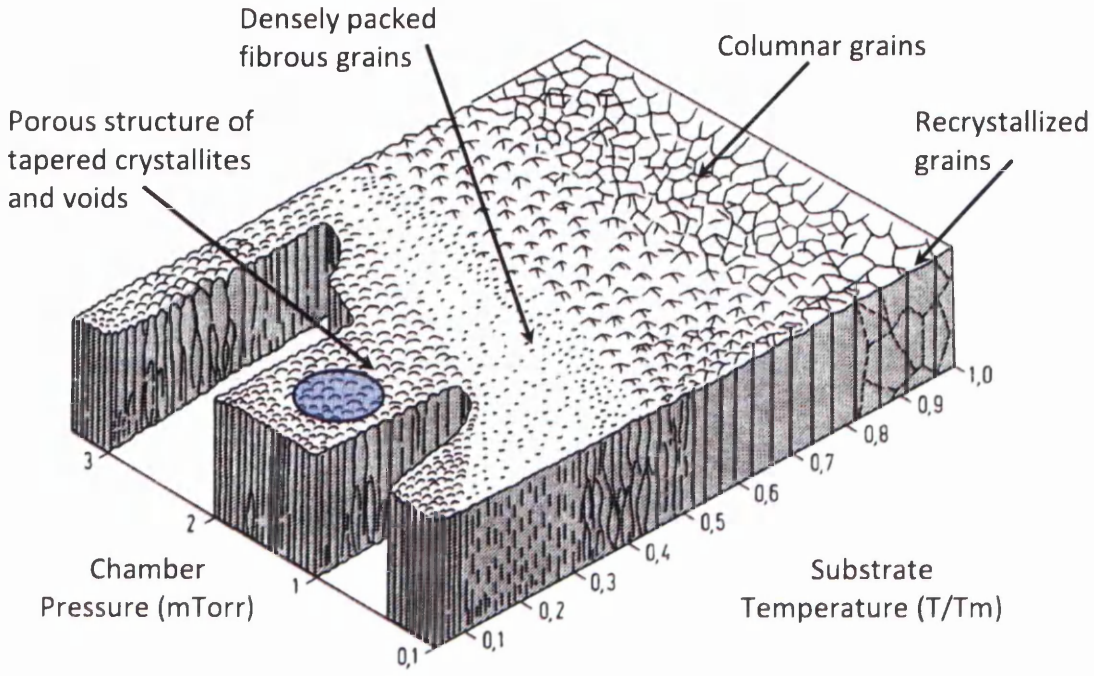

Figure 3.4. The Thornton structure model showing changes in thin film morphology with respect to Argon pressure and substrate temperature, adapted from [38]. T and Tm are substrate and melting temperatures, respectively.

In this work a Kurt Lesker 75 PVD system was used to deposit ZnO seed layers on any substrate. It has been reported by Yoshino et al. [41] that the orientation of ZnO films was disordered when the substrate surface was rough. They investigated the effect of substrate material system on sputtered ZnO films using Al, Au, Ni, Cu and glass substrates; showing that ZnO films on glass, Au and Al had good c axis orientation. A ZnO target (99.99 %) was used in the system to deposit 10 - 50 nm thick layers of ZnO on many different substrates 16 cm away, operating with a typical vacuum pressure of $\leq 1x10^{-5}$ Torr. Deposition was done at room temperature with an RF sputtering power of 70 W at 13.56 MHz in a 90 % argon to 10 % oxygen atmosphere with a gas flow rate such that the sputtering pressure was typically $\leq 2x10^{-3}$ Torr. For T / Tm in Fig. 3.4, T and Tm are substrate and melting temperatures, respectively.

The temperature of Swansea's class 1000 clean room is maintained at 21 °C which can be approximated to 300 K, and the melting temperature of ZnO is 1975 °C (see Table 2.1) which can be approximated to 2300 K; therefore T/Tm = 0.13. This value when combined with the chamber pressure typically used above allows the blue region shown in Fig. 3.4. to be established. According to the Thornton structure zone model, the parameters used in this work will yield seed layers consisting of crystallites and voids. However it has been shown by Zhang et al. [42] that a significant increase in film crystallinity can be obtained by increasing the O_2 / Ar gas ratio during sputtering due to a decrease in sputtering rate. This is further supported by R. Ondo-Ndong et al. [43] who report a decrease of the FWHM of the XRD obtained (002) peak from 0.73 to 0.32 with the addition of 10 % oxygen. For XRD spectra, a reduction in FWHM or increase in intensity of a single peak means the peak orientation is preferred and therefore the sample is of high crystal quality.

This crystal quality improvement is due to the method of thin film formation via sputtering, which typically occurs in the following fashion. Single atoms of the ejected material nucleate on the substrate surface, and if energy for atom migration is sufficiently large enough to coalesce with other atoms, small islands will form. Because the energy needed to evaporate a single atom is considerably less than for a pair of atoms, the growth of island dominates, and a thin film begins to form. This process is extremely substrate temperature sensitive as additional thermal energy with allow atoms to coalesce more rapidly. It has been shown by Y. J. Kim et al. [44] that an increase of energy due to use of higher substrate temperatures (typically exceeding 300 °C) will result in breaking of the Zn-O bond and subsequent re-evaporation of the deposited thin film instead of allowing atoms to move to stable sites. Therefore if the ejected material is deposited at room temperature the condensed atoms do not have enough kinetic energy and therefore mobility to move across atomic steps to fill positions of a lower potential energy; thus creating voids and imperfections in the thin film. G. Kumar et al. [45] profiled the effect of substrate temperature on the grain size and orientation of ZnO thin films using RF magnetron sputtering. They observed an increase in grain size from 11.72 to 48.52 nm for 100 to 300 °C, respectively. However, their XRD analysis showed preferential (002) c-axis alignment for all samples. Therefore, as it has been reported by G. Kenanakis et al. [33] that seed layer grain size determines ZnO nanowire diameter, then deposition of ZnO thin films at room temperature would likely yield higher aspect ratio nanowires more applicable for this work. It has been shown that it is

often reported in the literature that ZnO nanowire morphology is affected by the properties of the seed layer. The effects of seed layer thickness and roughness will be extensively covered in the results section 7.5.

3.5. Hydrothermal Growth of ZnO Nanowires

In this work ZnO nanostructures were grown hydrothermally by thermal decomposition of hexamethylenetetramine (HMTA), and the following pages will explain the method in great detail. HMTA [$C_6N_4H_{12}$] and zinc nitrate [$Zn(NO_3)_2$] are the commonly used chemicals in the literature for hydrothermal growth of ZnO crystals. ZnO is formed as $Zn(NO_3)_2$ provides a source of Zn^{2+} ions, while the solution [H_2O] provides O^{2-} ions. The role that HMTA plays during crystal growth is still hotly debated in the literature. However, it is generally accepted that it is an ammonia (NH_3) source, because at elevated temperature HMTA slowly decomposes releasing ammonia that is hydrolysed creating hydroxyl ions (OH^-) that react with the Zn^{2+} ion [46]. Yamabi et al. [47] have suggested that HMTA may function locally, by decomposing during the reaction and increasing pH above 9 at the crystal surface. Greene et al. [48] have suggested that HMTA may improve nanowire aspect ratio by coordinating with Zn^{2+} in solution keeping free zinc ion concentration low. This is because dehydration of the zinc hydroxide intermediates governs ZnO growth, therefore the kinetics of the reaction may very well be dependent on the release rate of the hydroxide.

HMTA is often reported in the literature to assist in determining the morphology of the nanostructures in ways other than supply of hydroxide ions. It has been reported many times in the literature that HMTA functions as a capping (or chelating) agent on the non-polar facets of the ZnO crystal, impeding attachment of precursor species and therefore promoting growth along the c-axis in the [0001] direction. It is for this reason that if the crystal growth rate is too rapid the nanowires form with hexagonal prism like end structures. It has been shown by Sugunan et al. [49] that HMTA inhibits growth in planes other than (0001) due to being a chelating agent that attaches to the non-polar facets/sides of the nanowires blocking access to Zn^{2+} ions promoting (0001) growth. Conversely, it has been proposed by McPeak et al. [50] to be unlikely that HMTA functions as a capping agent as they obtained similar morphology without the presence of HMTA, by using in situ attenuated total reflection Fourier transform infrared

spectroscopy to determine that no HMTA is absorbed onto the surface of ZnO from solution. While the role of HMTA is often debated, it is well accepted by the ZnO research community that it behaves as a chelating or capping agent, blocking the non polar facets on the ZnO crystal, inhibiting lateral growth by modification of surface free energy so that axial growth dominates. There has also been work on other capping agents, such as sodium dodecyl sulphate, ethylenediamine, and polythylenimine (PEI) which work in a similar fashion to HMTA, in which a non-polar molecule attaches to the non-polar facets locally impeding reactions. Conversely, other capping agents exist that inhibit axial growth promoting lateral growth; such as sodium citrate [51]. PEI, an organic surfactant is also used in microbiology as a cell adhesive coating for plastic substrates [52]. It works the same as HMTA by preferential adsorption onto specific crystal facets and subsequent modification of surface free energy. Law and Green [53] have obtained nanowires of great aspect ratio using PEI and this was replicated in this work, See Appendix III.

3.5.1. Thermal Decomposition of HMTA

Though many variations of the reaction exist, the following reaction order is generally excepted in the literature [54]:

$$C_6H_{12}N_4 + 6H_2O \longrightarrow 4NH_3 + 6CH_2O \quad \textbf{(3.3)}$$

$$NH_3 + H_2O \longleftrightarrow NH_4^+ + OH^- \quad \textbf{(3.4)}$$

$$Zn(NO_3)_2 \longrightarrow Zn^{2+} + 2NO_3^- \quad \textbf{(3.5)}$$

$$Zn^{2+} + 4NH_3 \longleftrightarrow Zn(NH_3)_4^{2+} \quad \textbf{(3.6)}$$

$$Zn^{2+} + 2OH^- \longleftrightarrow Zn(OH)_2 \quad \textbf{(3.7)}$$

$$Zn(OH)_2 \longleftrightarrow ZnO + H_2O \quad \textbf{(3.8)}$$

As already discussed HMTA is vitally important as it provides a constant source of hydroxyl ions and is an ammonia source, now the specific chemistry shall be

discussed. It is commonly accepted in the literature that HTMA [$C_6H_{12}N_4$] is a buffer, readily hydrolysing in water to gradually produce formaldehyde [CH_2O] and ammonia [NH_3], as shown in Equation (3.3). Under increased temperature the ammonia is hydrolysed creating hydroxyl ions [OH^-] via the intermediate production of ammonium hydroxide [NH_4OH] base upon decomposition, as shown in Equation (3.4). The slow release of Ammonia is crucial to the successful deposition of ZnO, as if the HMTA were to simply hydrolyse spontaneously producing a very large quantity of hydroxyl ions then the nutrient supply would be consumed quickly prohibiting the growth of well orientated ZnO nanowires. It is often considered in the literature that HMTA buffer decomposition rate is independent of the reaction that produces ZnO [55].

Equation (3.4) has skipped the formation of the ammonium hydroxide intermediate, showing instead the ammonium and hydroxyl ions. It should be noted that an increase in solution temperature will cause the reaction to shift towards the direction in which heat is absorbed, in this case dissociation of the complex as per Le Chatelier's principle [56] which states *"When a constraint is applied to a system in equilibrium the system adjusts itself so as to nullify the effects of this constraint."* Therefore, an increase of the solution temperature provides more energy to break bonds allowing more of the complex intermediate to be dissociated into ions. From the literature it can be seen that the ammonia produced must be essential for two different tasks. Thermal decomposition of HTMA yields the necessary environment for the formation of $Zn(OH)_2$, the zinc hydroxide intermediate, as Equations 3.5-7 show. $Zn(OH)_2$ has been extensively reported in the literature to dehydrate into ZnO when heated via traditional oven, water bath or even microwave [57]. Equation 3.5. shows the zinc nitrate salt dissolving in water due to its weak ionic bonds.

All reactions (other than dissolution of zinc nitrate) are actually in equilibrium and can therefore be adjusted by changing reaction variables, such as solution temperature and concentration, driving the reaction forwards or backwards, according to Le Chatelier's principle. Reaction variables will be extensively investigated in chapter 7. The constant release of hydroxyl ions yields an increase in solution pH, as well as improvement to the nucleation and growth rate of ZnO crystals by means of a growth-dissolution-recrystallization process as reported by Govender et al. [20]. Hsu et al. [58] report their 20 mM equimolar Zinc Nitrate / HMTA solution to initially be pH 6.7 at 60 °C. This is in good agreement with the 25 mM solution used in this work, which was initially pH 6.81 at 90 °C, where the difference is due to solution temperature and

concentration. It has been reported by Wang et al. [59] that both $Zn(NH_3)_4^{2+}$ and $Zn(OH)_2$ may coexist in the solution, but that this is unlikely due to $Zn(OH)_2$ having a higher stability constant than $Zn(NH_3)_4^{2+}$. This means that $Zn(OH)_2$ is more likely to be formed than $Zn(NH_3)_4^{2+}$, which will simply break down to form $Zn(OH)_2$ as shown in Equations 3.6 and 3.7. Now that the mechanism of chemical bath deposition (or hydrothermal growth) has been covered the fundamentals required to better understand each step will be discussed.

3.5.2. Importance of Solution pH

It is often shown in the literature that the hydrothermal growth of ZnO nanowires should be conducted in highly basic solution, pH 10 – 13. However, when pH was examined in this work no benefits could be found between growth in basic solutions and pH 6.81. sodium hydroxide was added to the solution dropwise till the optimum pH of 10.6 was achieved, as Song et al. [60] had reported this yields the highest aspect ratio nanowires; though in this work use of solutions at pH 10.6 often resulted in no nanowires being formed at all. This was likely due to poor refinement of the recipe, as growth in basic solution was attempted very early on in this work before concentration ratio had been investigated, as Kawano and Imai [61] suggest an non equimolar split between the precursors to yield longer nanowires. It was reported by Verges et al. [9] in the beginning of the hydrothermal methods life that basic conditions are crucial for crystal growth as divalent metal ions do not easily hydrolyse in acidic solution. However, it has been suggested by Greene et al. [48] that for growth at pH < 9, an additive such as HMTA decomposing during the reaction may actually locally increase the pH to above 9 at the crystal surface. Additionally, Govender et al. [20] has suggested that adsorption of ions from solution to substrate may simply arise due to electrostatic attraction of species on the charged surface of ZnO, and Joo et al. [14] have shown that this attraction is pH sensitive due to amphoteric surface hydroxyl groups.

3.6. Fundamentals of Chemical Bath Deposition

But what does this mean, and how does conducting the chemical deposition at pH 6.81 affect the interaction of particles, growth kinetics and ultimately the chemistry of the solution? The following section will explain these fundamentals in further detail

by exploring texts by W. Hinds [62], G. Hodes [18], G. Muller [63], K. Sangwal [64], S. Stoker [65], A. West [56] and S. Zumdahl [66].

3.6.1. Solution pH

In most chemical bath depositions it is best for the pH to remain steady at the desired value, this is because it has been shown by Joo et al. [67] that the electrostatics of polar and non polar facets of ZnO are pH sensitive. Therefore, a buffer is required to maintain the desired pH. G. Hodes [18] has written about the chemistry of chemical bath deposition in substantial detail, and gives the following example of using ammonium salt as a buffer (used to stabilise solution pH), where the equilibrium of ammonia in water is given by Equation 3.4. The solution becomes basic (> 7) as hydroxide ions are formed when ammonia dissolves in water. pH can be calculated from the equilibrium constant, (K) which is a number that characterises the relationship between concentrations of precursors and products in a system in equilibrium. Using a hypothetical chemical reaction (equation 3.9a) the equilibrium constant expression is (equation 3.9b) [65]:

$$1A + 2B \longleftrightarrow 3C + 4D \qquad \textbf{(3.9a)}$$

$$K_{eq} = [C]^3[D]^4 / [A]^1[B]^2 \qquad \textbf{(3.9b)}$$

Where letters A and B are precursors, C and D are products, and numbers are their coefficients. Also, square brackets mean the concentrations are expressed in terms of molarity. For example, the equilibrium expression for equation 3.4. would be [18]:

$$K_{eq} = \frac{[NH_4^+][OH^-]}{[NH_3]} = 1.8 \times 10^{-5} \text{ at } 25\ ^\circ\text{C} \qquad \textbf{(3.10)}$$

Note that the concentrations of pure liquids (water) and pure solids, which are constants are never included in an equilibrium expression [65], hence the absence of H_2O from Equation 3.10. The pH can now be calculated as long as the concentrations are known. For example, a 1 M solution of ammonia ($[NH_3] = 1$) would yield pH 11.62,

as equation 3.4 shows NH_4^+ and OH^- concentrations are equal then $[OH^-]$ is found to be 4.2×10^{-3} M; and the ion product of water is $[H^+][OH^-] = 10^{-14}$ at 25 °C. If 0.1 M NH_4^+ (as NH_4Cl) were added to the solution then the $[OH^-]$ value would drop and pH would become 10.25, conversely if acid were added then hydrogen ions would be consumed via conversion of NH_3 to NH_4^+ as per equation 3.4. This buffering action requires a slight base or acid to function, hence most hydrothermal growth techniques in the literature are operated in weak base or acid along with its salt. However, we have shown that the addition of ammonium ions (example via addition of NH_4Cl) also decreases solution pH, therefore allowing the processes to operate a normal solution pH [18].

3.6.2. Crystal Growth Rate

Crystallisation rate (equation 3.11) can be expressed as the product of four terms, length, frequency, structure of the (solution-crystal) interface and the free energy difference between the solution and crystal phases; where the density of atoms between the two phases plays a significant role in the interface [63].

$$v = av^+ fu_k \tag{3.11}$$

Where a is the atomic diameter of the growth unit, v^+ is the rate of atom attachment to active growth sites on the crystal surface, f is the amount of active interface sites and u_k determines the rate at which atoms join and leave the crystal according to :

$$u_k = 1 - \exp\left(\frac{\Delta G}{kT}\right) \tag{3.12}$$

Where ΔG is the local free energy difference between the solution and crystal phases, k is Boltzmann's constant, and T is the temperature. When a new crystal layer attempts to nucleate on the surface there is a kinetic barrier to overcome, G. Muller applies nucleation theory to the formation of new layers yielding equation 3.13. for the nucleation rate I [63].

$$I = I_0 \exp\left(-\frac{T^*}{\Delta T}\right) \tag{3.13}$$

Where T* depends on edge free energy of surface steps, and ΔT shows undercooling, On a smooth crystal surface, the density of active growth sites, f in (from equation 3.11.) changes with amount of growth sites provided by the nucleation process. However, nucleation rate is not necessarily proportional to crystal growth rate and several other models (other than equation 3.11) have been reported to explain crystal growth rate. The Lifshitz-Slyozov-Wagner (LSW) model is more commonly used to determine crystal growth (equation 3.14), though it does have its limitations.

$$r^n - r_0^n = kt \tag{3.14}$$

Where r is crystal radius at time t, r_0 is radius at time = 0, and k is the growth rate constant; n is a parameter describing the growth mechanism. For example, n = 2 is growth under interfacial reaction control and n = 3 is growth under diffusion control [17]. Ashfold et al. [55] have conducted Atomic Absorbance Spectroscopy (AAS, technique used to determine concentration of elements and compounds in solutions) and pH investigation in situ and found that while the Zn^{2+} concentration steadily decreases over 9 hours the pH only changes for the first 2.5 hours. They postulate that this is due to the removal of the zinc hydroxide intermediate, which becomes thermodynamically unstable and dissolves at lower Zn^{2+} concentrations. This is because after adding zinc nitrate to their solution, pH decreased from 5.66 to 4.51 then returned back to 5.64 after 2.5 hours and remained constant thereafter, indicating that HMTA was a buffer. Comparing measured and calculated concentration indicated crystal growth was due to precipitation, where $Zn(OH)_2$ was an intermediate compound which was used to form nanowires due to thermodynamic breakdown into constitute components [17].

It has been shown by Wong et al. [68] who further explores LSW theory that mass transport or interface reactions are the rate limiting elements, where species at the solution-crystal interface are distributed depending on the local concentration of the crystal (solid phase). Concentration gradients exist across the solution-crystal interface leading to transport of species from high to low concentration regions via capillary forces. These forces promote growth of larger particles at the expense of smaller ones,

and the concentration of a given species in solution at equilibrium with a spherical solid particle is yielded from the Gibbs-Thomson equation [68]:

$$C_r = C_\infty \exp\left(\frac{2\gamma V_m}{RT}\frac{1}{r}\right) \tag{3.15}$$

Where C_r is the concentration for particles of radius r, C_∞ is the concentration of flat surfaces, γ is the interfacial energy, V_m is the molar volume of solid phase, R is the gas constant, and T is the temperature.

As reported by W. Hinds [62], Raoult's Law dictates that the presence of a dissolved salt in water reduces the equilibrium vapour pressure above the water surface, commonly known as the 'Solute Effect'. Since crystal growth / precipitation are solubility-related processes, where a solid crystal or precipitate forms when a solute exceeds its solubility in the solution; then the 'Solute Effect' is an important one for the hydrothermal growth technique. As well as species concentration the likelihood of a particle being involved in crystal growth can be derived using Raoult's Law, as inequality between precursor vapour pressures leads to a positive or negative change in solution vapour pressure [69]. This theorem says that a solution comprised of mainly soluble nuclei will begin the reaction / deposition process at a much lower supersaturation than a solution primarily containing insoluble nuclei [62]; controlling how saturation ratio and particle size interact.

It is hopefully already quite apparent to the reader that several approaches to growth kinetics and nucleation theory exist in the literature. Due to the large variations s in growth kinetics and crystallisation models this work will never attempt to calculate the supersaturation ratio, species concentration, crystal growth rate, nucleation rate or solubility product. Readers wishing to find such information should read texts by W. Hinds [62], G. Hodes [18], G. Muller [63], K. Sangwal [64], S. Stoker [65], A. West [56] and S. Zumdahl [66].

3.7. Summary

This chapter has introduced the reader to a compilation of ideas and hypotheses regarding the mechanisms behind hydrothermal growth of ZnO nanowires. Where it has

been explained previously that this fabrication method became the focus of research to facilitate the application of ZnO nanowire arrays on glass substrates that are unable to withstand the high temperatures of furnace based techniques. The reason for supersaturating the solution for precipitation of ZnO has been covered. The basic chemical processes during hydrothermal growth have been discussed, even though these are often hotly debated and vary in the literature; and the fundamental chemistry of chemical bath deposition and growth kinetics has been included for those readers interested. The information given in this chapter shall be sufficient for better understanding of concepts and the authors' hypotheses in chapter 7.

3.8. References

[1] Y. Qin, R. Yang, and Z. L. Wang, "Growth of Horizonatal ZnO Nanowire Arrays on Any Substrate," *J. Phys. Chem. C*, vol. 112, no. 2, pp. 18734–18736, Nov. 2008.

[2] T. G. G. Maffeis, M. W. Penny, A. Castaing, O. J. Guy, and S. P. Wilks, "XPS investigation of vacuum annealed vertically aligned ultralong ZnO nanowires," *Surf. Sci.*, pp. 5–9, Sep. 2011.

[3] X. W. Sun, S. F. Yu, C. X. Xu, C. Yuen, B. J. Chen, and S. Li, "Room-Temperature Ultraviolet Lasing from Zinc Oxide Microtubes," *Jpn. J. Appl. Phys.*, vol. 42, no. Part 2, No. 10B, pp. L1229–L1231, Oct. 2003.

[4] M. H. Huang, Y. Wu, H. Feick, N. Tran, E. Weber, and P. Yang, "Catalytic Growth of Zinc Oxide Nanowires by Vapor Transport," *Adv. Mater.*, vol. 13, no. 2, pp. 113–116, Jan. 2001.

[5] B. Xiang, P. Wang, X. Zhang, S. a Dayeh, D. P. R. Aplin, C. Soci, D. Yu, and D. Wang, "Rational synthesis of p-type zinc oxide nanowire arrays using simple chemical vapor deposition.," *Nano Lett.*, vol. 7, no. 2, pp. 323–8, Feb. 2007.

[6] Y. F. Hsu, Y. Y. Xi, K. H. Tam, A. B. Djurišić, J. Luo, C. C. Ling, C. K. Cheung, A. M. C. Ng, W. K. Chan, X. Deng, C. D. Beling, S. Fung, K. W. Cheah, P. W. K. Fong, and C. C. Surya, "Undoped p-Type ZnO Nanorods Synthesized by a Hydrothermal Method," *Adv. Funct. Mater.*, vol. 18, no. 7, pp. 1020–1030, Apr. 2008.

[7] Y. Wei, W. Wu, R. Guo, D. Yuan, S. Das, and Z. L. Wang, "Wafer-scale high-throughput ordered growth of vertically aligned ZnO nanowire arrays.," *Nano Lett.*, vol. 10, no. 9, pp. 3414–9, Sep. 2010.

[8] S. Xu, Y. Wei, M. Kirkham, J. Liu, W. Mai, D. Davidovic, R. L. Snyder, and Z. L. Wang, "Patterned Growth of Vertically Aligned ZnO Nanowire Arrays on Inorganic Substrates at Low Temperature without Catalyst," *J. Am. Chem. Soc.*, vol. 130, no. 45, pp. 14958–9, Nov. 2008.

[9] M. A. Verges, A. Mifsud, and C. J. Serna, "Formation of rod like zinc oxide microcrystals in homogeneous solutions," *J. Chem. Soc. Faraday Trans.*, vol. 86, no. 6, pp. 959–963, 1990.

[10] S. Baruah and J. Dutta, "pH-dependent growth of zinc oxide nanorods," *J. Cryst. Growth*, vol. 311, no. 8, pp. 2549–2554, Apr. 2009.

[11] S. Xu, Y. Shen, Y. Ding, and Z. L. Wang, "Growth and Transfer of Monolithic Horizontal ZnO Nanowire Superstructures onto Flexible Substrates," *Adv. Funct. Mater.*, vol. 20, no. 9, pp. 1493–1497, Apr. 2010.

[12] R. A. Laudise and A. A. Ballman, "Hydrothermal synthesis of Zinc Oxide and Zinc Sulfide," *J. Phys. Chem.*, vol. 64, no. 5, pp. 688–691, 1960.

[13] B. Wen, Y. Huang, and J. J. Boland, "Controllable Growth of ZnO Nanostructures by a Simple Solvothermal Process," *J. Phys. Chem. C*, vol. 112, no. 1, pp. 106–111, Jan. 2008.

[14] J. Joo, B. Y. Chow, M. Prakash, E. S. Boyden, and J. M. Jacobson, "Face-selective electrostatic control of hydrothermal zinc oxide nanowire synthesis: Supplimentary Information," *Nat. Mater.*, vol. 2, pp. 1–23, 2011.

[15] L. N. Demianets, D. V. Kostomarov, I. P. Kuz'mina, and S. V. Pushko, "Mechanism of growth of ZnO single crystals from hydrothermal alkali solutions," *Crystallogr. Reports*, vol. 47, no. S1, pp. S86–S98, Jan. 2002.

[16] Z. Zhang and J. Mu, "Hydrothermal synthesis of ZnO nanobundles controlled by PEO-PPO-PEO block copolymers.," *J. Colloid Interface Sci.*, vol. 307, no. 1, pp. 79–82, Mar. 2007.

[17] B. Weintraub, Z. Zhou, Y. Li, and Y. Deng, "Solution synthesis of one-dimensional ZnO nanomaterials and their applications," *Nanoscale*, vol. 2, pp. 1573–1587, 2010.

[18] G. Hodes, *Chemical Solution Deposition Of Semiconductor Films*. CRC Press, 2002, p. 388.

[19] G. Dhanaraj, K. Byrappa, V. Prasad, and M. Dudley, *Springer Handbook of Crystal Growth*. Springer, 2010, p. 1856.

[20] K. Govender, D. S. Boyle, P. B. Kenway, P. O'Brien, and P. O. Brien, "Understanding the factors that govern the deposition and morphology of thin films of ZnO from aqueous solution," *J. Mater. Chem.*, vol. 14, no. 16, pp. 2575–2591, 2004.

[21] S. K. Ong, *Natural Processes and Systems for Hazardous Waste Treatment*. ASCE Publications, 2008, p. 280.

[22] L.-W. Ji, S.-M. Peng, J.-S. Wu, W.-S. Shih, C.-Z. Wu, and I.-T. Tang, "Effect of seed layer on the growth of well-aligned ZnO nanowires," *J. Phys. Chem. Solids*, vol. 70, no. 10, pp. 1359–1362, Oct. 2009.

[23] C. Xu and D. Gao, "Two-Stage Hydrothermal Growth of Long ZnO Nanowires for Efficient TiO 2 Nanotube-Based Dye-Sensitized Solar Cells," *J. Phys. Chem. C*, vol. 116, pp. 7236–7241, 2012.

[24] Y. Lee, T. Sounart, D. Scrymgeour, J. Voigt, and J. Hsu, "Control of ZnO nanorod array alignment synthesized via seeded solution growth," *J. Cryst. Growth*, vol. 304, no. 1, pp. 80–85, Jun. 2007.

[25] R. a. Brown, J. E. Evans, N. a. Smith, A. Tarat, D. R. Jones, C. J. Barnett, and T. G. G. Maffeis, "The effect of metal layers on the morphology and optical properties of hydrothermally grown zinc oxide nanowires," *J. Mater. Sci.*, vol. 48, no. 14, pp. 4908–4913, Mar. 2013.

[26] S. Baruah and J. Dutta, "Effect of seeded substrates on hydrothermally grown ZnO nanorods," *J. Sol-Gel Sci. Technol.*, vol. 50, no. 3, pp. 456–464, Feb. 2009.

[27] M. Guo, P. Diao, and S. Cai, "Hydrothermal growth of well-aligned ZnO nanorod arrays: Dependence of morphology and alignment ordering upon preparing conditions," *J. Solid State Chem.*, vol. 178, no. 6, pp. 1864–1873, Jun. 2005.

[28] L. E. Greene, M. Law, D. H. Tan, M. Montano, J. Goldberger, G. Somorjai, and P. Yang, "General route to vertical ZnO nanowire arrays using textured ZnO seeds.," *Nano Lett.*, vol. 5, no. 7, pp. 1231–6, Jul. 2005.

[29] D. W. Bahnemann, C. Kormann, and M. R. Hoffmann, "Preparation and characterization of quantum size zinc oxide: a detailed spectroscopic study," *J. Phys. Chem.*, vol. 91, no. 14, pp. 3789–3798, Jul. 1987.

[30] R. B. M. Cross, M. M. De Souza, and E. M. Sankara Narayanan, "A low temperature combination method for the production of ZnO nanowires.," *Nanotechnology*, vol. 16, no. 10, pp. 2188–92, Oct. 2005.

[31] D. Polsongkram, P. Chamninok, S. Pukird, L. Chow, O. Lupan, G. Chai, H. Khallaf, S. Park, and A. Schulte, "Effect of synthesis conditions on the growth of ZnO nanorods via hydrothermal method," *Scan. Electron Microsc.*, vol. 403, pp. 3713–3717, 2008.

[32] J. Qiu, X. Li, W. He, S.-J. Park, H.-K. Kim, Y.-H. Hwang, J.-H. Lee, and Y.-D. Kim, "The growth mechanism and optical properties of ultralong ZnO nanorod arrays with a high aspect

ratio by a preheating hydrothermal method.," *Nanotechnology*, vol. 20, no. 15, p. 155603, Apr. 2009.

[33] G. Kenanakis, D. Vernardou, E. Koudoumas, and N. Katsarakis, "Growth of c-axis oriented ZnO nanowires from aqueous solution: The decisive role of a seed layer for controlling the wires' diameter," *J. Cryst. Growth*, vol. 311, no. 23–24, pp. 4799–4804, Dec. 2009.

[34] M. Ohyama, H. Kozuka, and T. Yoko, "Sol-gel preparation of ZnO films with extremely preferred orientation along (002) plane from zinc acetate solution," *Thin Solid Films*, vol. 306, pp. 78–85, 1997.

[35] S. Yamabi and H. Imai, "Growth conditions for wurtzite zinc oxide films in aqueous solutions," *J. Mater. Chem.*, vol. 12, no. 12, pp. 3773–3778, Nov. 2002.

[36] S. Zhu, C. Su, S. L. Lehoczky, P. Peters, and M. A. George, "Pressure effects in ZnO films using off-axis sputtering deposition," *J. Cryst. Growth*, vol. 211, pp. 106–110, 2000.

[37] J. A. Thornton, "Influence of apparatus geometry and deposition conditions on the structure and topography of thick sputtered coatings," *J. Vac. Sci. Technol.*, vol. 11, no. 4, p. 666, Jul. 1974.

[38] F. C. M. van de Pol, F. R. Blom, and T. J. A. Popma, "R. F. Planer Magnetron Sputtered ZnO Films I: Structural Properties," *Thin Solid Films*, vol. 204, pp. 349–364, 1991.

[39] J. Bin, H. Joon, S. Gil, C. Seong, and S. Hong, "Deposition of ZnO thin films by magnetron sputtering for a film bulk acoustic resonator," *Thin Solid Films*, vol. 435, pp. 179–185, 2003.

[40] Y. E. Lee, J. Bin Lee, and Y. J. Kim, "Microstructural evolution and preferred orientation change of radio-frequency-magnetron sputtered ZnO thin films," *J. Vac. Sci. Technol. A Vacuum, Surfaces, Film.*, vol. 14, no. 3, pp. 1943–1948, 1996.

[41] Y. Yoshino, K. Inoue, M. Takeuchi, T. Makino, Y. Katayama, and T. Hata, "Effect of substrate surface morphology and interface microstructure in ZnO thin films formed on various substrates," *Vacuum*, vol. 59, pp. 403–410, 2000.

[42] Y. Zhang, G. Du, D. Liu, X. Wang, Y. Ma, J. Wang, J. Yin, X. Yang, X. Hou, and S. Yang, "Crystal growth of undoped ZnO films on Si substrates under different sputtering conditions," *J. Cryst. Growth*, vol. 243, no. 3–4, pp. 439–443, Sep. 2002.

[43] G. Ferblantier, M. Al Kalfioui, a. Boyer, a. Foucaran, R. Ondo-Ndong, and M. Al Kalfioui, "Properties of RF magnetron sputtered zinc oxide thin films," *J. Cryst. Growth*, vol. 255, no. 1–2, pp. 130–135, Jul. 2003.

[44] Y. J. Kim, Y. T. Kim, H. K. Yang, J. C. Park, J. I. Han, Y. E. Lee, and H. J. Kim, "Epitaxial growth of ZnO thin films on R-plane sapphire substrate by radio frequency magnetron sputtering," *J. Vac. Sci. Technol. A Vacuum, Surfaces, Film.*, vol. 15, p. 1103, 1997.

[45] G. A. Kumar, M. V. R. Reddy, and K. N. Reddy, "Effect of substrate temperature on structural and optical properties of nanostructured ZnO thin films grown by RF magnetron sputtering," *Int. Conf. Nanosci. Eng. Technol. (ICONSET 2011)*, pp. 56–60, Nov. 2011.

[46] L. Schmidt-mende and J. L. Macmanus-driscoll, "defects , and devices ZnO has received much attention over the past few years because," *Rev. Lit. Arts Am.*, vol. 10, no. 5, pp. 40–48, 2007.

[47] S. Yamabi and H. Imai, "Growth conditions for wurtzite zinc oxide films in aqueous solutions," *J. Mater. Chem.*, vol. 12, no. 12, pp. 3773–3778, Nov. 2002.

[48] L. E. Greene, B. D. Yuhas, M. Law, D. Zitoun, and P. Yang, "Solution-grown zinc oxide nanowires.," *Inorg. Chem.*, vol. 45, no. 19, pp. 7535–43, Sep. 2006.

[49] A. Sugunan, H. C. Warad, M. Boman, and J. Dutta, "Zinc oxide nanowires in chemical bath on seeded substrates: Role of hexamine," *J. Sol-Gel Sci. Technol.*, vol. 39, no. 1, pp. 49–56, May 2006.

[50] K. M. McPeak, T. P. Le, N. G. Britton, Z. S. Nickolov, Y. a Elabd, and J. B. Baxter, "Chemical bath deposition of ZnO nanowires at near-neutral pH conditions without hexamethylenetetramine (HMTA): understanding the role of HMTA in ZnO nanowire growth.," *Langmuir*, vol. 27, no. 7, pp. 3672–7, Apr. 2011.

[51] S. P. Fillery and F. F. Lange, "Aqueous lateral epitaxy overgrowth of ZnO on (0001) GaN at 90°C: Part I. Increasing the critical thickness," *Thin Solid Films*, vol. 518, no. 21, pp. 6022–6029, Aug. 2010.

[52] A. R. Vancha, S. Govindaraju, K. V. L. Parsa, M. Jasti, M. González-García, and R. P. Ballestero, "Use of polyethyleneimine polymer in cell culture as attachment factor and lipofection enhancer.," *BMC Biotechnol.*, vol. 4, p. 23, Oct. 2004.

[53] M. Law, L. E. Greene, J. C. Johnson, R. Saykally, and P. Yang, "Nanowire dye-sensitized solar cells.," *Nat. Mater.*, vol. 4, no. 6, pp. 455–9, Jun. 2005.

[54] S. Xu and Z. L. Wang, "One-dimensional ZnO nanostructures: Solution growth and functional properties," *Nano Res.*, vol. 3, no. 9, pp. 676–684, Aug. 2011.

[55] M. Ashfold, R. Doherty, N. Ndiforangwafor, D. Riley, and Y. Sun, "The kinetics of the hydrothermal growth of ZnO nanostructures," *Thin Solid Films*, vol. 515, no. 24, pp. 8679–8683, Oct. 2007.

[56] A. R. West, *Basic Solid State Chemistry*. Scotland, Great Britain: Joh Wiley & Sons Ltd., 1988, p. 415.

[57] H. E. Unalan, P. Hiralal, N. Rupesinghe, S. Dalal, W. I. Milne, and G. a J. Amaratunga, "Rapid synthesis of aligned zinc oxide nanowires," *Nanotechnology*, vol. 19, no. 25, p. 255608, Jun. 2008.

[58] J. W. P. Hsu, Z. R. Tian, N. C. Simmons, C. M. Matzke, J. a Voigt, and J. Liu, "Directed spatial organization of zinc oxide nanorods.," *Nano Lett.*, vol. 5, no. 1, pp. 83–6, Jan. 2005.

[59] H. Wang, J. Xie, K. Yan, and M. Duan, "Growth Mechanism of Different Morphologies of ZnO Crystals Prepared by Hydrothermal Method," *J. Mater. Sci. Technol.*, vol. 27, no. 2, pp. 153–158, Feb. 2011.

[60] J. Song, S. Baek, and S. Lim, "Effect of hydrothermal reaction conditions on the optical properties of ZnO nanorods," *Phys. B Condens. Matter*, vol. 403, no. 10–11, pp. 1960–1963, May 2008.

[61] T. Kawano and H. Imai, "Fabrication of ZnO Nanoparticles with Various Aspect Ratios through Acidic and Basic Routes," *Cryst. Growth Des.*, vol. 6, no. 4, pp. 1054–1056, Apr. 2006.

[62] W. C. Hinds, *Aerosol Technology: Properties, Behavior, and Measurement of Airborne Particles*, 2nd ed. John Wiley & Sons Ltd, 1999, p. 504.

[63] K. A. Jackson, "Actual Concepts of Interface Kinetics," in *Crystal Growth - From Fundamentals to Technology*, G. Müller, J.-J. Métois, and P. Rudolph, Eds. Elsevier, 2004, p. 434.

[64] K. Sangwal, *Additves and Crystallization Processes*. Chichester: John Wiley & Sons Ltd, 2007, p. 468.

[65] S. H. Stoker, *General, Organic, and Biological Chemistry*, 4th ed. Cengage Learning, 2006, p. 896.

[66] S. S. Zumdahl, *Chemical Principles*, 6th ed. Boston, MA: Houghton Mifflin Company, 2009, p. 1179.

[67] J. Joo, B. Y. Chow, M. Prakash, E. S. Boyden, and J. M. Jacobson, "Face-selective electrostatic control of hydrothermal zinc oxide nanowire synthesis," *Nat. Mater.*, no. July, pp. 1–6, 2011.

[68] E. M. Wong, J. E. Bonevich, and P. C. Searson, "Growth Kinetics of Nanocrystalline ZnO Particles from Colloidal Suspensions," *J. Phys. Chem. B*, vol. 102, no. 40, pp. 7770–7775, Oct. 1998.

[69] D. L. Reger, S. R. Goode, and D. Warren Ball, *Chemistry: Principles and Practice*, 2nd ed. Cengage Learning, 2009, p. 1120.

Chapter 4. Characterization of Zinc Oxide Nanowires

4.1. Introduction

This chapter will introduce and explain the fundamental science and operational techniques employed for all equipment used in characterization of Zinc Oxide nanowire arrays in this work. This chapter will primarily focus on main equipment used to characterize the nanowires. Scanning Electron Microscopy (SEM) was used to measure nanowire size, distribution and alignment, X-ray Microanalysis (EDX) was used to confirm stoichiometry of the nanowires, Atomic Force Microscopy (AFM) was used to observe stiffness and adhesion properties of the arrays and Photoluminescence was used to check the crystal quality of the produced ZnO nanowires as defects are revealed in the spectrum.

4.2. Scanning Electron Microscopy

Scanning Electron Microscopy (SEM) is a microscopy technique that allows the user to obtain extremely high resolution and high magnification 2D images of any structure by raster scanning a sample with a beam of electrons; improving on the typical Rayleigh resolution limitations imposed by wavelength in optical microscopy significantly. Modern optical microscopes have a resolution of around 200 nm (using a x100 objective lens with numerical aperture (NA) of 1.4) [1] however electron microscopes can resolve up to 1 nm (at 15 kV with a highest working magnification of x800,000) [1].

4.2.1. System Components

Fig. 4.1. shows the main components of the Hitachi S-4800 field emission SEM (FESEM) used in this work, primarily SEM works using five main components. A cold cathode field emission electron source provides a 3 - 5 nm diameter incident beam of

[1] http://www.microscopyu.com/articles/formulas/formulasresolution.html

electrons to interact with the sample, 1000 times brighter than older conventional Tungsten filament based microscopes [1]. Electromagnetic lenses are used to shape the beam of electrons by applying an electromagnetic field to bend their route. Flemings' left hand rule suggests the electrons take a helical path down the column [1]. There are two sets of lens used in the SEM, a condenser lens is used to control the diameter and current of the electron beam, while an objective lens is used after the condenser lens to adjust the focal point of the beam.

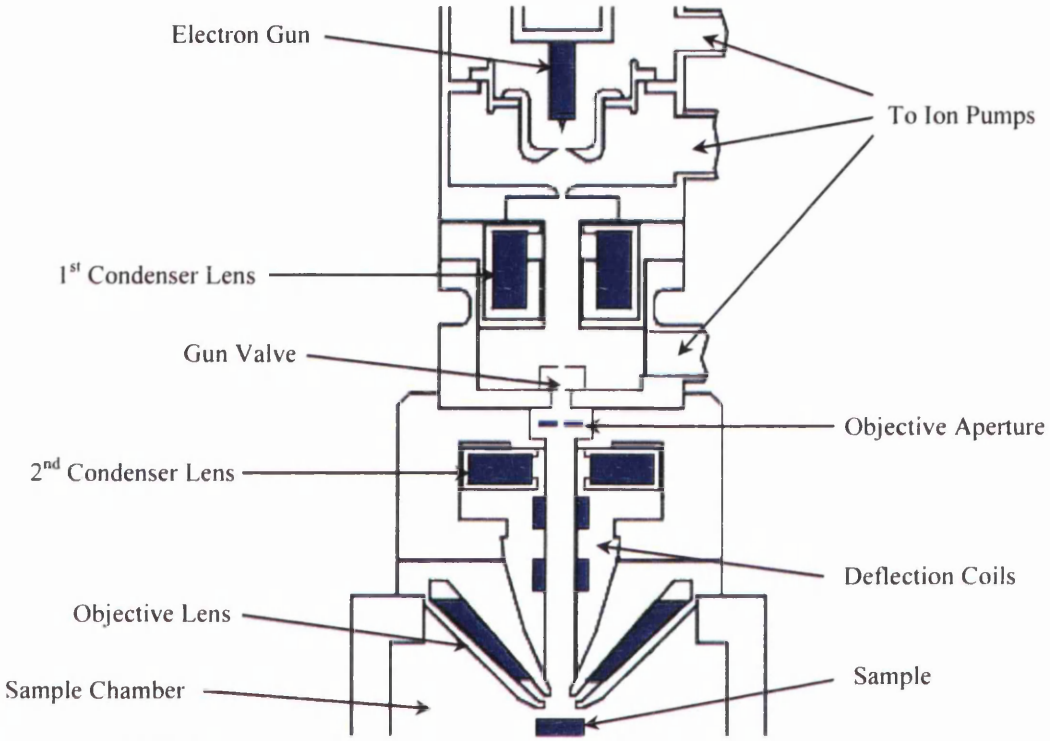

Figure 4.1. Cross-sectional View of a Hitachi S-4800 SEM Column, adapted from [1].

As the electron beam meets the first condenser lens the beam is focused below the lens and converged on the objective lens below it, adjustment of the distance of the focal point from the objective lens controls the initial spot size of the electron beam; with distances closer to the lens yielding a smaller spot. A mechanical objective aperture is also employed for further control of the diameter of the electron beam that reaches the sample; the Hitachi S-4800 has 3 different aperture sizes, 100 μm, 50 μm and 30 μm [1]. The deflection coils are used to raster the electron beam across the sample, hence 'scanning' electron microscope.

The improved resolution due to use of electrons compared to optical microscopy also yields a significant improvement on the depth of field (Z-range in focus) for SEM

images. This is perfect for characterizing arrays of nanowires as even at magnifications of x50,000 this range can be as large as 2 – 3 μm depending on the aperture used, see Table 4.1. Fig. 4.2. shows the flexibility in the extensive magnification range available using SEM to go from measuring facets of a single ZnO nanowire to observation of the uniformity of the nanowire array. Notice however that in Fig. 4.1a. that observation of differences between layers on the non polar facet ($10\bar{1}1$) is inhibited due to the depth of field being only around 160 nm as the 50 μm aperture was used. But use of a smaller aperture normally worsens signal to noise ratio at such high magnifications, severely affecting contrast due to decreased brightness of the electron beam. This can however be compensated for by increasing the spot size using the condenser lens, though this leads to reduced resolution; therefore careful selection of settings is required to obtain an image that is both in focus and of good contrast.

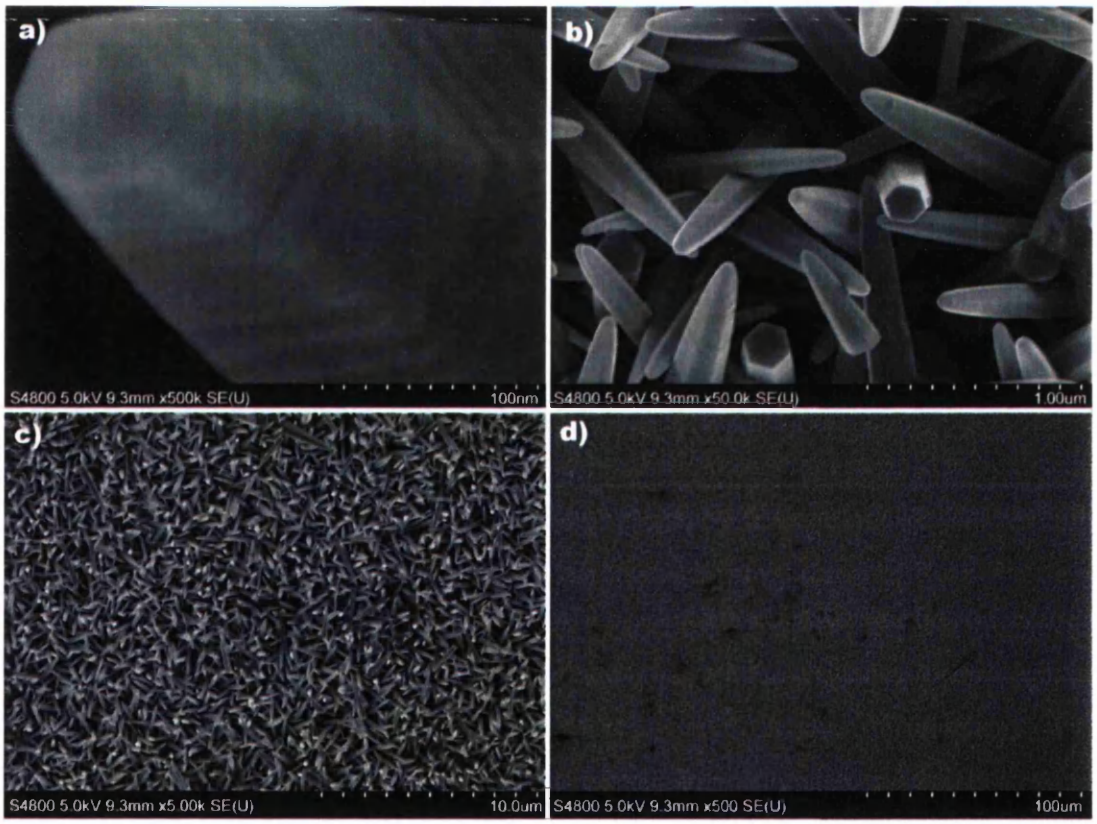

Figure 4.2. Secondary Electron (SE) images of an array of ZnO nanowires showing the wide range of image magnifications available, where a) is 500,000x , b) is 50,000x , c) is 5,000x and d) is 500x.

Table 4.1. Effect of Aperture size on depth of field (WD = 10mm), adapted from [2].

	Depth of Field when using:		
Mag.	**100µm Aperture**	**50µm Aperture**	**30µm Aperture**
500x	80 µm	160 µm	267 µm
5,000x	8 µm	16 µm	26.7 µm
50,000x	800 nm	1600 nm	2.67 µm
500,000x	80 nm	160 nm	267 nm

4.2.2. Field Emission

Traditionally the electron beam was created by thermionic emission by passing a large current through a tungsten filament; this method however produces a rather large beam 1 – 2 µm in diameter with a limited life time of around 300 hours. Modern SEMs use field emission instead to extract electrons from a sharp tip leading to a much smaller beam diameter of around 3 - 5 nm with a far greater lifetime of around 10000 hours [1]. Electrons are contained within a metal due to a potential barrier that is assumed to be infinitely thick (as to inhibit tunnelling of electrons) and of a height determined by the metal's work function. In thermionic emission electrons from the Fermi level (see Fig. 4.3a) are able to overcome this potential barrier by thermionic excitation. In field emission an electric field is applied reducing the thickness of the barrier to the point where electrons are able to tunnel through and be 'field emitted' from the sharp tip; this is done by applying an extracting voltage (V_{ext}) between the cathode and first anode determining the emission current and an accelerating voltage (V_{acc}) to the second anode to determine the final kinetic energy, see Fig. 4.3b.

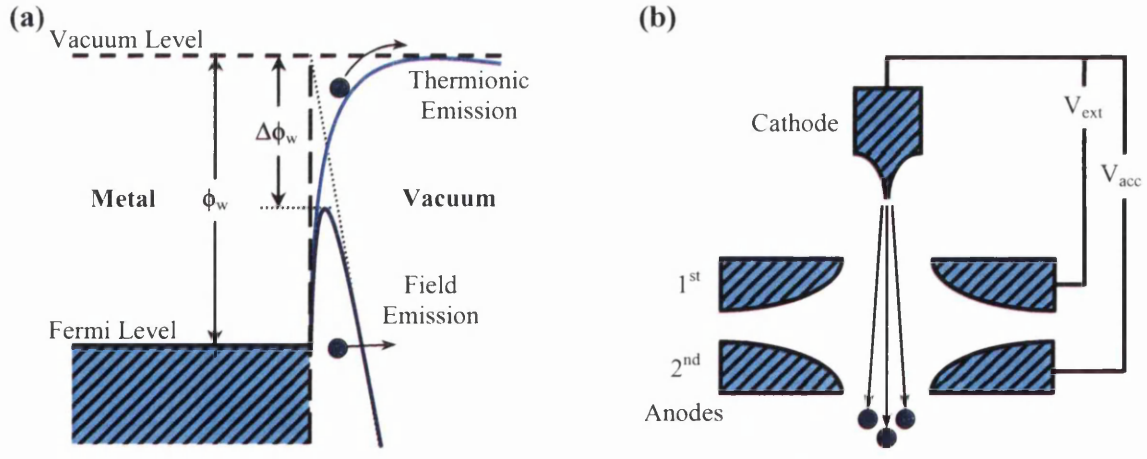

Figure 4.3. (a) Band diagram of potential barrier (work function, ϕ_w) at the metal-vacuum interface for both field and thermionic emission. (b) Operation of a Bulter type field emission gun. Adapted from [3].

This design requires a small emission cone angle (less than 5 degrees) to ensure minimal bombardment of the first anode, therefore limiting harmful ion production that could damage the tip. The tip is also held under ultra-high vacuum condition at around 10^{-6} Pa to further reduce ion production and damage due to residual gas [1]. Modern FEG (field emission guns) allow the tip to be 'flashed' whereby a current of between 30 – 50 μA is passed through the tip, heating it considerably enough to remove the contamination layer and if sufficient current is selected a few monolayers of tip material to eliminate any deformities that may have developed [1].

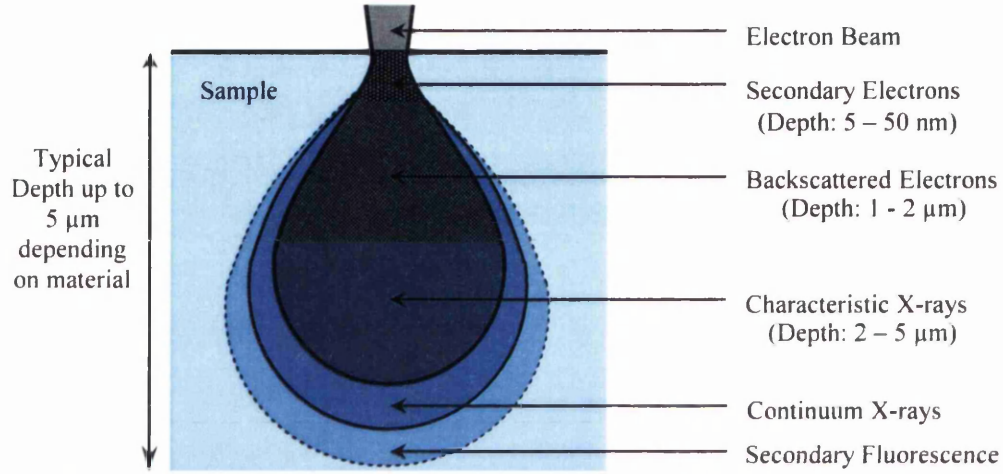

Figure 4.4. Diagram depicting the interaction volumes for the majority of electron-sample interactions created by the electron beam. For clarity Auger electrons have been omitted. Adapted from [4].

Fig. 4.4. Compares the interaction volumes for the various emissions created from interactions with the electron beam. The number of secondary and backscattered electrons emitted from the sample from each incident electron are described by the secondary electron coefficient (δ) and backscattered electron coefficient (η) respectively [5]. Secondary electrons are produced from inelastic scattering, where the incident electron interacts with the nucleus transferring some energy and subsequently changing path. Backscattered electrons are produced from elastic scattering, where the incident electron interacts with a positive nucleus with little energy loss altering the path of the electron by up to 180 degrees. The atomic number (Z) of the nucleus has a dramatic effect on the scattering angle; therefore backscattered electrons are highly atomic number sensitive and are used for further analysis of materials [5]. Characteristic X-rays are also produced from inelastic scattering, where an atoms inner shell electrons are ejected by incident electrons and the holes filled by higher shell electrons dropping an

energy level required energy to be conserved by emitting characteristic X-rays. The simultaneous occurrence of such intricate processes yields the interaction volume, whose shape is mainly due to elastic scattering causing a spread of the electron beam whereas inelastic scattering lead to cumulative energy loss for each even inhibiting spread within the sample. Having the smallest interaction volume secondary electrons yield the highest spatial resolution compared to the other signals; they are therefore used for the majority of imaging as they carry most of the surface topographical information.

4.2.3. Image Aberration

When an SEM operator takes the time to carefully focus and adjust settings before image capture then the final image can yield wonderful levels of detail, as SEM has such a high spatial resolution. However there are many variables that can affect the path of electrons introducing artifacts in the image, this is called aberration as it is a distortion of the normally obtained images. The most common forms of aberration are:

- Spherical aberration due to off axis focusing of electrons
- Chromatic aberration due to a spread of electron energies from the gun
- Astigmatism due to the shape of the electron beam, where deviation from a perfect symmetrical spot will yield stretched and unfocused images.

Since all the above are resolution limiting then to achieve the highest magnifications the effect of each form of aberration must be reduced [1].

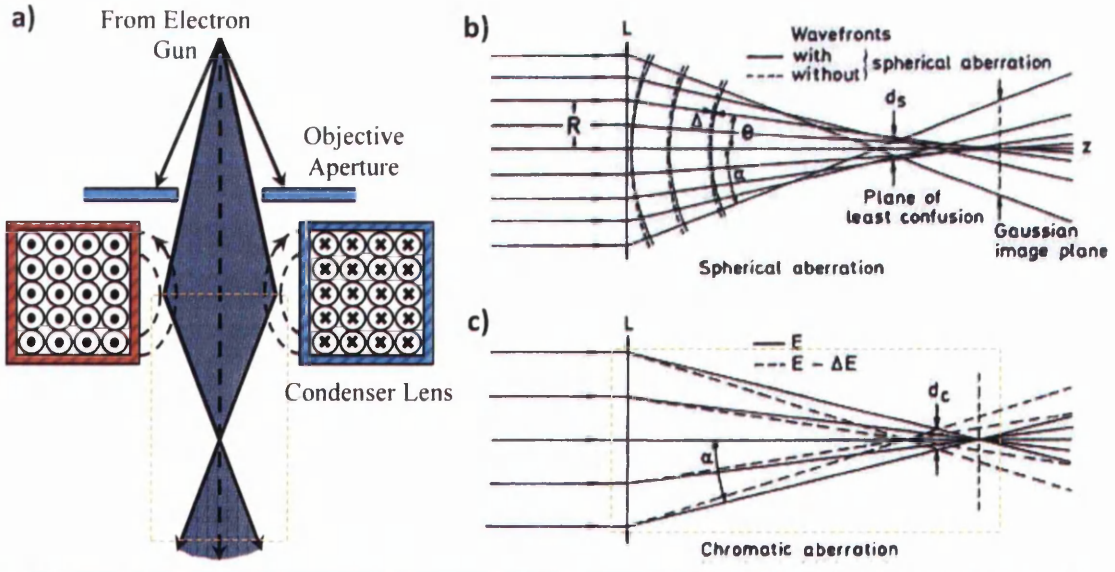

Figure 4.5. Diagrams depicting a) the focal length of an electron beam after a magnetic field is applied, b) spherical aberration and c) chromatic aberration. Adapted from [3].

Fig. 4.5a shows a more simplified aperture and lens configuration than was shown in Fig 4.1., where Fig 4.5bc shows two forms of aberration. As discussed briefly before, the purpose of the aperture is to stop electrons that leave the tip off axis as well as to allow the beam to be narrowed, which is used to change depth of field. Conversely a larger aperture is used to increase the amount of electrons arriving at the samples and therefore is beneficial for any microanalysis work such as energy dispersive x-ray analysis; covered in section 4.3. The purpose of the lens is to change the path of the electrons by applying a magnetic field to reshape the electron beam and alter the focal length. Since the lens is simply an electro magnet comprised of a coil of wire around the beam then the focal length of the resulting electron beam post lens can be adjusted by simply adjusting the current of the lens to adjust the magnetic field applied to the beam. However, the electromagnetic lens (just like their optical counter parts) can introduce substantial artifacts if the lens it not set up correctly and the beam is not uniformly focused on a single point. Aberration of SEM lens happens via two main methods, spherical and chromatic [6], with both adversely affecting the final image.

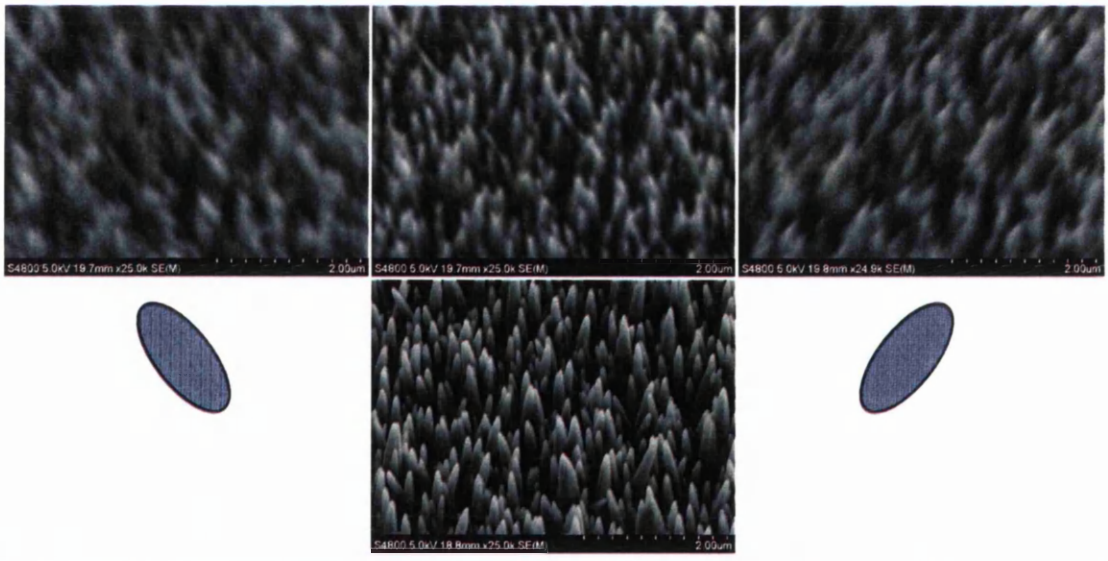

Figure 4.6. Correction method for astigmatism, with both left and right images originating from an elliptical spot of sample surface, the middle is from a circular spot and the bottom image is the middle image in focus. All images were acquired at 25,000x magnification from ZnO nanowires.

Fig. 4.5b shows spherical aberration of the beam where parallel rays of electrons are shown to hit the lens and those on the outsides of the lens are over corrected with their new paths leading to a focal plane that is closer to the lens. Weak lenses used in a SEM for low magnification, large working distance sample finding have large spherical

aberrations [3]. Fig. 4.5c shows chromatic aberration of the beam where the accelerating voltage (or electron energy) of the beam causes the electrons to spread more or less depending on their velocity [6]. This is why the microscope should always be run through the setup and alignment process each time an aperture, working distance or accelerating voltage is changed. Fig. 4.6 shows astigmatism of the beam where the beam is non-uniformly focused by the lens and forms a non-circular spot on the sample. The upper left image is stretched in one direction and the upper right in the opposite, and these positions represent the upper and lower focal points created by the irregular shape of the beam; and are highlighted as blue ovals in Fig. 4.7. The upper middle image is taken at the midpoint between the two focal points, and the image below shows how the sample should looked with no (little) astigmatism and focused correctly. Aberration due to astigmatism is corrected using smaller stigmata coils which apply a field opposite to the main lens coil in both X and Y directions, allowing careful adjustment to the shape of the electron beam until it is circular.

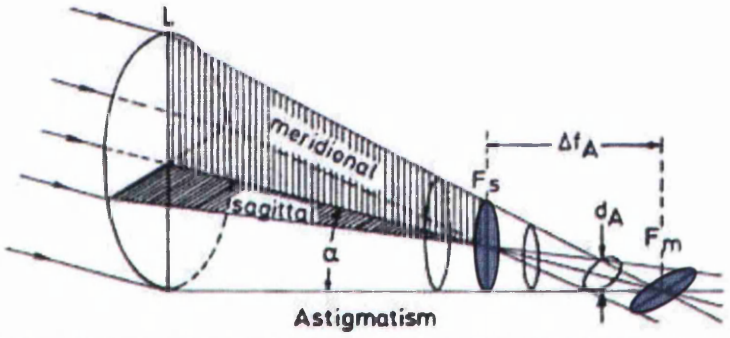

Figure 4.7. Diagram showing Astigmatism of the electron beam, where the upper and lower focal points that are stretched in opposite directions are highlighted by blue ovals; adapted from [3].

4.2.4. Low kV Imaging

Fig. 4.4. compared the interaction volumes for the various emissions in a hypothetical sample, but did not include the effect of accelerating voltage on the volume of each emission. At higher kV the electrons are accelerated more and the electron beam penetrates and diffuses more within the sample resulting in signals (electrons coming out of the sample) being generated from deeper within the sample; often obscuring fine surface structures. Going back to Fig. 4.4., it can be seen that the resulting signal will also comprise of more BSEs and so the image will also begin to show contrast based on composition [4]. In chapter 8 the structure and morphology of U-2 OS cells on the ZnO

nanowires will be characterized using SEM. Typically imaging biological material (non-conductive) at high kV requires either fixation in Osmium Tetraoxide, which is a lipid stain that embeds a heavy metal into the cell membranes, yielding higher electron scattering rate [7]; or the sample is coated in metal (typically Gold or Palladium) to allow charge to dissipate effectively. However, both these techniques create artifacts and so imaging at a low accelerating voltage (1kV) is often preferred. The lower electron energy reduces the mean free path for electrons entering the sample and secondary electrons escaping it; this allows for a much better representation of surface topography of materials comprising of light elements such as those in biological tissues. This will be covered in more detail in section 6.2.

4.2.5. Edge Effects

Fig. 4.8. shows the effect of sample topography on the interaction volume and escape of electrons from the sample, where peaks and edges allow electrons to escape more readily from the sample, creating high contrast areas; as shown in Fig. 4.9a. Electrons preferentially escape from edges and peaks, meanwhile depressions in the sample can shield regions of sample from the detector leading to poor signal intensity in those regions. Back scattered electrons released from areas facing the detector can enhance this difference in contrast based on topography phenomenon. Often topographic contrast can be reduced by lowering the accelerating voltage of the beam. If this is not an option (i.e. in the case of elemental analysis where the sample needs to be saturated with electrons) then tilting the sample towards the detector can often improve contrast by reducing topographical contrast artifacts due to charging [2].

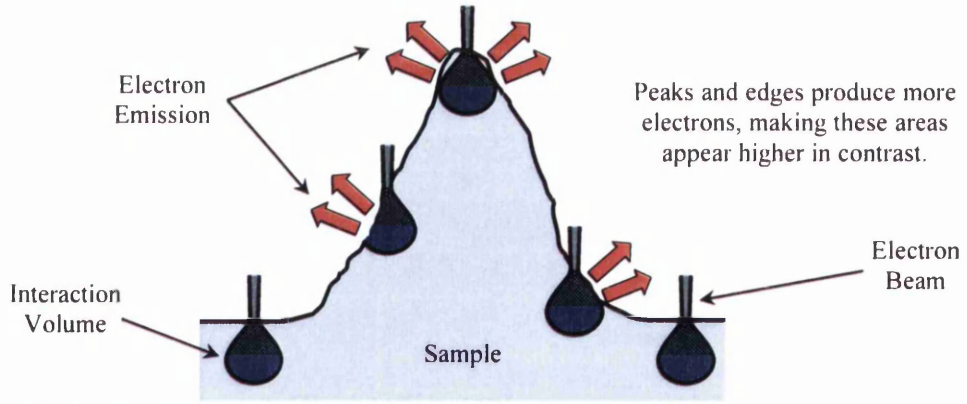

Figure 4.8. Diagram showing the effect of sample topography on the interaction volume and escape of electrons from the sample. Adapted from [8].

4.2.6. Charging artifacts

Charging of the sample during imaging acquisition is likely the most impeding hindrance of SEM imaging, though these charging artifacts can often be easily resolved with careful selection of incident electron beam parameters; such as accelerating voltage and spot size. Charging artifacts are derived from a build-up of excess electrons within the surface of the sample, creating an electric field that can deflect the incident electron beam producing undesirable distortions to the captured image. This build up charge can also randomly be released from the sample leading to erroneous lines from the detector, and is generally a major problem with non-conductive (insulating) samples.

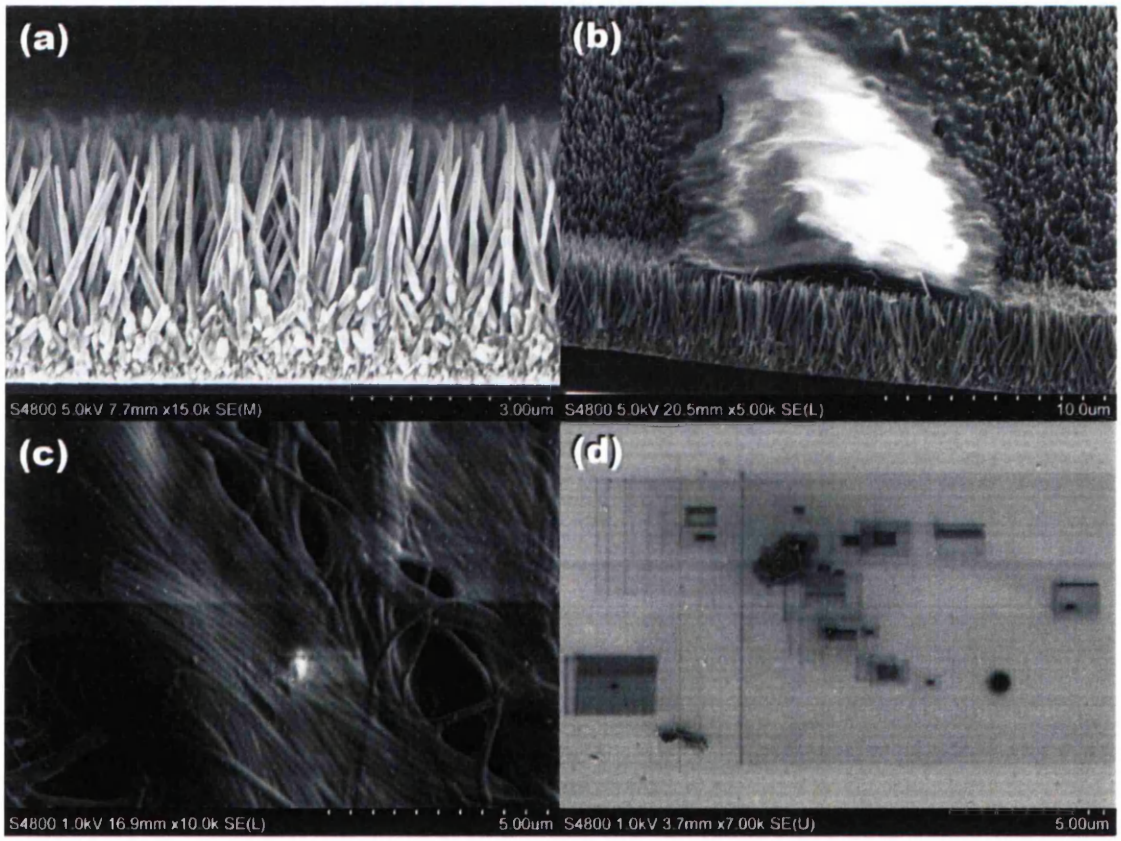

Figure 4.9. SEM images show (a) edge charging, (b) area charging, (c) line charging and (d) residual charging.

Fig. 4.9. depicts some of the most common artifacts observed during SEM imaging of non-conductive materials, where (a) shows edge charging in Zinc Oxide nanowires, (b) area charging in an epithelial endometrial Ishikawa cell on nanowires, (c) erratic line by line release of electron build up in a cryo-SEM image of bovine explanted tendons and (d) residual charging left behind after high magnification

inspection of Zinc Oxide seed layer particles. Edge charging occurs in the smaller features of the sample, where electrons build up at the edges of heightened topography or isolated areas of the sample causing small features to become uncharacteristically bright compared to the rest of the image. Area charging causes certain areas to grow increasingly bright with SEM adjustments having little effect, these are normally caused by completely ungrounded areas of the sample. Line by line charging happens when a build-up of electrons begin to randomly release from the sample causing the image to fluctuate line by line in brightness, this typically will occur when taking a low magnification image of an area where a high magnification image was previous acquired. For residual charging artifacts electrons that still remain in the sample from previous high magnification imaging are added to the low magnification image resulting in either bright or dark areas depending on the materials value of E_2; see Fig. 4.11.

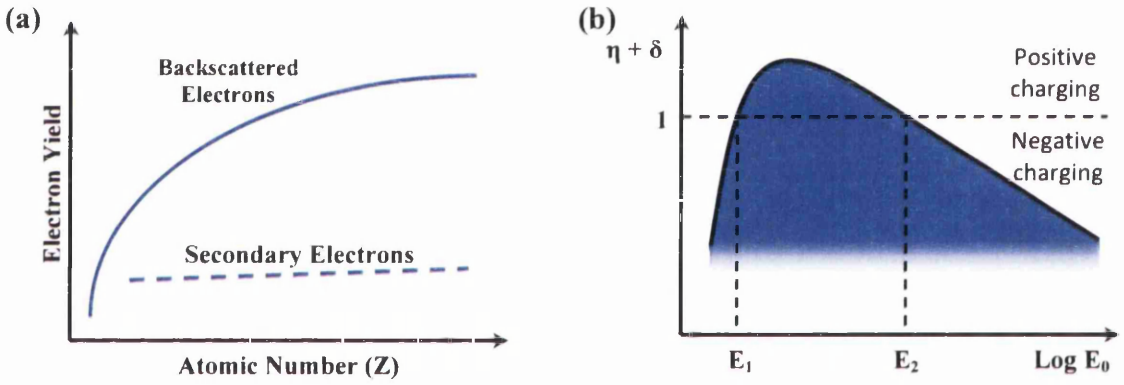

Figure 4.10. (a) Effect of atomic number on the yield of backscattered electrons (η) and secondary electrons (δ), from [5]. (b)Total electron emission as a function of incident beam energy (E_0), from [2]. E_1 and E_2 are the first and second crossover points.

Fig. 4.10. Shows electron emission coefficient plotted as a function of incident beam energy (E_0), if both backscattered primary electrons (η) and secondary electrons (δ) are considered; the highlighted region is where the amount of emitted electrons exceeds the amount of incident electrons in a non-conductive sample; as defined by the two incident energy values E_1 and E_2 where $\eta + \delta = 1$. Typically E_1 is a few hundred electron volts and E_2 is around 1 – 5 keV. When the incident beam energy is below E1 then less electrons leave the sample than the amount that enter so the sample builds up negative charge, until sufficiently charged to deflect the electron beam. When the beam energy is between the two crossover points then more electrons are emitted from the

sample than enter it, positively charging the sample attracting low energy secondary electrons. These mechanisms result in unity for $\eta + \delta$ as an equilibrium between incident current and emitted current is reached [2].

If the electron beam is less than E_1 then $\boldsymbol{\eta + \delta < 1}$ meaning that less electron enter than leave the sample resulting in a net negative charge. $E > E_2$ also produces a net negative charge, again further decreasing $\boldsymbol{\eta + \delta}$ until the specimen is sufficiently negatively charge enough to reflect the electron beam. It has been shown by Oatley et al. [9] that operation at $E > E_2$ is unsatisfactory as E_2 can vary considerably between different regions of the sample. It is therefore more desirable to operate the SEM with an electron beam energy in the region of $E1 < E < E2$. This is often achieved around 1 keV and allows imaging of insulators without metal deposition [2].

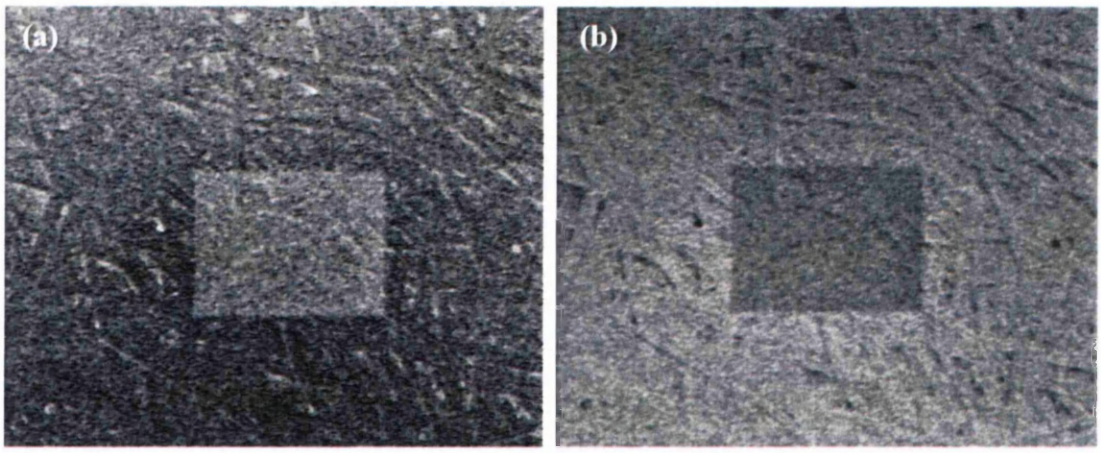

Figure 4.11. Determining E_2 for low accelerating voltages in non-conducting samples, where the SEM images are of paper taken at electron beam accelerating voltages of (a) 2.5 keV and (b) 1.2 keV. It can be seen that a) is negatively charge and kV and b) is positively charging. Reproduced from [1].

Hitachi provides the following procedure for determination of E_2 value [1]:

- Set the magnification to 100x and scan at TV rate
- Increase the magnification to 1000x as quickly as possible
- Count to five, then drop back to 100x magnification
- Look at the scan square that is visible in the centre of the screen
- If the scan square is brighter than the background then the sample is negatively charging and the beam energy is greater than E_2 (or possibly less than E_1).
- If the scan square is darker than the background then the sample is positively charging and the beam energy is less than E_2 (and greater than E_1).

4.3. Energy Dispersive X-ray Spectroscopy (Elemental Analysis)

Knowledge of the internal structure of a material can be useful to determine the source of material systems physical and optical properties. Using elemental analysis techniques such as Energy Dispersive X-ray Spectroscopy (EDX), Wavelength Dispersive X-ray Spectroscopy (WDX) or X-ray Photoelectron Spectroscopy (XPS) can obtain detailed information on internal structure and chemical make-up of a material. EDX and WDX data can be obtained in-situ with SEM topographical analysis, as when the electron beam hits the material, characteristic x-rays are generated at discrete wavelengths and energies revealing the different elements within the sample. To interpret chemical characterisation results a good understanding of the principles behind EDX is required; the following sub-section will look at the physics behind EDX giving examples taken from this studies work.

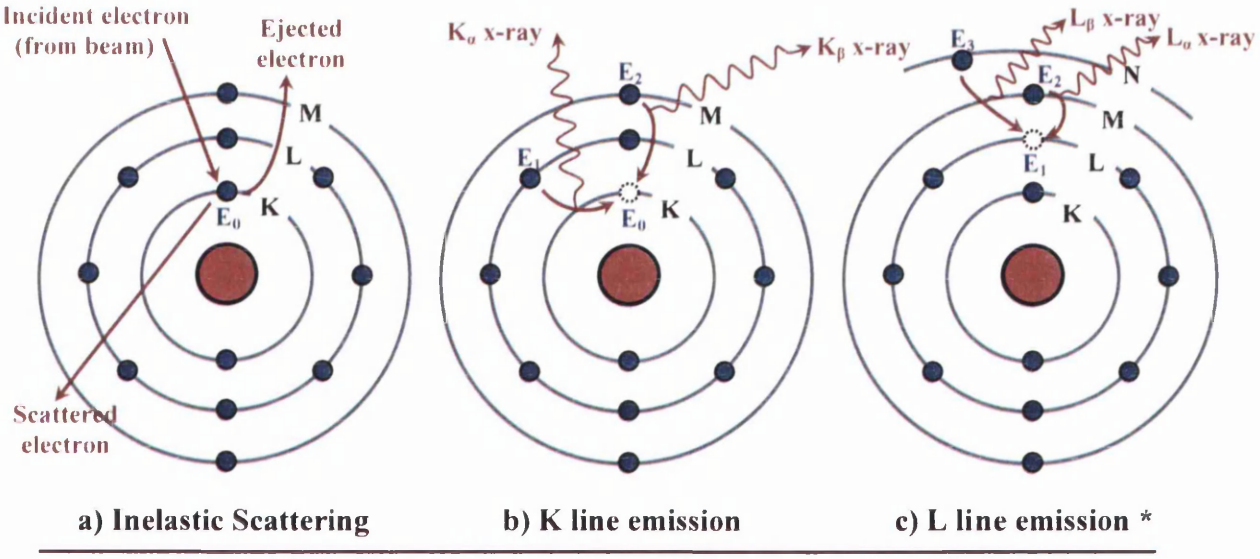

Figure 4.12. K and L line X-ray emission process due to incident electrons from the SEM electron beam. Adapted from [10].

When the electron beam hits the sample electrons are ejected from atoms by incident electrons, creating vacancies throughout the material, see Fig. 4.12. When an electron from the L or M shell drops an energy level to fill a K shell vacancy a characteristic x-ray is emitted of energy equal to the drop in energy level. If the electron drops a single level (L to K) this creates a Kα x-ray, if the electron drops two levels (M to K) a Kβ x-ray is emitted. The occupancy of the K shell hole creates either a L or M shell vacancy, which when occupied by a M or N shell electron emits a Lα or Lβ

characteristic x-ray respectively. The x-ray energies are unique to the element that created them allowing quantitative analysis of materials chemical characteristics when compared to known x-ray energies [11], see Table 4.2.

The electron beam is only able to ionize atoms if the incident electrons have energy greater than the binding energy of the inner shell electrons of the atom. Since binding energies differ for each element EDX compares the energy of the x-rays to determine the element of origin. Also as the K shell is closest to the nucleus and is therefore more tightly bound its binding energy is greater than other shells, meaning that if the beam energy is sufficient to produce a K_α or K_β x-ray emission then L and M shells will also emit x-ray if shells above them are occupied [10]. This is why in Table 4.2. gold is the element with the highest probably to produce M_α x-ray emission as its atomic number is 79 and it has 6 occupied shells. Absorption edge energy is the energy required to excite x-ray emission and is equivalent to the elemental emission lines to be observed. However, to maximise characteristic emission against continuum (brehmstrahlung) emission to yield sufficient signal to noise ratio the EDX user must exceed the minimum absorption edge energy by at least a factor of 1.5 [2].

As mentioned the characteristic energy of a given x-ray emission varies with atomic number, to obtain the atomic number from the x-rays Moseley's law is used to determine the element producing the K, L or M line emission. Which shows that the square root of the photon frequency is proportional to the atomic number of the emitting atom [12]. Equation 4.1. shows Moseley's law explaining the relationship between Energy (E) and atomic number (Z) where C_1 and C_2 are constants that depend on line type and can be considered equal for K line emission; further knowledge of these principles lay far beyond the scope of this thesis. When Moseley's relationship is used in conjunction with Planck's relation (Equation 4.2.) then it can be understood how either EDX or WDX can be used to determine the element of origin by obtaining the atomic number from either x-ray energy or wavelength.

$$\sqrt{E} = C_1(Z - C_2) \tag{4.1}$$

$$E = {}^{hc}/_{\lambda} \tag{4.2}$$

[2] Dr Jean-Paul Mosnier, Dublin City University, Personal Communication, 21st January 2014

$$Z \propto {}^{1}/_{\lambda^{1/2}} \tag{4.3}$$

Traditionally EDX detectors have used Silicon crystals doped with lithium, called 'Si(Li)' as sensors. Incoming X-rays ionize the sensor's atoms producing a charge proportional to the X-ray energy that is detected by a Field Emission Transistor (FET) attached to the crystal. However Si(Li) sensors need extremely cold temperatures to operate, requiring constant consumption of liquid nitrogen during operation. However recently Silicon Drift Detector (SDD) sensors have become widely available as they only require a few degrees below freezing to operate and so can be operated with Peltier cooling and have far great surface area allowing for a much higher acquisition rate [13]. The detector used in this work is an Oxford Instruments X-Max, and uses a SSD sensor, see Fig. 4.13.

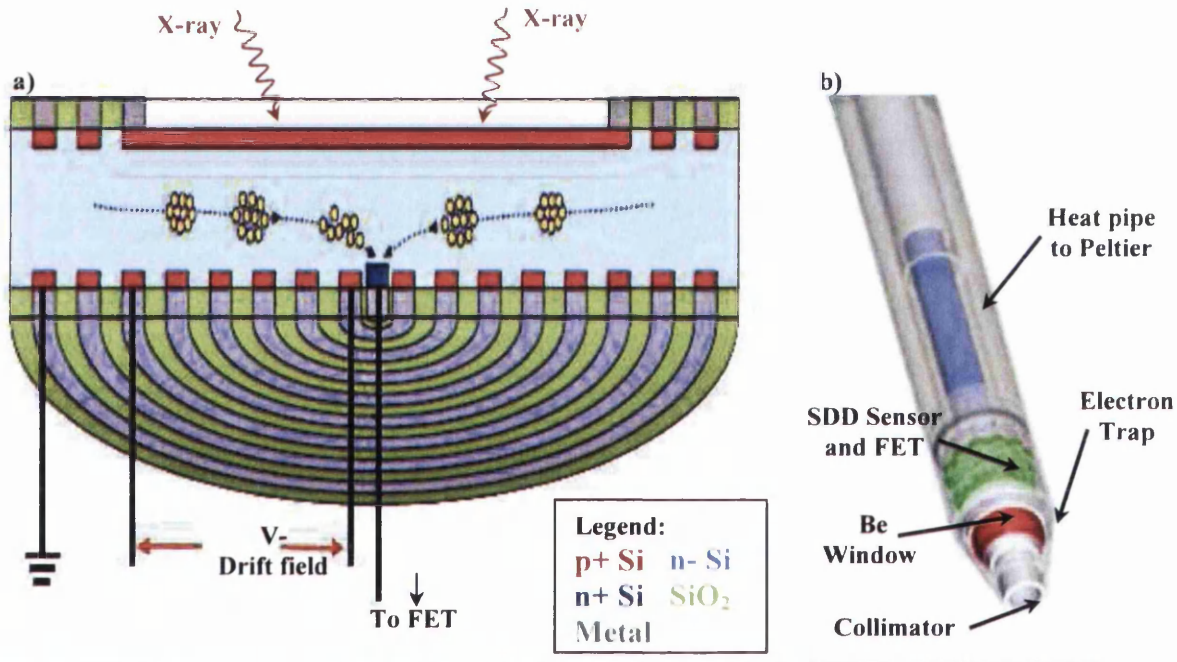

Figure 4.13. Diagram of the Oxford Instruments X-Max 100 EDX SDD detector used in this work, where a) shows operation of SSD and b) labels all components, from [13].

Fig. 4.13b. shows the EDX detector that is inserted into the SEM chamber, it comprises of four main components essential to operation; they are the sensor and FET, the Beryllium window, the electron trap and the collimator. The collimator's aperture collects X-rays from only the area of the sample excited by the electron beam. The X-Max uses a polymer based window supported on a mesh grid to allow detection of low

energy X-rays as low as 100 eV. Due to the thinness of the window some high energy electrons are able to tunnel through, and to avoid them interfering with the charge of the SSD an electron trap consisting of a looped magnet is installed to deflect an incoming electrons before they reach the sensor. The sensor itself works by applying a field gradient using the rings of metal in Fig. 4.13a. These back surface electrodes collect the charge from ionized atoms due to the X-ray and send it to the anode which is connected to the FET. The transistor is connected directly to the back of the SSD and is used to amplify the charge and send a voltage output to the electronics. The process generates heat and requires cooling so a Peltier element attached via a heat pipe to cooling fins in the detector casing is attached to the SSD and FET.

Chemical characterization techniques such as EDX can yield an understanding of the causes behind trends seen in other characterization techniques. For example when comparing the PL of two hydrothermally grown nanowire arrays with precursor ratios of 2:1 and 1:1 (discussed in chapter 8) the 2:1 nanowires will have a larger 550 nm centred defect peak; indicating the lattice contains a higher degree of defects. When analysed with EDX this difference in optical properties between the two recipes can be attributed to oxygen vacancies within the lattice as quantitative x-ray analysis shows a 52.24 to 47.76 and 51.46 to 48.54 ratio for zinc to oxygen for precursor ratio's 2:1 and 1:1 respectively. However, the origins of such observations need to be considered, as it is known that while EDX yields information from the bulk PL can often be surface sensitive [14].

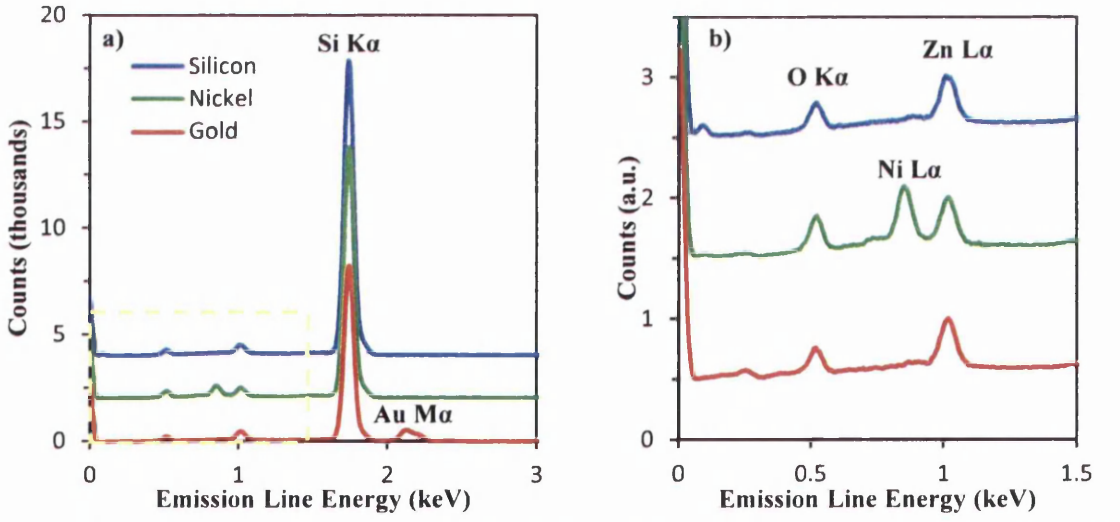

Figure 4.14. Comparison of gold and nickel layer between silicon substrate and ZnO seed layer, with a silicon only control, from [15]. Nickel and Silicon have been offset by 2000 and 4000 counts respectively. Notice the intensity of the silicon peak due to the PVD layers having a combined thickness of 55 nm

Table 4.2. Element emission line energies, from [11]

Element	Line Energy (KeV)	Emission Line
Oxygen	0.5249	Kα1
Nickel	0.8515	Lα1
Zinc	1.0117	Lα1
Silicon	1.7399	Kα1
Gold	2.1229	Mα1

Fig. 4.14. and Table 4.2. are examples of typical quantitative results obtained from EDX, where three similar samples have been analysed. All with a silicon substrate and a 20 nm thick ZnO seed layer, but two samples have a 35 nm metal layer between the substrate and the seed layer. This work has been published by Brown et al. [15] who showed that with EDX there was a significant difference between the ZnO seed layers, and attributed the observed differences to a change in roughness of the seed layer. EDX can be used to produce results revealing the atomic percentage of all the elements within the material; this can be useful for detailed quantitative analysis of samples. Table 4.3. shows an example of atomic % data.

Table 4.3. Example of information obtained from EDX spectrum. Al, Cu and Si have been omitted.

Element	Line	App. Conc.	k ratio	Intensity Corrn.	Weight %	Weight % Sigma	Atomic %
Carbon	K	1.03	0.00476	0.5732	1.74	0.47	5.27
Oxygen	K	43.96	0.15778	1.8406	23.17	0.35	52.67
Potassium	K	0.92	0.00754	1.1936	0.75	0.14	0.69
Zinc	L	63.23	0.63235	0.8249	74.35	0.5	41.37

In this work EDX was used to provide elemental analysis of zinc to oxygen ratios to provide quantitative comparisons between different crystal growth recipes. Therefore knowledge of how atomic percentage is acquired is necessary for good understanding of the results; and is discussed further in Appendix III where quantitative analysis of EDX spectra for polyethylenimine (PEI) is examined. The INCA analysis software[3] used in this study runs through several calculations to derive the final distribution of elements as a total of 100 percent. The following text will explain the importance of each step.

[3] http://www.oxford-instruments.com/products/microanalysis/wavelength-dispersive-systems-wds/wave-software

As there is contribution from nonlinear background across the entire energy range the INCA software applies filtered least squares fitting method to each peak to remove the background continuum x-rays [16]. Statham's [17] 'top hat filter' is used to filter each peak yielding zero background contribution and perfect Gaussian elemental peaks so that areas can be measured to obtain apparent concentration. Once the background is removed the elemental peak intensities are divided by similar saved standards collected under the same conditions, such as accelerating voltage, probe current, live-time; essentially normalizing the collected peak intensities to known data. This ratio is called the k ratio [10]. INCA corrects the data's intensity further by compensating for inter element effects using Pouchou and Pichoir's [18] exponential matrix correction model, yielding an intensity correction that is the ratio of the combined sample correction to the combined standard correction for each element. It should be noted that if intensity correction is close to 1 that little correction has been applied to the elemental peak, and ideally this value should be between 0.8 and 1.2 [19].

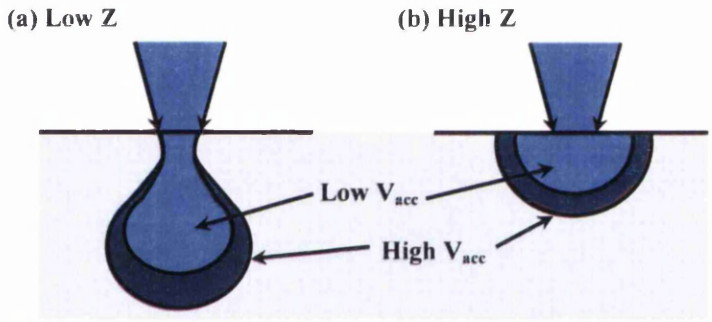

Figure 4.15. Distribution of incident electrons (from beam) with change in accelerating voltage, where dark blue depicts increased Vacc; and where a) is a low and b) a high atomic number material, adapted from [20].

Weight % is obtained after intensity correction, and values are scaled up to make 100 yielding percentage. Though weight % is not useful in this study as it provides little insight into the arrangement or ratio of the zinc and oxygen atoms, which is given by atomic %. Weight % sigma shows the statistical error in calculation and can be used to gauge signal to noise ratio. As if the value exceeds twice the amount in weight % then the amount of element in the sample is typically below the detection limits and should be omitted. Atomic % is the value used is this study and is used to compare differences between zinc to oxygen ratio for different ZnO growth recipes. It is simple when atomic weights are considered to see that weight % cannot reflect on the ZnO lattice ratio, as zinc and oxygen have atomic weights of 65.38 and 15.99 respectively. EDX has clearly

detected more oxygen than zinc atoms are present within the sample. However care should be taken when analysing data as selection of accelerating voltage and probe current will affect the interaction volume of the beam and lead to measurements from substrate as well as sample, see Fig. 4.14a. Note that raw data is not shown and that changing the list of elements will cause the software to automatically rescale wt% and at% to 100%; for example in Table 4.3. contributions from a copper SEM stub clip, the Aluminium stub itself and the Silicon substrate have been omitted.

EDX is unable to distinguish between compounds like X-ray Photoelectron Spectroscopy can, as the energy of x-ray emission is independent of the materials chemistry. With Kirkbridge [21] reporting that EDX suffers from a lack of specificity regarding the oxidation state of complex anions; where it cannot for example distinguish between chloride and chlorate, nor between sulfur, sulfide and sulfate. For example the oxygen peak obtained from ZnO (sample) and SiO_2 (substrate) will be in the same position for both materials. This means careful consideration needs to be given to the interaction volume of the beam, see Fig. 4.16. depicts a Monte Carlo simulation of electrons in Iron with different accelerating voltages.

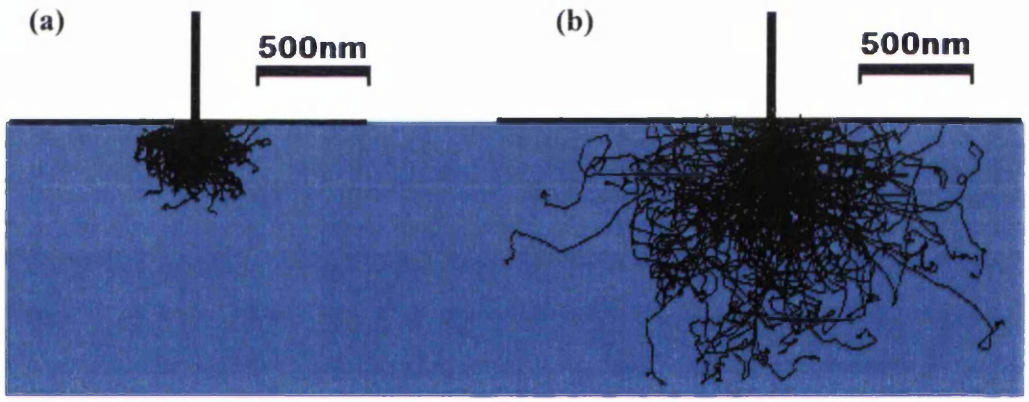

Figure 4.16. Monte Carlo simulation of interaction volume at a) 10 KeV and b) 20 KeV in iron [2].

EDX of nanowire arrays of length less than 1μm would lead to information from the substrate being obtained at 10 kV; the system would be unable to distinguish between the oxygen in the glass substrate and in the ZnO nanowire leading to a false reading of the zinc to oxygen ratio. Therefore care has to be taken when setting the electron beam to ensure that the correct balance between counts per second and interaction volume is obtained. In this work a 5 kV accelerating voltage and 20 μA

probe current were used for all quantitative analysis to guarantee no contribution from glass substrates was detected. However such low accelerating voltage leads to less x-ray emission producing a reduction in the number of counts per second acquired; therefore increasing the spectra's signal to noise ratio.

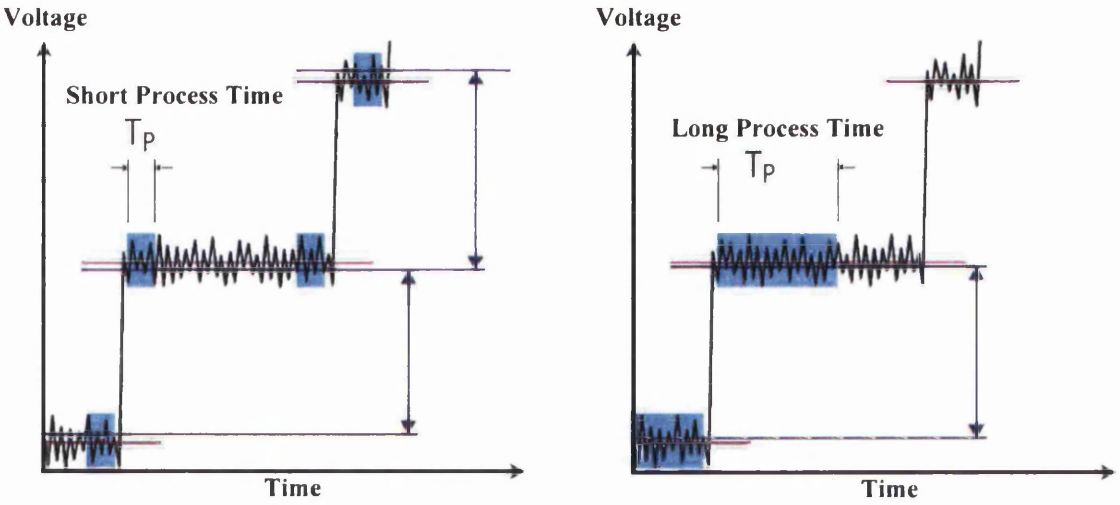

Figure 4.17. Effect of process time during acquisition on accuracy of results, adapted from [13].

The signal to noise ratio (SNR) can be improved at the cost of element peak resolution by reducing the process time, which is the amount of time the software spends reducing the noise from the SSD/FET signal during processing. The process time was often reduced from 6 to 5 (arbitrary time units) to reduce the amount of counts lost. With a high processing time data is often missed as more accumulate, the percentage of data lost is called the dead-time. Regardless of the SNR obtained the minimum process time was never set below 5, as this is the value recommend as the minimum amount of process time required to still achieve high enough resolution to not obscure overlapping peaks in the spectra, nor lose any data[4]. Fig. 4.17. shows the importance of a longer process time, were the blue boxes are indicating the time taken to average away the noise for a more accurate voltage measurement. See how for a short process time the measured value (blue line) and the actual value (red line) differ more than for the long process time; assuming that each ramp was for the same element then it is clear that a short process time results in a broadening of the peaks (an increase in FWHM) due to the inaccurate removal of noise, as shown in Fig. 4.18. However a long

[4] Judith Root, Oxford Instrument's Applications Specialist, Personal Communication, 5th October 2010

process time can miss steps resulting in a larger dead-time and worse SNR; though these can be compensated for by adjusting the electron beam or increasing the time taken to acquire the spectra. It should be noted that the process time was never set below 5 for any data shown in this thesis.

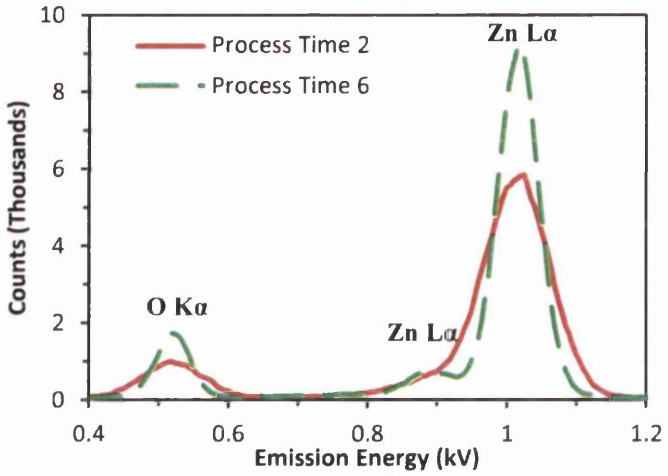

Figure 4.18. Effect of process time on accuracy of results. Where it can be seen that a short process time, i.e. larger bins to allocate data too results in the zinc satellite peak at 0.9 keV being masked.

4.3.1. Stoichiometry of ZnO

Elemental analysis results from EDX can be used to obtain atomic percentage of any material; it therefore allows crude analysis of Stoichiometry (the ratio of two elements in a compound). However it is important to determine the effect of the interaction volume and surface area to volume ratio of the samples. Cobley et al. [22] have shown with EDX that although the ratio of oxide to W appears to change from tip to shaft of a W tip, it is in fact just the effect of surface to volume ratio changing as the diameter of the tip increases. It is also important to consider the effect of the beam on the sample, given the large accelerating voltages required to obtain sufficient amount of X-rays. Goldstein [2] warns that the energy provided by the electron beam can cause cracking of hydrocarbons resulting in deposition of carbon on the sample. Both these observations may affect stoichiometry determination, for example if ZnO nanowires are on a glass substrate (SiO_2) then care must be taken not to include counts from the substrate. It should also be known that stoichiometry values obtained using EDX are for guidance only as the margin of error has been reported to be as high as ±2 % [23].

4.4. Photoluminescence (Optical Properties)

Photoluminescence (PL) is the process of absorption and re-emission of light, and can be used to understand the electronic structure of a solid. As discussed in chapter 2, when a material is excited (in this case by a light source) electrons are given enough energy to traverse from valence to conduction band across the band gap. However when an electron transitions back to the valence band it recombines with a hole emitting a photon of energy equivalent to the amount lost dropping; for direct band gap materials see Fig. 2.2a. p.9. A spectrometer is able to detect the wavelength of the photon, proportional to its energy and plots the intensity of the spectrum, Fig 4.19. This means that PL is able to observe deep level recombination sites due to defects as well as shallow donor and acceptor levels, allowing a measure of the lattice quality. Understanding the mechanisms controlling the optical properties of ZnO nanowires was crucial to optimization of the growth recipes discussed in chapter 3, as well as answering the brief of this project by achieving the foundations of creating a functional device. It is due to the importance of these findings that the majority of the 586 nanowire arrays fabricated during the course of this work were characterized for optical properties using PL. This section will expand on the theory in chapter 2 and explain the mechanisms behind the PL of ZnO nanowires with relevant real data examples, such as Fig. 4.19.

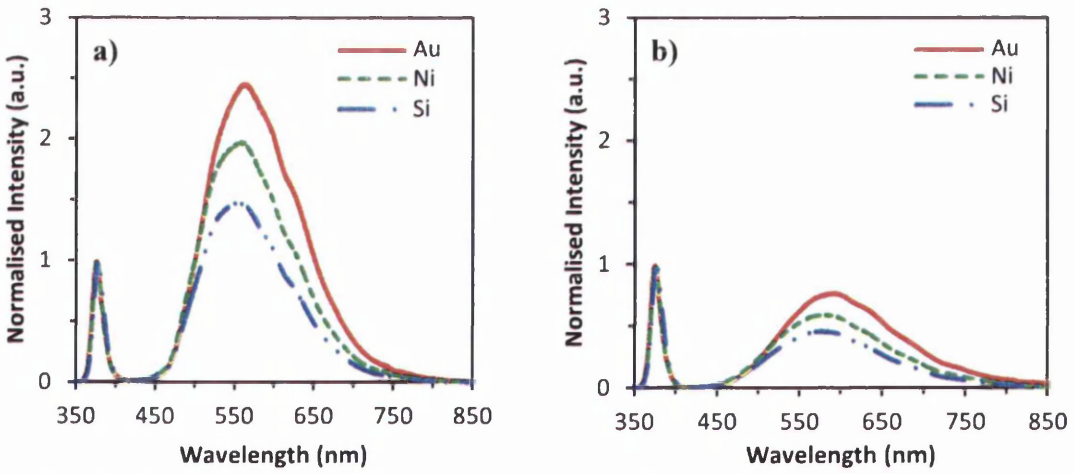

Figure 4.19. Comparison of gold and nickel layers between a silicon substrate and ZnO seed layer, with a silicon only control, where a) and b) have not and have been calibrated for absolute irradiance, respectively. From ref. [24].

The original intent was to address the ZnO nanowire array optically to access the level of nanowire bending quickly and accurately, it was originally proposed that using second harmonic generation (SHG) a non linear optical process as the basis for imaging will allow a much higher spatial resolution to be obtained compared to imaging based on conventional fluorescence, due to re-emission of absorbed light inhibiting fluorescence techniques much like the reduced resolution of BSE SEM images discussed earlier. Fig. 4.20. shows the closed beam fibre optic based system with a 325nm HeCd laser source that was used in this work. This was done to increase the beneficial power per unit area reaching the sample as using a Mercury lamp would have resulted in reduced amount of optical excitation energy greater than the band gap. At 325 nm, the HeCd is providing 3.82 eV which exceeds the energy requirement to promote the electrons to traverse the 3.3 eV ZnO band gap.

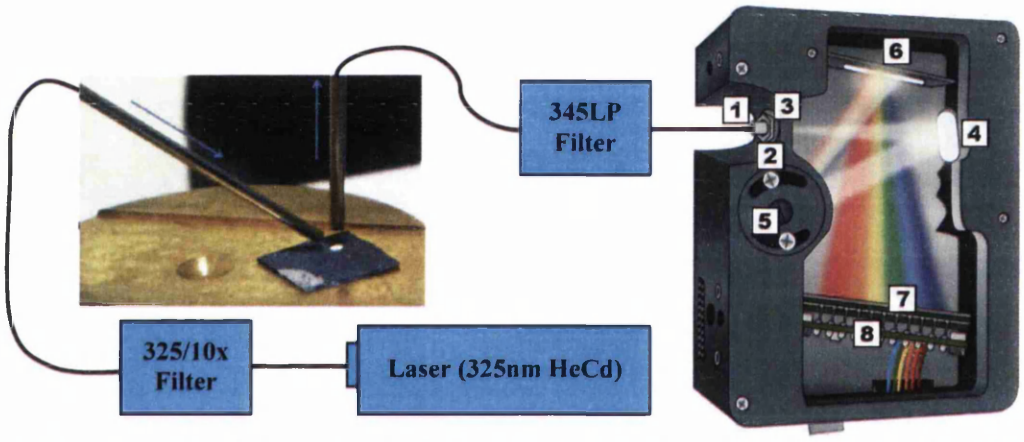

Figure 4.20. Layout of photoluminescence apparatus as used in this work with a detailed layout of the internal structure of the spectrometer used. USB2000+ diagram adapted from [25]. The components of the spectrometer are as follows; 1) SMA connector, 2) Slit, 3) Filter, 4) Collimating mirror, 5) Grating, 6) Focusing mirror, 7) Detector collection lens, and 8) CCD detector.

The spectrometer detects the intensity of light at different wavelengths, since in radiative recombination the wavelength of the photon is equivalent to the energy loss of the electron dropping; PL can reveal the band gap of the material as well as any defect induced deep levels within the forbidden region. The apparatus comprised of a Melles Girot 6 mW TEM_{00} 325 nm HeCd laser as the excitation source, fibre optic coupled into a filter block housing a 325/10x filter to remove noise peaks. The laser used suffered from irregular emission, with emission in wavelengths other than 325 nm observed. The band pass filter was coupled to the excitation wand that was directed towards the

samples at 45 ° degrees to normal and kept 2 – 3 mm away from the sample. The emission wand was directed normal to the sample to collect re-emission, some diffuse reflectance and most importantly little specular reflectance from the excitation source. To eliminate the spectrometers exposure to the excitation source a 345LP (345 nm long pass) filter was used to transmit only the spectral range needed.

The spectrometer used was an ocean optics USB2000+UV-VIS selected with a ruled grating of groove density 600 to give a blaze wavelength of 400nm, yielding a best efficiency range of 250 – 800 nm [26]. Fig. 4.20. reveals the inside of the spectrometer, where light enters the spectrometer through the optic fibre via the SMA connector, and the amount is controlled by a 25 μm by 1000 μm rectangular slit and a filter to restrict the spectral range. Once the wavelength range and intensity have been controlled the light beam then encounters the collimating mirror which focuses the light onto the diffraction grating. The grating (depending on the density and the blazing wavelength) splits the light beam into discrete wavelengths, similar to a prism breaking light up into its constituent spectral colours; though here the blazing wavelength dictates the peak wavelength in an efficiency curve. The now discrete wavelengths hit a focusing mirror and are directed to the CCD detector for analysis.

4.4.1. Calibration of Data

The Ocean Optic's USB2000+ spectrometer needs to be calibrated with the current apparatus set up in Fig. 4.20. as erroneous data can often be collected from spectrometers than are not calibrated with a reference lamp. A calibration lamp from Ocean Optics was used to correct the detector for grating response, taking into account the absolute irradiance where the detector is more or less sensitive at certain wavelengths. By building a profile of the spectrometers sensitivity across the spectrum results can be adjusted using this profile to yield calibrated results[5], see Fig. 4.19. While conducting the calibration process all filters and fibres had their collimating lens adjusted to ensure the excitation source was a perfect Gaussian, see Fig. 4.21. To further improve accuracy of results the sample was left exposed to the beam for at least 30 seconds before acquiring data, as to avoid the thermal quenching effect. Kong et al. [27] have reported difficulty in observing UV emission from bulk ZnO at room temperature

[5] http://oceanopticsfaq.com/products/spectrometers/post-process-of-absolute-irradiance/

because the intensity of the emission would decrease rapidly with the increase of temperature.

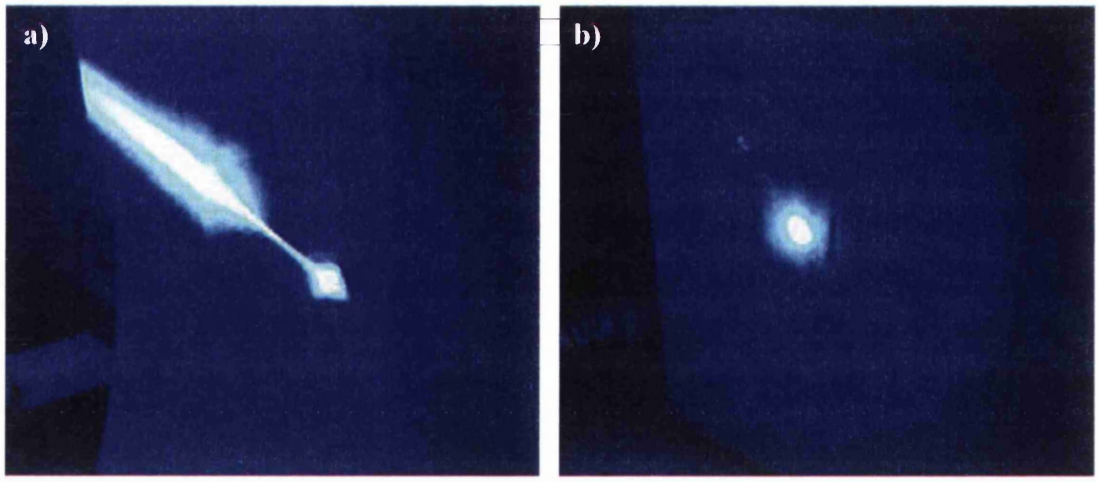

Figure 4.21. Photographs showing results of beam alignment, where a) is before and b) is after. Paper was used to see beam shape via emission, as excitation is invisible due to the HeCd's 325 nm wavelength.

4.4.2. Determination of Deep Level Components

Photoluminescence (PL) can be used to obtain more detailed sample information if the spectra is broken down in contributing components, as detailed analysis allows interpretation being defects in the lattice and surface states on the surface. Using equation 4.2 and Planck constant in electron volts ($h = 4.136E^{-15}eV.s$) we are able to convert from wavelength to electron volts to observe the distance of the band gap and the levels of recombination sites within the band gap. As discussed in section 2.2. undoped ZnO often has multiple deep level defect recombination sites within the band gap. Fig. 4.22a. shows the PL of a typical ZnO nanowire array created by the author, where it can be seen that the defect peak appears to be comprised of no less than three peaks. For example by comparing the results to findings in the literature one is able to postulate that the origins of these three component peaks centred at 2, 2.16 and 2.3 eV are likely due to singly charged oxygen vacancies (V_{O^+}), oxygen vacancy zinc instititual complexes ($V_O Zn_i$) and zinc substitutional in oxygen site (O_{Zn}), respectively [28].

Work by Ha et al. [29] has shown that the ZnO crystal lattice maybe 'healed' by thermal excitation in argon or oxygen. The PL results in Fig. 4.22. clearly shows a drastic improvement to the optical properties of the nanowires with significantly less contribution from deep level emission; as shown by the reduction of DLE peak area by

591 %. By careful analysis and review of literature annealing ZnO nanowires can be used to determine the components that contribute to the DLE emission peak.

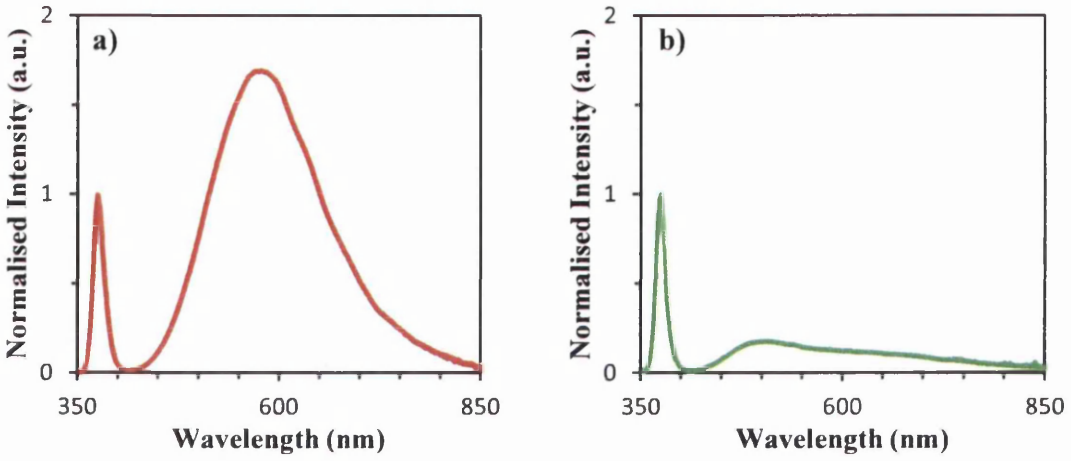

Figure. 4.22. The photoluminescence of ZnO nanowires (a) before and (b) after annealing at 500 °C for 1 hour in Argon filled environment. Note that the higher starting intensity of DLE peak compared before annealing is due to this sample being much older than the other samples used throughout this thesis.

The graphs in Figure 4.23. are produced by Fityk [30] where the program has broken down each spectra into 5 Gaussian's that represent the most commonly reported deep level band gap states from the literature; and are matched to Table 4.4. More specifically the software has been told to determine peak positions with commonly reported values from the literature used with ~10 % tolerance to unsure random Gaussian's were not selected by Fityk for the best fit; unless to compensate for extreme misfit of data. It should be noted that the above spectra are not calibrated for absolute irradiance and should be used as a guide to the amount of change in the components that comprise each spectra.

Table 4.4. Commonly accepted photoluminescence peaks for ZnO nanowires.

λ (nm)	ΔE (eV)	Description	Ref.
377.11	3.39	Band to Band	B. Ha et al. [29]
385.28	3.32	Band to Acceptor	B. Ha et al. [29]
528.02	2.42	O_{Zn}	B.Lin et al. [31]
580.02	2.21	$V_O Zn_i$	P. Xu et al. [32]
640.37	2.00	V_O^+	S. Lima et al. [33]

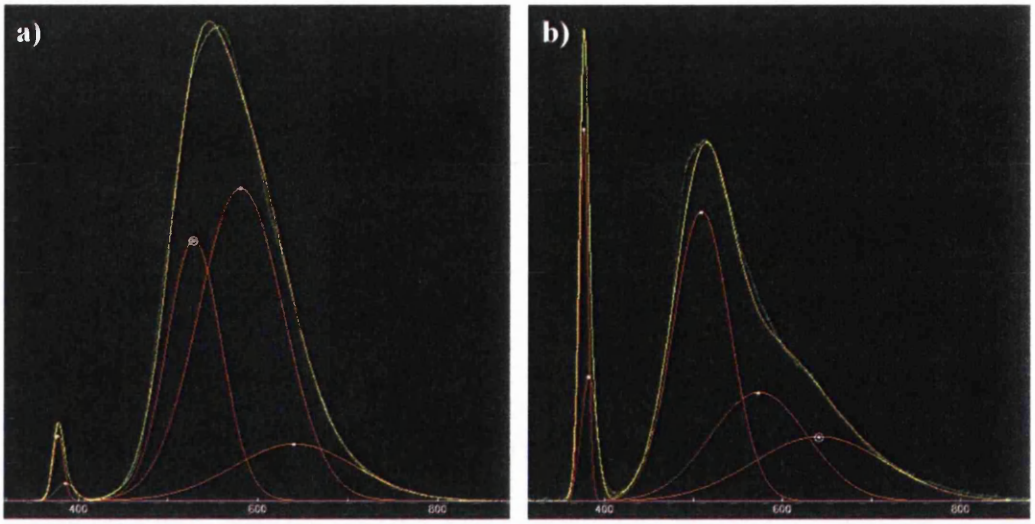

Figure 4.23. The photoluminescence spectra for a ZnO array (A) before and (B) after annealing at 500 °C for 1 hour in Argon. The graphs are produced by Fityk [30] where the program has broken down each spectra into 5 Gaussian's that represent the most commonly reported deep level band gap states from the literature.

More interestingly, Figure 4.23 shows that the DLE visible emission band is certainly comprised of multiple components as annealing only partially removed the DLE peak, blue shifting the peak from 575 to 500 nm. Ha et al. [29] has broken down the typical ZnO spectra into 5 components, 2 for NBE and 3 for DLE, labeled Blue (479 nm), Green (524 nm) and Yellow (595 nm). They attribute Blue to intrinsic defects such as O and Zn vacancies and interstitials, Green to single-ionised oxygen vacancy and Yellow to single negatively charged oxygen interstitials. The Green emission has also been attributed to single-ionised oxygen vacancy in ZnO by Vanheusden et al. [34] with Li et al. [35] reporting similar breakdown of their spectra, with their DLE comprised of two weak green emission bands centred at 485 nm and 530 nm. Ku et al. [36] suggests a different origin of the green band emission in hydrothermally grown nanowires, with OH- proposed to be the surface-trapping centre because green emission intensity correlates with surface hydroxide concentration. Song et al. [37] has suggested that the peak at about 530 nm is due to the radiative recombination of a photogenerated hole in the valence band with an electron occupying the deep oxygen vacancy energy band.

Wang et al. [38] revealed that post oxygen annealing their nanowires did not have any significant change in stoichiometry, although they did gain a dramatic reduction in the green to UV band intensity ratio (from 0.4 to 0.023). With this information and the previously discussed breakdown of spectra it could be concluded that although the amount of oxygen has not changed within the nanowires the

interstitials have been given sufficient energy to fill vacancies. A similar result was reported by Gupta et al. [39] who reported that the improvement with annealing was due to a reduction of stress within the crystal lattice; which supports both this works results and spectra breakdown by Ha et al. [29]. There are limitations with PL analysis of deep levels within the band gap as they maybe of either point defects (interstitials, anti-sites, substitionals, and vacancies) or surface states (dangling bonds); especially given the low power per unit area of the HeCd laser (2 W/cm^2) used in this work. However it has been reported by Lyu et al [40] that the green luminescence band remains unaffected by power as, when the excitation intensity is increased from 60 to 1000 W/cm^2 only the UV emission peak increases. Lyu et al. state that the green band emission reaches saturation with low excitation intensity because its energy density is lower than that of the free excitons. This means that the morphology of the nanowires should always be taken into consideration. It has been show by Shalish et al [41] that the diameter of ZnO nanowires affects the NBE to defect peak ratio. They concluded that surface states play a role as a change in nanowire size lead to a change in surface to volume ratio.

Photoluminescence analysis is essential to determine the optical properties of the ZnO nanowires grown in this work, where each variable changed can have its effect on optical property observed easily. This section has explained the importance of understanding the various wavelengths (or deep energy levels within the band-gap) that make up the deep level emission (DLE) band, as they can be used to determine the crystal quality of the ZnO nanowire. Also, the significance of considering the origin of these DLE components has been shown by thermal annealing of ZnO nanowire to remove surface states and heal the lattice.

4.5. Summary

This chapter has shown and explained the majority of techniques and equipment used for characterisation of ZnO nanowires in this work. It has covered Scanning Electron Microscopy (SEM) for determination of nanowire morphology (Length, Width, Alignment, Density). X-ray Microanalysis (EDX) was used to confirm stoichiometry of the nanowires, though the dangers of taking values without thought was discussed. Finally Photoluminescence of ZnO nanowires was used to determine their optical 'crystal quality' and contributions from defects and surface states were

discussed. The following chapter jump into Biology, covering the background of the mammalian cell, cell mechanics and adhesion, followed by the techniques used in this work to determine cell biocompatibility with ZnO nanowires.

4.6. References

[1] Hitachi, "Instruction Manual for Model S-4800 Field Emission Scanning Electron Microscope," 2002.

[2] J. I. Goldstein, D. E. Newbury, P. Echlin, D. C. Joy, C. Fiori, and E. Lifshin, *Scanning Electron Microscopy and X-Ray Microanalysis - A Text for Biologists, Materials Scientists, and Geologists*, 2nd Ed. Plenum Press, New York, 1981, p. 673.

[3] L. Reimer, *Scanning Electron Microscopy: Physics of Image Formation and Microanalysis*, 2nd ed. Springer, 1998, p. 527.

[4] J. J. Bozzola and L. D. Russell, *Electron Microscopy: Principles and Techniques for Biologists*. Jones and Bartlett, 1992, p. 542.

[5] P. J. Goodhew, J. Humphreys, and R. Beanland, *Electron Microscopy and Analysis*, Third. Taylor & Francis, 2001, p. 251.

[6] L. Reimer, *Image Formation in Low-Voltage Scanning Electron Microscopy*. SPIE Press, 1993, p. 143.

[7] W. L. Jongebloed, I. Stokroos, J. J. Van der Want, and D. Kalicharan, "Non-coating fixation techniques or redundancy of conductive coating, low kV FE-SEM operation and combined SEM/TEM of biological tissues.," *J. Microsc.*, vol. 193, no. Pt 2, pp. 158–70, Feb. 1999.

[8] A. Khursheed, *Scanning Electron Microscope Optics and Spectrometers*, 1st ed. World Scientific, 2011, p. 402.

[9] C. W. Oatley, "The early history of the scanning electron microscope," *J. Appl. Phys.*, vol. 53, no. 2, p. R1, Feb. 1982.

[10] J. J. Friel, *X-ray and Image Analysis in Electron Microscopy*, 2nd ed. Princeton Gamma-Tech, 2003, p. 97.

[11] J. A. Bearden, "X-Ray Wavelengths," *Reviews of Modern Physics*, vol. 39, no. 1. pp. 78–124, 1967.

[12] R. A. Serway, C. J. Moses, and C. A. Moyer, *Modern Physics*, 3, illustr. Cengage Learning, 2005, p. 600.

[13] Oxford Instruments, "Silicon Drift Detectors Explained," 2012. .

[14] A. M. Munro, *Effects of Surface Chemistry and Electronic Environment on Cadmium Selenide Nanocrystal Photoluminescence*. ProQuest, 2008, p. 112.

[15] R. A. Brown, J. E. Evans, N. A. Smith, A. Tarat, D. R. Jones, C. J. Barnett, and T. G. G. Maffeis, "The effect of metal layers on the morphology and optical properties of hydrothermally grown zinc oxide nanowires," *J. Mater. Sci.*, vol. 48, no. 14, pp. 4908–4913, Mar. 2013.

[16] Oxford Instruments, "Tru-Q Application Note," 2011. .

[17] P. J. Statham, "Limitations to Accuracy in Extracting Characteristic Line Intensities From X-Ray Spectra," *J. Res. Natl. Inst. Stand. Technol.*, vol. 107, no. 6, pp. 531–546, 2002.

[18] J.-L. Pouchou and F. Pichoir, "Quantitative Analysis of Homogeneous or Stratified Microvolumes Applying the Model 'PAP,'" in *Electron Probe Quantitation*, K. F. J. Heinrich and D. E. Newbury, Eds. Springer, 1991, p. 400.

[19] Oxford Instruments, "INCAEnergy: Applications training notes," 2009.

[20] P. Duncumb and P. K. Shields, "The present state of quantitative x-ray microanalysis Part I: Physical basis," *Br. J. Appl. Phys.*, vol. 14, pp. 617–625, 1963.

[21] K. P. Kirkbride, "Spectroscopic Techniques," in *ANALYTICAL TECHNIQUES*, J. A. Siegel, Ed. Oxford: Elsevier, 2000, pp. 179 – 191.

[22] R. J. Cobley, R. A. Brown, C. J. Barnett, T. G. G. Maffeis, and M. W. Penny, "Quantitative analysis of annealed scanning probe tips using energy dispersive x-ray spectroscopy," *Appl. Phys. Lett.*, vol. 102, no. 2, p. 023111, 2013.

[23] A. T. Motta, J. A. Faldowski, L. M. Howe, and P. R. Okamoto, "In Situ Studies of Phase Transformations in Zirconium Alloys and Compounds Under Irradiation," in *Zirconium in the Nuclear Industry: Eleventh International Symposium, Issue 1295*, G. P. Sabol and E. R. Bradley, Eds. ASTM International, 1996, pp. 557 – 579.

[24] R. A. Brown, J. E. Evans, N. A. Smith, A. Tarat, D. R. Jones, C. J. Barnett, and T. G. G. Maffeis, "The effect of metal layers on the morphology and optical properties of hydrothermally grown zinc oxide nanowires," *J. Mater. Sci.*, Mar. 2013.

[25] Ocean Optics, "USB 2000+ Optical Bench Options," 2012. [Online]. Available: http://www.oceanoptics.com/Products/benchoptions_usb4.asp. [Accessed: 04-May-2014].

[26] Ocean Optics, "Choosing a Grating & Wavelength Range," 2012. [Online]. Available: http://www.oceanoptics.com/Products/bench_grating_usb.asp. [Accessed: 04-May-2014].

[27] Y. C. Kong, D. P. Yu, B. Zhang, W. Fang, and S. Q. Feng, "Ultraviolet-emitting ZnO nanowires synthesized by a physical vapor deposition approach," *Appl. Phys. Lett.*, vol. 78, no. 4, p. 407, Jan. 2001.

[28] K. H. Tam, C. K. Cheung, Y. H. Leung, A. B. Djurišić, C. C. Ling, C. D. Beling, S. Fung, W. M. Kwok, W. K. Chan, D. L. Phillips, L. Ding, and W. K. Ge, "Defects in ZnO nanorods prepared by a hydrothermal method.," *J. Phys. Chem. B*, vol. 110, no. 42, pp. 20865–71, Oct. 2006.

[29] B. Ha, H. Ham, and C. J. Lee, "Photoluminescence of ZnO nanowires dependent on O2 and Ar annealing," *J. Phys. Chem. Solids*, vol. 69, no. 10, pp. 2453–2456, Oct. 2008.

[30] M. Wojdyr, "Fityk: a general-purpose peak fitting program," *J. Appl. Crystallogr.*, vol. 43, no. 5 Part 1, pp. 1126–1128, Oct. 2010.

[31] B. Lin, Z. Fu, and Y. Jia, "Green luminescent center in undoped zinc oxide films deposited on silicon substrates," *Appl. Phys. Lett.*, vol. 79, no. 7, p. 943, 2001.

[32] P. Xu, "The electronic structure and spectral properties of ZnO and its defects," *Nucl. Instruments Methods Phys. Res. Sect. B Beam Interact. with Mater. Atoms*, vol. 199, pp. 286–290, Jan. 2003.

[33] S. Lima, "Luminescent properties and lattice defects correlation on zinc oxide," *Int. J. Inorg. Mater.*, vol. 3, no. 7, pp. 749–754, Nov. 2001.

[34] K. Vanheusden, W. L. Warren, C. H. Seager, D. R. Tallant, J. A. Voigt, and B. E. Gnade, "Mechanisms behind green photoluminescence in ZnO phosphor powders," *J. Appl. Phys.*, vol. 79, no. 10, p. 7983, May 1996.

[35] F. Li, Z. Li, and F. J. Jin, "Structural and luminescent properties of ZnO nanorods prepared from aqueous solution," *Mater. Lett.*, vol. 61, no. 8–9, pp. 1876–1880, Apr. 2007.

[36] C.-H. Ku, H.-H. Yang, G.-R. Chen, and J.-J. Wu, "Wet-Chemical Route to ZnO Nanowire-Layered Basic Zinc Acetate/ ZnO Nanoparticle Composite Film," *Cryst. Growth Des.*, vol. 8, no. 1, pp. 12–19, 2008.

[37] G. Song and Y.-T. Yang, "Effects of annealing on the photoluminescence of terbium-doped zinc oxide nanocrystalline," in *27th International congress on High-Speed Photography and Photonics*, 2007, p. 62796Z–62796Z–6.

[38] D. Wang and N. Reynolds, "Photoluminescence of Zinc Oxide Nanowires: The Effect of Surface Band Bending," *ISRN Condens. Matter Phys.*, vol. 2012, pp. 1–6, 2012.

[39] V. Gupta and A. Mansingh, "Influence of postdeposition annealing on the structural and optical properties of sputtered zinc oxide film," *J. Appl. Phys.*, vol. 80, no. 2, p. 1063, Jul. 1996.

[40] S. Chul, Y. Zhang, H. Ruh, H. Lee, H. Shim, E. Suh, and C. Jin, "Low temperature growth and photoluminescence of well-aligned zinc oxide nanowires," *Chem. Phys. Lett.*, vol. 363, no. September, pp. 134–138, 2002.

[41] I. Shalish, H. Temkin, and V. Narayanamurti, "Size-dependent surface luminescence in ZnO nanowires," *Phys. Rev. B*, vol. 69, no. 24, pp. 1–4, Jun. 2004.

Chapter 5. Cells and Cell Mechanics

5.1. Introduction

This chapter will cover all the basic information needed to understand the main discussion in chapter 8, such as the cell cycle, proliferation, motility, protein adsorption and the analysis of zinc oxide array surface properties for observation of cell-substratum interaction. The chapter will start from the ground up assuming the reader has limited knowledge in molecular biology, such that the components of the cell and their functions will be initially but very briefly explained before moving onto discuss membrane domains and cell polarity (important in cell-substratum adhesion). Presenting the information in an introductory style should help facilitate rapid digestion for engineers and physicists of literature needed to understand the results chapters.

5.2. The Mammalian Cell

The eukaryote (meaning a cell that has two-membrane nuclear envelope and distinct cytoplasmic organelles) cell shown in Fig. 5.1. is the cell type that will be used throughout this work and is referred to as a mammalian when derived from mammals.

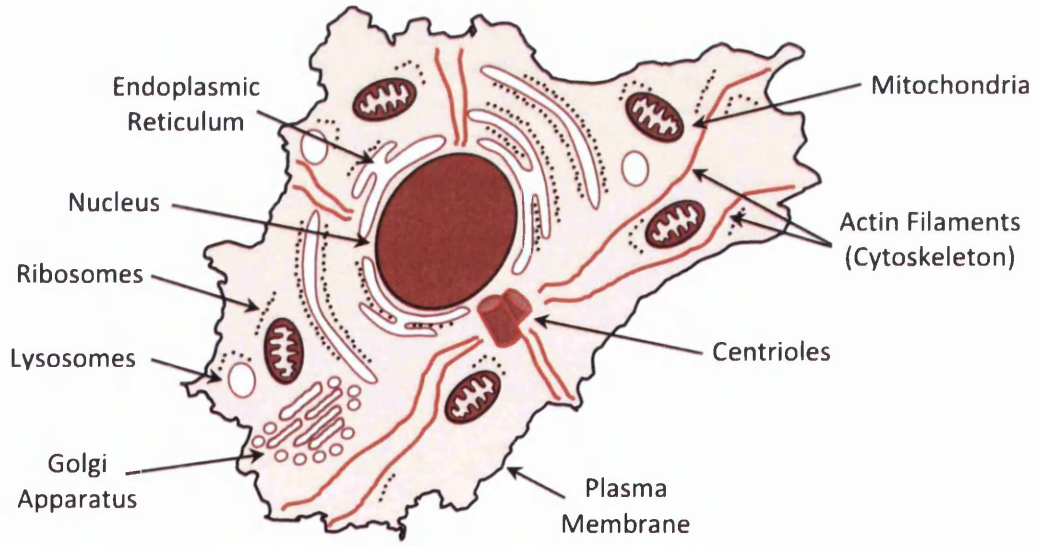

Figure 5.1. Diagram of a typical mammalian cell using in this work, with components labelled. Eukaryotic cells range from 10 – 30 μm in diameter. Adapted from [1].

The mammalian cell is comprised of the following [2]:

- Endoplasmic Reticulum & Ribosomes
  - *These are flattened sheets and tubes of membrane that extend the cytoplasm close to the nucleus and assist in synthesis of lipids and proteins, with attached Ribosomes (engaged in protein synthesis).*

- Nucleus
  - *Separated by an envelope consisting of 2 membranes. They contain Deoxyribo Nucleic Aci (DNA) in 23 chromosomal vessels, which contain information to replicate all cell components.*

- Lysosomes
  - *Vesicles that contain enzymes used for intracellular digestions.*

- Golgi Apparatus
  - *Stacked, flattened membrane sacs that sort and modify macromolecules for delivery (via small vesicles) and secretion.*

- Mitochondria
  - *Combine Oxygen and food molecules to form Adenosine TriPhosphate (ATP), which is used to transports chemical energy within cells for metabolism.*

- Cytoskeleton
  - *Arrays of protein filaments form networks to give the cell its shape and provide the beginning of movement. The cytoskeletal network is often organised from a pair of Centrioles.*

- Plasma Membrane
  - *The boundary between extra and intracellular, a continuous sheet of lipid molecules about 5 nm thick, with various proteins embedded.*

5.2.1. The Cell Cycle

Most of the biocompatibility work in chapter 8 will look at the proliferation of U-2 OS, an osteosarcoma cell (taken from a tumour of the tibia by Ponten and Saksela [3]). Therefore, better understanding of the cell cycle and proliferation process, the organelles of the cell and some basics of cell adhesion and mechanics are the minimum requirement for reading the results chapter. Fig. 5.2. shows the cell cycle both in terms of the process for an individual cell, and the effect of doubling time on the whole culture. The majority of components are continuously replicated throughout the interphase period (comprising G_1, S and G_2) between cell divisions that comprises 90 % of the cell cycle, however, DNA synthesis only occurs for a limited section of the interphase, called the **S phase** for 'synthesis' as chromosomes are replicated forming

two identical sets of chromatids. The cell now waits until it is ready to split, this is called the **G_2 phase** for 'gap'. Next the **M phase** for 'mitotic' as this phase begins nuclear division (mitosis) and cytoplasmic division (cytokinesis). Where the daughter cell begins the interphase of a new cell cycle, and begins the **G1 phase** as it waits to begin component and DNA synthesis all over again; the whole process typically takes 24 hours [2]. Although it is commonly accepted that the time taken is dependent on environmental variables [4].

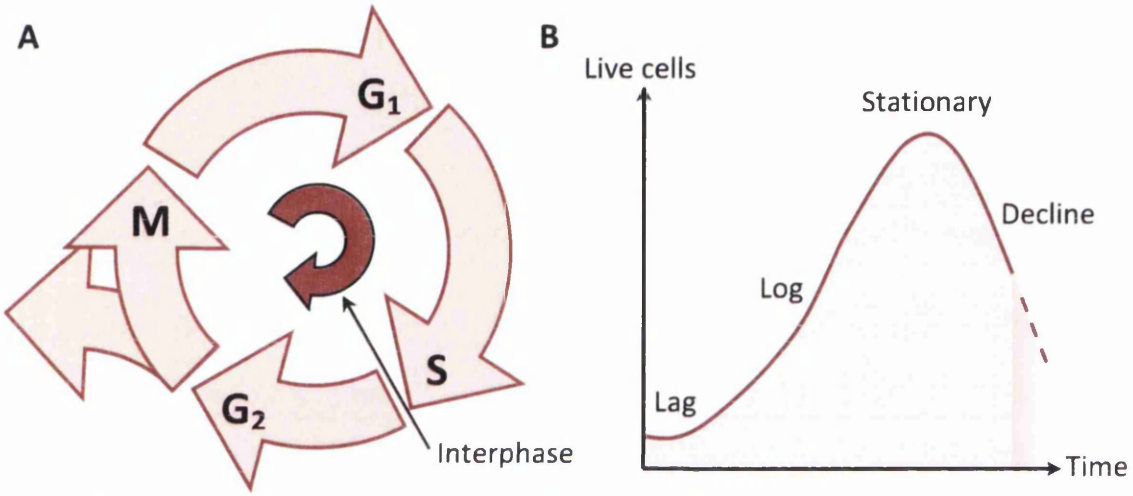

Figure 5.2. Diagrams showing, (A) the Cell Cycle, where (S) is Synthesis, (M) is Mitosis, and (G) is Gap Phase; and (B) the Population growth curve for cells in medium. The darker concentric circular arrow shows the interphase (comprising G_1, S and G_2) which comprises of 90 % of cell cycle time. Adapted from [2] and [5].

5.2.2. Population Doubling Time and Confluency

Population Doubling Time (PDT) is the time taken to double the population of cells cultured, essentially the proliferation rate of the cell line and therefore is dependent on the cell cycle time. It is often suggested in the literature that three main parameters are required to effectively characterise the proliferation rate (cell growth rate) of any cell line, specific growth rate (μ), PDT, lag time and maximum cell density, as per Murhammer et al. [6]. It has been reported by Musa et al. [7] that for the majority of osteosarcoma cell lines (included U-2 OS) the proliferation rate increased normally with incubation duration until population saturation at 10,000 cells/cm^2; whereby the population hits stationary growth phase as shown in Fig. 5.2b.

Growth in tissue culture vessel typically follows the sine wave in Fig. 5.2b. and comprises of the following components [8]:

- Lag Phase
  - *Period where no increase in cell number is seen, as reported by Vitte el al. [9] adherent cells need to attach to the substratum before they can decide what to do next, thus introducing lag.*

- Log Phase
  - *Exponential growth occurs here as cells grow at their maximum rate.*

- Stationary Phase
  - *Cell increase is offset by cell death as the supply of nutrients has become scarce and toxic waste products have accumulated.*

- Decline Phase
  - *Due to prolonged nutrient starvation and exposure to toxic waste products cells begin to die rapidly.*

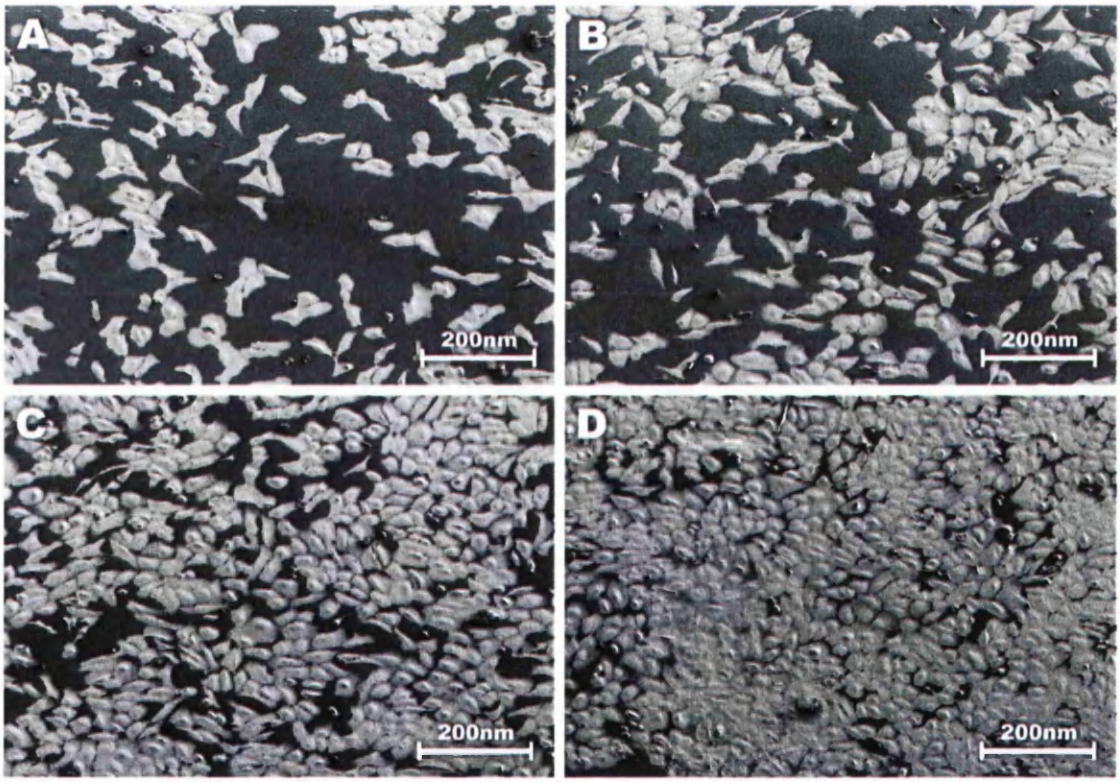

Figure 5.3. Scanning electron micrographs showing typical confluency of U2-OS cells on ZnO nanowire substratum at (A) 4, (B) 24, (C) 48 and (D) 72 hours incubation in McCoy's 5A modified medium at 37 °C 5 % CO_2. Initial seeding was 1 x10^5 cells.

Fig. 5.3. shows change in confluency of U-2 OS cells on ZnO nanowires over 72 hours. Cells should be passaged before they are fully confluent at sub 90 % confluency to avoid changes in phenotype (cell behaviour and characteristics). The cells in this

work were never passaged more than 20 times, and often for key experiments a frozen aliquot would be removed from liquid nitrogen to ensure passage number for experiment was < 10. The passage number is important as it has been reported by Ferraretto et al. [10] that at > 18 passages CACO-2 osteosarcoma cells exhibited different cell shape / spreading area and additional microvilli (brush bristle like protrusion from cell membrane which effect cell secretion and adhesion) on cell surface. Therefore the cells should be passaged in Figure 5.3c., where determination of the PDT allows an approximation of the right time to sub culture (passage) cells to avoid over confluency. Musa et al. [11] determined a PDT of 29.15 hours using an Alamar Blue (AB) assay. The AB assay is a tetrazolium-based dye (like MTS) incorporating resorufin as an oxidation-reduction indicator that produces a colorimetric change based on metabolic activity that can be plate read (see chapter 6) to determine the number of live cells present. Using these values and knowledge that population increase is exponential in the log phase due to cell doubling; then the cell doubling time (g) can be quantified using [8]:

$$g = \frac{0.301(t_x - t_0)}{\log N_x - \log N_0} \qquad (5.1)$$

Where N_0 is the initial number of cells at time t_0 and N_x is the number of cells at time t_x. Using equation 5.1 and cell counts from a 72 hour MTS assay (see chapter 6) the PDT for U-2 OS cells in this work was determined to be 21.16 hours and 21.26 hours for 4000 and 2000 cells seeded, respectively. Knowing the cell lines PDT is vital to experiment preparation, but is even more powerful when used to compare PDTs of control and sample substrata, where PDT value can indicate cell behaviour due to the substratum and other environment factors [12].

5.3. Cell Adhesion and Mechanics

Understanding the mechanisms behind cell-substratum interaction and adhesion is vitally important as it is often reported as the main environmental variable that

decides if the cell activates pathways involved in growth, apoptosis, differentiation, and motility. This decision process has been best described by Vitte et al. [9] where they explain that a recently adhered cell may undergo apoptosis, or remain alive and proliferate, or it may remain on the site of adhesion or may start migrating. While several of these decisions will be investigated in this work, it will likely be difficult to efficiently manage to pursue two areas of research in tandem, this is why the focus will be on substratum surface properties and their correlation with observed cell behaviour and proliferation. This will be done by analysing surface properties such as roughness, adhesiveness, charge and hydrophobicity to be able to more accurately hypothesise why certain behavioural traits are and differences in cell proliferation are observed for different substrata. These are therefore fully investigated in Chapter 8 alongside proliferation and cell spreading area results.

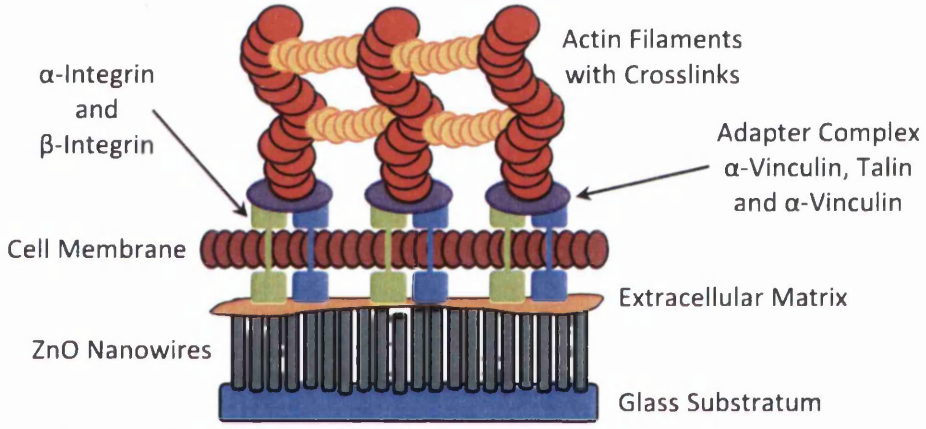

Figure 5.4. Diagram of cell-substratum adhesion, where focal adhesions are formed when actin bundles connect with the substrate via adhesion molecules such as integrin, talin and Vinculin. Note components not drawn to scale. Adapted from [15].

The process of cell adhesion has been investigated by many, and it is generally accepted by the research community that the mechanisms used are complex and can vary by cell type [13]. Work by Kasza et al. [14] has indicated that cell-substratum interactions are primarily controlled by cell membrane receptor integrin which is attached to the cytoskeleton on the cytoplasmic side as well as traversing the membrane, providing a link between the extracellular matrix (ECM), the cell membrane and more importantly the cytoskeleton. The cytoskeleton is formed from fibrous bundles of actin filaments and microtubules which are cross-linked providing integrity, these actin bundles are adhered to integrin via an adapter complex, typically reported to comprise

of Talin, Vinculin and Actinin [15], see Fig. 5.4. The tension between the ECM and the cytoskeleton due to changes in substratum topography and roughness has been reported by Ter Brugge et al. [16] to alter the cell's shape, leading to changes in integrin formation and interference with intracellular signalling events.

Since integrin signals control the progression of the cell cycle Boudreau and Jones [17] have investigated the mechanism of adhesion and its effect on cell structure and behaviour, where they hypothesise that the link between substratum surface properties and their effect on integrin adhesion and the cytoskeleton may also have an effect on gene transcription. Changes to gene transcription (where DNA is copied into RNA by RNA polymerase, for selective synthesis of gene product) could affect the production of macromolecular parts vital for the cell to function correctly. Therefore the effect on substratum properties on cell shape and spreading area will be indicative of the health of the cell [18]. This will be investigated extensively in chapter 8.

5.3.1. Cell Migration

As a lot of the later chapters in this work aim to observe cell behaviour, and cell spreading area, proliferation and motility can be adversely affected by changes in substratum properties, then the method of cell migration (i.e. the motility of the cell) will be discussed. When a cell migrates across the substratum with one edge leading with the majority of the cytoplasm, the sections at the rear can remain adhered and get drawn into long retraction fibres, see Fig. 5.5b. These can often break suddenly leaving behind a fragment of adherent plasma membrane and cytoplasm [2]; as observed in in Fig. 8.15b. The method of migration is generally accepted to comprise of 3 main processes, shown in Fig. 5.5b-e. The leading edge of the cell must extend in a single direction, where this direction can be determined by any number of environmental variables, such as chemotaxis or secretion of cytokines by other cells [19]. The leading edge must adhere to the substratum and then pull along the rest of the cell in the direction of the leading edge. It is generally believed that a Brownian ratchet motion for actin filaments is used to drive cell locomotion in the direction of the leading edge, where actin filaments are constructed by polymerisation [20]. Filipodium often protrude from these leading and retracting edges of the cell sensing the environment; however they cannot be seen in Fig. 5.5e. as filipodia are normally 100 - 200 nm in diameter with no taper [21].

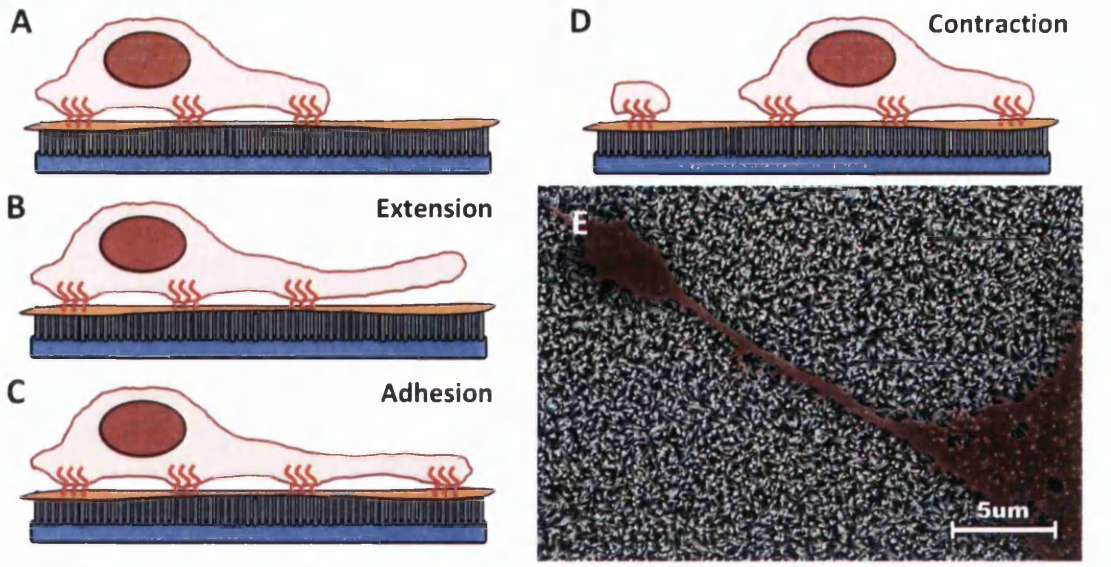

Figure 5.5. Diagram of cell (A) locomotion cycle, showing (B) Extension, (C) Adhesion and (D) Contraction. Orange coating on ZnO nanowire substratum is ECM and red lines are Actin bundles. (E) Scanning Electron Micrograph of U-2 OS showing the contraction fibre opposite side of the leading edge. Adapted from [2].

As discussed earlier, a cell has several decisions to make once it has adhered to the substratum and that the surface properties often effect this decision. However, the complex nature of attributing single variables as the cause for certain aspects of cell behaviour makes investigation of cell mechanics somewhat difficult. It can also not be easily concluded that a motile cell is a healthy one as Ayala et al. [22] have reported that cell motility is inversely proportional to cell surface area; an aspect of cell behaviour extensively researched in this work, see Fig. 8.28.

5.3.2. The Role of α-Vinculin in Adhesion Complexes

Immunocytochemisty (fluorescence microscopy) and Immunogold (Scanning Electron Microscopy, SEM) were conducted to better understand the formation of focal adhesions on ZnO nanowires. α-vinculin antibodies were used to identify where focal adhesions are made on ZnO nanowire arrays of different morphology and surface properties as well as a glass coverslip control. This decision was made as [23] reports that vinculin is under low force in contracting focal adhesions (see Fig. 5.5d.) at the trailing edge of migrating cells, but conversely also required to stabilize adhesions under force. Since vinculin appears to be vitally important under both extension and

contraction forces it would likely provide more information than observing actin alone. Therefore, Fig. 5.6. shows a diagram of the microscopic structure of a single focal adhesion, where the interior domains of integrins attach to actin stress fibres via linker proteins (vinculin and talin) and the exterior domains of integrin bind with ligands to form integrin–ligand bonds between cell surface and substratum, forming the focal adhesion [24]. The focal adhesion adapter complex is shown in Fig. 5.6. and mechanically couples the actin filament cytoskeleton to the cytoplasmic portion of the integrins (that traverse the membrane and adhere to the ECM). The adaptor complex contains actin-related molecules such as vinculin, talin and pallaxin, as well as signalling molecules that promote stimulus–response coupling [25].

As previously discussed, the process of cell migration is dynamic and ever changing to environmental variables that involves the continuous formation and maturation of substratum/extra cellular matrix (ECM)–cell adhesion sites. The formation of focal adhesions due to differences in substratum properties ideally needs to be accessed in this work by both IEM and IF, as a substantial amount of literature exists for investigation of focal adhesion with immunofluorescence. Stricker et al. [26] fabricated an array of 1 μm diameter fibronectin circles separated by 2 μm on a substrate to promote U-2 OS cells to form focal adhesions at these circles. What they found was that actin bundles terminated at vinculin-rich focal adhesion that were co-localised with the array of fibronectin circles. Stricker et al. observed these results by conducting immuno-fluorescence of vinculin where a control substratum completed coated in fibronectin was used to show vinculin distribution throughout the cell body.

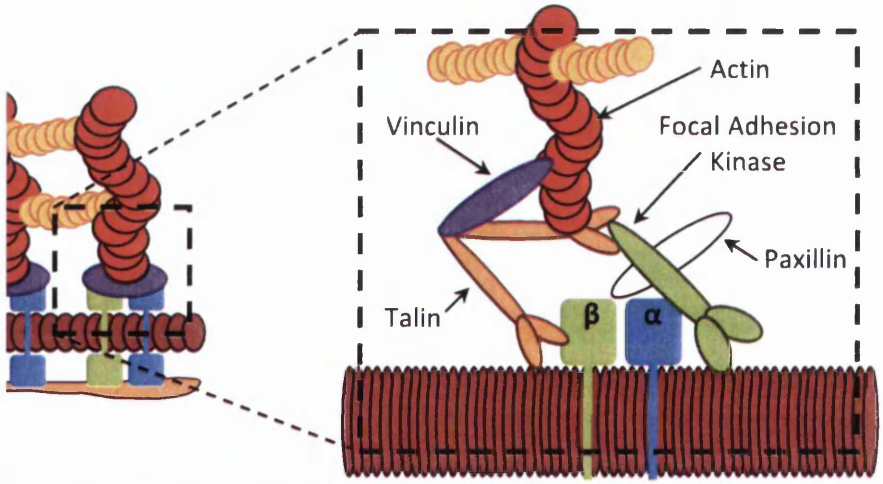

Figure 5.6. Diagram showing formation of focal adhesion and intercellular adaptor complex, where Vinculin can be seen to attach actin filament to Talin. Adapted from [27].

It has been reported by Scheider [28] that by coating microstructures with fibronectin (bioactive substance that promotes adhesion) cells bind differently to different area of topography. They observed this by labelling cell with anti-vinculin antibodies conjugated with Gold colloids to allow high resolution analysis on the electron microscope. IEM is the most likely technique this work will take when investigating focal adhesions. However, Baxter et al. [29] have investigated the extent of cell spreading by observing the location and intensity of focal adhesions assessed by the amount of vinculin labelling. Something similar could be done in tandem with IEM in this work.

5.4. Summary

This chapter has introduced molecular biology to the reader starting with the components of the mammalian cell, working onto the cell cycle and determination of population doubling time. Cell migration and focal adhesion were the next important topics and it is hoped that this brief introductory chapter has given the reader sufficient background for the analysis of the following results chapters.

5.5. References

[1] B. Alberts, A. Johnson, J. Lewis, M. Raff, K. Roberts, and P. Walter, *Molecular Biology of the Cell*. Garland Science, 2002, p. 1146.

[2] B. Alberts, A. Johnson, J. Lewis, M. Raff, K. Roberts, and P. Walter, *Molecular Biology of the Cell*. Garland Science, 2002, p. 1146.

[3] J. Ponten and E. Saksela, "Two established in vitro cell lines from human mesenchymal tumours," *Int. J. Cancer*, vol. 2, no. 5, pp. 434–447, Sep. 1967.

[4] J. Willey, L. Sherwood, and C. Woolverton, "Microbial Growth," in *Prescott's Principles of Microbiology*, 1st ed., 2009, pp. 126–152.

[5] A. Jones, R. Reed, and J. Weyers, *Practical Skills in Biology*, 2nd Ed. Harlow, England: Prentice Hall, 1998, p. 292.

[6] D. W. Murhammer, "Useful Tips, Widely Used Techniques, and Quantifying Cell Metabolic Behavior," in *Baculovirus and Insect Cell Expression Protocols 388*, New York, NY: Humana Press, 2007, pp. 3–22.

[7] M. Musa, T. P. Kannan, and S. Mustafa, "Cell Proliferation Study of Human Osteosarcoma Cell Line (U2OS) using Alamar Blue Assayand Live Cell Imaging," *J. Dent. Med. Sci.*, vol. 8, no. 2, pp. 60–65, 2013.

[8] A. Jones, R. Reed, and J. Weyers, *Practical Skills in Biology*, 2nd Ed. Harlow, England: Prentice Hall, 1998, p. 292.

[9] J. Vitte, a M. M. Benoliel, a Pierres, and P. Bongrand, "Is there a predictable relationship between surface physical-chemical properties and cell behaviour at the interface?," *Eur. Cells Mater.*, vol. 7, pp. 52–63, 2004.

[10] A. Ferraretto, C. Gravaghi, E. Donetti, S. Cosentino, B. M. Donida, M. Bedoni, G. Lombardi, A. Fiorilli, and G. Tettamanti, "New methodological approach to induce a differentiation phenotype in Caco-2 cells prior to post-confluence stage.," *Anticancer Res.*, vol. 27, no. 6B, pp. 3919–25, 2007.

[11] M. Musa, T. P. Kannan, and S. Mustafa, "Cell Proliferation Study of Human Osteosarcoma Cell Line (U2OS) using Alamar Blue Assayand Live Cell Imaging," *J. Dent. Med. Sci.*, vol. 8, no. 2, pp. 60–65, 2013.

[12] J. Willey, L. Sherwood, and C. Woolverton, "Microbial Growth," in *Prescott's Principles of Microbiology*, 1st ed., 2009, pp. 126–152.

[13] V. Saravia and J. L. Toca-Herrera, "Substrate influence on cell shape and cell mechanics: HepG2 cells spread on positively charged surfaces.," *Microsc. Res. Tech.*, vol. 72, no. 12, pp. 957–64, Dec. 2009.

[14] K. E. Kasza, A. C. Rowat, J. Liu, T. E. Angelini, C. P. Brangwynne, G. H. Koenderink, and D. a Weitz, "The cell as a material.," *Curr. Opin. Cell Biol.*, vol. 19, no. 1, pp. 101–7, Feb. 2007.

[15] R. Ananthakrishnan and A. Ehrlicher, "The forces behind cell movement.," *Int. J. Biol. Sci.*, vol. 3, no. 5, pp. 303–17, Jan. 2007.

[16] P. J. ter Brugge, S. Dieudonne, J. a Jansen, and P. J. Brugge, "Initial interaction of U2OS cells with noncoated and calcium phosphate coated titanium substrates.," *J. Biomed. Mater. Res.*, vol. 61, no. 3, pp. 399–407, Sep. 2002.

[17] N. J. Boudreau and P. L. Jones, "Extracellular matrix and integrin signalling: the shape of things to come.," *Biochem. J.*, vol. 339 (Pt 3, pp. 481–8, May 1999.

[18] L. Bacáková, E. Filová, F. Rypácek, V. Svorcík, and V. Starý, "Cell adhesion on artificial materials for tissue engineering.," *Physiol. Res.*, vol. 53, pp. S35–45, Jan. 2004.

[19] C. A. Parent and P. N. Devreotes, "A Cell's Sense of Direction," *Science (80-.).*, vol. 284, no. April, pp. 765–770, 1999.

[20] A. Mogilner and G. Oster, "Cell motility driven by actin polymerization.," *Biophys. J.*, vol. 71, no. 6, pp. 3030–45, Dec. 1996.

[21] A. C. Taylor, "Microtubules in the Microspikes and Cortical Cytoplasm of Isolated Cells," *J. Cell Biol.*, vol. 28, pp. 155–168, 1966.

[22] R. Ayala, C. Zhang, D. Yang, Y. Hwang, A. Aung, S. S. Shroff, F. T. Arce, R. Lal, G. Arya, and S. Varghese, "Engineering the cell-material interface for controlling stem cell adhesion, migration, and differentiation.," *Biomaterials*, vol. 32, no. 15, pp. 3700–11, May 2011.

[23] C. Grashoff, B. D. Hoffman, M. D. Brenner, R. Zhou, M. Parsons, M. T. Yang, M. a McLean, S. G. Sligar, C. S. Chen, T. Ha, and M. a Schwartz, "Measuring mechanical tension across vinculin reveals regulation of focal adhesion dynamics.," *Nature*, vol. 466, no. 7303, pp. 263–6, Jul. 2010.

[24] D. Kong, B. Ji, and L. Dai, "Stabilizing to disruptive transition of focal adhesion response to mechanical forces.," *J. Biomech.*, vol. 43, no. 13, pp. 2524–9, Sep. 2010.

[25] M. E. Chicurel, C. S. Chen, and D. E. Ingber, "Cellular control lies in the balance of forces.," *Curr. Opin. Cell Biol.*, vol. 10, no. 2, pp. 232–9, Apr. 1998.

[26] J. Stricker, B. Sabass, U. S. Schwarz, and M. L. Gardel, "Optimization of traction force microscopy for micron-sized focal adhesions.," *J. Phys. Condens. Matter*, vol. 22, no. 19, p. 194104, May 2010.

[27] C. Lawson, S.-T. Lim, S. Uryu, X. L. Chen, D. a Calderwood, and D. D. Schlaepfer, "FAK promotes recruitment of talin to nascent adhesions to control cell motility.," *J. Cell Biol.*, vol. 196, no. 2, pp. 223–32, Jan. 2012.

[28] L. Scheideler, "Investigation of cell reactions to microstructured implant surfaces," *Mater. Sci. Eng. C*, vol. 23, no. 3, pp. 455–459, Mar. 2003.

[29] L. C. Baxter, V. Frauchiger, M. Textor, I. ap Gwynn, and R. G. Richards, "Fibroblast and osteoblast adhesion and morphology on calcium phosphate surfaces.," *Eur. Cell. Mater.*, vol. 4, no. 0, pp. 1–17, Sep. 2002.

Chapter 6. Methods of Cell Analysis

6.1. Introduction

This chapter will discuss the techniques, procedures and protocols used to investigate the biocompatibility of ZnO nanowires with U-2 OS cells as well as in depth analysis of cell-substratum interaction due to substratum surface properties. These areas will be covered in the following order:

- SEM and Cryo SEM of Cell Behaviour
- ImmunoGold SEM of Cell-Substratum Interaction
- Promega's MTS Assay
- Invitrogen's LIVE DEAD Assay
- Analysis of Substratum Surface Properties
    - Roughness and Adhesion (AFM)
    - Wettability (Contact Angles)
    - Charge (Zeta Potential)

Typically in all (cell related) experiments U-2 OS cells were cultured in McCoy's modified 5A medium supplemented with 10 % fetal bovine serum, 1 % penicillin/streptomycin (antibiotics used to prevent bacterial contamination of the cell culture) and 1 % glutamine (an amino acid, a cellular energy source). Cells were incubated in a 5 % CO_2 environment at 37 °C in T75 Corning flasks. Once a ~90% confluency was obtained cells were trypsinized, centrifuged, pellet re-suspended and 10 µl added to an automated cell counter (TC10, Bio-Rad) with Trypan Blue for live cell concentration. The 49 – 64 mm^2 glass substrates were washed twice in 100 % ethanol then PBS prior to being added to the 48-well plate. Cells were carefully pipetted on top of the substrate and allowed 2 minutes to attach before being supplemented with 500 µl fresh media as suggested by Francis et al. [1]. Plates were incubated at 37 °C in 5 % CO_2 for 72 hours and cell populations at 0 hours were 2000 and 8000 cells taken from a 2.5 x10^5 /ml stock solution.

Fig. 6.1. shows the TC10 automatic hemocytometer determining live cell concentration, once a known concentration of cells per ml of medium was found the

amount of solution to seed the required amount of cells could be determined using equation 6.1 [2].

$$c_1 v_1 = c_2 v_2 \tag{6.1}$$

Where C is the number of cells per unit volume and V is the volume, 1 represents the known (i.e. values obtained from using a hemocytometer) while 2 represents the required values. This equation is also vital when diluting stock solutions for micro biology assays, as they are often of high concentration for storage. Once the cells have been cultured for the desired amount of time (72 hours in the majority of experiments) they will be used for various experiments, the details of which with be discussed in the appropriate sections.

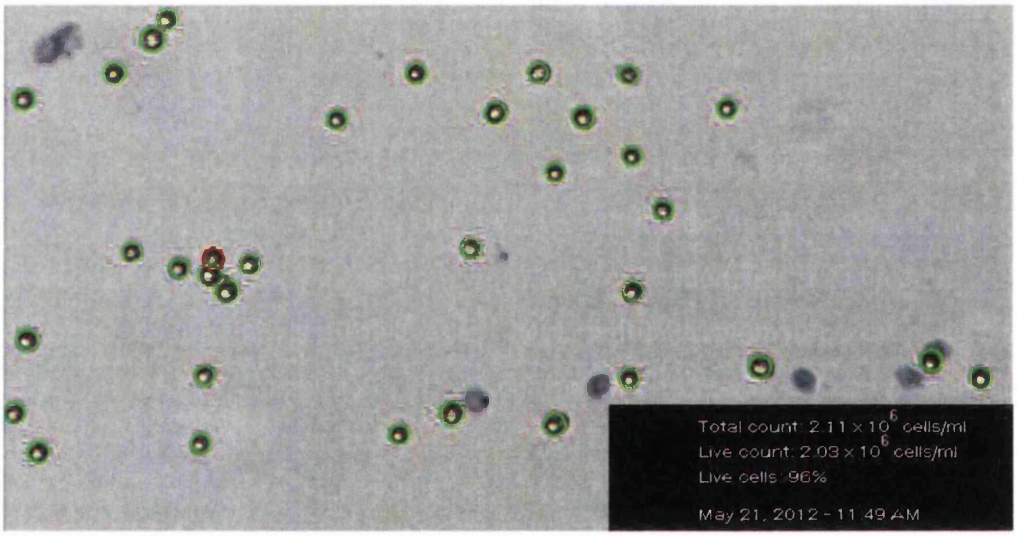

Figure 6.1. Light Microscopy image of re-suspended U-2 OS cells taken in TC10. Cells containing Typan Blue (a cell impermanent stain) are assumed necrotic and not counted allowing a more accurate cell concentration to be obtained for seeding / experiments.

6.2. Scanning Electron Microscopy (SEM) of Cells

Fixatives are used to preserve the cytoplasmic structure of a cell to allow the cells shape or components within the cell to be investigated without worry that the cell will denature (change shape), detach or even fragment due to the hypotonic nature of some solutions used to dye a cell. In this work the effect of different fixatives was

investigated, where it was found that 4 % paraformaldehyde in sodium cacodylate buffer yielded the least perturbed cells, with fillipodium still well preserved. The protocol was well refined and for normal SEM examination the substrata would be removed after the cell culture period (typically 72 hours) and washed twice in pre-warmed Hanks Balanced Salt Solution (HBSS) for 2 minutes each before being fixed by immersion in 4 % paraformaldehyde in sodium cacodylate buffer for 10 minutes at room temperature. Excess fixative was removed with a 2 minute de-ionized water wash at room temperature, followed by immersion in a graded ethanol series (70%, 80%, 85%, 90%, 95% and 100%) for 5 minutes in each before allowing the sample to air dry ready for imaging. HBSS was used instead of Phosphate Buffer Saline (PBS) as it has been reported by Francis et al. [1] to reduce the amount of artifacts seen when imaging. Samples were then imaged at 1 - 5 kV with SEM (Hitachi S4800) with no metal coating, nor negative staining with uryl acetate, nor oxygen enrichment via post fixation with osmium tetraoxide (OsO_4); as none of these procedures were required and so no additional artifacts were introduced to the images.

The literature shows that post fixation with OsO_4 destroys actin filaments [3] impacting the shape of the cell which is vitally important in predicting cell behaviors such as Viability, Migration, Proliferation and Differentiation [4]. It is also well known that the ethanol dehydration process can shrink cellular material [5], it was therefore determined that 5 minute immersion in each ethanol-water solution yielded the most ideal results. 5 minutes was found to be sufficiently long enough as to not perturb surface detail, yet short enough to avoid too much shrinkage (cryoSEM used for comparison). However, in some situations where no alternative was available (glass cover-slip control) the cells would need to be coated in metal to stop excessive charging on the sample, as discussed in chapter 4. This section shall discuss how samples were handled for fixed cells, Cryo frozen cells and ImmunoGold cells containing 5 nm Gold colloids.

6.2.1. Metal Deposition

Following the above procedure cells were dehydrated and dried in air ready for SEM analysis, typically at 1 – 5 kV. However, it was often the case that samples would show signs of 'charging' as discussed in chapter 4. If increasing the working distance

and tilting the sample towards the lower detector does not reduce the amount of charging then samples were often coated with a thin (17 nm) layer of gold. Fig. 6.2a. shows a 10 μm section from a Bovine Uterus explant showing a lumen, where severe area charging at 1 kV due to having a non-conductive sample on an insulating glass microscope slide. Fig. 6.2b. shows the same lumen as before but now the sample has been coated with a thin layer of gold, now all contrast is sample contrast and not due to charging, as discussed in section 4.2.5.

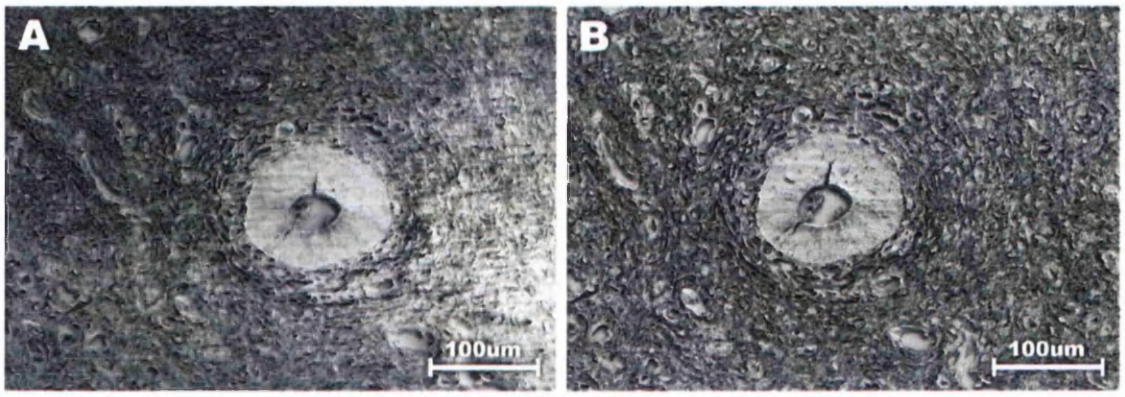

Figure 6.2. Scanning Electron Micrographs showing changes in contrast due to area charging in the section of a Bovine Uterus Explant, where (A) is not coated and (B) is coated with a 17 nm layer of gold.

Although it appears that if such area charging artifacts could be avoided then all samples should be coated in Gold, the coating process can also introduce considerable amount of artifacts into the image. Fig. 6.3a. shows the collagen fibrils of a Bovine Tendon Explant, where ridges can just about be made out in one or two fibrils, as well as clusters of glycoproteins. Fig. 6.3b. shows the sample coated with a thin layer of Gold where ridges can now be clearly seen in all fibrils, allowing measurement yielding a periodic ridge-groove spacing of 64 ±10 nm. This is similar to that reported by Yamamoto et al. [6] who found a ridge-groove spacing of 63 and 67 nm for cornea and sclera collagen fibrils, respectively. It can be seen how beneficial this additional metal layer is to the acquisition of quantitative data for analysis. However, the coating of glycoprotein clusters in gold has resulted in a considerable degree of artifact creation, with random lump and shapes of gold around the collagen fibrils. The decision to sputter coat a metal layer onto a sample therefore depends on the level of detail or magnification required in the current experiment.

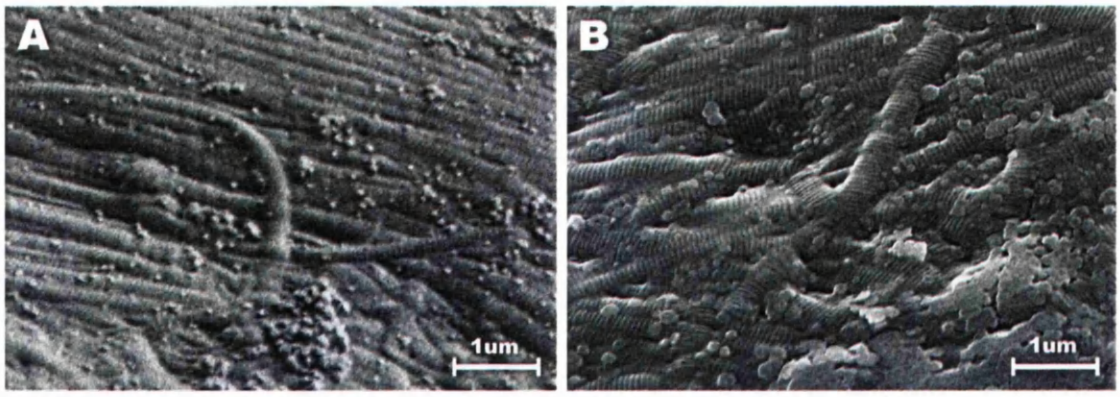

Figure 6.3. Scanning Electron Micrographs showing changes in surface detail due to metal coating in a Bovine Tendon Explant, where (A) is not coated and (B) is coated in a 17 nm thick layer of gold.

6.2.2. Cryo SEM

The introduction to this section discussed the shape changing effect of sample fixation, this needs to be discussed further. The literature often debates fixation, however it is widely accepted that it is the time taken for formaldehyde to form cross-links that dictates whether the sample will withstand the stress of dehydration [7]. If the experiment requires detailed observation of cell-substratum interaction and cell behaviour (via analysis of cell spreading area) then an alternative to cell fixation for SEM is the use of a cryo stage. This allows frozen samples to be maintained at temperatures as low as minus 192 °C by passing nitrogen gas through a liquid nitrogen heat exchanger and then through the cryo stage within the SEM chamber. Use of a cryo stage allows samples to be rapidly frozen in liquid nitrogen then transferred and their temperature maintained on the cryo stage for imaging. The cryo stage can also be temperature adjusted with a built in heater allowing the temperature of the cryo stage to be raised to about minus 90 °C to sublimate ice from the sample surface.

Fig. 6.4a. shows an Ishikawa cell on ZnO nanowires straight after loading with the cryo stage held at the operating temperature of minus 192 °C. Here the nanowires appear clustered due to the coating of ice on their surface, and the cell membrane appears strangely textured with significant area charging. Although the samples are blotted prior to freezing in liquid nitrogen, and the transfer from liquid nitrogen to the preparation chamber (which contains another cryo-stage for sublimation, cleaving tools and a sputter coater) is done in a sealed chamber to minimise exposure to air moisture, ice is still formed. Fig. 6.4b. shows the same cell post sublimation at minus 90 °C for 10 minutes, where nanowires can more clearly be defined. Sublimation can also be useful

in removal of certain biological materials, often certain components of the extra cellular matrix (ECM) have different sublimation etching rates, and so heavy sublimation can lead to removal of material enhancing definition / clarity of an image.

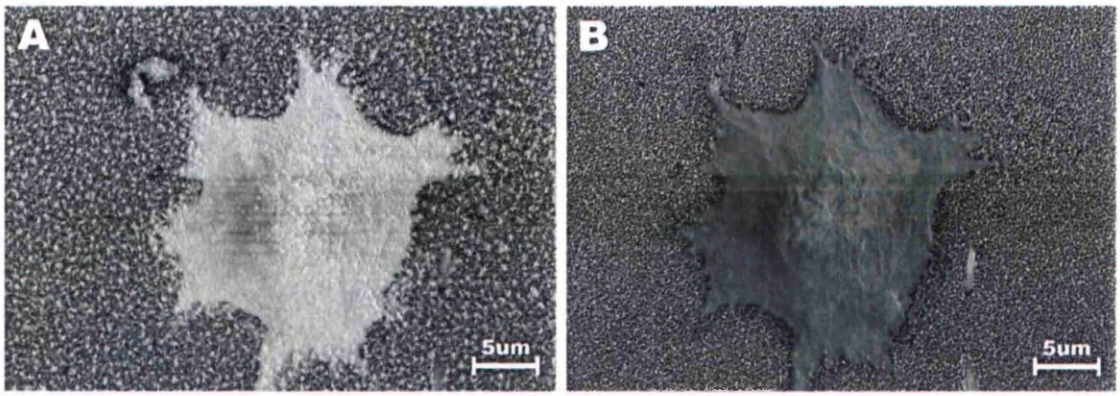

Figure 6.4. Cryo Scanning Electron Micrographs of an Ishikawa cell on ZnO nanowires, (A) before and (B) after sublimation at -90 °C for 10 minutes.

Fig. 6.5b. shows a Cryo-SEM image of Bovine Tendon Collagen Fibrils, where the ECM has been removed via sublimation leaving behind only the Collagen Fibrils. This is because non-membraneous organelles or formed components such as microtubules / actin filaments can be revealed by 'deep etching' sublimation as it is often reported that flexible molecules (e.g. mucin, protein that forms gels for lubrication) would be easily affected by sublimation [8].

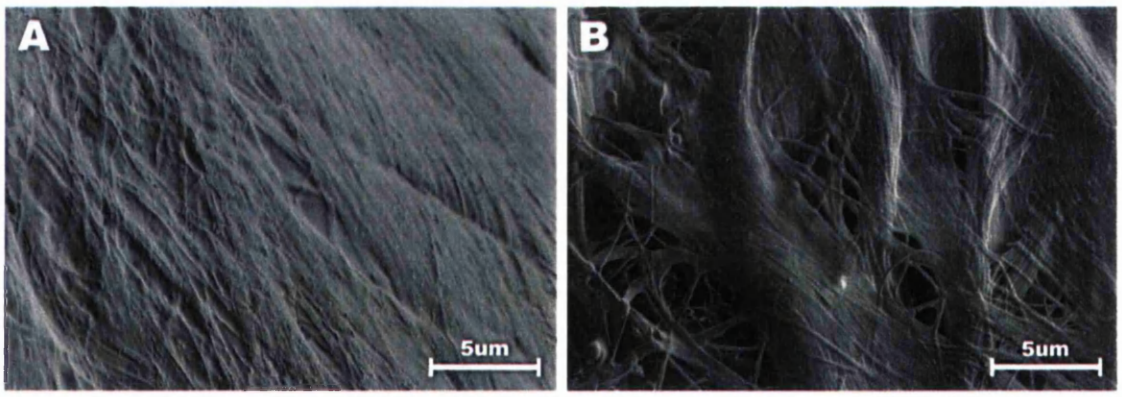

Figure 6.5. Cryo Scanning Electron Micrographs of Collagen Fibrils from a Bovine Tendon explant, where, (A) is before and (B) after sublimation at -90 °C for 10 minutes.

6.2.3. Immuno Electron Microscopy (IEM)

ImmunoElectron Microscopy (IEM) often called ImmunoGold labeling as the process involves application of antibodies to the permeabilised cells to localize an antigen, followed by subsequent conjugation of the antibody (i.e. attachment) with a gold colloid [9]. This specific targeting works because antibodies (also known as Immunoglobulin) are large Y-shaped proteins used by the immune system to detect and identify foreign objects, tagging a unique part of the cellular component (called a target) with an antigen [10], see Fig. 6.6a. Where Immunoglobins (Ig) act on pathogens by agglutinating them (or clumping particles together), opsonizing them and activating reactions against them [11]. Opsonization is the process of coating foreign particles with an antibody ready for recognition and ingestion by an phagocytic cell [12]. By using antibodies to target specific cell components then conjugating these antibodies with Gold colloids, areas of interest can be easily seen because of the change in SEM image contrast due to the difference in Z number between a cell and gold.

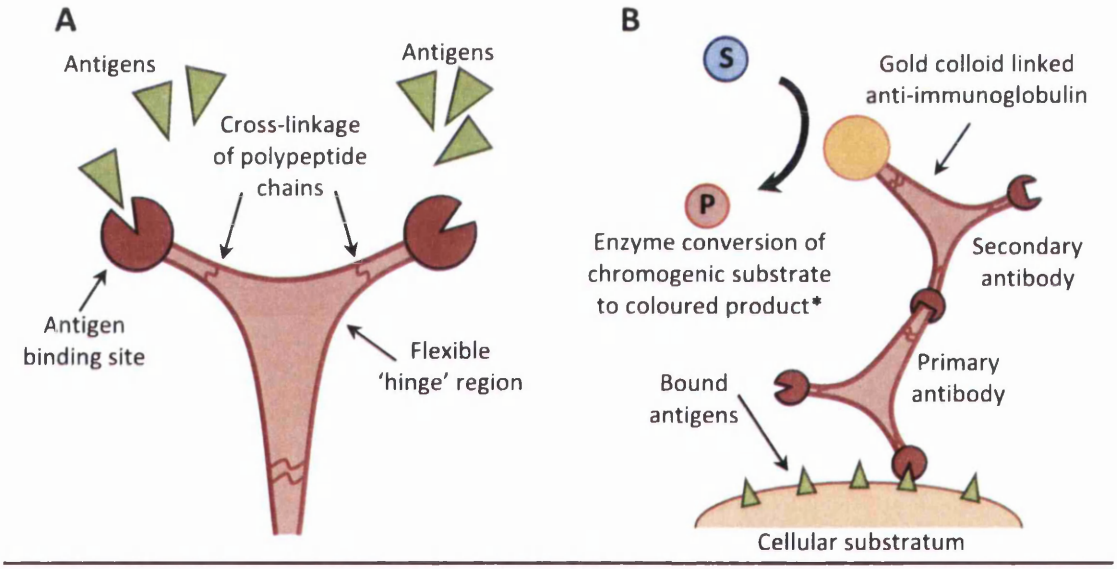

Figure 6.6. Diagrams showing (A) a typical IgG antibody and (B) the indirect ELISA process. In (B) the secondary antibody targeting the primary can be conjugated with either a colloid or an enzyme used to yield a coloured product for colourimetric assay and Immunofluorescence, marked by an asterisk. Adapted from [13].

Fig. 6.7. shows a backscattered electron image (BSE detector is Z number sensitive, see chapter 4) of a fillipodium from a single U-2 OS cell on ZnO nanowires (seen as high contrast, high Z number hexagons) with even higher contrast (higher Z number) 5 nm gold colloids; indicated by white arrows for clarity. Here image contrast

is derived from electron density and atomic weights (i.e. Z number) rather than topographical inform ation; allowing clear distinction between low contrast carbon 'background' of the U-2 OS cell membrane, ZnO nanowires and high contrast gold colloids conjugated to anti-vinculin antibodies. These colloids were confirmed to be within the membrane as they are hard to distinguish using the secondary electron detector and the sample was also imaged in cross-section; see appendix IV.

It was discussed previously that an antigen attaches to the pathogen and an antibody targets the antigen, while this is true it is not the method used by enzyme-linked immunosorbent assays (ELISA) in this case as a primary and secondary antibody were used. Where the secondary targets the primary, this is called indirect ELISA [13], see Fig. 6.6b. For Fig. 6.7. the primary antibody, anti-vinculin (from mouse)* concentration was 1:100 and secondary antibody, anti-mouse (from goat)* conjugated with 5 nm gold colloids concentration was 1:30. *Where the species the antibody is raised in determines selectivity, allowing multiple components (typically two) to be targeted in a single assay as long as all species used for culture are unique.

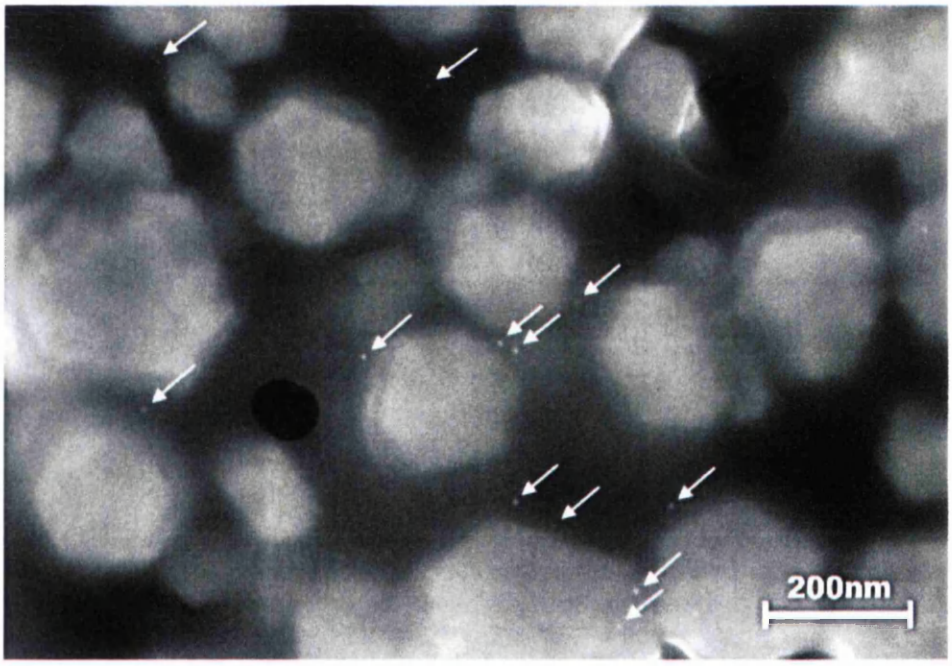

Figure 6.7. Backscattered Electron Micrograph showing multiple 5 nm gold colloids within the lamellipodium of a U-2 OS cell; as indicated by white arrows. Notice how BSE images allow distinction between gold and zinc oxide as two colloids can be observed above the [0001] facet of a ZnO nanowire.

To obtain the sample imaged in Fig. 6.7. the following protocol was used:

- Remove Media and Rinse in 'pre-warmed' HBSS x2 [at 37 °C]
- Fix Cells with 4 % PFM [5 minutes at Room Temperature (RT)]
- Wash in PBS x3 [at RT]
- Permeabilise with 0.1 % Triton-X100 in PBS [5 minutes at RT]
- Wash in PBS x3 [at RT]
- Blocking with 1 % BSA in PBST [30 minutes at RT]
- Incubate Primaries in 1 % BSA in PBST overnight [12 hours at 4 °C] *(humidified)*
- Wash in PBS x2 [at RT]
- Incubate Secondaries in 1 % BSA in PBS [1 hour at RT]
- Wash in PBS x2 [at RT]
- Immerse in Dist. Water x1 [5 minutes at RT]
- Ethanol Series Dehydration [70, 80, 90, 95 and 100 % - 5 minutes each at RT]
- Air Dry [1 hour at RT]

This protocol was refined over several experiments of trial and error as well as many concentration plates for Primary and Secondary antibodies to determine optimum concentrations. Primary no Secondary and Secondary no Primary controls were also conducted to confirm results obtained were not false positives due to non-specific binding of antigens. Immunogold can be used to target multiple proteins, as colloidal gold markers can be purchased in 5, 10 and 20 nm diameters easily allowing one to differentiate between two or more different antigens on a single sample, typically one with a small gold marker and one with a larger one [14]. Due to the size of gold markers U-2 OS cells were permeabilised with a high concentration (0.1 %) of Triton-X in PBS and blocked with 1 % Bovine Serum Albumin in PBST (0.05 % Triton-X), to allow sufficient permeabilisation for gold colloids as per Bozzola and Russell's protocol [15]. Imaging of leading ends of the fillipodia was difficult due to beam interaction and area charging, and unfortunately a metal coating could not be used as it would mask the 5 nm gold colloids; therefore SEM does have its limitations for certain aspects of life sciences.

6.3. Viability Assays

Two commercially available off the shelf assays, Promega's MTS and Invitrogen's LIVE DEAD were used to determine ZnO nanowire biocompatibility with U-2 OS cells. In both sets of experiments cells were cultured for 72 hours on ZnO nanowire substrata along with glass and no substratum (well only) controls and assay reagents introduced at 72 hours (68 hours for MTS as incubation period 4 hours). 72 hours was chosen as it was the maximum limit for the cells in a 48 well plate with 500 µl of medium, as the PDT was determined to be on average 21.2 hours, in chapter 5. Culturing cells for longer than this period with glass control cover slips led to considerable changes in cell population medium change, likely due to tweezers and Gilson's. The following sub-sections will discuss both assays and their protocols with problems discussed towards the end of this section.

6.3.1. Promega's MTS Assay

To test the viability of U-2 OS cells on ZnO nanowires different array morphologies were grown by adjusting the ratio of precursor chemicals, yielding two significantly different substrata called 2:1 and 1:1 due to their precursor ratio. The importance of this ratio and the difference in surface properties will be discussed in chapters 7 and 8, respectively. As discussed in the introduction, U-2 OS were seeded on 2:1 and 1:1 nanowires, a glass control and a well only control and cultured in McCoy's modified 5A medium for 72 hours in a 5 % CO_2 environment at 37 °C. Cell populations were 2000 (Low) and 8000 (High) cells, typically taken from 2.5 x10^4 cells/ml stock solution obtained after passaging a sub-confluent T75 Corning flask culture. Due to the adherent nature of U-2 OS, the 49 – 64 mm^2 glass substrates were added prior to seeding of the cells in the 48-well plate; however, each substratum was cleaned in 100 % ethanol prior to being added to the 48-well plate to prevent contamination.

The response of cells to the addition of hydrothermally grown zinc oxide nanowires has been experimentally examined by observing the activity of the mitochondrial enzyme succinate dehydrogenase (SDH) in U-2 OS Cells. After a specified incubation period (0, 24, 48 and 72 hours) specimens were not removed from the wells and 50 µl of MTS (3-(4,5-dimethylthiazol-2-yl)-5-(3-carboxymethoxyphenyl)-2-(4-sulfophenyl)-2H-tetra-zolium; Promega) solution was added to each well, (except

for media controls used for background removal) and then re-incubated for 4 hours. 50 µl was found after several assays to be sufficient for the amount of cells present, as following Promega's[1] suggested 20 µl / 100 ml for a 96 well plate always led to an excess of MTS at 388 nm, see Fig. 6.9b. 500 µl of medium was used in each well as this was the upper medium volume limit for a 48 well plate to still enable gaseous diffusion through the liquid, as per equation 6.2 [16].

$$Media\ \ (Min-Max)\ \ Volume = \frac{(0.2-0.5)\ \ Volume\ \ (ml)}{Well\ \ \ Area\ \ (cm^2)} \qquad \textbf{(6.2)}$$

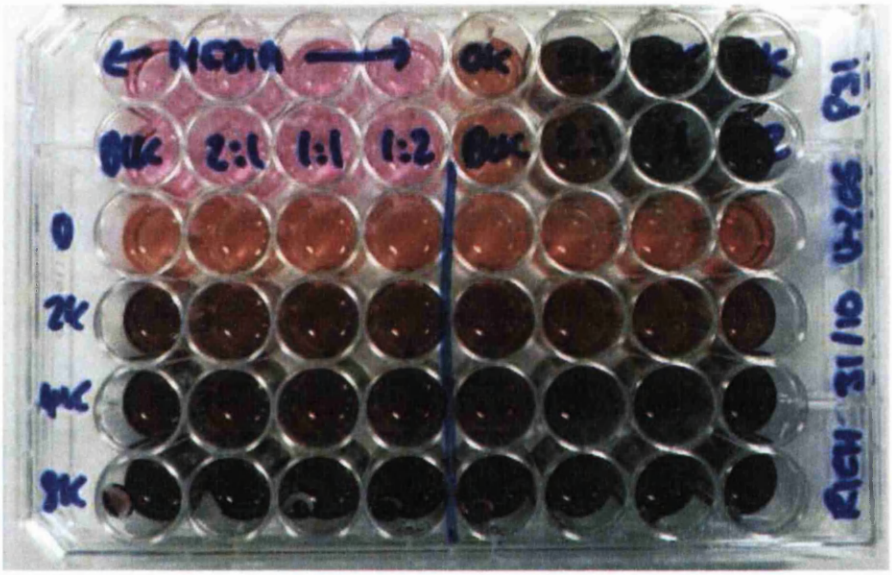

Figure 6.8. Image of change in well colour due to addition and incubation of 50 µl MTS and its conversion into purple Formazan dye after 4 hours incubation at 37 °C 5 % CO_2.

MTS is part of a family of tetrazolium based solutions used to examine the proliferation of cells. The MTS solution was used as it is bio-reduced by cells into formazan dye that is soluble in tissue culture medium, whereas others variants are typically non-soluble. Berridge and Tan [17] have reported that this conversion can only be accomplished by SDH enzymes in metabolically active cells, and therefore when the optical density of the formazan dye (absorbance peak ~492 nm) is measured it directly

[1] http://www.promega.com/~/media/Files/Resources/Protocols/Technical%20Bulletins/0/CellTiter%2096%20AQueous%20One%20Solution%20Cell%20Proliferation%20Assay%20System%20Protocol.ashx

relates to the number of live cells in each well. The MTS solution is far superior to previous tetrazolium based reagents as it eliminates the necessity to solubilise the formazan dye after incubation (required for MTT, XTT etc) reducing errors, as SDH converts MTS into a stable media soluble formazan dye as reported by Goodwin et al. [18] omitting the solubilising step and yielding more accurate results. Although this was the case the plate was still shaken softly for 1 minute at room temperature in a double orbital to assure formazan was uniformly distributed throughout the media, before reading the plate with a plate reader (FLUOstar OPTIMA, BMG Labtech) for photon absorbance at a wavelength of 490nm. Fig. 6.8. shows a typical plate after 4 hours incubation with MTS, where differences in cell concentration can be observed by a change in the amount of purple dye present in each well.

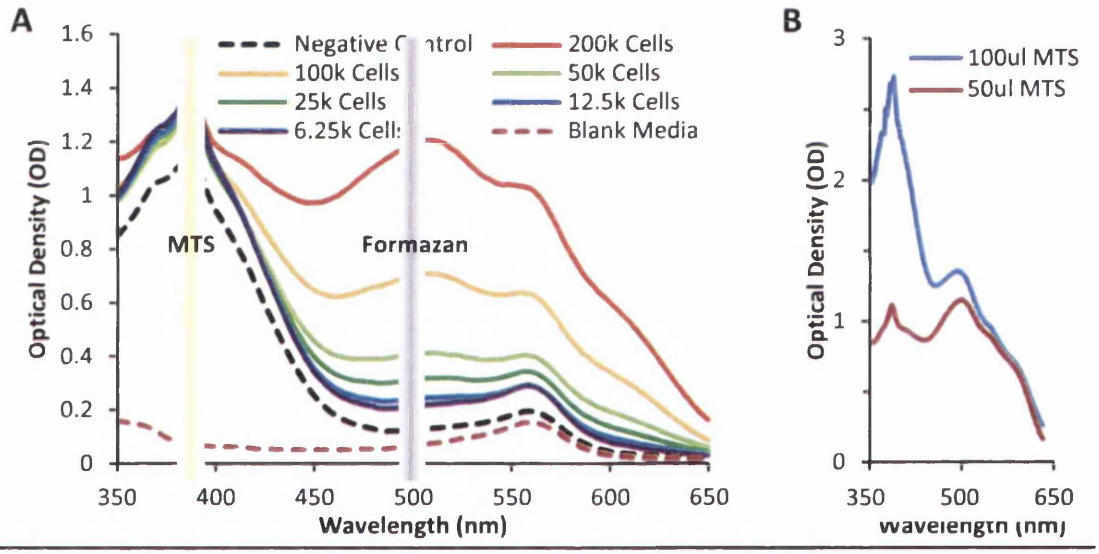

Figure 6.9. Graphs show (A) the Optical Density of MTS (yellow vertical line) and Formazan (purple vertical line) dyes for 8 samples, acquired from 4 sets of triplicates (n=12); and (B) the effect of MTS concentration on spectra (200,000 cells). The data from (A) is used to determine a calibration gradient to allow any future OD value (only for 4 hours incubation in 48 well plate) to be read off as cell number.

Four 48 well plates were made for time points at 0, 24, 48 and 72 hours; the experiment being repeated 4 times for statistical significance. Since the MTS reagent required 4 hours incubation the initial time point is 4 hours not 0, whereas all other time points had MTS added 4 hours prior to their end point (i.e. 20, 44 and 68 hours). Substrata were removed for plate reading as the plate reader has its excitation source and emission detector on opposite sides of the plate (i.e. top and bottom). Removed

substrata were fixed and dehydrated as stated above in preparation for SEM analysis to confirm MTS results, yielding Fig. 5.3.

Fig. 6.10. shows a simplified and labelled version of Fig. 6.8. that explains what wells are used to obtain control values of optical density. The 'Well Only' control is used to confirm that the cell PDT is conforming to the as derived calibration curve. The main two controls are a 'Media Only' control that does not contain MTS, and a 'No Cell' control that contains MTS; where these controls allow the background contribution from the medium and MTS at 490 nm to be removed, respectively. Their contribution to absorbance at 490 nm can be clearly seen as the two dashed lines in Fig. 6.9. where the black line shows a 'No Cell' control and the pink line a 'Media Only' control. These values can be used to remove the background contribution to real data increasing the accuracy of results; using Equation 6.3. and these controls cell survival rate can be determined [19].

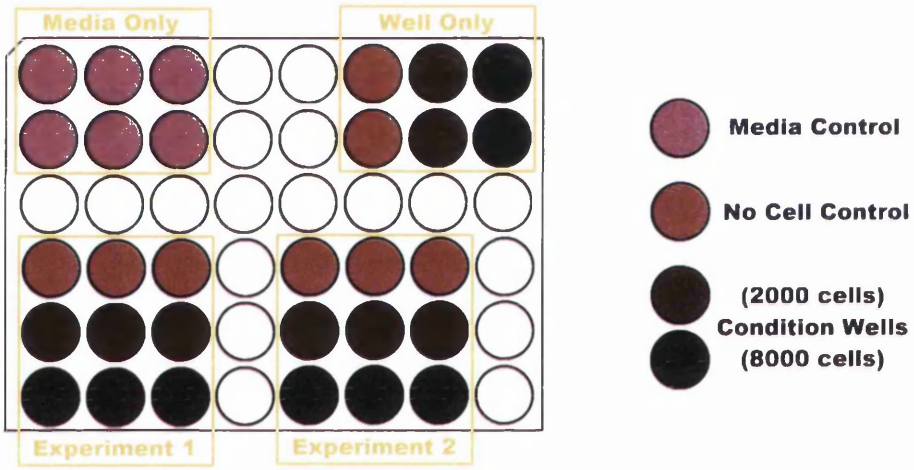

Figure 6.10. Diagram shows the typical layout of an MTS Assay in a 48 well plate, similar to the photograph shown in Fig. 6.8. Here experiments are run in duplicate for 3 samples. Media controls (no MTS) and No cell controls (with MTS) are used to determine survival rate, equation 6.3.

The MTS assay provides ample information to determine the biocompatibility of ZnO nanowires, however, since MTS counts only the LIVE cells it is unable to distinguish between reduction in cell number due to cell death or reduction of proliferation rate (increase of PDT). Due to this limitation it is often suggested in literature that a lactose dehydrogenase assay (LDH) should be conducted in tandem to confirm if necrosis is reducing proliferation or just adverse conditions inhibiting mitosis keeping cells in their lag phase. This is because cells contain LDH and it is only

released upon cell death. Smith et al. [19] present a thorough MTS/LDH based protocol to determine if reduced proliferation is due to growth inhibition or cell death , and this should be conducted if the work were repeated; which will be discussed in chapter 9.

$$Survival(\%) = \left(\frac{Sample - Media}{Neg.Control - Media} \right) x100 \qquad \textbf{(6.3)}$$

6.3.2. Invitrogen's LIVE DEAD Assay

Invitrogen's LIVE DEAD assay was used to support MTS results as it can easily distinguish between reduction in total cell number due to increased cell death or reduction in proliferation rate; this is because numbers for both LIVE and DEAD cells are recorded, yielding a live cell percentage. As results are highly sensitive to handling of the substrate (unlike MTS due to its colourific nature), it was found that removal of the substrata using curved tweezers yielded less contribution to dead cell % due to rough handling as it was less likely to crush cells. This was because the glass cover slip substratum could be lifted from the solution by its edges, rather than clamping either side as was often done with straight tweezers.

The LIVE DEAD assay uses CalceinAM a cell permeable non fluoresencent dye to determine live cell number as fully functioning cells will convert calcein acetomethoxy (AM) to calcein a cell impermeable green fluorescent dye (494 nm Excitation / 517 nm Emisson)[2]. This is done by removal of the AM group within the cell via intercellular esterases, which is a hydrolase enzyme that splits esters into acid and alcohol by hydrolysis. Calcein is an ideal dye as it is self quenching at concentrations below 100 mM [3], where 0.6 – 1 μM was used in this work, meaning background intensity of unwashed away calcein will be insignificantly low. Again, as with MTS the requirement of active enzymes means that only live cells will produce intense uniform green fluorescence in live cells. Ethidium Homodimer-1 (EthD-1) is a cell impermeable red fluorescent dye that has a high affinity for nucleic acid and is weakly fluorescent until bound to DNA (528 nm Excitation / 617 nm Emission)[2] to determine cell death via the condition of the cells cytoplasmic membrane. This is because both the process of necrosis and apoptosis causes the cells membrane to break down allowing cell

[2] www.lifetechnologies.com/order/catalog/product/L3224?ICID=search-product

impermeable dye transit from extracellular to intracellular environments. Therefore, data obtained from the LIVE DEAD assay allows more detailed analysis and interpretation of results, as well as by yielding cell numbers for both live and dead cells as can be seen in Fig. 6.11.

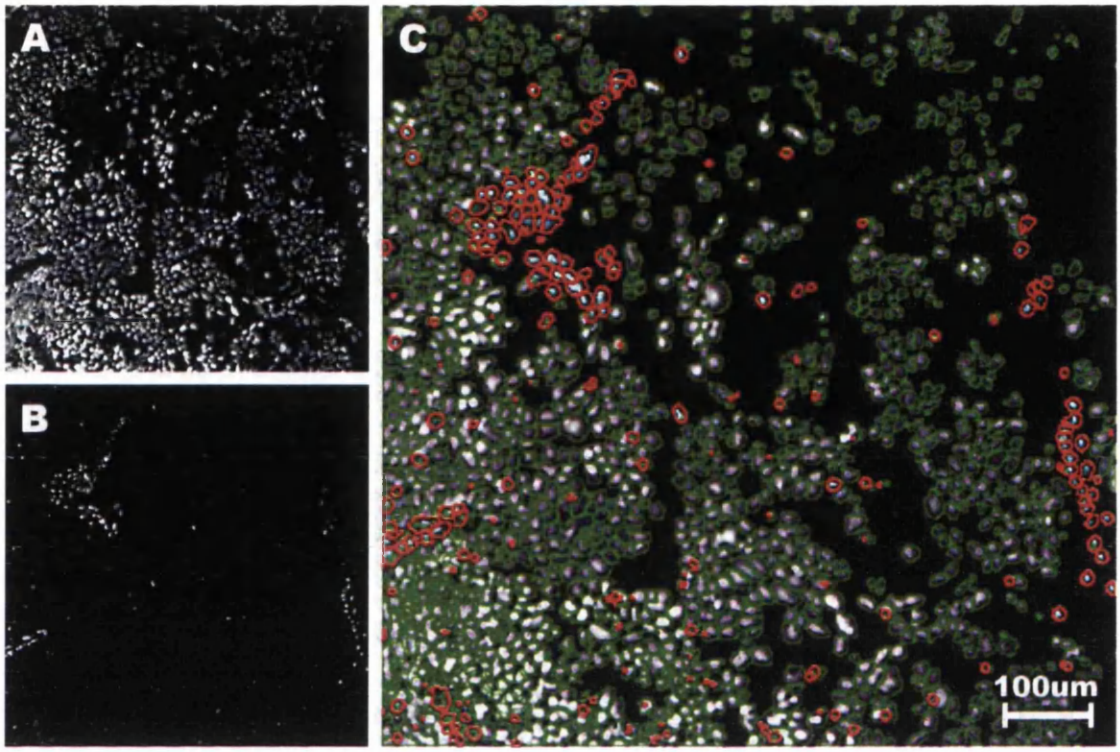

Figure 6.11. Immuno-fluorescence micrographs showing Invitrogens LIVE DEAD Assay applied to live U-2 OS cells on ZnO nanowires 72 hours after seeding, where live and dead populations are determined using ImageJ [20] NIH image processing software. Here (A) is CalcienAM, (B) is EthD-1 and (C) is a merge of (A) and (B) with ImageJ's determination of LIVE and DEAD cells.

For the LIVE DEAD assay cells were cultured on ZnO nanowires for 3 days as mentioned frequently before, however this assay is a live cell assay and is done with live unfixed cells (to allow CalceinAM to hydrolyze via esterase enzymes). Stain stock was made in pre-warmed PBS using the optimised concentrations:

- 0.15 µl per 1 ml from 4 mM Calcein stock gives 0.6 µM well concentration
- 1 µl per 1 ml from 57 mM DAPI stock gives 57 µM well concentration*
- 1 µl per 1 ml from 2 mM EthD-1 stock gives 2 µM well concentration

* The high concentration of DAPI (4',6-diamidino-2-phenylindole) used was due to problems with the assay and the significant difference intensity levels for DAPI between live and dead cells on ZnO nanowires; this will be discussed next.

6.3.3. Problems and Limitations

Unfortunately there were many problems faced when using an opaque substrate in a microbiology laboratory, though the majority of problems were from the standardization of inverted microscopes. The ZnO nanowire substrata often needed to be flipped upside down in the wells to allow fluorescence microscope to obtain an image. This lead to all manner of focusing problems, such as in Fig. 6.15. where the glass cover slip has snapped and so two parts of the image sit at two different focal planes. GE's IN Cell 2000 microscope was finally adopted as the only microscopy used in this work since it had laser auto focusing that could detect the diffraction change at the interface between two different phases (i.e. solid cells and liquid medium)[3]. After much trial and error protocols were saved that told the system to hunt for this interface (red triangle in Fig. 6.12.) with laser autofocus before running through several exposures at difference Z-heights either side of the auto focused Z-height to obtain the best image. The whole process was very time extensive.

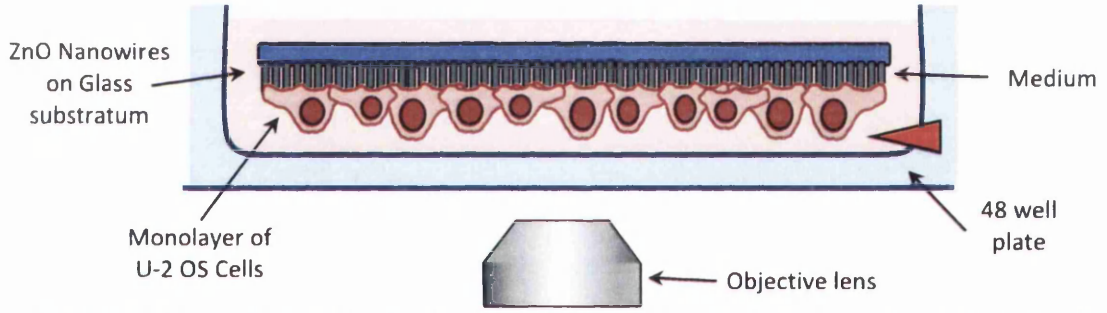

Figure 6.12. Diagram showing the flipping of cell substratum in the well to allow correct focusing of the GE IN Cell 2000 software, which is an inverted microscope system.

Fig. 6.11. shows a typical image from a LIVE DEAD assay (typically 10 – 15 of these were taken at random from each well of triplicate for each sample) where ImageJ had to be used to measure calcein and EthD-1 intensity as GE's 'workstation' software was unable to work effectively without a homogeneously even staining of DAPI for all cells. Unfortunately, it was found that both DAPI and Hoechst 33342 (specifically for live cell use)[4] would produce much higher intensity emission when bound to the nucleic acid of dead cells. It was assumed that this was due to dead cells offering additional

[3] www.gelifesciences.com/webapp/wcs/stores/servlet/productById/en/GELifeSciences-UK/29027886
[4] http://tools.lifetechnologies.com/content/sfs/manuals/mp21486.pdf

binding time due to there being no cell membrane to traverse. Whatever the reason dead cells yielded higher intensity DAPI emission, and since the autofocusing protocol could only be set up to automatically focus on the highest intensity then live cell nuclei would often be out of focus; and due to their lower intensity GE's workstation would often dismiss and ignore these cells, yielding skewed results. Time was never spent to further optimize nucleic acid counter staining as ImageJ was happy to distinguish cells based on intensity levels from both dyes regardless of DAPI contribution.

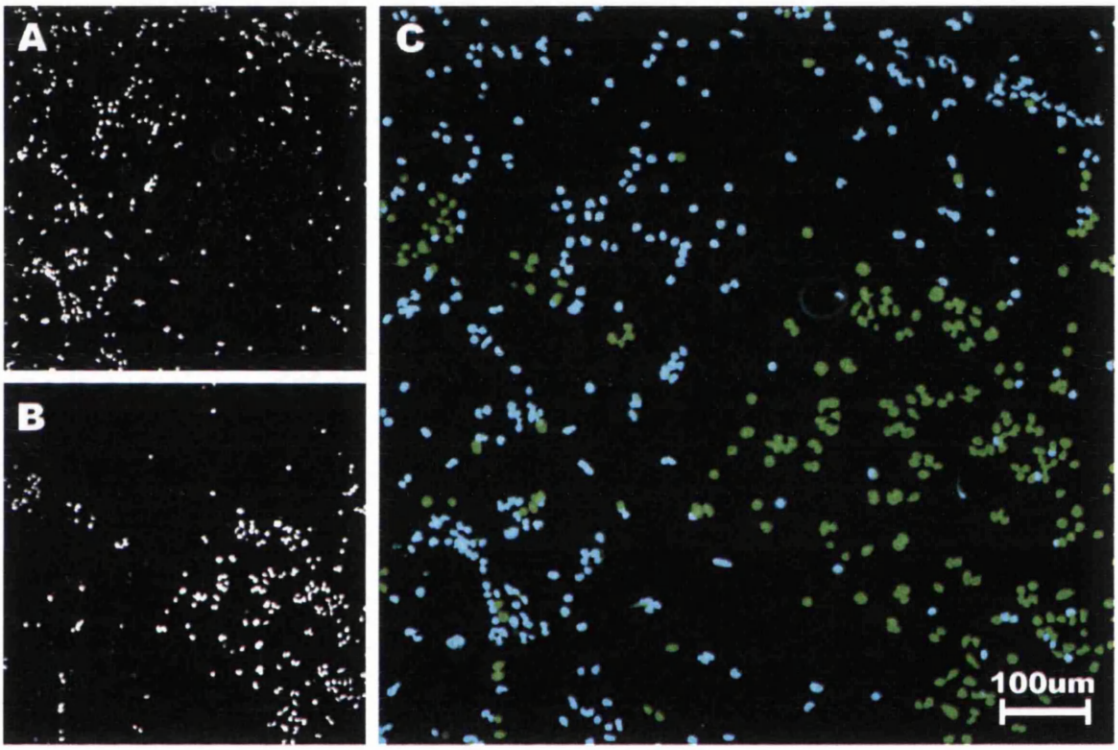

Figure 6.13. Immuno-fluorescence micrographs showing the problem with Hoechst 33342 counter stain with U-2 OS on ZnO nanowires 72 hours after seeding, where (A) is DAPI, (B) is CalceinAM and (C) is a merge of (A) and (B). Notice how in (A) live cell DAPI is a much lower intensity than for dead cells. Note that the result was the same for Hoechst 33342.

6.4. Immunocytochemistry

Immuno Electron Microscopy was discussed first as it is featured much more predominantly in this thesis than Immuno-fluorescence Microscopy, this is mainly due to the much larger magnification range available, (see Fig. 4.2.) allowing more detailed analysis of cell-substratum interaction. However, it is also partly to do with the focusing

problem discussed in Fig. 6.12., where Fig. 6.15. more accurately describes this problem. Fig. 6.14. shows U-2 OS cells after 72 hours incubation on ZnO nanowires, where the actin filaments have been targeted by primary antibodies (raised in Mouse) and marked with FITC fluorescent dye (green emission) conjugated to secondary antibodies (raised in Goat). However, even at 40x magnification the detail is insufficient for detailed analysis.

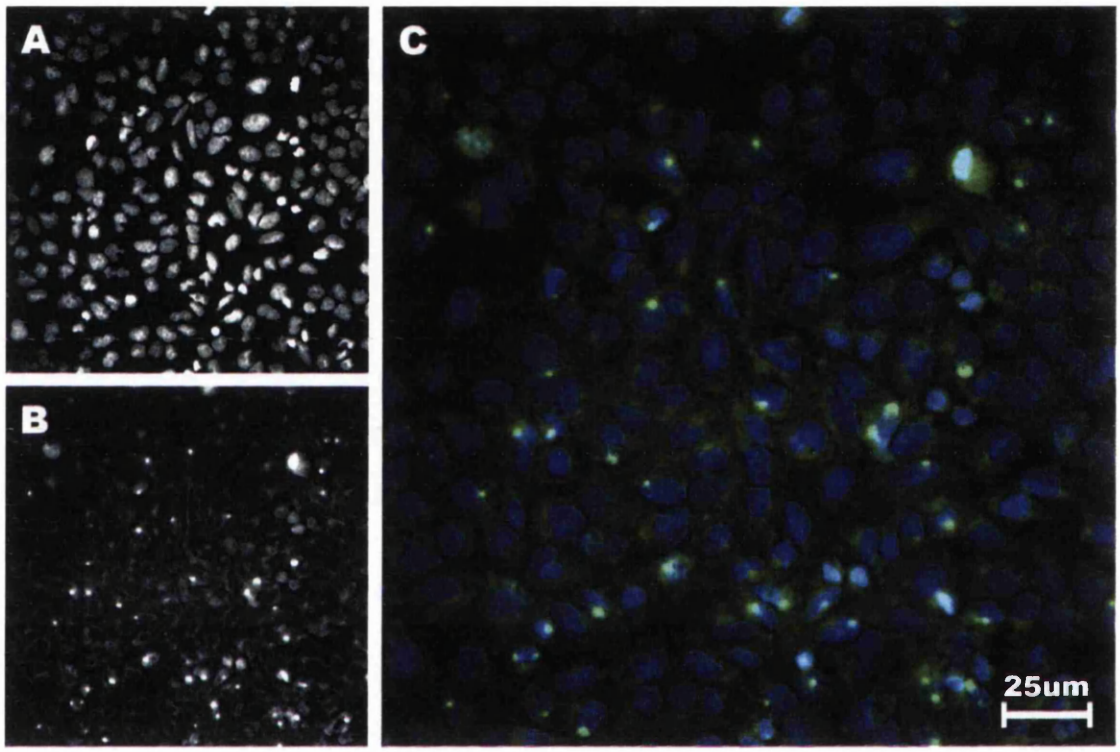

Figure 6.14. Immunofluoresence image of (A) DAPI and (B) FITC (AntiActin) where (C) is merge, experiment with U-2 OS cells on ZnO nanowires after 72 hour incubation.

To obtain the sample imaged in Fig. 6.14. the following protocol was used:

- Remove Media and Rinse in 'pre-warmed' HBSS x2 [at 37 °C]
- Fix Cells with 4 % PFM [10 minutes at 4 °C]
- Wash in PBS x3 [at Room Temperature (RT)]
- Permeabilise with 0.05 % Triton-X100 in PBS [5 minutes at RT]
- Wash in PBS x3 [at RT]
- Blocking with 5 % Goat* Serum in PBS [30 minutes at RT]
- Incubate Primaries in 1 % BSA in PBS overnight [12+ hours at 4 °C]
- Wash in PBS x2 [at RT]

- Incubate Secondaries in 1 % BSA in PBS [1 hour at RT]
- Wash in PBS x2 [at RT]
- Counter stain Nuclei with DAPI [2 minutes at RT]
- Wash in PBS x3 [at RT] leaving cells in final wash for imaging

* Goat serum used to block non-specific binding as the secondary used raised in goat.

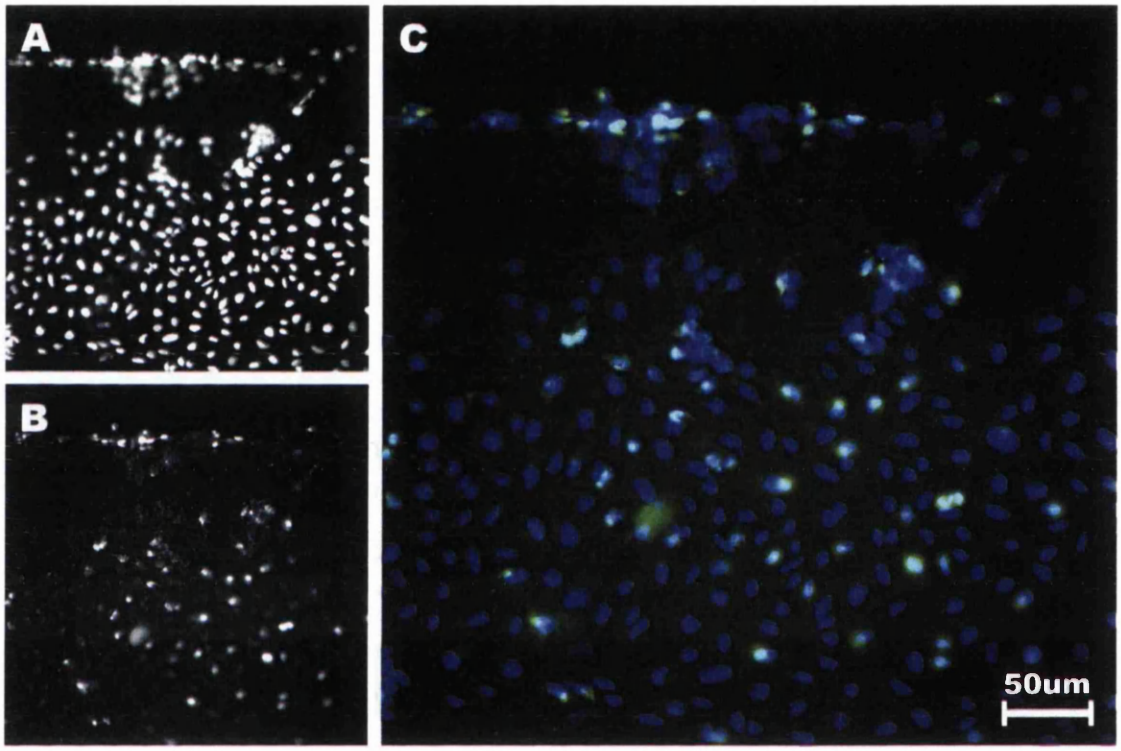

Figure 6.15. Immuno-fluorescence image of (A) DAPI and (B) FITC (AntiActin) where (C) is merge, experiment with U-2 OS cells on ZnO nanowires, were the glass substratum can be seen to have cracked either flipping or changing Z-height so that the focus of the image is inconsistent.

Concentrations of antibodies used to obtain the immuno-fluorescence images in Figs. 6.14-5. were 1:50 for anti-actin (raised in mouse) and 1:32 for FITC conjugated anti-mouse (raised in goat). Fig. 6.15. further highlights the problem of using a sample with high roughness in an inverted microscope, where all hardware and software are designed to determine the cell-medium interface for auto-focusing. Here the substratum has split into two pieces with the split running in a positive gradient across the image. While the image at first appears to be in focus on one side and out of focus on the other, it can be seen when comparing DAPI and FITC images that each emission has been auto focused to a different side of the crack. Auto focus is typically determined for each

dye (emission wavelength) by measuring the Z-height of only one of the dyes then assuming that other dyes will be in focus at this Z-height; this can lead to focusing errors. Alternatively, the system can be told to auto focus every emission wavelength, checking either side of a predetermined Z-height by turning off laser autofocus. This however creates the problems between wells due to the poor tolerance of No. 0 glass cover slip thickness of 80 – 120 μm[5].

6.5. Substratum Surface Properties

The importance of the surface properties of the substratum are very important when determining cell behaviour, in this section the characterization of surface charge, roughness, adhesion and wettability shall be discussed in detail. It has been reported by Vitte et al. [21] that when a cell has just adhered to a surface it has several decisions to make. The cell may undergo apoptosis, or remain alive and proliferate, it may remain on the site of adhesion or may start migrating; where the properties of the substratum surface can alter the cells decision.

6.5.1. Roughness and Adhesion with AFM

Surface roughness can have a substantial effect on cell-substratum interaction that may cause changes to motility, proliferation and overall behavior of the cell. It has been reported by Chung et al. [22] that nanometer scale roughness can improve the adhesion and proliferation of human endothelial cells (HUVECs) on a biomaterial surface. Similar to this work their results were quantified using MTT assay where they found that an increase in surface roughness of only 10 – 100 nm enhanced proliferation of HUVECs. Therefore, analysis of surface roughness is important to determine how different surface properties of the ZnO nanowire arrays may alter cell behaviour.

In this work a Nanowizard II (JPK Instruments) Atomic Force Microscope (AFM) was used to take surface roughness and adhesion force measurements from various substrates. Data acquisition was performed in contact and tapping modes to acquire force curves and images for adhesion force and RMS roughness, respectively. Roughness measurements were obtained from 15 areas across 3 substrata for each

[5] www.webshop.fishersci.com/insight2_uk/getProduct.do?productCode=12372108&resultSetPosition=0

sample. Images were obtained using a Silicon tip of 8 nm radius (RTESP) which was thermally calibrated yielding a frequency of 334.65 kHz. A slow scanning velocity of 0.5 μm/s was used to inhibit dragging and artifact incorporation. Force curves were obtained using an 8 μm diameter latex colloid glued to a tip-less cantilever and a constant normal force of 25 nN was applied. A latex colloid (see Fig. 6.16.) was used to mimic cell-nanowire interaction by inhibiting Z extension between the wires that occurs with a standard tip. Therefore application of DMT theory could be used to obtain adhesion force [23], where force required to overcome sphere-plane contact is equal to the attraction force determined during point of contact.

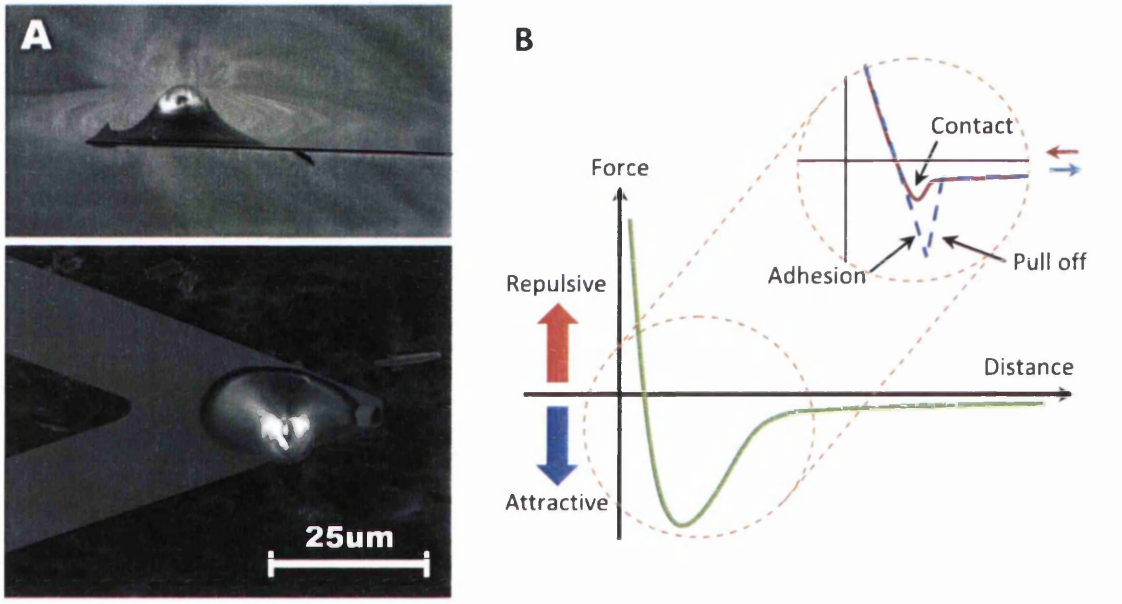

Figure 6.16. (A) Scanning Electron Micrographs of 8 μm latex colloid attached to cantilever from side and from underneath at 45 °. (B) Graphs showing the Lennard-Jones potential [24] path of the cantilever tip, showing change in force with Z-height.

Fig. 6.17. shows the effect of different values of loop gain on individual line profiles of an AFM image, the diagram shows that loop gain controls the way in which the feedback electronics react to the error signal that is provided. This parameter has a significant impact on the appearance of the final AFM image, since many artifacts are introduced to the image, reducing its accuracy and overall quality. These 'artifacts' are added to the image in the form of random anomalies (*with loop gain they will normally have periodicity*), and they don't exist on the sample in reality and are merely introduced electronically to the image, normally via noise or in the case of a blunt an image with shapes that repeat often; see Fig. 6.18.

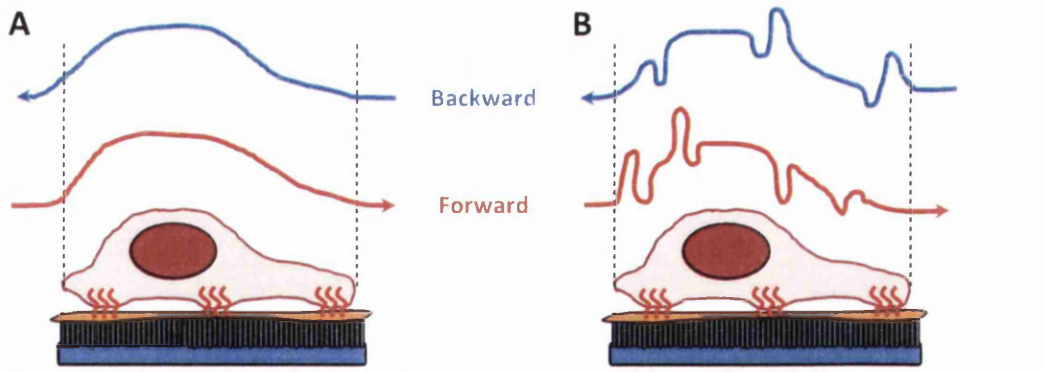

Figure 6.17. Diagram shows the effect of feedback gain on the resulting scan lines of an AFM image, where (A) is low gain and (B) high gain. Notice how low gain initially looks to provide the best solution however it takes a long time to compensate for changes in topography and so sudden changes can often be missed, it is also more likely that the tip will crash (in contact mode) leading to tip blunting; see Figure 6.18. However, high gain will over compensate for changes in topography so that the tip will oscillate producing substantial artifacts.

For an AFM image to acquire high spatial resolution the convolution between the tip and the sample must be extremely low, with a new sharp tip (such as the 6 nm terminated RTESPA) being used, though in reality such a tip will be easily blunted if used in contact mode. Though it has been shown by Rico et al. [25] that blunt tips can be beneficial for cell imaging and measurement of adhesion force. Fig. 6.18. shows three diagrams demonstrating the effect of tip shape when imaging a triangular feature on a substratum. The diagram shows that a perfect tip is able to closely copy the shape of the original morphology on the sample surface. This is the ideal situation, often the tip becomes blunted, rapidly so during force curve analysis; therefore a force curve tip is never used for imaging; and in this work the force sensing tip was an 8 μm diameter latex colloid used to imitate cell cytoplasm and nanowire substratum interaction. Fig. 6.18b shows that a blunted tip will create a rounded copy of the features on the substratum surface, where as an irregular tip which can often be created when debris attach to the tip after a bad contact, this tip results in a convolution of the tip and surface feature shapes.

It has been reported by Chen et al. [26] that cell-substratum adhesion force is best investigated in tandem with zeta potential and measured contact angles to yield a more accurate determination of the necessary / favourable conditions for cell adhesion. Therefore, both contact angles and surface charge shall be discussed next.

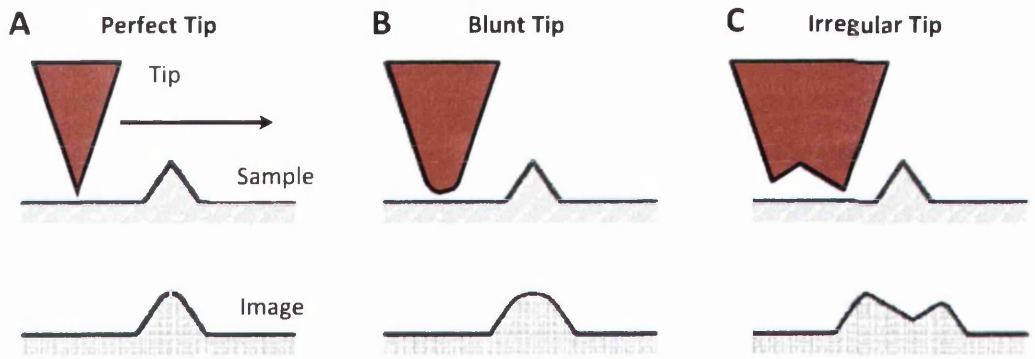

Figure 6.18 Diagram showing the effect of AFM cantilever tip sharpness on image reproduction (and artifacts) where, (A) is a perfect tip, (B) a blunt tip and (C) an irregular tip. Note that this image reproduction would only happen in contact mode. Adapted from [27].

6.5.2. Wettability with Contact Angles

It has been reported by Lampin et al. [28] that substratum roughness and wettability affect both cell adhesion and migration of chick embryo vascular cells, where an increase in substratum roughness promoted cell adhesion as a result of enhanced hydrophobicity which favoured the adsorption of adhesive proteins. More importantly they suggest that the hydrophobicity (affected by surface roughness) determines cell migration. Therefore, substratum surface hydrophobicity (or wettability) was investigated by measuring the contact angles of 1 µl droplets of DI water on each sample, where small contact angles (< 90 °) correspond to high wettability and large contact angles (> 90 °), correspond to low wettability, see Figure 6.19a. Liquids form spherical droplets in air as this is the most energy efficient shape that yields the minimum surface area for a fixed volume, when a liquid come in contact with a solid an intermolecular force forms to contract the surface called surface tension [29]. By examining the interfacial tensions between solid-liquid, solid-vapour and liquid-vapour the mechanical equilibrium of a single droplet of liquid on a solid substratum can be explained by Young's [30] equation 6.4.

$$\gamma_{lv} \cos\theta = \gamma_{sv} - \gamma_{sl} \qquad (6.4)$$

Where γ_{lv}, γ_{sv} and γ_{sl} represent the interfacial tensions and θ is the contact angle. To determine interface tensions multiple solutions of known γ_l are used to plot $cos\theta$ versus the test liquids surface tension, so that other interface tensions may be derived

[31]. In the literature surface tensions are not generally taken into consideration for determination of cell behaviour due to surface wettability, however the contact angle is a well-established means of comparing substrata. Arima and Iwata [32] report that the number of adhered Human umbilical vein endothelial cells (HUVEC) reached a maximum with a water contact angle of 40 °, while cell adhesion increased with decreasing water contact angle up to 60 – 70 °. For HeLa cells the maximum number of cells adhered was obtained with a water contact angle of 50 °. Therefore, cell adhesion is mainly determined by surface wettability, but is also affected by its surface density, and the type of cell. Also, Benesch et al. [33] report that the process of protein adsorption is substratum hydrophobicity sensitive, where hydrophobic surfaces are often shown to adsorb more proteins than hydrophilic surfaces. This will have a considerable effect on cell behaviour and shows the importance of determining the wettability of the substratum in this work.

Table 6.1. compares contact angles from three different substrata, where the ***Statistic Significance*** of the data has been shown in the form of a Student's Ttest p values, see section 6.6. for further explanation. In life sciences these values would be typically be shown on a bar diagram comparing groups to a control to indicate how significant the difference between the two means is (group and control). It is generally accepted that a p value of less than 0.05 shows that the means of two sets of data are significantly different, and this is typically shown on a bar diagram as an asterisk, where * indicates $p<0.005$ and ** $p<0.05$ compared to the control. The asterisk is used to denote the p value which is a measure of how different the two sets of data are, this is very important in micro biology and so will be discussed in detail after zeta potential.

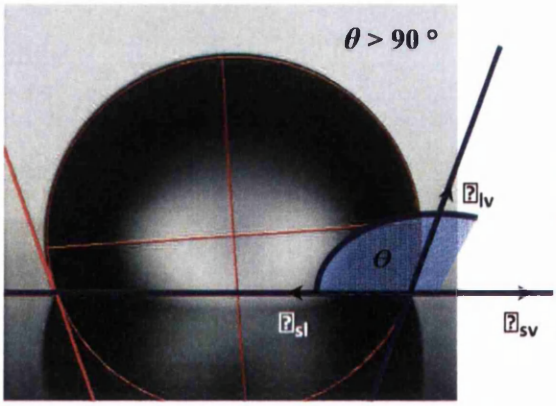

Table 6.1. Shows mean contact angles (n=9), with Statistical difference between metal layer and silicon control derived from Ttest values.

	Silicon	Gold	Nickel
Mean	62.8	75.0	40.4
Std Dev	2.2	2.7	4.2
Statist Diff.	-	3.9×10^{-11}	1.5×10^{-15}

Figure 6.19. Photograph shows a contact angle formed from a sessile liquid drop on a smooth homogeneous surface, with components from equation 6.4 labelled.

6.5.3. Surface Charge with Zeta Potential

To be able to better understand the interactions of cells with nanowires discussed in chapter 5 and investigated in chapter 8, the knowledge of surface charge needs to be obtained as it has often been attributed that it affects cell behaviour at the cell-substrate interface [21]. In this work the Zeta-potential was obtained for nanowire arrays to use to support cell spreading area findings, where a correlation between the surface charge of the nanowires and the behaviour of the cells was witnessed; see chapter 8. In this sub-section the interaction of particles in a solution is explained and comparisons made with other surface property revealing techniques, this work is important as it will be shown in chapter 8 that the ZnO nanowires grown in this study are soluble over 7 days in medium. Often when a material is immersed in liquid it will begin to dissolve depending on the strength of the solvent. The materials particles will contain chemical groups that when dissolved will ionize, producing a charged surface that will preferentially attract ions of positive or negative opposite to its own charge. These dissolved charged particles can be used to determine the surface charge of the submerged nanowire array and so the theory will be discussed here. Determining the surface charge of the ZnO nanowire substrata is important as it is well established in the literature that negatively charged osteoblasts prefer to adhere to a negatively charged substratum, typically because negatively charged substrata promote additional protein adsorption [34].

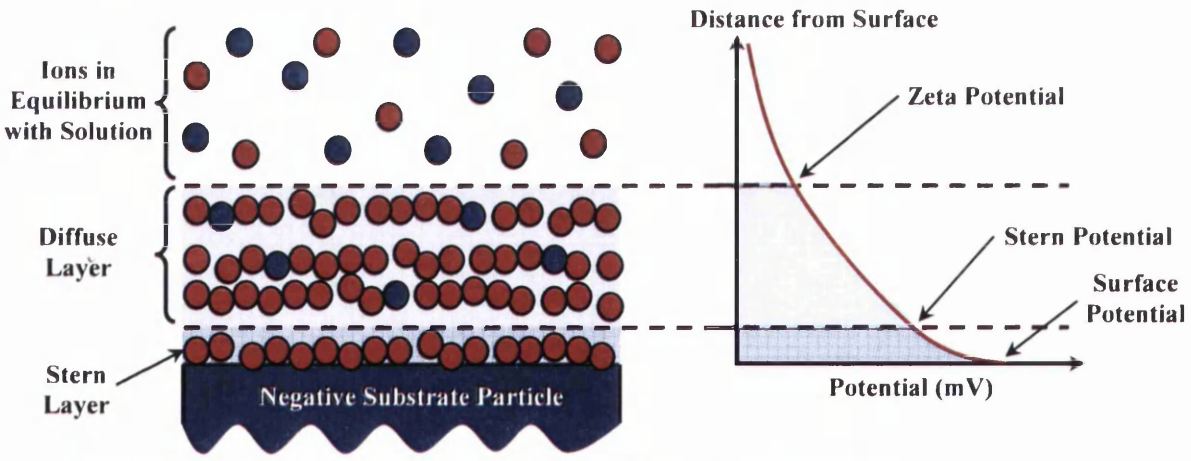

Figure 6.22. Diagram showing the double layer model of a charged colloid, where a) shows the distribution of positive and negative ions around a negatively charged colloid and b) the relationship to zeta potential; adapted from [35] and [36]. Red circles are positive counter-ions and blue circles are negative co-ions.

Fig. 6.22. shows Sattler's double layer model used here to visualize the ionic charges in the solution surrounding colloidal particle, and depicts the effect of a negative colloid on the surrounding solution when its neutralizing ions are suddenly removed. The positive 'counter-ions' form a well adhered layer around the surface of the colloid called the 'Stern layer' which repels additionally attracted positive ions (in the same fashion that applying a voltage to the gate of a transistor inhibits current by repelling charge). This creates a diffuse layer of predominantly positive ions that decreases in concentration until it achieves equilibrium with the surrounding liquid; where co-ions and counter-ion numbers are equal [37]. It should be noted that co-ions are named as such as they're the same charge as the colloid, so the terms counter and co are interchangeable depending on the sample.

This distribution of ions creates a surface potential between the colloid and liquid as a double layer is formed to neutralize the negatively charged colloid, creating a voltage difference of several millivolts. Fig. 6.22. shows how this voltage potential drops when moving away from the surface within the Stern layer and then more rapidly drops within the diffuse layer. The point at which the two layers meet is called the slip plane and represents the boundary between well adhered Stern layer ions and loosely adhered diffuse ions; which are left behind if the particle/colloid travels within the liquid. The charged particle will move within the liquid if a voltage gradient is applied, this principle is called Electrophoresis and is the study of the velocity of movement of charged particle relative to the solution under and applied electric field. By manipulating this principle a 'Zetasizer' machine (such as the Malvern Zetasizer 2000 used here) applies a voltage gradient across a curette containing the sample solution and observes the velocity of particle movement. This velocity is called the electrophoretic mobility and is related to the zeta potential using the Henry equation [38].

It is well established in the literature that negatively charged osteoblasts prefer to adhere to a negatively charged substratum, where a zeta potential of approximately -5 to -15 mV is ideal as most biological cells have zeta potentials in this range. Therefore limiting non-specific binding and forcing receptor-mediated interaction that allows binding only when there is a receptor-ligand bond strong enough to overcome the electrical repulsion [39]. Chen et al. [26] has shown cell-substratum adhesion due to surface charge is a mixture of long-range Lifshitz - Van der Waals, electrical double layer and short-range Lewis acid-base interaction forces.

This section has shown the importance of comparing surface charge between substrata and its effect on cell-substratum interaction in the literature has also been discussed. It is often accepted that zeta potential theory is extremely well suited to analysis of living cells and cell-substratum and cell-cell interaction. This is because they can be modelled to be spherical in suspension, are surrounded with a hydrophobic plasma membrane and bear a net negative surface charge [21].

6.6. Null Hypothesis in Statistics

Hypothesis testing statistics are used to compare multiple data sets from multiple samples, typically whether or not one or more samples can be determined as having different means; or if data is randomly distributed. Statistics are unable to prove a hypothesis, but it is able to determine how likely it is to be wrong. This is the null hypothesis, we do not test to see if a 'treatment' has an effect, what we test is if it has no effect [13]. Statistical hypothesis tests typically yield a value, p that is the probability of there not being a difference between data sets, where a p value lower than 0.005 is statistically significant and lower than 0.01 is highly significant [40]. The degrees of freedom when comparing data sets needs to be considered, as this choice alters formulae used for calculating the probability of there not being a difference. Two tailed tests are often used as this means that we have no certainty that the treatment will have a positive of negative effect compared to the control; in one tailed tests we expect one of the data sets to be bigger than the other [41].

In this work Student's (William Sealy Gosset's pen name) T-test was used to determine if sets of data obtained from experiments using different substrata (typically an array of ZnO nanowires) and a control (typically a glass cover slip) were significantly different from each other. This is because in most cases data sets were normally distributed with minimal skew, see histograms in Fig. 6.23. showing the distribution of cell area measurements for results shown in section 8.5.1. where for each sample the mean is within the highest % bin. This data can be T-tested, and the probability of there not being a difference between the zinc oxide nanowire arrays and the glass control examined.

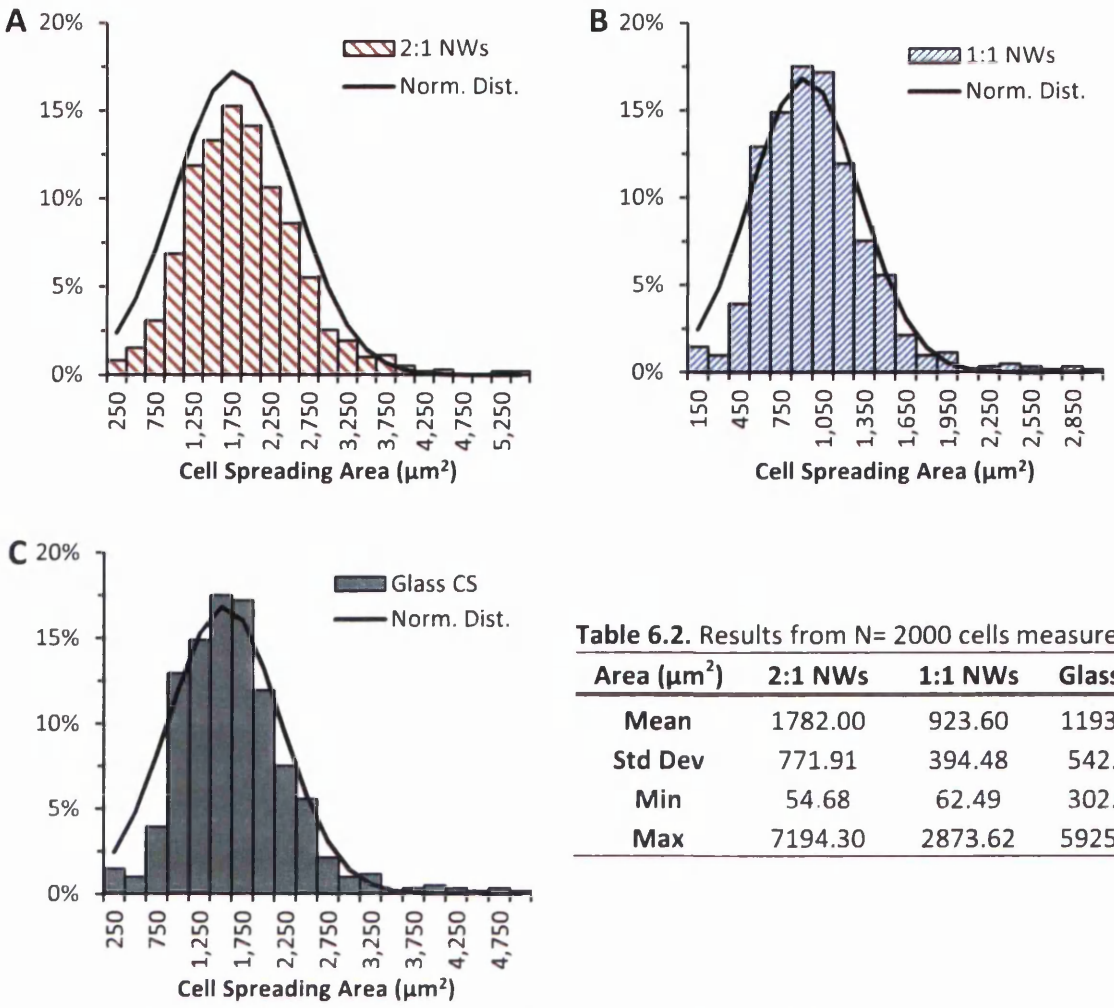

Table 6.2. Results from N= 2000 cells measured.

Area (µm²)	2:1 NWs	1:1 NWs	Glass CS
Mean	1782.00	923.60	1193.24
Std Dev	771.91	394.48	542.10
Min	54.68	62.49	302.91
Max	7194.30	2873.62	5925.15

Figure 6.23. Histograms showing the normal distribution of data from 2000 measurements of U-2 OS cell spreading area after incubation for 72 hours in McCoy's 5A modified medium at 37 °C 5 % CO_2 and fixed with 4 % Paraformaldehyde. Where the substrata are (A) 2:1 nanowires, (B) 1:1 nanowires and (C) Glass cover slip control.

6.7. Summary

This chapter has briefly covered the use of SEM for phase 2 (Biocompatibility) of the work as SEM operation was discussed in detail in chapter 4. However, time has been taken to explain specific methods for use of SEM and Cryo SEM to observe Cell behaviour as well as IEM (ImmunoGold SEM) to observe the fine details of Cell-Substratum Interaction. Biocompatibility assays have been shown with protocols either listed or discussed for both Promega's MTS Assay and Invitrogen's LIVE DEAD Assay. The surface properties of the substratum and methods used to access these properties have been shown, AFM of surface roughness and cell-substratum adhesion

force, contact angles for assessment of substratum hydrophobicity and zeta potential to determine surface charge. A brief look at the importance of statistics was conducted; with emphasis on null hypothesis testing without getting into specifics. This information should prepare for the following results chapters.

6.8. References

[1] L. W. Francis, D. Gonzalez, T. Ryder, K. Baer, M. Rees, J. O. White, R. S. Conlan, and C. J. Wright, "Optimized sample preparation for high-resolution AFM characterization of fixed human cells.," *J. Microsc.*, vol. 240, no. 2, pp. 111–21, Nov. 2010.

[2] F. H. Stephenson, *Calculations for Molecular Biology and Biotechnology: A Guide to Mathematics in the Laboratory*, 2nd ed. Academic Press, 2010, p. 460.

[3] J. Boyles, L. Anderson, and P. Hutcherson, "A new fixative for the preservation of actin filaments: fixation of pure actin filament pellets.," *J. Histochem. Cytochem.*, vol. 33, no. 11, pp. 1116–1128, Nov. 1985.

[4] L. Bacáková, E. Filová, F. Rypácek, V. Svorcík, and V. Starý, "Cell adhesion on artificial materials for tissue engineering.," *Physiol. Res.*, vol. 53, pp. S35–45, Jan. 2004.

[5] A. Boyde and E. Maconnachie, "Treatment with lithium salts reduces ethanol dehydration shrinkage of glutaraldehyde fixed tissue," *Histochemistry*, vol. 66, no. 2, pp. 181–187, 1980.

[6] S. Yamamoto, H. Hashizume, J. Hitomi, M. Shigeno, S. Sawaguchi, H. Abe, and T. Ushiki, "The Subfibrillar Arrangement of Corneal and Scleral Collagen Fibrils as Revealed by Scanning Electron and Atomic Force Microscopy," *Arch. Histol. Cytol.*, vol. 63, no. 2, pp. 127–135, 2000.

[7] J. A. Kiernan, "Formaldehyde, formalin, paraformaldehyde and glutaraldehyde: What they are and what they do.," *Micros. Today*, vol. 00, no. 1, pp. 8–12, 2000.

[8] P. Echlin, *Low-Temperature Microscopy and Analysis*, 1st ed. Springer, 1992, p. 539.

[9] P. J. Peters and J. Pierson, "Immunogold Labeling of Thawed Cryosections," in *Introduction to Electron Microscopy for Biologists*, 1st ed., T. D. Allen, Ed. San Diego: Elsevier, 2008, pp. 131–149.

[10] B. Alberts, A. Johnson, J. Lewis, M. Raff, K. Roberts, and P. Walter, *Molecular Biology of the Cell*. Garland Science, 2002, p. 1146.

[11] J. M. Lackie, *The Dictionary of Cell & Molecular Biology*, 4th ed. Oxford: Academic Press, 2007, p. 545.

[12] S. Kumar, *No TitleTextbook of Microbiology*, 1st ed. JP Medical Ltd., 2012, p. 784.

[13] A. Jones, R. Reed, and J. Weyers, *Practical Skills in Biology*, 2nd Ed. Harlow, England: Prentice Hall, 1998, p. 292.

[14] J. Doerr-Schott and C. M. Lichte, "A triple ultrastructural immunogold staining method. Application to the simultaneous demonstration of three hypophyseal hormones.," *J. Histochem. Cytochem.*, vol. 34, no. 8, pp. 1101–1104, Aug. 1986.

[15] J. J. Bozzola and L. D. Russell, *Electron Microscopy: Principles and Techniques for Biologists*. Jones and Bartlett, 1992, p. 542.

[16] R. I. Freshney, *Culture of Animal Cells: A Manual of Basic Technique*, 5th ed. Wiley-Blackwell, 2005, p. 672.

[17] M. V. Berridge and A. S. Tan, "Characterization of the Cellular Reduction of 3-(4,5-dimethylthiazol-2-yl)-2,5-diphenyltetrazolium bromide (MTT): Subcellular Localization,

Substrate Dependence, and Involvement of Mitochondrial Electron Transport in MTT Reduction," *Arch. Biochem. Biophys.*, vol. 303, no. 2, pp. 474–482, 1993.

[18] C. J. Goodwin, S. J. Holt, S. Downes, and N. J. Marshall, "Microculture tetrazolium assays: a comparison between two new tetrazolium salts, XTT and MTS.," *J. Immunol. Methods*, vol. 179, no. 1, pp. 95–103, Feb. 1995.

[19] S. M. Smith, M. B. Wunder, D. A. Norris, and Y. G. Shellman, "A Simple Protocol for Using a LDH-Based Cytotoxicity Assay to Assess the Effects of Death and Growth Inhibition at the Same Time.," *PLoS One*, vol. 6, no. 11, p. e26908, Jan. 2011.

[20] M. D. Abràmoff, P. J. Magalhães, and S. J. Ram, "Image Processing with ImageJ," *Biophotonics Int.*, vol. 11, no. 7, pp. 36–42, 2004.

[21] J. Vitte, a M. M. Benoliel, a Pierres, and P. Bongrand, "Is there a predictable relationship between surface physical-chemical properties and cell behaviour at the interface?," *Eur. Cells Mater.*, vol. 7, pp. 52–63, 2004.

[22] T.-W. Chung, D.-Z. Liu, S.-Y. Wang, and S.-S. Wang, "Enhancement of the growth of human endothelial cells by surface roughness at nanometer scale," *Biomaterials*, vol. 24, no. 25, pp. 4655–4661, Nov. 2003.

[23] B. . Derjaguin, V. . Muller, and Y. . Toporov, "Effect of contact deformations on the adhesion of particles," *J. Colloid Interface Sci.*, vol. 53, no. 2, pp. 314–326, Nov. 1975.

[24] J. E. Lennard-Jones, "Cohesion," *Proc. Phys. Soc.*, vol. 43, no. 5, pp. 465–482, 1931.

[25] F. Rico, P. Roca-Cusachs, N. Gavara, R. Farré, M. Rotger, and D. Navajas, "Probing mechanical properties of living cells by atomic force microscopy with blunted pyramidal cantilever tips.," *Phys. Rev. E. Stat. Nonlin. Soft Matter Phys.*, vol. 72, no. 2 Pt 1, p. 021914, Aug. 2005.

[26] Y. Chen, H. J. Busscher, H. C. van der Mei, and W. Norde, "Statistical analysis of long- and short-range forces involved in bacterial adhesion to substratum surfaces as measured using atomic force microscopy.," *Appl. Environ. Microbiol.*, vol. 77, no. 15, pp. 5065–70, Aug. 2011.

[27] M. R. Castell, "Scanning Tunneling Microscopy of Surfaces and Nanostructures," in *Nanocharacterisation*, A. Kirkland and J. L. Hutchison, Eds. Royal Society of Chemistry, 2008, p. 304.

[28] M. Lampin, Warocquier-Clérout, C. Legris, M. Degrange, and M. F. Sigot-Luizard, "Correlation between substratum roughness and wettability, cell adhesion, and cell migration.," *J. Biomed. Mater. Res.*, vol. 36, no. 1, pp. 99–108, Jul. 1997.

[29] Y. Yuan and T. R. Lee, "Contact Angle and Wetting Propeties," in *Surface Science Techniques*, vol. 51, G. Bracco and B. Holst, Eds. Berlin, Heidelberg: Springer Berlin Heidelberg, 2013, pp. 3–34.

[30] T. Young, "An Essay on the Cohesion of Fluids," *Philos. Trans. R. Soc. London*, vol. 95, no. January, pp. 65–87, Jan. 1805.

[31] D. Janssen, R. De Palma, S. Verlaak, P. Heremans, and W. Dehaen, "Static solvent contact angle measurements, surface free energy and wettability determination of various self-assembled monolayers on silicon dioxide," *Thin Solid Films*, vol. 515, no. 4, pp. 1433–1438, Dec. 2006.

[32] Y. Arima and H. Iwata, "Effect of wettability and surface functional groups on protein adsorption and cell adhesion using well-defined mixed self-assembled monolayers.," *Biomaterials*, vol. 28, no. 20, pp. 3074–82, Jul. 2007.

[33] J. Benesch, A. Askendal, and P. Tengvall, "Quantification of adsorbed human serum albumin at solid interfaces: a comparison between radioimmunoassay (RIA) and simple null ellipsometry," *Colloids Surfaces B Biointerfaces*, vol. 18, no. 2, pp. 71–81, Aug. 2000.

[34] E. Gongadze, D. Kabaso, S. Bauer, T. Slivnik, P. Schmuki, U. van Rienen, and A. Iglič, "Adhesion of osteoblasts to a nanorough titanium implant surface.," *Int. J. Nanomedicine*, vol. 6, pp. 1801–16, Jan. 2011.

[35] P. C. Hiemenz and R. Rajagopalan, *Principles of Colloid and Surface Chemistry*, 3rd, Revis. CRC Press, 1997, p. 672.

[36] K. D. Sattler, *Handbook of Nanophysics: Nanoparticle and Quantum Dots*. CRC Press, 2010, p. 716.

[37] Zeta-Meter, "Zeta Potential: A complete Course in 5 Minutes," 2012. .

[38] Malvern, "Zeta Potential: An Introduction in 30 Minutes," *Zetasizer Nano series technical note*, 2012. .

[39] J. D. Clogston and A. K. Patri, "Zeta Potential Measurement," in *Methods in Molecular Biology*, J. M. Walker, Ed. 2011, pp. 63–70.

[40] G. Cumming, F. Fidler, and D. L. Vaux, "Error bars in experimental biology.," *J. Cell Biol.*, vol. 177, no. 1, pp. 7–11, Apr. 2007.

[41] R. E. Kirk, *Statistics: An Introduction*. Cengage Learning, 2008, p. 672.

Chapter 7. Characterisation of Crystal Growth

7.1. Introduction

The following chapter will cover the crystal growth and characterization of hydrothermally grown zinc oxide (ZnO) nanowires, where different growth variables and their effect on nanowire morphology will be investigated in the following order:

- Comparison of Substrates
- Solution Temperature
- Time
- Seed Layer Thickness and Roughness
- Solution Concentration and Ratio of Precursors
- Minor Variables and Reproducibility

The effect of the above on and subsequent results will show the path taken in this work to obtain the final recipes used through-out the cell viability work in the following chapter. But before these topics are discussed the reason for using the hydrothermal growth method will be discussed.

Before starting the second phase of the project (cell viability) it was necessary to extensively investigate the many variables of the hydrothermal technique (see chapter 3) to provide a certain level of knowledge to accurately tailor the morphology, mechanical and optical properties of any nanowire array fabricated. Initially the investigation focused on examining the morphology (length, width, density, alignment) of the nanowires obtained when altering individual variables (see appendix II for a selection of experiments and variables used); providing a starting point for subsequent research. Only once a recipe had been well established could further investigation of the nanowire properties (mechanical, surface and optical) be conducted (see chapter 8). It was previously mentioned in chapter 3 that the hydrothermal technique was not originally implemented at the start of this work. The traditional gold catalyst based high temperature (>1000 °C) Vapour Liquid Solid (VLS) Chemical Vapour Deposition (CVD) technique was used instead, as this technique was well established within the department [1].

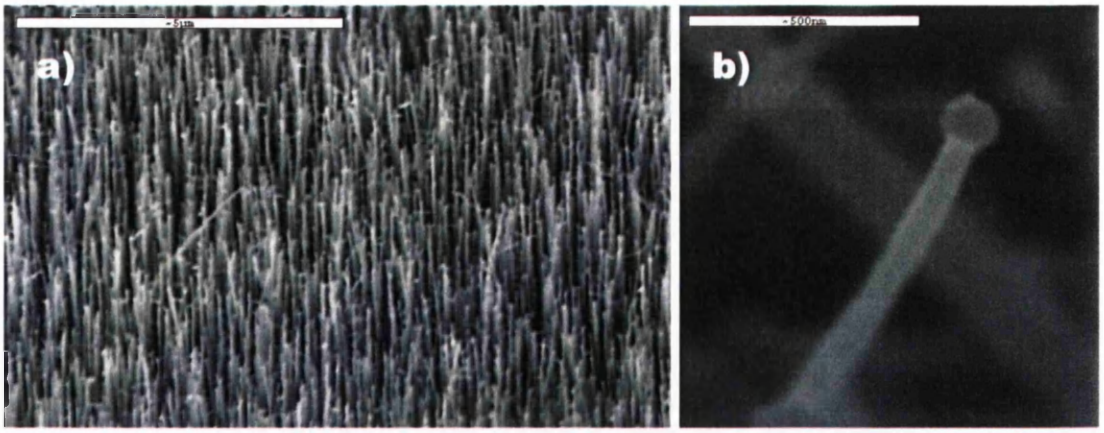

Figure 7.1. ZnO nanowire array fabricated using the VLS-CVD technique, where b) shows the Gold catalyst on the end of a nanowire. Scale bars are 5μm and 500nm for a) and b) respectively. These images were taken using a Jeol JSM-6100 SEM. *[GaN substrate at ~969°C (furnace at 1050°C) for 30mins in 49sccm Ar and 1sccm O_2]*

Fig. 7.1 shows ZnO nanowires obtained using the VLS technique, with the recipe displayed in *[italics]*. While this technique has been shown in the literature [2] to create extremely well aligned high aspect ratio ZnO nanowires, it could however be no longer be used once it was concluded that optically transparent substrates would be required for confocal microscopy (see chapter 6). Therefore a move to glass No 0 cover slips (90 - 130 μm) was made, after it was shown in the literature by Qin et al. [3] that the low temperature hydrothermal method could grow ZnO nanowires on any substrate. The following section will show the highlights of the work, depicting the journey taken to obtain a recipe to yield reproducible arrays of high aspect ratio, well aligned ZnO nanowires; with the final recipe to be used in chapter 8.

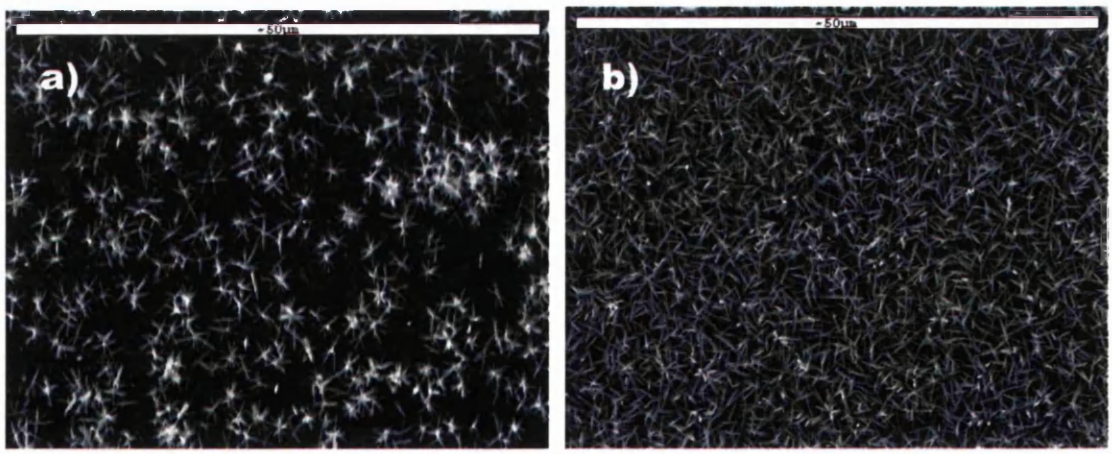

Figure 7.2. ZnO nanowire array fabricated using the hydrothermal technique, where precursor concentration is a) 2.5mM and b) 25mM. Scale bars are 50μm. These images were taken using a Jeol JSM-6100 SEM. *[95°C for 2hrs in 250ml 2.5mM and 25mM 1:1 sol. – no stirring – Si(111) w/ 2x Zinc Acetate spin coating cycles]*

While the decision to adopt the hydrothermal method was originally made to fabricate nanowires on a transparent substrate, initial experiments were conducted using silicon (111) to confirm the method worked as described. Fig. 7.2 shows the first ZnO nanowire arrays fabricated using the hydrothermal method, where a precursor concentration of 2.5 mM and growth temperature of 95 °C were chosen after finding encouraging observations reported by Xu et al. [4]. However it was decided that the concentration should be increased by an order of magnitude to increase the certainty of obtaining nanowire growth, as this concentration was mentioned in the earliest hydrothermal work by Verges et al. [5]. As the method had yielded results first time no other ZnO nanostructure fabrication methods were explored and therefore a methodical study into the effect of variables on ZnO nanowire morphology using the hydrothermal method was conducted.

7.2. Comparison of Optically Transparent Substrates

It has been shown by Qin et al. [3] that the hydrothermal technique can be used to grow ZnO nanowires on any substrate, at 80 °C for 12 hours in 2.5 mM solution. However, previous experiments showed 2.5 mM was insufficient to obtain uniform nanowire growth, therefore solution concentration was increased by an order of magnitude to 25 mM to improve nanowire density and preferential c-axis growth. The solution concentration was increased as Bai et al. [6] reported a significant increase in XRD (002) peak intensity and decrease in FWHM when their solution concentration was increased from 10 mM to 25 mM. Therefore indicating that nanowires grown at higher concentrations are better aligned, as confirmed later in Fig. 7.28b. Several experiments were conducted using glass cover slips, plastic cover slips, and a-plane sapphire substrates to determine the most suitable transparent substrate for compatibility with confocal microscopy. At this point silicon had been used extensively, and so is included in this set of experiments as a control substrate.

Fig. 7.3. shows cross-sectional SEM images of the 4 substrates after growth at 80 °C for 9 hours in 25mM equimolar solution, showing significant changes in the morphology of ZnO nanowires grown on different substrates; especially for the plastic substrate. The observed major discrepancies could be due to the plastics much lower glass transition temperature, of 80 °C compared to soda-lime glasses 550 °C [7]. This is undoubtedly to cause as the poly-vinyl chloride (PVC) cover slips were witnessed to

distort and alter shape slightly during growth, this combined with the substrates increased roughness likely effected the distribution of seed layer particles on the substrate drastically effecting the growth of the nanowires. This trend was also observed by Yamabi et al. [8], who reported that the density of ZnO nanostructures grown on Glass and Silicon substrates was far less than on a plastic (PET) substrate.

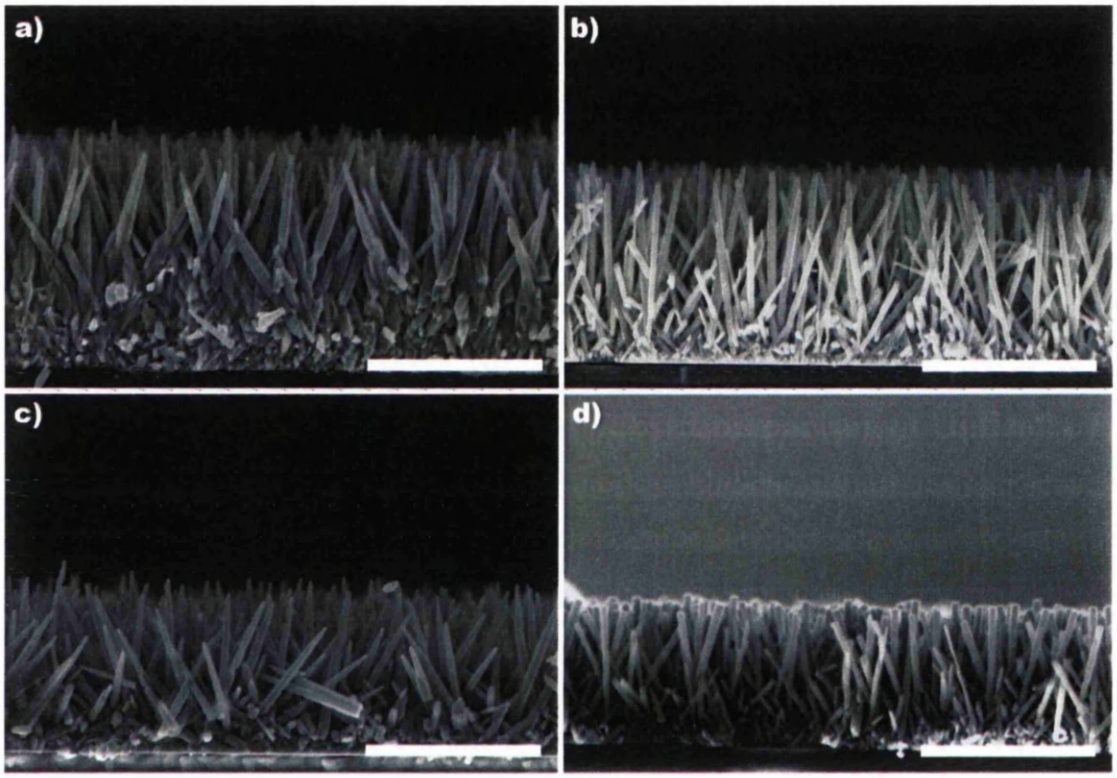

Figure 7.3. Cross-sectional SEM images of ZnO nanowires on different substrates, where a) is Silicon, b) is Glass, c) is Sapphire and d) is Plastic; all of similar surface area. All scale bars are 2µm. *[80°C for 9hrs in 500ml of 25mM 1:1 sol. – 8min stir (2min hot)– Multiple Subs w/ 20nm PVD Seed]*

Fig. 7.3. shows changes in nanowire morphology between the 4 substrates, with the Silicon substrate yielding the longest, widest and least dense nanowires. The Plastic substrate yielded the smallest and densest nanowire array, were it can also be observed that the shape of the ends of the nanowires in the (0001) plane is flat compared to the others more 'rounded' polar planes. The tapered or rounded ends are typical of the layer by layer growth method proposed by Luadise et al. [9] where they state that the decreasing surface area of each hexagonal layer (during c-axis growth) is due to differing growth rate of the non-polar and polar planes; leading to the disappearance of the (0001) facet. In this experiment it appears that the growth rate of plastic is sufficiently slow enough to allow full formation of the [0001] polar facet. This

observation accentuates that there are many non-solution variables affecting the morphology of the nanowires yet to be explored, as the solution used was identical for all substrates.

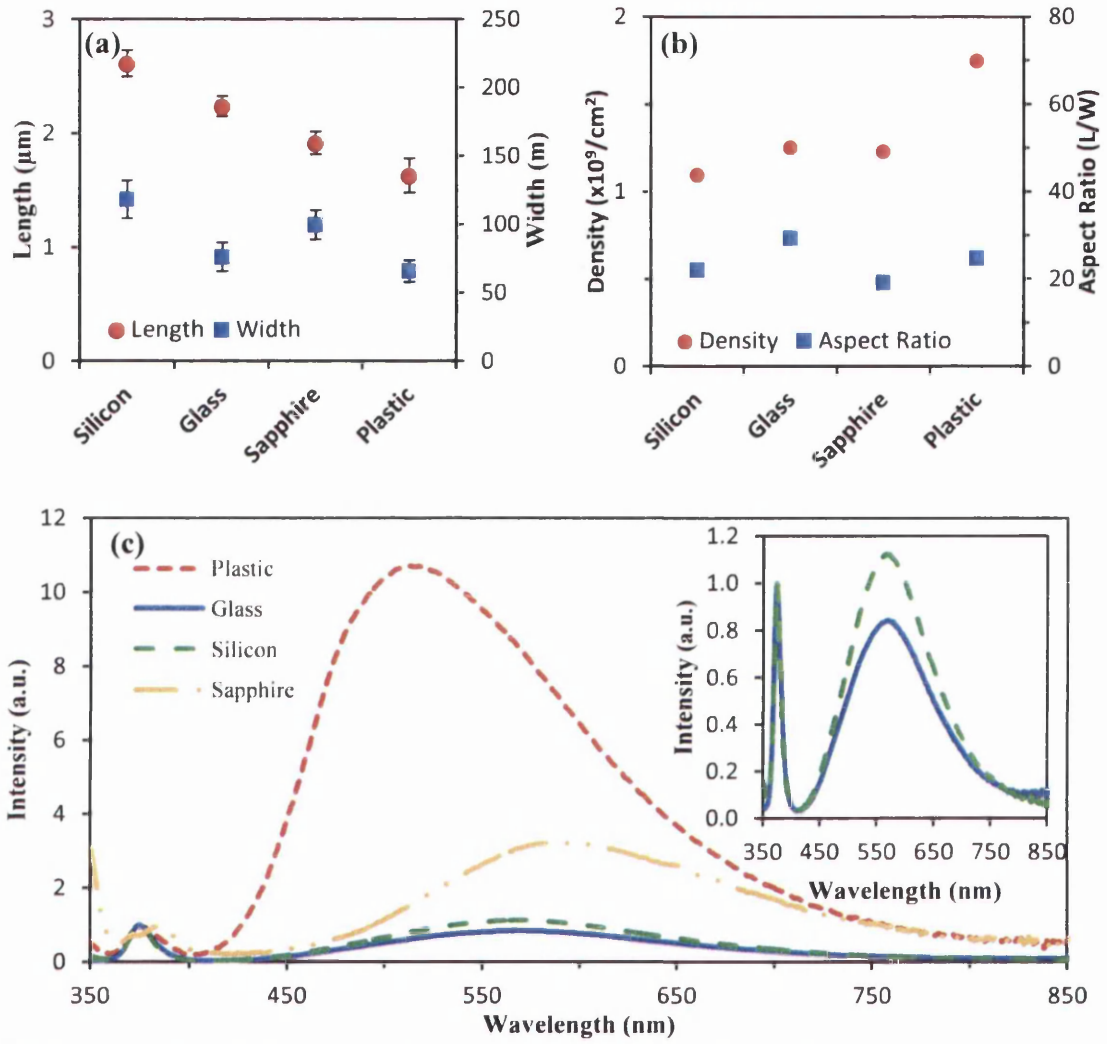

Figure 7.4. Graphs show mean of measurements taken from [Fig. 7.3.], where (a) shows the length and width taken from 90 measurements for each across 3 different areas, where error bars represent ±SD of 3 areas. (b) shows aspect ratio and density. Graph (c) is the Photoluminescence spectra of the Zinc Oxide nanowires on different substrates, where the main graph shows all substrates used in the experiment and inset shows the selected Glass substrate vs. the Silicon control. A 325nm HeCd excitation source used and results are the mean of 3 acquisitions from 3 different areas. Data is normalized to the near band edge.

From Fig. 7.4b it can be observed that the glass substrates yield the best aspect ratio, and therefore glass is the best candidate to use for optically transparent substrates. It is believed that substrate roughness is the cause of the observed differences as Yoshino et al. [10] deposited ZnO thin films on various substrates and observed similar differences. They profiled the crystallinity of nanowires from each substrate using XRD

analysis of the (0002) peak, and showed that thin films deposited on glass had an exceptionally high degree of crystallinity as indicated by the smallest FWHM of 3.93 °, compared to 14.23 ° for Ni. Similarly, it was discovered in this work [11] that growth rate was significantly affected when Ni films were deposited on the substrate below the ZnO seed layer, which was mainly attributed to changes in the roughness and grain size of the seed layer deposited, with the growth rate decreasing with increasing roughness. This work will be discussed in more detail in sub-section 7.5.4. It could be therefore that the differences in Fig. 7.4a are simply due to changes in substrate roughness.

In Fig. 7.4c it can be seen that plastic substrates have the largest 510 nm centered visible broadband emission of all the samples, likely due to substrate contribution. However, although background spectra for blank substrates have been acquired it has not been removed from the spectra to allow fair comparison (see chapter 4); as such a process may not be available during other life sciences microscopy techniques and any devices created from this work would be unable to neglect this contribution. The inset spectra shows the difference between silicon and glass substrates, it is suggested that this difference in the 570 nm centered defect band is likely due to a change in ZnO nanowire morphology as indicated in Fig. 7.3 leading to additional contribution from surface states compared to the bulk as discussed in chapter 4. This notion is supported by Shen et al. [12] who hypothesized that observed spectral shifts maybe due to increased surface defect density compared to the bulk because of differences in surface-to-volume ratios. However, regardless of the mechanism behind said differences if the same recipe is employed for both silicon and glass, and glass yields higher aspect ratio nanowires with improved optical properties, then the choice of which substrate to use is obvious.

Also, glass coverslips are extremely brittle and can be cut into similar size pieces easily, allowing post growth coverslips covered with uniformly distributed nanowires to be further divided allowing one sample to be used in multiple experiments. This is especially important for the biological experiments (see chapter 8) as each needs to be done in at least triplicate (n=3) to confirm observed results have statistical significance. From here on 24 by 24 mm glass coverslips are used exclusively after the initial findings, as they can be fractured into 9 substrates with identical morphology. Now that a suitable optically transparent silicon replacement substrate had been selected, substantial effort was invested to refine the recipe to improve the aspect ratio of ZnO nanowires grown on glass coverslips.

7.2.1. Substrate orientation

It has been reported by Wang et al. [13] that the orientation with respect to the beaker (i.e. not crystallographic) of the substrate during hydrothermal growth could drastically affect the alignment and morphology of the nanowires; so the effect of substrate placement was investigated. They show that a substrate that is parallel to the solution surface yields a high Reynolds number, indicating turbulent flow; compared to a substrate held perpendicular to the solution surface that yields and much lower Reynolds number, indicating laminar flow. With the later producing more well aligned nanowires. It is believed that this laminar flow creates a boundary layer that forces reactants to arrive at the substrate surface via diffusion at a steady rate, instead of all at once. However, when repeating Wangs' work in this project it was observed that the submerged substrate collected significant colloidal growth, see Fig. 7.5d. Also, holding the substrate in a PTFE frame seed layer side down parallel to the solution surface created minimal deviations in nanowire morphology at the edges of the sample; meaning that the substrate could not be fairly be cut into 9 pieces.

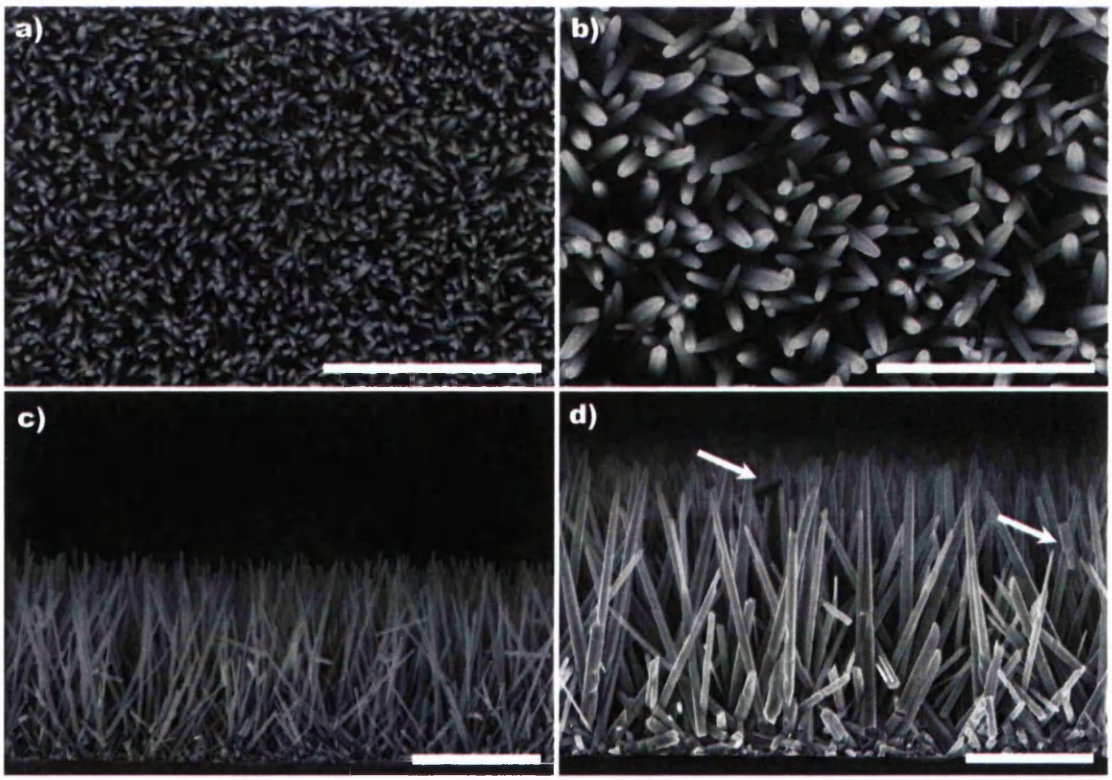

Figure 7.5. SEM images of ZnO Nanowires on glass substrates that have been grown at different orientations, where a) and c) were floated on the solution surface and b) and d) were held in the middle of the beaker on a PTFE stand. All scale bars are 2 µm. White arrows indicate embedded colloidal nanorods. *[90°C for 9hrs in 250ml 25mM 1:1 sol. – 45min stir – Glass coverslip w/ 3x Zinc Acetate spin coating cycles]*

Becuase the Grant SUB Aqua Plus water baths used in this work are unstirred and heat the water from the bottom, when set to 90 °C a temperature gradient of 2 °C exists accross the 100 mm depth of water, and similarly within beaker solution too. It should be noted thermometer used is stated by the manufacturer to have an accuracy of ±0.3 °C. However this is actually helpful in the deposition of material as it determines where the precipitate is more likely to form, as it has been hypothesised in the literature [14] that if a temperature gradient exists within a beaker (i.e. if it is heated in an unstirred system) that it becomes more energetically favourable for the highly supersaturated solution to precipitate in the coldest region to re-establish equilibrium. As explained by the Le Chatelier principle discussed in chapter 3.

Fig. 7.5. shows that this is not the case with samples grown fully submerged in the solution mounted on a frame halfway between bottom of PTFE beaker and solution surface yeilding longer nanowires. Though it can be seen in Fig. 7.5a. that the width of the nanowires on the submerged substrate is 171 % larger, changing from 62 ± 8 nm for floated to 167 ± 25 nm for submerged substrates. This drastic change is likely due to a concentration gradient existing in the beaker as all colloidal precipitates settle to the bottom of the beaker after 1 - 2 hours of growth (see section 7.3). Assuming that the sediment is formed initially from the precipitation of the $Zn(OH)_4^{2-}$ complex intermediate could likely provide the submerged sample with a much higher concentration of Zn^{2+} and OH^- ions. Although work by Wang et al. [15] has shown that when the concentration of Zn^{2+} precursor exceeds 0.025 mol/L that there should be almost no gradient present. Therefore, the observed difference between submerged and floated samples is more likely an affect of the previously mentioned temperature gradient, so this will also be investigated further.

Whatever the mechanism this change in width reduces the aspect ratio by 38% from 50 nm for the floated substrate to 31 nm for the submerged, meaning that although growth rate has improved significantly the youngs modulus of the nanowires will be significantly different; affecting force measurements in phase 3. For example Chen et al. [16] have reported the youngs modulus of a ZnO nanowire to only deviated from the bulk for diameters of less that 120 nm. So although we would expect the submerged nanowires to yield ~140 GPa the floated nanowires could be significantly different. Fig. 7.16c shows that the photoluminesence spectra is negatively affected in the visible defect band with submerged substrates containing considerably more defects than

nanowires grown on the floated substrate. The PL further supports the assumption of increased ion concentration near the bottom of the beaker, as it has been reported by Ku et al. [17] that OH^- maybe a surface trapping center as they observe a direct correlation between green-band emission intensity and surface hydroxide concentration. It could however also be due to the contribution from colloidal nanorods as highlighted by white arrows in Fig. 7.5d. Fig. 7.6d. shows the reverse of the glass coverslip of the submerged substrate mounted on the frame, where it can unfortunately be seen that substaintial colloidal growth has adhered to the surface. This image was aquired after additional D.I. water rinsing cycles were conducted.

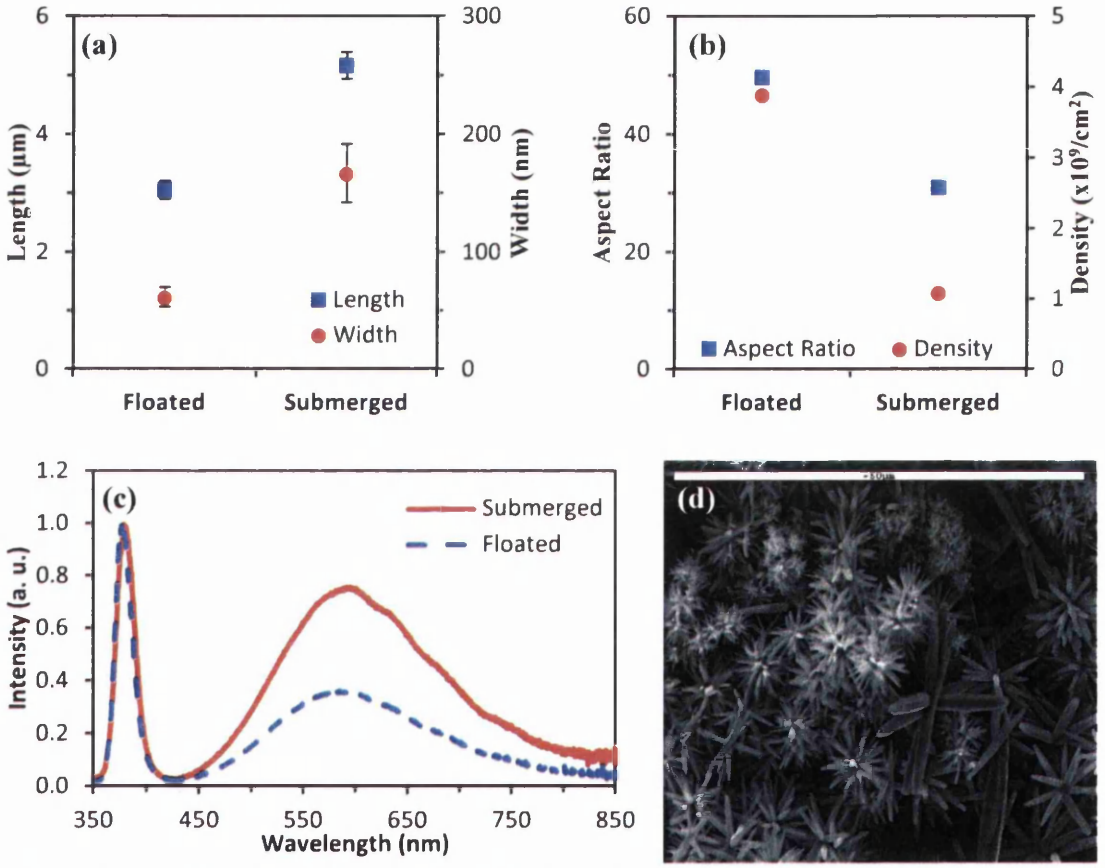

Figure 7.6. Graphs show effect of substrate orientation on a) length and width and b) aspect ratio and density. For a) data was taken from 90 measurements for each time point across 3 different areas and error bars represent ±SD of the 3 areas. For c) photoluminescence data is normalized to the near band edge. For d) SEM image showing reverse of substrate grown submerged in solution showing substantial colloidal growth attachment, in the form of nanoflowers. This image was taken after repeated rinse cycles to remove the nanostructures. Scale bar is 50µm.

7.3. Temperature

The effect of temperature on the morphology of the nanowires was investigated for 60, 70, 80 and 90 °C as this range of temperatures featured prominently in the literature. The hydrothermal method is a wet chemical technique so it would therefore be logical to assume that an increase in growth temperature would yield an increase in crystal growth rate, due to increased production rate of elementary layers. However significant changes in the crystal quality of nanowires grown at higher temperature were observed via undesirable changes in photoluminescence spectra; see Fig. 7.9.

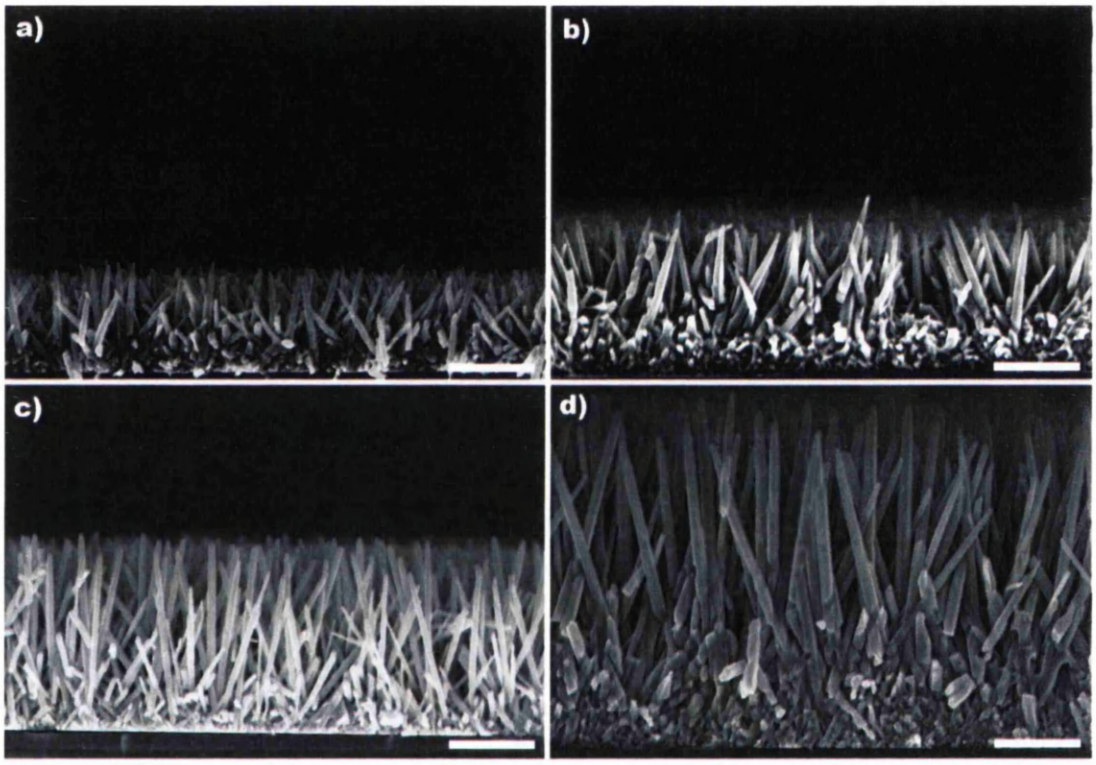

Figure 7.7. SEM images of nanowires grown at a) 60°C, b) 70°C, c) 80°C and d) 90°C. All scale bars are 1μm. *[60-90°C for 9hrs in 500ml 25mM 1:1 sol. - 70min stir (2min hot) – Si(111) w/ 20nm PVD seed layer]*

Fig. 7.7. shows cross-sectional SEM images of ZnO nanowire arrays grown at each of the above temperatures, a direct linear relationship between length/width and temperature was observed, see Fig. 7.8. This is expected and was discussed in chapter 3, and is mainly due to the stability constant of a complex being temperature dependent, as the OH^- concentration at any particular pH varies considerably with temperature [18]. An increase of the solution temperature provides more energy to break bonds allowing

more of the complex intermediate to be dissociated into ions. Therefore the direct linear relationship is derived from an increase in complex ion availability.

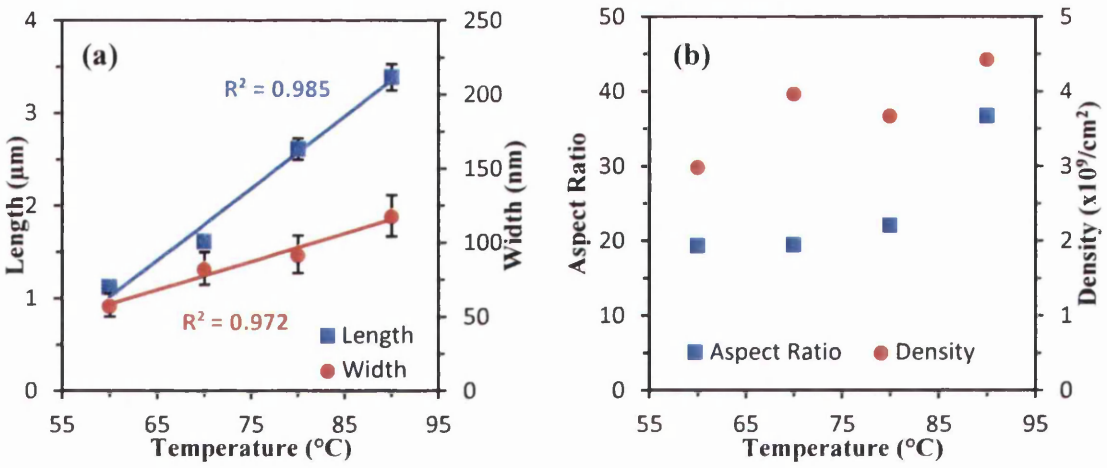

Figure 7.8. The relationship between solution temperature and crystal morphology is shown for ZnO nanowire (a) length and width and (b) aspect ratio and density. Error bars represent ±SD of 3 areas.

Fig. 7.8a compares the average length and width of nanowires as a function of temperature; the means were obtained from 90 measurements where 30 measurements were taken from 3 separated areas on the sample for statistical fairness. Therefore the error bars represent the ± standard deviation of the mean across 90 measurements. This is the minimum standard for all morphology measurements in this thesis unless otherwise stated, and therefore will not be mentioned again. In total **11,520** nanowires have been measured to produce the results in this thesis. The increase in crystal growth rate between each 10 °C increment is similar for both length and width of nanowires with an observed 40% increase from 60 °C to 70 °C and 30% increase from 80 °C to 90 °C. The datum's have been kept apart in the graph for clarity. The determinate coefficient (R^2) yielded from the least squares linear trend lines are 0.985 and 0.972 for length and width respectively, it can therefore be seen that the linear relationship observed between solution temperature and growth rate is stable. Zhang et al. [19] has hypothesized that the mechanism behind the diameter / temperature relationship is due to the production rate of NH_3, where at low temperature (60 °C) the release of NH_3 is slow and more Zn^{2+} are transformed into ZnO nuclei in the function of hydroxyl. Therefore homogeneous precipitate dominates causing significant reduction in available precursor ions for heterogeneous deposition on the substrate. The relationship between

length and temperature can be fitted with the linear gradient $y = 77.954x - 3661.4$, if $x =$ 50 °C then this equation yields only 236 nm; therefore growth below 60°C regardless of other variables is unlikely; this lower limit of solution temperature has been reported previously [20]. Denianets et al. [21] have shown that the activation energies for growth of the (0001), (000$\bar{1}$), and (10$\bar{1}$0) faces in are equal to 59 ±3, 66 ±3 and 68 ±3 kJ/mol, respectively. The large difference in length compared to the subtle difference in width between 60 and 90 °C is therefore likely due temperature extenuating the differences in activation energy requirement between the different crystal facets.

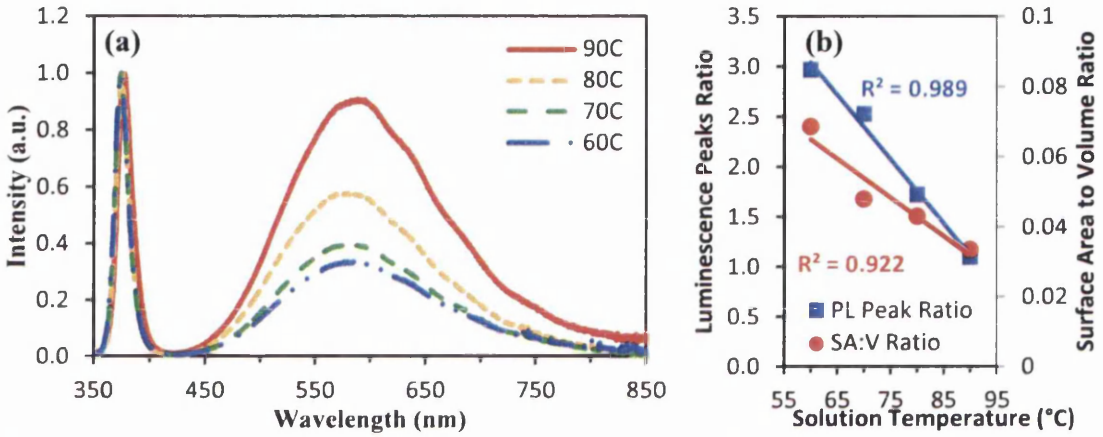

Figure 7.9. The relationship between solution temperature and crystal quality is shown using (a) Photoluminescence spectra of Zinc Oxide nanowires grown at different precursor solution temperatures, and (b) the change in deep level emission with respect to the near band edge emission. A 325nm HeCd excitation source was used and results are the mean of 3 acquisitions from 3 different areas. Data is normalized to the near band edge peak.

Fig. 7.9a shows the photoluminescence (PL) spectra of nanowires shown in Fig. 7.7, with Fig. 7.9b highlighting the change in ratio between the NBE and DLE peak intensities with increasing solution temperature. It can be seen that the temperature has a significant effect on the intensity of the DLE, with nanowires grown at a higher solution temperature being of lower optical quality. This could be assumed initially to be due to a difference in surface area to volume ratio as PL is often considered to be surface state sensitive; certainly work by Ku et al. [17] has suggested that the origins of the green band emission (DLE) are correlated with surface hydroxide as well as the frequently published single ionized oxygen vacancy (O_i^-). For below-bandgap excitation, absorption is weaker and the excitation source penetrates deeper into the sample. Therefore the PL spectra shown in this work is will comprise of contributions from both surface and substrate due to the HeCd's 3.81 eV (325 nm) above bandgap emission; as

ZnO is 3.37 eV (376 nm). In all photoluminescence results the surface quality of the ZnO nanowires will dominate the results, this is because the skin depth / penetration depth of our 325 nm HeCd is worked out to be 63 nm, using Elliot-Toyozawa theory similar to that of Sans et al. [22]. This is in good agreement with findings by Choi et al. [23] who determine the optical skin depth of their 325 nm HeCd excitation source to be about 83 nm in ZnO. The equations used to determine the optical skin depth can be found in work by Lynch and Hunter [24].

Conversely to the above, the plot in Fig. 7.9b shows that the trend observed is independent of surface area to volume ratio (SAVR). This observation is supported by the data as a 51 % drop in SAVR from 60 to 90 °C, yielded PL peak ratio drop by 63 % from 2.97 to 1.10, indicating either a substantial increase in DLE peak intensity; as all data is normalized to NBE peak. If the system was purely surface sensitive, and therefore the majority of DLE was comprised from recombination at surface states then the dramatic increase in volume wouldn't affect the DLE peak intensity. Therefore it can be hypothesized that the 171 % increase in DLE area from 60 to 90 °C is due to an increase in crystallographic defects during the growth procedure. It has been shown by Demianets et al. [21] that a growth rate 1.5 times that of the control yielded crystal that contained a large number of intrinsic defects and that were predominately non-stoichiometric. This is likely why there's little difference in DLE intensity between 60 and 70 °C, which had growth rates of 125 and 179 nm/hr, respectively. Making 70 °C only 1.44 times faster than 60 °C, however 90 °C had a growth rate of 377 nm/hr making it just over 3 times faster than 60 °C; supporting the observations by Demianets.

In chapter 4 a detailed review of the literature revealed the many possible reasons for deep level emissions, specifically concentrating on the source of green emissions such as singly ionized oxygen vacancies, zinc vacancies and oxygen antisites. However it was suggested by Tam et al. [25] that the green centered emission may be associated with oxygen deficiency during crystal growth. As the free oxygen content of water decreases linearly with increasing temperature, it can be assumed that the substantial increase in the DLE peak in Fig 7.9a is due to oxygen vacancies in the crystal. This experiment has revealed that crystal growth at higher solution temperatures yields longer, higher aspect ratio nanowires but at the cost of crystal quality; therefore the final application of these ZnO nanowires should be considered. A more detailed breakdown of the DLE emission is covered in chapter 8, where nanowires are annealed post growth to further determine the origin of the visible emission in ZnO nanowires.

Given that phase 3 of the project is application of the nanowires for force sensing, planning for this phase is vital and therefore it maybe assumed that an increased length may lead to increased device sensitivity. However, several publications show that the diameter is the determining factor in deciding the Young's modulus of the nanowire. For example, Wang et al. [26] show that Young's modulus is inversely proportional to the diameter of nanowire, and demonstrate that the size-dependent elastic properties of a nanowires derive from stress-induced surface stiffening. It has been suggested by Agrawal et al. [27] that the size-dependance of Young's modulus ZnO nanowires only exists for nanowires less than 100 nm in diameter, and that nanowires larger than this should exhibit the bulk value of 140 GPa. This will be investigated in chapter 8. However, Lee et al. [28] calculated the band gap using density functional theory (DFT), finding that the band gaps of ZnO nanowires depended on the size and geometry of the nanowire. Since it was initially discussed that the mechanism for force sensing would involve monitoring band gap change then it was decided that fabrication of nanowires with a high aspect ratio was of great importance to maintain device sensitivity; and therefore 90 °C would be used from here on.

7.4. Time experiments

The effect of time on the morphology of the nanowires was investigated by observing one sample every hour for 9 hours, and comparing length, width, alignment, and density; using the previously selected solution temperature of 90 °C. The literature reveals an extensive range of times used for the hydrothermal technique, some as short as 1 hour while others leave their experiment for 50. Although the use of any growth time is available using the hydrothermal method, it has been suggested by Baruah and Dutta [29] that the growth solution should be refreshed every 5 hours to allow continued availability of precursors therefore maintaining optimal crystal growth rate. Doing this they managed over a 20 hour growth period to increase the length of their ZnO nanowires by 4 μm from 6 μm for the un-refreshed beaker to 10 μm for the refreshed. However, even after extensive review of the literature a 9 hour growth time was selected due to time constraints and lack of manpower. Running the experiment unsupervised for 9 hours allowed for two experiments to be conducted a day, typically at 2 pm – 11 pm and 1 am – 10 am; allowing for faster determination of key variables

and conditions for hydrothermal growth. This is the major cause of this work producing 602 samples over 848 hours of experiments. However it was decided that an hour by hour examination would be conducted to determine if a 9 hour growth time was ideal as well as confirm if precursor solution could be reduced to values more typical of those seen in the literature. In this set of experiments a precursor concentration of 10 mM was used as per Vayssieres [30] to crudely observe the effect of concentration on the aspect ratio of the ZnO nanowires.

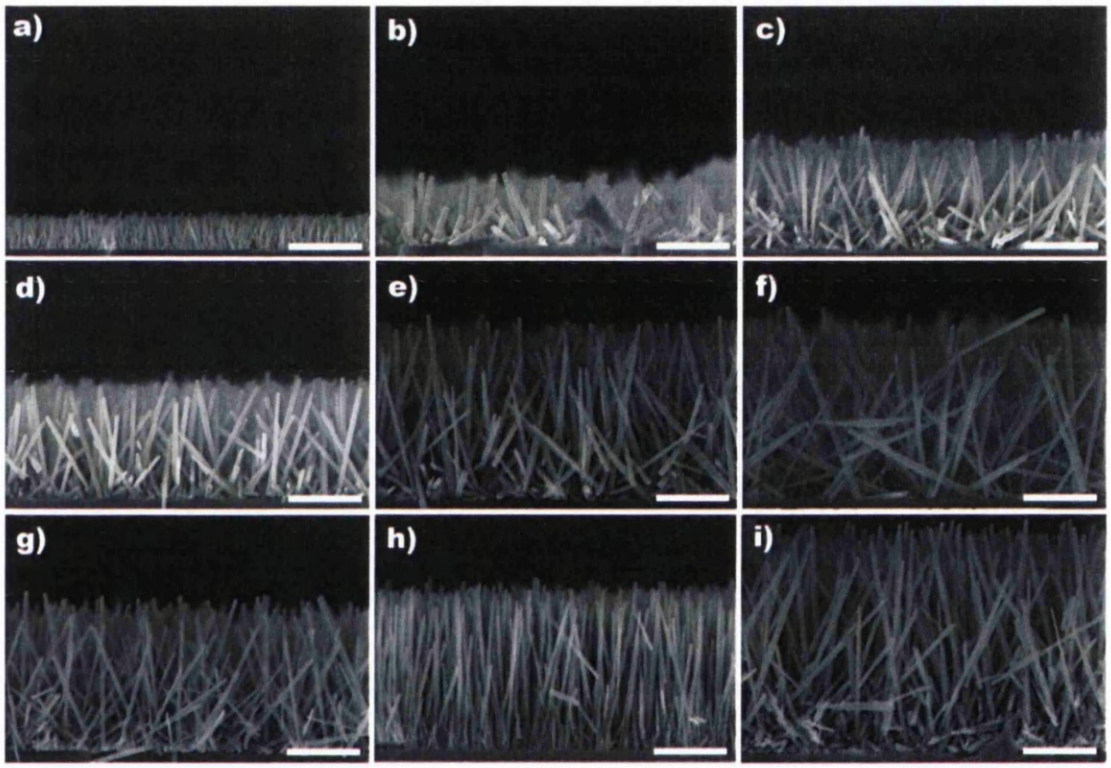

Figure 7.10. Cross-sectional SEM images of ZnO nanowires on glass substrates grown for different times , where a) – i) represents 1–9 hours respectively. Inconsisty in trend arise from spin coated seed layer, where reduced length and width are replaced by increased density and allignment. All scale bars are 1μm. *[90°C for 9hrs in 250ml 10mM 1:1 sol. - 40min stir (2min hot) – Glass coverslip w/ 2x Zinc Acetate spin coating cycles]*

Fig.7.10. shows considerable inconsistencies in the density and alignment of the wires, especially with 7 and 8 hours being drastically denser than the other wires. The nanowires at 1 hour are also drastically denser, but this could simply be due to the growth mechanism, as the nuclei density effect as described by Wang et al. [31] may explain the increased density. They suggest that ZnO possesses a 'fourling' structure that will want to ideally grow 4 spines from single nuclei. However, if two nuclei are sufficiently close then their laterally growing spines tend to come in contact suppressing

lateral growth. Further examples of this inconsistence in density likely due to inhomogeneous coating of ZnO nuclei can be seen in Figs. 7.10., 7.14. and 7.16. where the cause of this non uniform density distribution is not due to the crowning effect so commonly observed in spin coated samples [32]. Ji et al. [33] studied the effect of seed layer thickness on ZnO nanowire array density and alignment, and proposed that nanowires grown on thicker seed layers were more well aligned due to an increase in nanowire diameter; this will be investigated in sub-section 7.5.2. Although the images in Fig. 7.10. may only represent a single area the results in Fig 7.11. represent the mean of 3 areas and as such should even out major discrepancies across the sample.

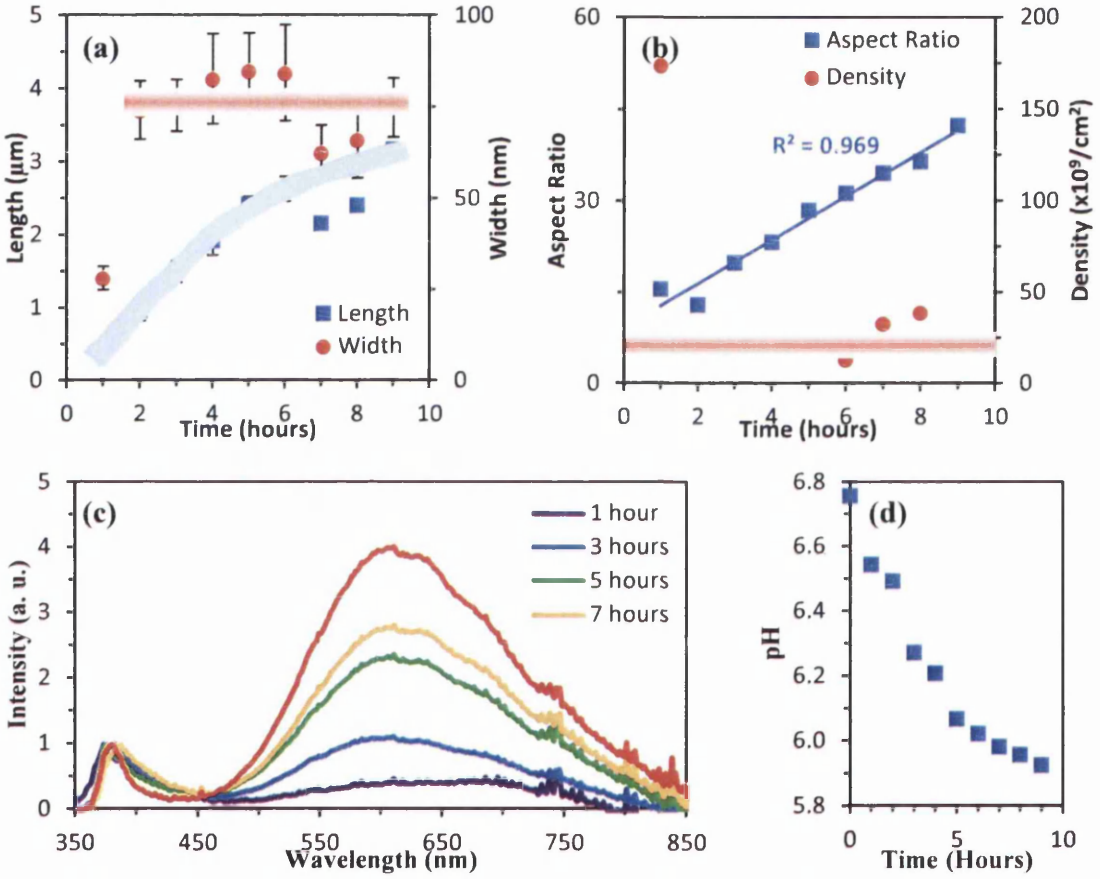

Figure 7.11. Data from analyses of nanowires from time experiments where, a) highlights the morphology change each hour from 1-9 hours, b) shows linear change in aspect ratio with time, c) shows via photoluminescence an almost linear dependence on the NBE-defect peak ratio with time and d) an increase in precursor solution with time. For a) and b) data taken from 90 measurements for each time point across 3 different areas and error bars represent ±SD of the 3 areas. Photoluminescence data is normalized to the near band edge and for clarity even time points have been omitted from the graph.

When the reaction is allowed to run for a substantial amount of time (>5 hours) the super saturation of Zn^{2+} ions in the solution is unable to be maintained due to the

constant depletion during crystal growth. Govender et al. [34] showed that the super-saturation (SS) of the precursor solution was prerequisite for crystallisation of ZnO, and that the level of SS determined the final morphology of the ZnO nanowires where highly SS solutions would be dominated by homogeneous nucleation. Fig. 7.11d shows the pH of the solution in this experiment over time, where a rapid reduction in pH can be observed from 0 - 4 hours. Since pH is a measure of OH^- ions and they are a key component of ZnO crystallisation that are produced steadily by HMTA (as discussed in chapter 3), it can be seen that the HMTA buffer after 4 hours is likely expired. However since the release rate of OH^- from the HMTA buffer is unknown it could be that 4 hours marks the reduction from highly SS to just SS at which homogeneous nucleation stops and heterogeneous nucleation now dominates. This theory would support the plateau of length increase in Fig. 7.11a but could not explain the subsequent reduction in length from 6 hours onward. Qiu et al [35] show that a reduction in the availability of precursors can lead to a dissolution and regrowth mechanism whereby a deficiency of Zn^{2+} ions in the solution will result in the ZnO crystals being dissolved to maintain equilibrium of Zn^{2+} ions within the solution, resulting in a shift to the left of equation 3.7 to adhere to the le Chatelier principle.

However, if this were the mechanism behind the reduction in nanowire length for 7 and 8 hours then why is the aspect ratio maintained in Fig 7.11b. Qiu et al. explain the kinetics of the mechanism, reporting that the dissolution rate of the (0001) polar plane is faster than the non polar planes due to a higher surface energy. But while it could be assumed this would lead to the formation of nanorods, the small surface area of the (0001) plane in comparison to the six other non-polar planes leads to further reduction of diameter. This theory doesn't match the pH results in Fig 7.11d and therefore the more likely mechanism is the expiration of the HMTA buffer, but this doesn't explain the continued growth of the ZnO nanowires. Additionally Govender et al. have witnessed that the time taken to introduce the substrate to the solution after the growth temperature is obtained, greatly affects the amount of homogenous nucleation. They found that conducting experiments in solution of visible turbidity (typically solutions left 30 minutes after reaching 90 °C) would result in substantial homogeneous precipitation. The transparency of the solution was investigated and is discussed in detail in sub-section 7.7.2. It is therefore likely that the deviation from the proposed curve (shown as blue background behind data) is due to the change in density (see Fig 7.11b) and that the total mass of ZnO produced would increase linearly with time.

7.4.1. Avoiding growth inhibition

It has been seen in the literature that the a reduction in crystal growth rate over time (as discussed in section 7.3) could be avoided by either adding additional zinc nitrate solution [36], or replenishing the whole solution [37]. It was determined in sub-section 7.1.1 that substrates would be floated on the surface of the growth solution to avoid contaminating the back of the substrate. It was difficult to introduce additional zinc nitrate solution to the beaker without breaking the surface tension of one or more of the floating substrates causing them to plummet to the bottom of the beaker. Since this yielded differences similar to that discussed in sub-section 7.2.1. then both adding new solution or moving the substrate to new solution were not investigated further. However, by increasing the solution volume from 250 to 500 ml subtle changes in morphology were observed. Fig. 7.12a. shows that precursor solution volume has a subtle impact on the morphology of the nanowires, where lengths of 3.2 and 3.7 µm were obtained for 250 and 500 ml, respectively. Widths were similar for both solution volumes, which is due to the degree of error created by the 'fourling' structure of nanowires grown from each nuclei during the initial stages of crystal growth, as these can often collide in a partially destructive way reducing width.

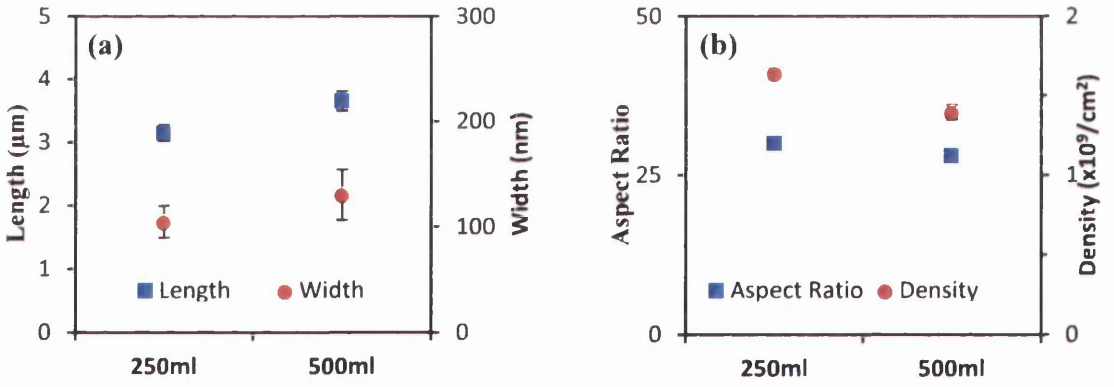

Figure 7.12. Graphs show effect of precursor volume on a) length and width and b) aspect ratio and density, where all other variables were kept identical. The error bars represent the ± standard deviation from 2 experiments or 180 measurements from 6 areas across 2 samples. *[90°C for 9hrs in 250ml and 500ml 25mM 1:1 sol. - 10min stir (1min hot) – Glass coverslip w/ 20nm PVD Seed]*

It is assumed that the additional length observed stems from an extension of the time taken for crystal growth rate to plateau due to reduction of available precursors as witnessed earlier in Fig 7.11a. However the additional space for extra substrates that

significantly increases sample yield means that 500 ml will be the preferred solution volume for all future experiments.

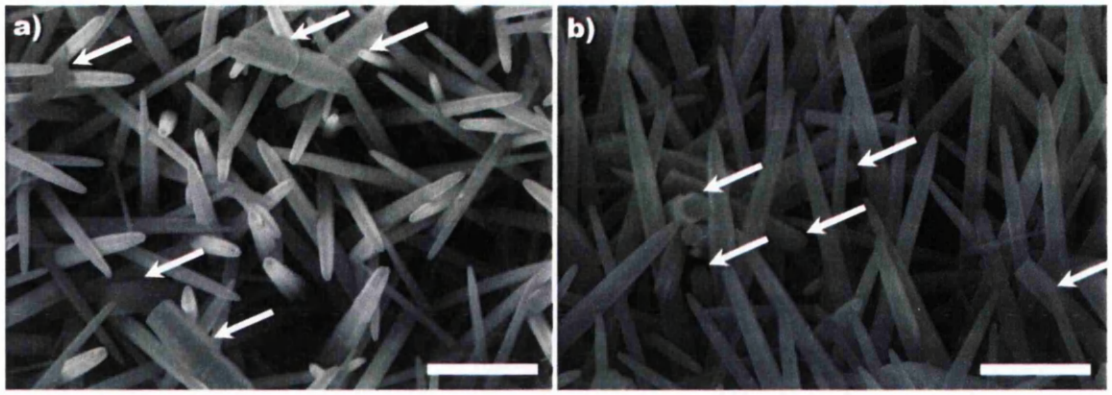

Figure 7.13. SEM images of ZnO nanowires taken a) normal and b) at 45 degrees to the substrate, where white arrows indicate the presence of colloidal growth. Here samples have been grown in one solution for 9 hours then new solution for a following 2 hours. Scale bars are 1µm. *[90°C for 9hrs then 60°C for 2hrs both in 500ml 25mM 1:1 sol. - 55min stir (5min hot) – Si (111) w/ 2x Zinc Acetate spin coating cycles]*

As discussed initially 500 ml beakers were employed to maintain precursor concentrations and super saturation of Zn^{2+} ions during growth, though as Fig. 7.12. shows very little is changed and therefore the method of replenishing the solution or re-growth of the samples as discussed in the literature by Tak and Yong [37] was explored. Fig. 7.13. shows that by re-growing samples in new precursor solution immediately after the first growth session unfortunately yields colloidal growth in between the nanowires, where colloids are highlighted by white arrows and easily recognisable due to their notched indents surrounding nucleation point in middle of each nanorod. No matter how many rinses and 'mild' sonication cycles were conducted the nanorods remained present and so contribute to the PL spectra in Fig 7.14c.

Fig. 7.14b shows that the aspect ratio of the wires is drastically reduced after the 2^{nd} growth, due to an increase in length and width of 30 % and 50 %, respectively. Unfortunately density comparison was impossible due to the number of colloidal nanorods observed in between the nanowires using ImageJ, though crude analysis by eye showed density was unaffected; as would be expected. 60 °C was selected from the literature as it had been suggested by Joo et al [38] that the low temperature of the growth solution would yield a low incorporation rate of non-zinc ions into the ZnO crystal, with their presence instead just limiting crystal growth. Unfortunately this was

not the case as shown by Fig 7.14c where samples that had been regrown yielded a significant increase DLE area with an increase of 47 % from the 1st to 2nd growth cycles.

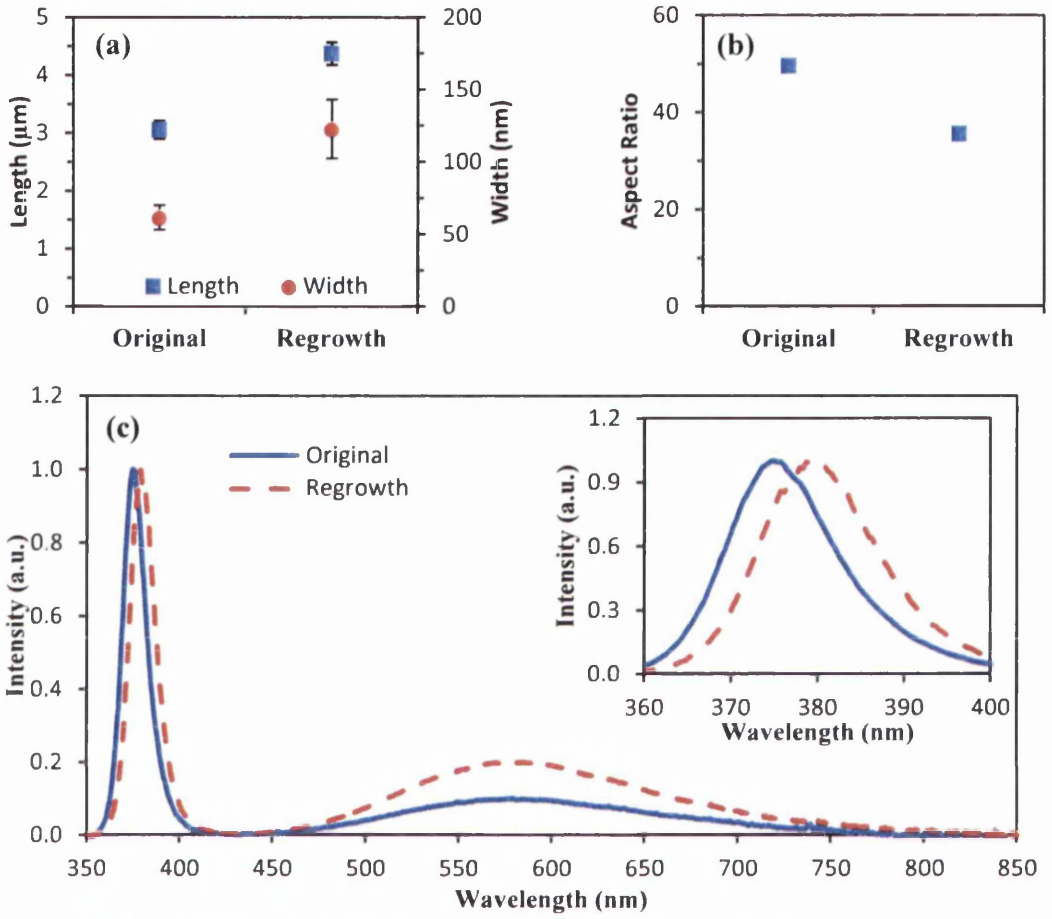

Figure 7.14. Graphs show a) length and width and b) aspect ratio, for before and after a 2nd growth stage was conducted. For a) data was taken from 90 measurements for each time point across 3 different areas and error bars represent ±SD of the 3 areas. For c) photoluminescence data is normalized to the near band edge, and inset shows red shift of near band edge after 2nd growth cycle.

The observed red shift in the NBE peak seen from 375 nm to 379 nm for 1st and 2nd respectively is likely due to contribution of colloidal nanorods to the spectra, white arrows in Fig. 7.13. Also the widths of the nanowires were 65 ± 8 nm and 123 ± 20 nm for 1st and 2nd, respectively; so assumption of quantum effects causing the shift is therefore unrealistic. Yang et al. [39] observed a 6 nm shift in NBE peak position between their sample and the bulk and attribute it to change in strain between samples. It is possible that a change in strain could exist between the samples in this work as the regrown sample contains many colloidal nanorods that have grown free of the restrictions of heterogeneous nucleation. This hypothesis is supported by an increase in

the FWHM of the NBE peak from 14.99 to 16.06 nm for Original and Regrowth, respectively; likely due to additional contribution from colloidal nanorods to NBE peak.

It can be concluded from the results that a two-step growth process should not be implemented due to the appearance of colloidal nanorods in the array and the negative affect the 2nd cycle had on both the aspect ratio and the optical properties. However, the doubling of growth solution from 250 to 500 ml did at least present the 47 % increase in surface area allowing up to four 500 mm^2 substrates to be floated.

7.5. Seed layer experiments

The following experiments assessed the effect of ZnO seed layer composition on the morphology of the nanowires, by investigating the methods employed for seed layer production (explained in chapter 3) and the effect that seed layer thickness and roughness have on the resulting nanowire array. Fig. 7.15. shows two glass substrates covered in ZnO nanowires after floating at 90 °C for 6 hours with identical variables other than a) was grown from a PVD coated substrate and b) from a spin coated one. The difference in uniformity is quite significant, though it should be noted that the spin coated substrate represents one of the worse examples obtained before significant time was invested to refine the process by exploitation of substrate wettability. Contact angles were measured for multiple zinc acetate carrier solvents, with typically the lowest angle solvent being selected for use, which in as in Fig. 7.16. was often ethanol. This section will provide the results and discussion only, see chapter 3 for procedures.

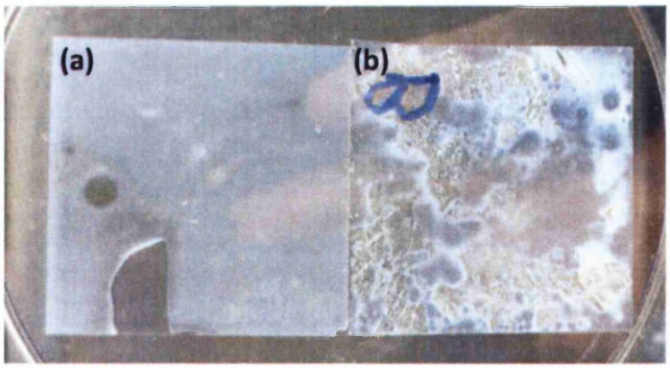

Figure 7.15. Photograph showing the difference in uniformity of nanowire growth across the substrate when using a) a PVD seed layer and b) a spin coated seed layer. The lack of growth on the bottom left of a) is due to attaching the substrate to the platen to hold the samples upside down in the PVD system. *[90°C for 9.5hrs in 500ml 25mM 1:1 sol. – 15min stir – Glass coverslip with a) 37nm ZnO PVD at 230°C and b) 2x Zinc Acetate spin coating cycles]*

7.5.1. Seed layer method

Fig. 7.16 shows high magnification SEM images of ZnO seed layers on silicon (111) substrates created via the spin coating and PVD procedures explained in section 3.4. The mean ferret diameter of the seed layers ZnO grains were 14 ± 3 nm and 12 ± 1 nm for spin and PVD coated substrates respectively; a significant difference. Note that the SEM images for the spin coated substrates were obtained from the centre of the sample to negate the crowning effect apparent in all spin coated samples regardless of solution viscosity, as calculated by Emslie et al. [40]. In chapter 3 it was explained that the zinc acetate solution spin coated onto the substrate requires an anneal at 360 °C to fully thermally decompose to form ZnO [41]. It is this thermal annealing step to thermally decompose zinc acetate that is the likely cause of such differences in grain size between spin coated and PVD coated substrates as PVD seed layers, which were deposited at room temperature. This is extremely important as it has been reported by Kenanakis et al. [42] that seed layer grain size has a direct effect on ZnO nanowire morphology, were they observe that nanowire width increases with increasing seed layer grain size.

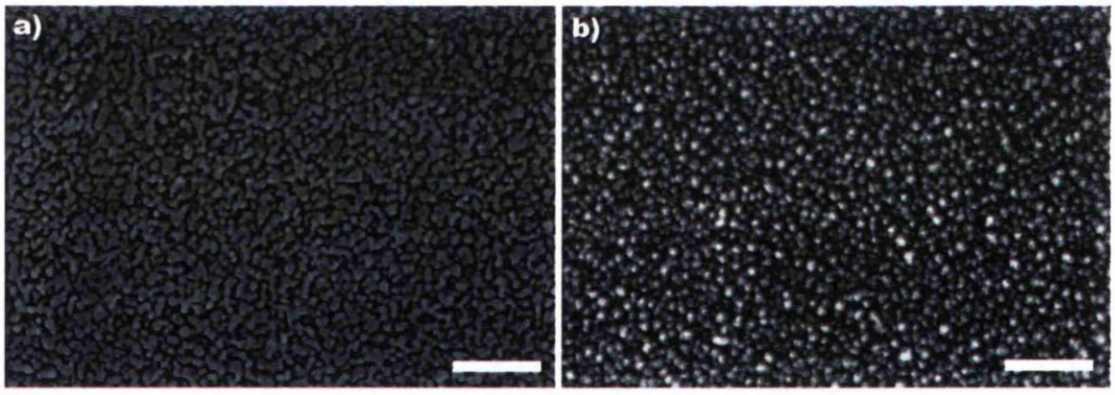

Figure 7.16. High magnification SEM images of ZnO seed layers created using a) the spin coating method and b) the PVD method. Scale bars are 100nm. Notice the sintering in a) due to annealing substrates at 360°C.

The difference in seed layer ZnO particle size was observed to have a significant effect on determining the outcome of nanowire morphology, generally nanowire arrays grown using spin coated samples were always of higher aspect ratio and more densely populated (for example Fig. 7.3d. compared to Fig. 7.10i.). Although it may appear that ZnO nanowires grown from spin coated seed layers would be more desirable due to their higher aspect ratio, their uniformity and reproducibility is questionable and

fluctuations in nanowire array density were often seen, see Fig. 7.17. This is likely due to non uniform thickness of the seed layer (as shown by Fig. 7.15b), as it has been shown by Wan-yu et al. [43] that seed layer grain size is affected by seed layer thickness and by Kenanakis et al. [42] that grain size determines nanowire width and therefore density/alignment. So it has been decided to use PVD coating for all future experiments, yielding more uniform and reproducible nanowire arrays.

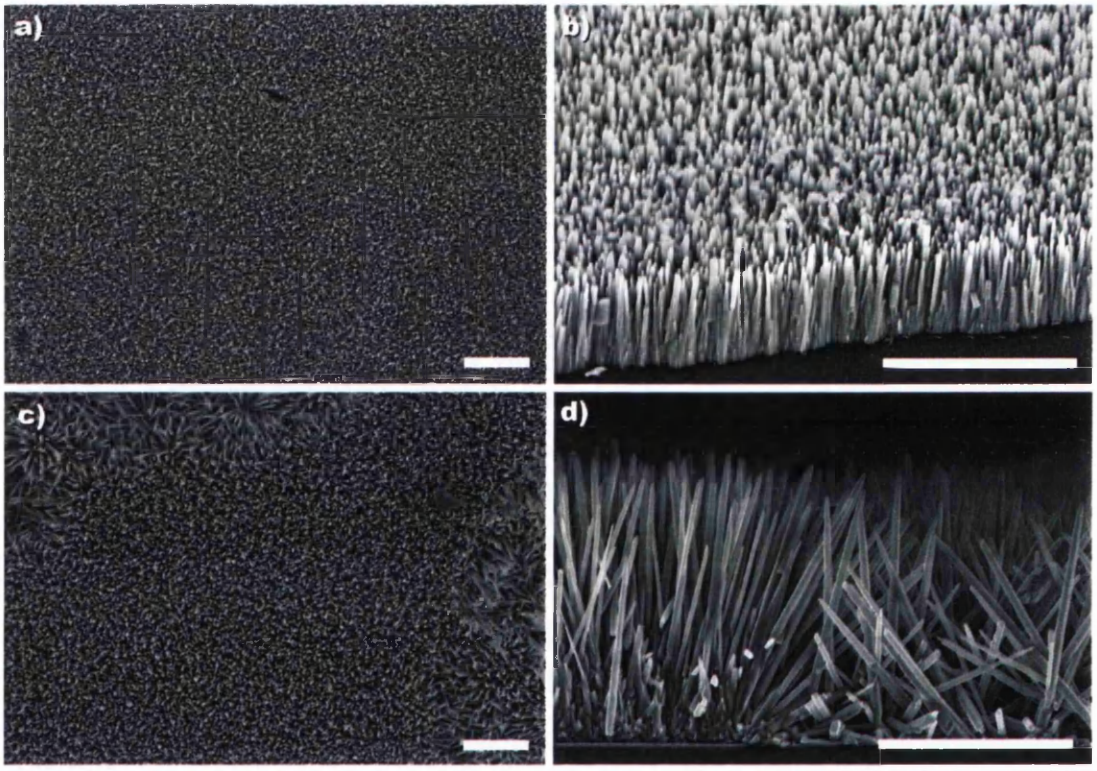

Figure 7.17. SEM images showing the differences in nanowire density across the array between a,b) PVD and c,d) spin coated seed layers. It was often observed that spin coated seed layer produced non-uniform distribution of nanowires across the substrate, however PVD always yielded evenly distributed nanowire density; apart from certain phenomenom such as shown in Fig. 7.17. Images a and c) are taken top down, b) at 45 degrees and d) in cross-section; notice the decrease in nanowire density from left to right. Scale bars are 3µm. *[90°C for 9hrs in 500ml 25mM 1:1 sol. – 35min stir – Glass coverslip with 3x Zinc Acetate spin coating cycles]*

From here on PVD coated substrates will be exclusively used due to the uniform growth they yield, that allows a single 24 x 24 mm^2 glass cover slip to be fractured into 9 equally sized substrates with identical morphology, This is especially important for the biology in chapter 8 as every experiment needs to be conducted (as a minimum) in triplicate to guarantee statistically significant data. Now that PVD was to be used substantial effort was invested into increasing the aspect ratio of ZnO nanowires grown on PVD coated substrates. Due to the size of a U-2 OS cell compared to a single

nanowire it was assumed that nanowires of higher aspect ratio could improve observation of cell-nanowire interaction for cell behavior analysis. Since Maffeis et al. [1] (a colleague) had already extensively profiled the PVD procedure and determined that the optimum gas flow rates for oxygen and argon were 5 and 45 sccm, respectively, to yield a chamber pressure of $\leq 3 \times 10^{-3}$ Torr. It was therefore deemed unnecessary to further investigate the gas ratio as this had already been extensively investigated in the literature, were it was shown that the addition of oxygen to the chamber improves c-axis orientation of the deposited thin film [44].

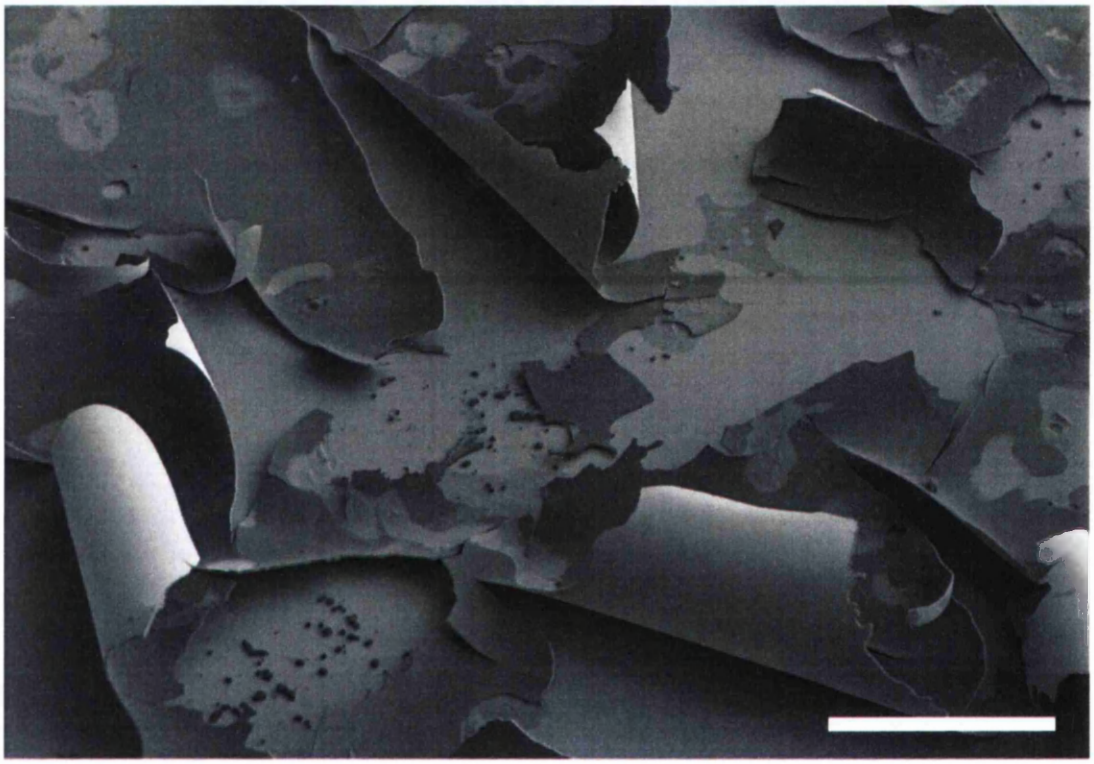

Figure 7.18. SEM image of nanowires post cell fixation after 2 days cell culture, showing nanowires detaching from glass coverslip, where nanowires were grown from spin coated seed layer. Scale bar is 200 µm. *[90°C for 3hrs in 500ml 25mM 1:1 sol. - 35min stir – Glass coverslip w/ 2x Zinc Acetate spin coating cycles]*

There are more fundamental problems in using spin coated seed layers to fabricate ZnO nanowire arrays, than irregular density and poor alignment. Fig. 7.18. shows ZnO nanowire arrays peeling from the substrate post cell fixation. After nanowire growth this sample has been washed in ethanol, seeded with 2.5×10^5 cells/ml, media added, incubated at 37 °C at 5 % CO_2 for 48 hours then washed in pre-warmed PBS, fixed by immersion in 3 % gluteraldehyde in sodium cocodylate buffer and dried in ethanol for SEM analysis. Fig. 7.18. shows that U-2 OS cells are present and firmly

adhered on both the nanowires and the glass cover slip; therefore the peeling happened prior to cell seeding, likely during the cleaning of the sample in ethanol. The effect of solution immersion on ZnO nanowires is covered more extensively in chapter 8, but has been discussed here to further support the decision to discontinue fabrication using spin coated seed layers.

7.5.2. Seed layer thickness

There is an unusual phenomenon that occurs when the substrate is held by a stainless steel washer and screw on the PVD substrate holder, where nanowires grown very near to the area where there is no seed layer always result in the production of much denser and more well aligned nanowires, see Fig. 7.19. Because the witnessed phenomenon could be explained by a change in seed layer thickness and EDX was used to confirm no elemental change due to the steel washer, then the relationship between PVD seed layer thickness and nanowire morphology was investigated.

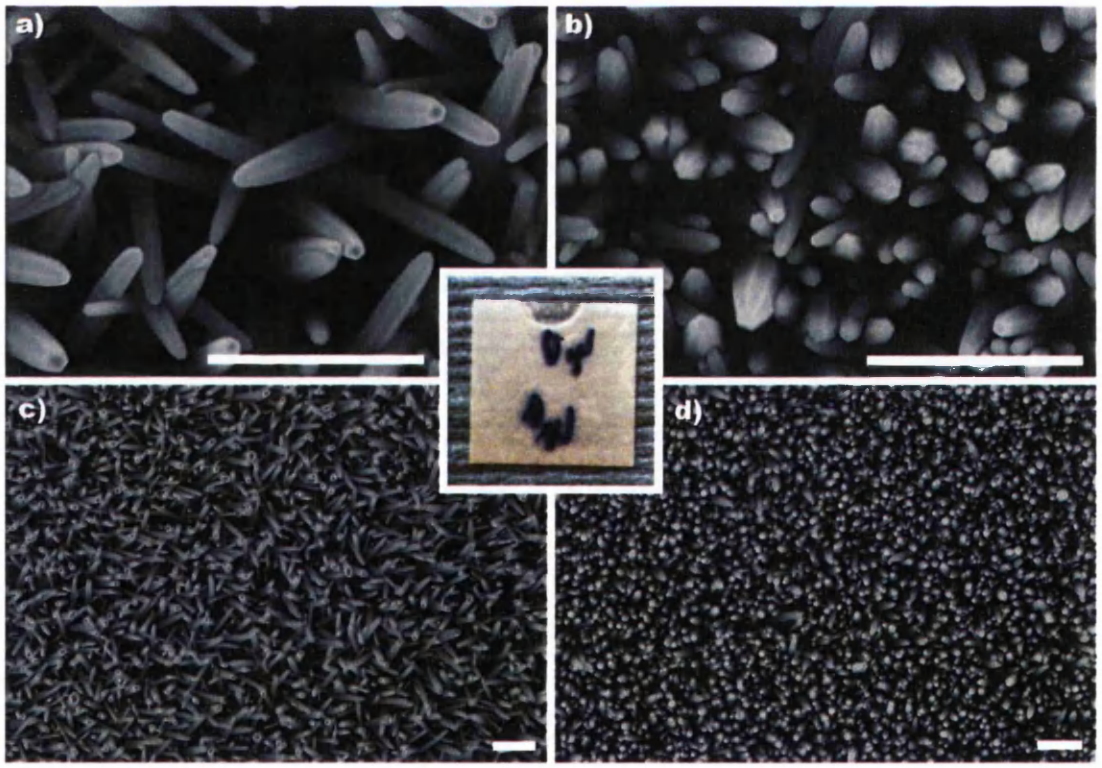

Figure 7.19. SEM images showing in increase in nanowire density at a, c) the edge of the sample near the clip compared to b, d) the centre of the sample. Inset shows a 24 x 24 mm glass cover slip post growth with clip mark clearly visible, note that the labels '40' are on the underside of the glass substrate. Scale bars are 1 µm. *[90°C for 9hrs in 500ml 25mM 1:1 sol. – 35min stir (2min hot) – Glass coverslip with 40nm ZnO PVD]*

Fig. 7.20. shows the effect of seed layer thickness on the morphology of the nanowires, with the thinnest 10 nm seed layer producing much less well aligned but longer nanowires while the thickest 50 nm seed layer produces much shorter and wider nanowires. Fig. 7.21 further expands on Fig. 7.20 and more clearly shows the relationship between thickness and morphology. This finding is in good agreement with previously discussed literature that showed the correlation between seed layer grain size and nanowire morphology. It can therefore be assumed that greater thicknesses allows for agglomeration of ZnO seed layer particles changing the grain size and roughness of the seed layer. The agreement between aspect ratio and nanowire alignment seen in Fig. 7.21b is significant and is likely due to the 72 % increase in nanowire width from 113 ± 21 nm for 10 nm to 194 ± 37 nm for 50 nm, and thus improving the alignment by reducing angular spread distribution by 63%. It can be assumed from these preliminary experiments that nanowire width and alignment are in an inversely proportional 1:1 relationship whereby if nanowire width is increased then divergence decreases and vice versa; this is similar to results reported in the literature [31].

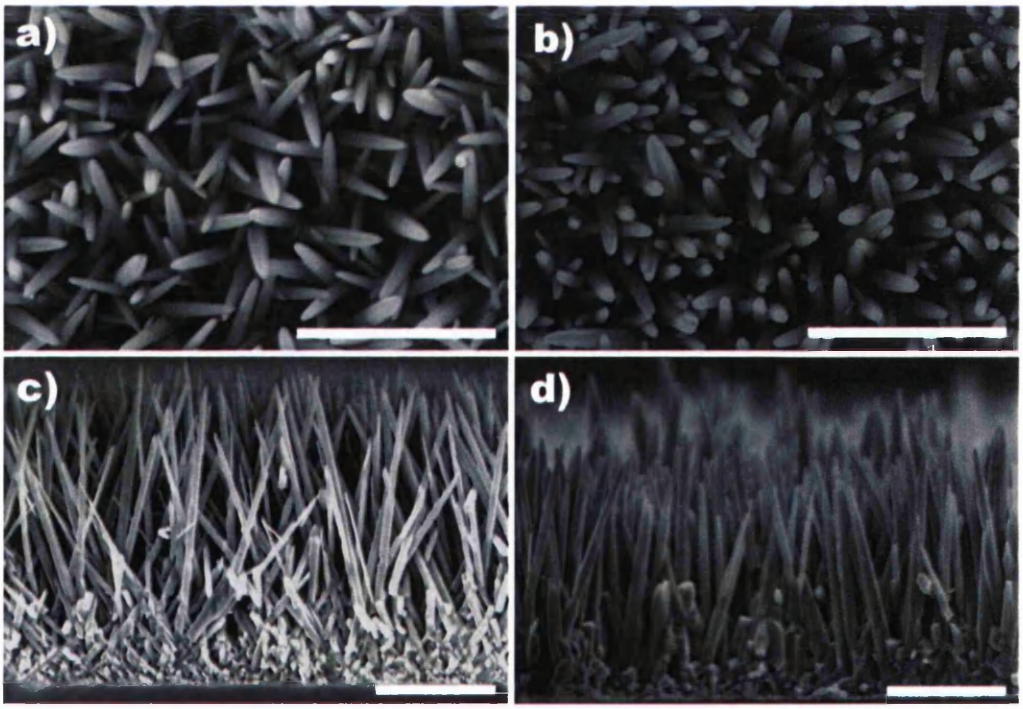

Figure 7.20. SEM images of ZnO nanowires grown on a) 10nm and b) 50nm PVD coated ZnO seed layers, where c) and d) are cross-sections for 10nm and 50nm thicknesses respectively. All scale bars are 2µm. *[90°C for 9hrs in 500ml 25mM 1:1 sol. – 35min stir (2min hot) – Glass coverslip with ZnO PVD]*

Ji et al. [33] report that the morphology of ZnO nanowires strongly depends on the thickness of their RF magnetron sputtered ZnO seed layers. They observed an increase in nanowire diameter from 50 to 70 nm as well as a decrease in density from 110 to 100 μm^{-2} while the seed layer thickness is varied from 20 to 240 nm. Similar to the results observed in Fig. 7.21. Xu et al. [45] suggest that larger seed layer grains would have a higher super-saturation and a higher initial growth rate, giving them a greater likelihood of developing into nanowires, therefore directly controlling final nanowire array density. Their hypothesis is supported by work by Lee et al. [46] who report that vertical alignment appears most prominent on thicker seed layers due to the increased density. This literature ties in well to work by Kenanakis et al. [42] who observe that seed layer grain size increases with increasing film thickness; likely due to the additional time atoms have to coalesce. Therefore it could be rashly concluded that thicker seed layers lead to better alignment due to a grain size controlling initial nanowire morphology mechanism. It is therefore critical to maintain a set seed layer thickness for all future experiments, how thick shall be discussed below.

The initial brief of this work was to create a force sensor to study cell-substrata interactions, since the mechanism required bending on the nanowires it was initially assumed that each nanowire would need to be well aligned within the array with a similar angle with respect to the substrate. Ideally this would mean that all nanowires were aligned 90° to the substrate, or perpendicular to it. This 'ideal' nanowire array is unlikely to be produced but even fabricating an array with an angular spread distribution of say 10 ° (i.e. all nanowires are aligned between 85 - 95° with respect to the substrate) would be more beneficial for monitoring of cell-substrate interaction. To determine the angular spread distribution for each sample alignment data was acquired from 90 measurements taken from cross sectional SEM images of 3 different areas; see Appendix V for more details. As the distribution of angles was not always normally distributed but often slightly bimodal, error bars have not been used in the histogram; Fig. 7.22. The histogram shows that the alignment drastically improves with increasing seed layer thickness, as data for substrates deposited with 50 nm thick seed layers show that 54 % of all measured nanowires have an angular spread of ≤5 degrees. Meaning that just over half of the nanowires in the array are aligned between 85 - 95° with respect to the substrate. Fig. 7.22b shows that for example any nanowire grown from a seed layer of thickness 10 nm may on average diverge from being orientated perpendicular to the substrate by ±12°. That is to say that the nanowires in the array

grown using 10 nm seed layer are on average aligned between 78 - 102° with respect to the substrate.

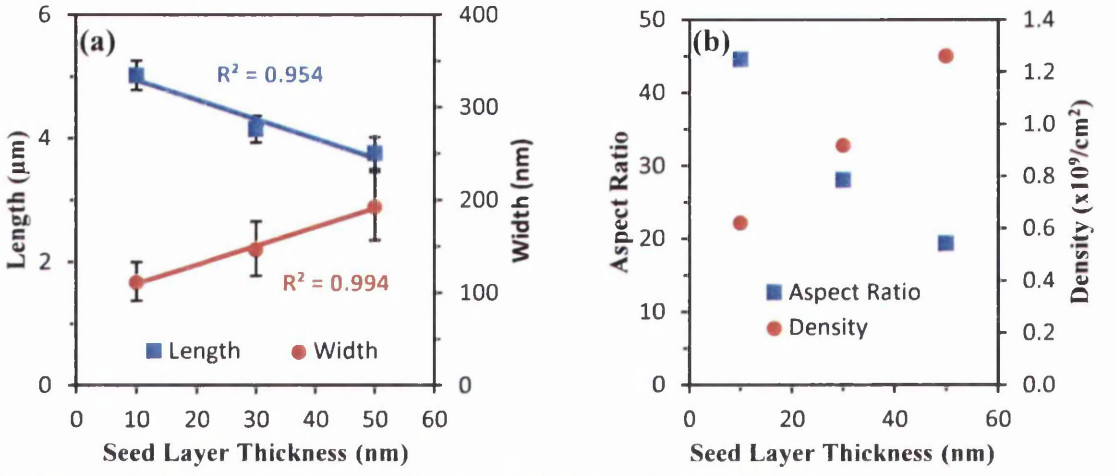

Figure 7.21. Graphs showing the effect of seed layer thickness on nanowire a) length and width, b) aspect ratio and the density of the nanowires. Data taken from 90 measurements for each thickness across 3 different areas and error bars represent ±SD of the 3 areas.

It would be incorrect to assume that seed layers with a thickness of 50 nm should be employed due to the improved alignment of the nanowires, as Fig. 7.21b. shows that although alignment is improved this is obtained at the cost of a change in array density. This increased density observed for 50 nm samples could be detrimental to quantification of mechanical properties with atomic force microscopy as well as force measurement with cells as there would likely be insufficient space for the nanowires to bend enough to produce a significant change in strain. Although without testing this is merely speculation. Fig. 7.22b. shows the photoluminescence spectra of the three seed layer thicknesses, showing the DLE band increases significantly with increasing seed layer thickness. Fig. 7.22c compares surface area to volume ratio to photoluminescence NBE to DLE peak ratio, where it can been seen that 10 nm yields the most ideal optical properties, likely due to the nanowires increased surface area compared to nanowires grown on other seed layer thicknesses. However, given the broad distribution of angles observed for nanowires grown on 10 nm thick seed layers then this thickness is not ideal to be taken forward in this work. Given that nanowires grown on 30 nm thick seed layers yield poor PL peak ratio but better angular spread distribution then the most ideal seed layer thickness would be between the two values. Therefore, a seed layer thickness of 20 nm shall be adopted from this point onwards.

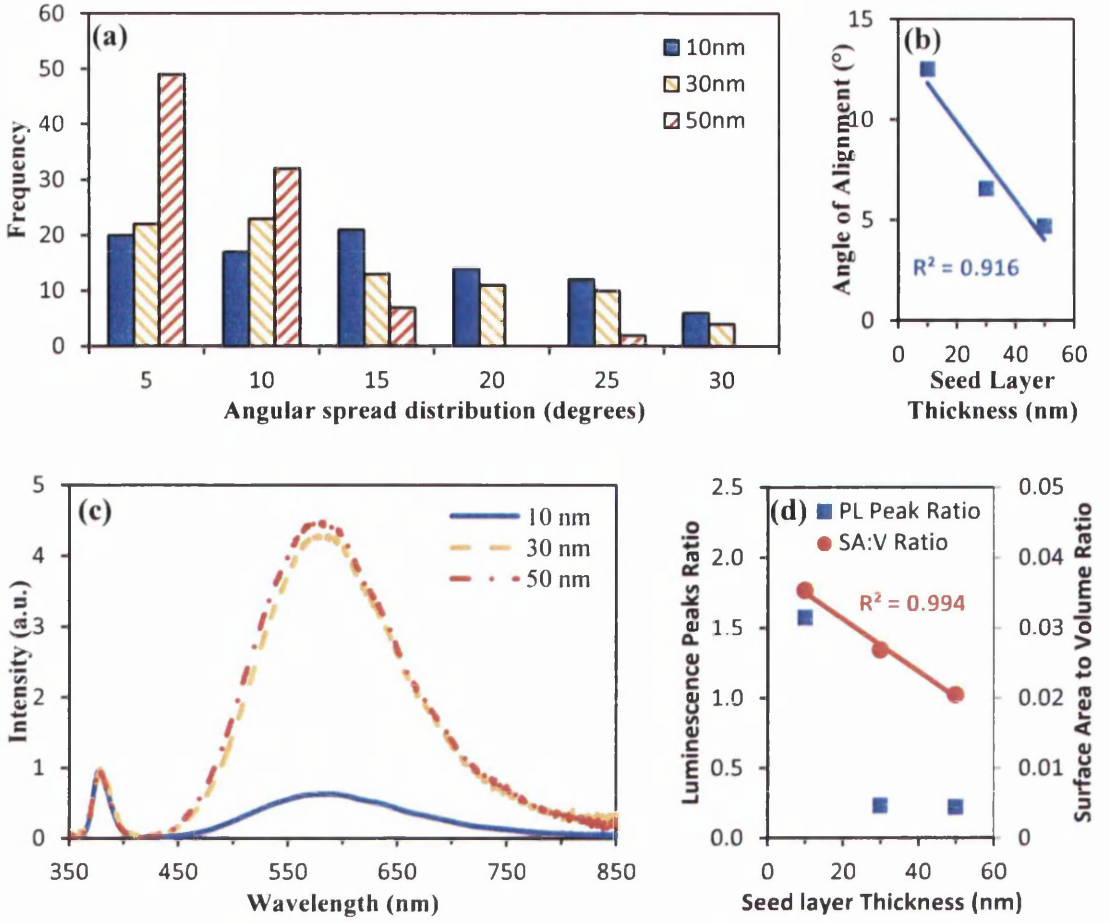

Figure 7.22. (a) Shows a histogram explaining the distribution of nanowire alignment, where values represent absolute angles of divergence from alignment of a nanowires c-axis perpendicular to the substrate, see Appendix V for more details. (b) shows change of angular spread / alignment with change in seed layer thickness. (c) Shows Photoluminescence graph showing the effect of seed layer thickness on the optical quality of the nanowires. 325nm HeCd excitation source used and results are mean of 3 acquisitions from 3 different areas. Data is normalized to the near band edge. (d) compares PL peak ratio to the Surface Area to Volume Ratio.

7.5.3. Annealing the seed layer

It has just been shown that the thickness of the deposited ZnO seed layer affects the morphology of nanowires, the following sub-sections explore the mechanisms behind the previously observed relationships. It is well established that when heat is applied to thin films the particles sinter leading to an increase in grain size [47], and for ZnO this is reported to happen between 600 – 1000 °C [45,46]. Being able to adjust the seed layer grain size is important as it has been reported that grain size directly effects the width of the nanowires [50]. Fig. 7.23. shows high magnification SEM images of a 20 nm PVD deposited seed layer before and after annealing at 500 °C in a tube furnace evacuated to 30 mbar with 200 sccm Argon flow for 1 hour. The SEM images were

obtained using a low accelerating voltage to minimise charging artefacts and beam induced heating that could lead to localised sintering of the seed particles. An image analysis program, Image J [51] was used to obtain the mean seed layer particle Feret diameters using a greyscale watershed algorithm freely available online [52]. It should be noted that the purpose of this set of experiments was to minimise / stop the occurrences of delamination of the seed layer and nanowires during tissue culture, as shown in Fig. 7.18. However, a change in seed layer grain size was observed even though samples were annealed at only 500 °C (the softening point of glass) so this change in grain size was investigated further.

It can be seen that the seed particles appear to have agglomerated during the process, with Fig. 7.24a showing that the seed particles mean ferret diameter has increased by 31 % from 11 ± 2 to 14 ± 2 nm. The graph also shows that the increased grain size has led to similar increase of 34 % from 141 ± 33 to 188 ± 29 nm for nanowire width after a 90 °C for 9 hours in 500 ml 25 mM 1:1 solution growth. This result is similar to that reported by Song et al. [50] who suggested that grain size was a template that determined nanowire width; this interpretation would explain the relationship between nanowire width and a seed layer thickness witnessed in this work. It should be noted that although there is a width change between the annealed and non-annealed seed layers the amount of material produced is very similar and must therefore be determined by the the concentration and precursor ratios of the solution; see Sub-section 7.6.2. This can be shown by comparing the annealed and non-annealed samples which have aspect ratios of 24 and 34 and densities of 6.3 x10^8 cm^2 and 9.3 x10^8 cm^2 respectively. However given this completely different morphology it would appear that the inverse relationship between density and nanowire width yields similar total sample (22 x 22 mm) ZnO volumes of 0.44 mm^3 and 0.40 mm^3 for annealed and non-annealed. The total volume of ZnO across the substrate was approximated by determining the volume of a single nanowire and multiplying the result by the total number of nanowires derived from the substrate area and nanowire array density.

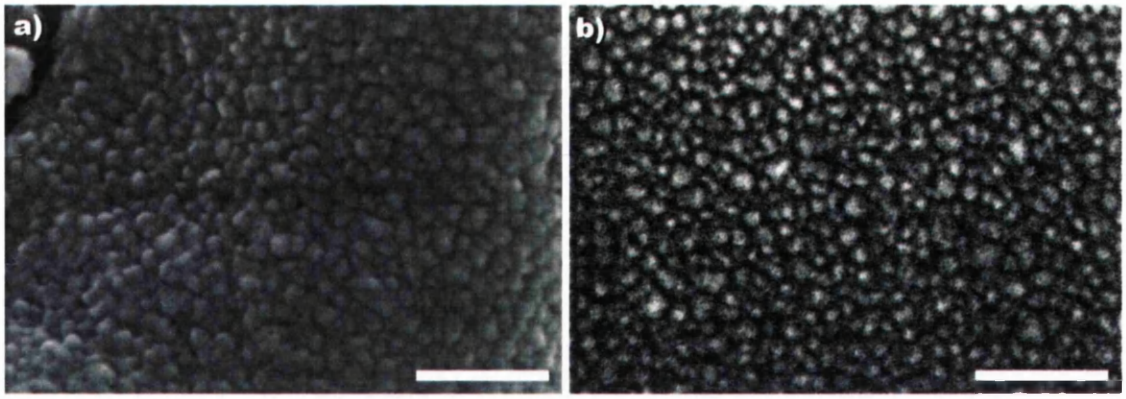

Figure 7.23. High magnification SEM images of PVD deposited ZnO seed layers, where a) is pre anneal and b) post anneal. Scale bars are 100nm. Notice the sintering of the seed particles in b).

This experiment confirms that thickness is not the only mechanism to effect obtained nanowire morphology, and that the feret diameter of the ZnO seed particles plays an important role in determining nanowire diameter. Fig. 7.24c shows the photoluminesence spectra for the two substrates post growth, it can be seen that there is little difference in the spectra again supporting that the system is bulk sensitive. Therefore taloiring nanowire morphology using seed layer morphology is ideal, however it is unclear how reproducible this trend may be when using seed layer thickness to control seed layer morphology so further investigation in neccesary. It has been reported by Yamabi and Imai [8] that seed layer morphology can be affected by substrate roughness so this will be investigated next as sintering of the seed layer although it lead to improved alignment (via increase of nanowire width) the drastic increase in nanowire width and reduction in density could be detrimental to force sensor applications and therefore annealing of the seed layer prior to the start of chemical bath deposition will not be used in the final recipes.

Using the Thornton model (discussed in chapter 3) would suggest the films to be of porous nature with unorganized crystallites yielding rough surfaces [53], as seen in Fig. 7.23b. Kumar et al. [54] profiled the effect of substrate temperature on the grain size and orientation of ZnO thin films using RF magnetron sputtering. They observed an increase in grain size from 12 to 49 nm for 100 to 300 °C, respectively; with all samples XRD analysis showing preferential (0002) c-axis alignment of grains. This is likely due to insufficient energy (due to lack of substrate heating) for deposited atoms to coalesce before the next layer has been deposited so that any slight fluctuation in substrate morphology would be highly influential on the resulting seed layer. Fig. 7.24d. shows

an AFM scan of a typical seed layer used in this work (un-annealed), from this image the RMS roughness can be obtained and was found to be nearly 1 nm. This is in good agreement with work by Kenanakis et al. [42] who observe an RMS of 2 nm for a 30 nm thick ZnO seed layer. The slight difference in roughness can be attributed to subtly differences in PVD method between the two works; e.g. oxygen / argon ratio etc... Roughness will be discussed further in the next sub-section.

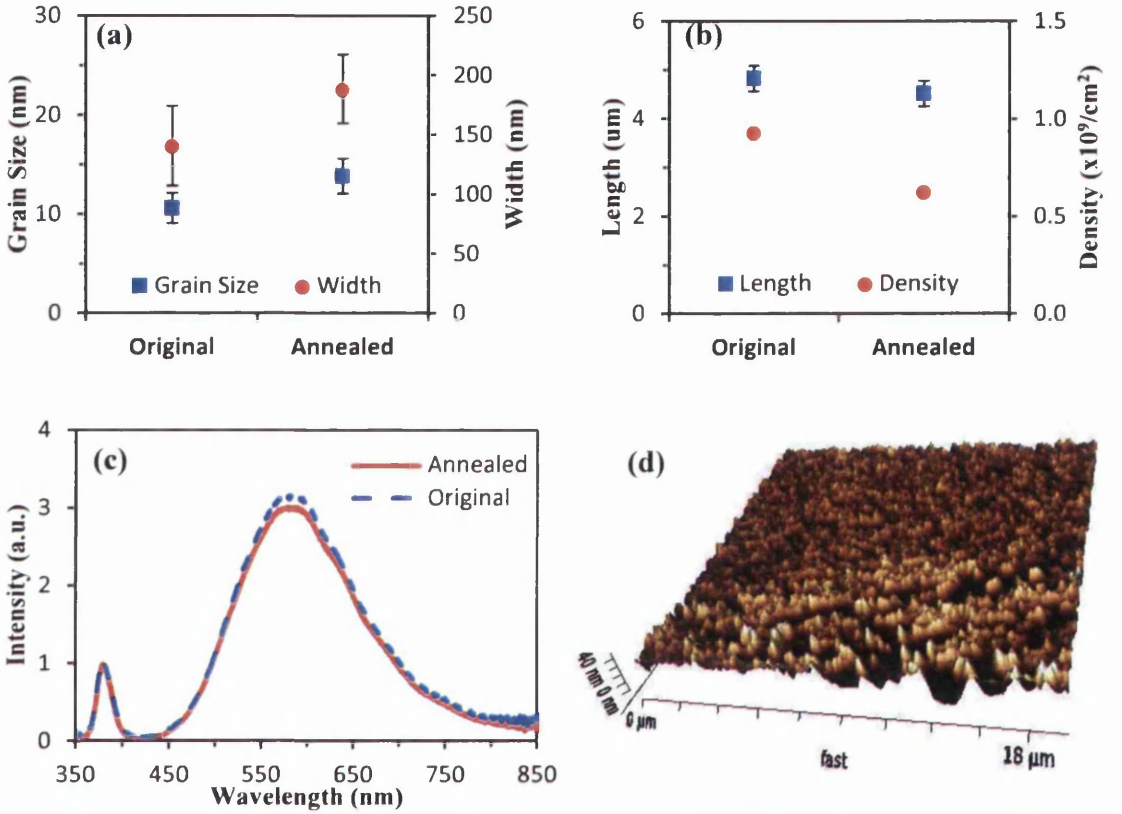

Figure 7.24. Graphs show effect of seed layer annealing on a) seed layer grain size and nanowire width and b) nanowire length and density, for annealed and non-annealed seed layers. For a) grain size measurement where taken using a ImageJ water-shedding algorithm [52]. All error bars represent ±SD of results. For c) photoluminescence data is normalized to the near band edge. Image d) shows a 20 x 20 µm 3D AFM image of a 20 nm thick ZnO seed layer on Silicon *[90°C for 9hrs in 500ml 25mM 1:1 sol. – 35min stir (2min hot) – Glass coverslip with 20nm ZnO PVD either annealed or not]*

7.5.4. Substrate roughness and lattice mismatch/metal buffers

It has been reported in the literature that nanowires grown on different substrates result in variation of produced nanowire morphology (see section 7.1) due to differences in surface roughness of the substrates [8]. The substrates used in this set of experiments were silicon or silicon pre-coated with a 35 nm gold or nickel layer, glass was not used for these experiments to allow careful mounting of all substrates (4 x 4 mm Si(111)) so

that it was possible to mask selected substrates for metal deposition whilst depositing a ZnO seed layer on all substrates. Thus, all substrates used in a single experiment were deposited at the same time under identical conditions. This would simply have been impossible using the standard 22 x 22 mm glass coverslips, Silicon was selected due to the similar nanowire morphology to glass observed in Fig. 7.3.

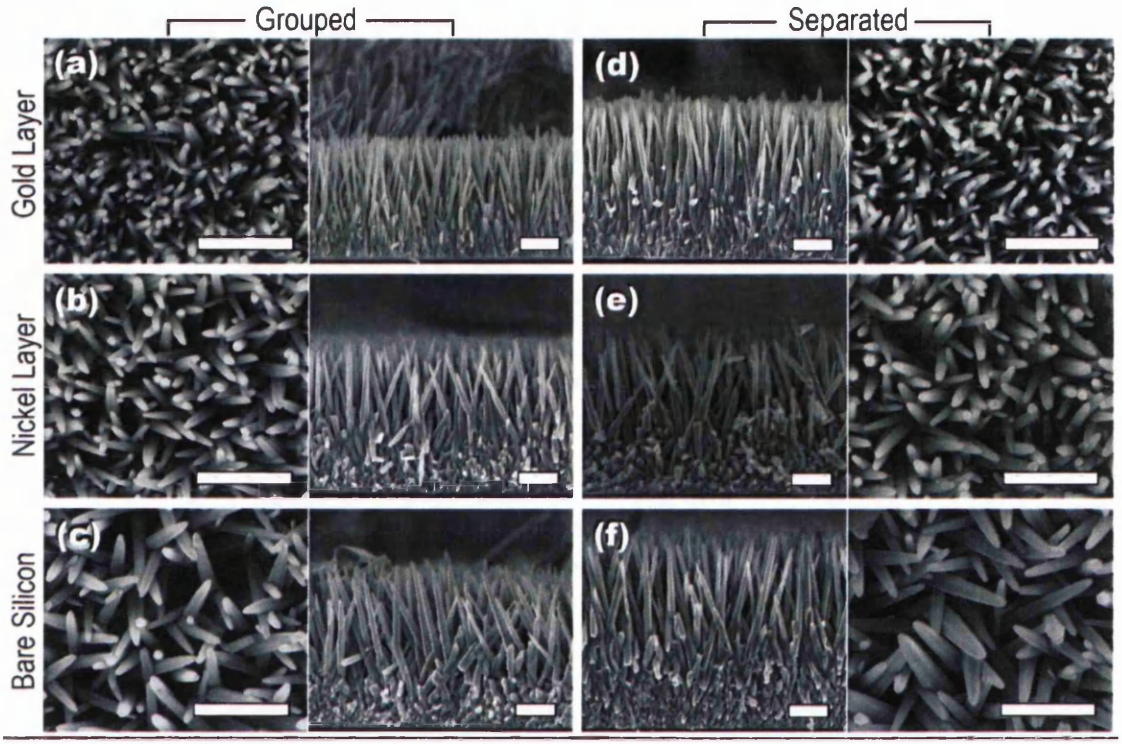

Figure. 7.25. FESEM images of ZnO nanowires acquired top down (a-c) and in cross section (d-f), comparing nanowires morphology as grown on (a,d) gold, (b,e) nickel and (c,f) silicon substrates. All scale bars are 1µm. *[90°C for 9hrs in 500ml 20mM 1:1 sol. – 5min stir (1min hot) – Silicon Substrate with either 35nm Au or 35nm Ni or just substrate and 20nm ZnO PVD]*

Fig. 7.25. shows the dramatic effect of introducing metal layers between the Silicon substrate and the PVD deposited ZnO seed layer on the density and morphology of the nanowires; again observing the inverse relationship of density to nanowire width. Nanowire length was seen to increase from 2.8 ±0.2 µm to 3.6 ±0.1 µm to 3.9 ± 0.2 µm, width increased from 82 ± 9 nm to 127 ± 17 nm to 149 ± 20 nm and density decreased from 129 to 16.3 to 9.4 $x10^8$ nanowires per cm^2 for gold to nickel to silicon respectively. These densities are in good agreement with those observed in literature, where Greene et al. [41], report a mean density of 5 $x10^{10}$ nanowires per cm^2 for nanowires 15 - 65 nm in width. Nanowires grown on metal layer coated substrates exhibit reduced crystal size compared to those grown without metals. There is a clear

preferential growth orientation along the (0001) crystallographic direction perpendicular to the substrates, however it can be seen that this alignment is most prominent on the gold substrate.

It has been reported in the literature that substrate roughness is a significant contributing factor to nanowire alignment [46]. As previously discussed, Kenankis et al. [42] have used Atomic Force Microscopy (AFM) to assess the importance of the seed layer roughness and mean grain size in obtaining well aligned ZnO nanowires. They report a correlation between seed layer particle size and RMS roughness with the obtained nanowire diameter after hydrothermal growth. Therefore the RMS roughness measurements were obtained using AFM to acquire 15 images in tapping mode from random areas on the substrate using a Silicon tip of 8 nm radius (RTESP, Bruker) with a calibrated spring constant and frequency of 55 mN/m and 292.7 kHz respectively; results are shown in Fig. 7.26b. It can be seen that the inclusion of metal layers under the seed layer drastically increases the RMS roughness of the seed layer, a trend supported by measuring the ferret diameters of seed grains from SEM.

Table 7.2: Summary of the morphology of the nanowires grown on Si, Ni coated Si and Au coated Si, either in the same beaker or in separate beakers. 90 nanowires for each surface were analysed. The total surface enhancement is defined as the total surface of the nanowires per square cm of substrate.

Growth Mode	Metal Coating	Length (μm)	Width (nm)	Density (NWs/cm^2)	Aspect Ratio	Total Surface Enhancement
Grouped	Au	2.8 ±0.2	82 ±9	1.3×10^{10}	34.2	88
	Ni	3.6 ±0.1	127 ±17	1.6×10^{9}	28.4	22
	None	3.9 ±0.2	149 ±20	9.4×10^{8}	25.9	16
Separated	Au	3.6 ±0.2	105 ±15	1.2×10^{10}	34.1	129
	Ni	3.7 ±0.2	147 ±25	1.2×10^{9}	25.3	20
	None	4.6 ±0.2	156 ±28	9.2×10^{8}	29.6	20

The increase in growth rate resulted in a width increase and a slight decrease in density. However, there remain significant differences between nanowires grown on the three surfaces, regardless of whether they were grown together or separately. The nanowires on Au are consistently smaller, thinner, with a higher aspect ratio and a density one order of magnitude higher than nanowires grown for the other two surfaces. These differences mean that the total area of the ZnO nanowires per substrate unit area (shown in the last column of Table 7.2) is much greater for the Au coated substrates, at 88 cm^2 per cm^2 of substrate for grouped growth (4.5 times that of Si), increasing to 129 for separate growth (6.5 times that of Si), because of the higher growth rate. This has

important implications to applications relying on high surface area, for example gas sensors. However in this work it is yet to be observed how significant surface area is to cell-nanowire interaction and this will be investigated further in chapter 8.

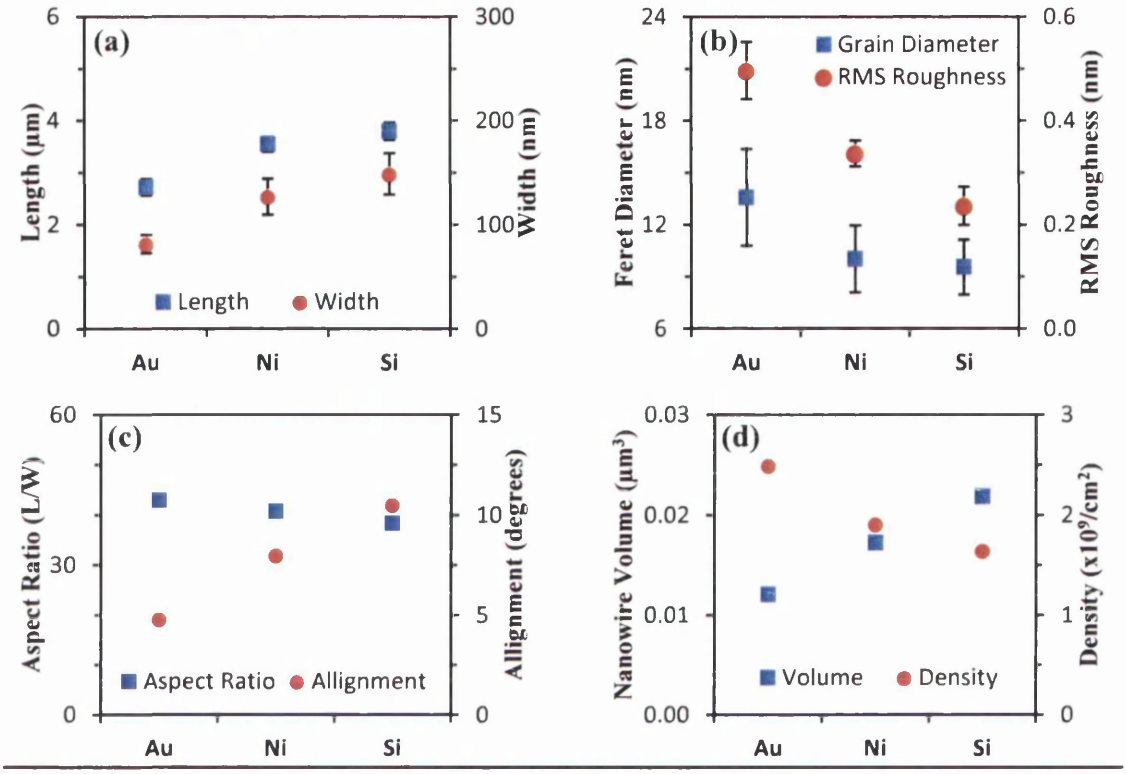

Figure 7.26. Graphs compare the effect of incorporating Au or Ni metal layers under the seed layer to Silicon control, where a) shows nanowire morphology, b) seed layer grain size and roughness, c) nanowire aspect ratio and alignment, and d) nanowire volume and array density.

Fig 7.26d. shows that the density of nanowires follows the same trend as grain size, which is opposite to the trends observed in the previous heat treatment of seed layer experiments. However the density is still inversely proportional to the obtained nanowire width and therefore growth mechanisms are similar, suggesting that the annealed seed layer in Fig.7.23. although yielded a larger seed grain size may have been less rough than the non-annealed sample meaning that the observed trend is more strongly dependent on seed layer roughness than grain size. It should be noted that if the substrate were heated during seed layer deposition then according to modified Thornton model by Kluth et al. [55] sufficient energy would be given to the deposited atoms to allow them to coalesce before the next layer has been deposited yielding a smoother c-axis orientated thin ZnO film [56]. This happens as ZnO nanoparticles need to combine to reduce interfacial free energy as molecules at the surface are energetically less

favourable than those in the interior [57]. Therefore for this set of experiments it was decided not to try heating during deposition, nor anneal post deposition so that any slight morphology created by the metal layer would be highly influential on the morphology of the resulting seed layer.

The results suggest that seed layer roughness alters the density of nanowires, likely via the mean free path fourling system described previously. Yamabi and Imai have reported ZnO to have a lower affinity for Silicon [58] which may explain the differences seen in seed layer grain size on the metal substrates, as a higher affinity for metals would influence seed layer growth rate yielding the slightly larger grain sizes observed for gold coated substrates. However findings in the literature [42], [50] contradict this trend, but this could be due to differences in recipes. For example, the observed mean length and width for nanowires grown on Silicon in this set of experiments differs from those observed in Fig. 7.3. due to differing recipes; where temperature and substrate surface area are key differences. The nanowires shown in Fig. 7.26. are substantially longer at 3.9 ± 0.2 μm compared those shown in Fig. 7.3. at 3.4 ± 0.1 μm, this is likely due to the relationship of solution temperature on the crystal growth rate of (0001) direction; as temperature experiments shown in Fig. 7.5. yielded 3.4 ± 0.1 μm in good agreement with results observed in Fig. 7.26. The slight differences between these results and those from all previous sections with similar recipes is likely due to substrate surface area discrepancies, with substrates in this experiment having a 56 % larger surface area than Silicon substrates using in temperature experiments.

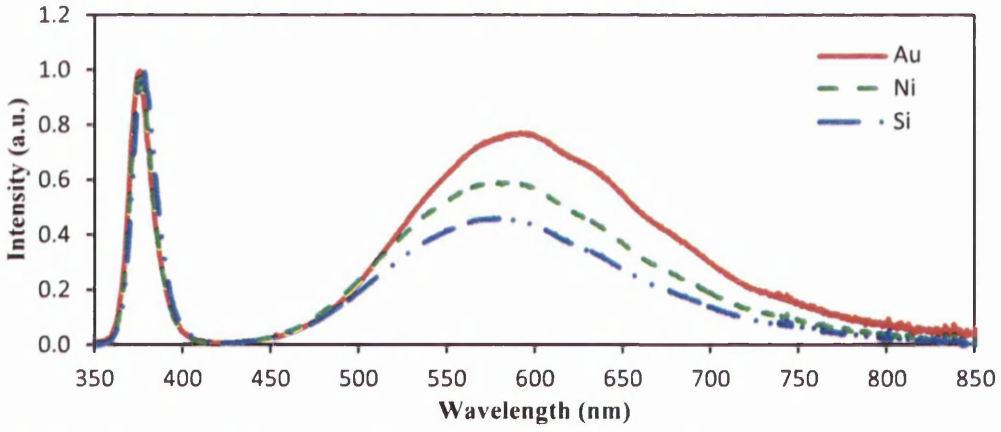

Figure 7.27. Photoluminescence of Zinc Oxide nanowires on substrates with different metal bilayers Au, Ni and Si control. 325nm HeCd excitation source was used and results are mean of 3 acquisitions from 3 different areas. All data is normalized to the near band edge.

Fig. 7.27. shows the photoluminescence spectra normalized to the near band edge emission of the nanowires seen in Fig.7.25. where introduction of a metal layer under the seed layer can be shown to negatively affect the optical properties of the nanowire with additional contribution from DLE within the band gap. Samples were annealed for 1 hour at 100 °C to remove surface state contribution, as shown by Shim et al. [59]. Interestingly while both silicon and nickel have defect bands that are within the broad visible light band centred at around 550 nm, it appears that gold is centered at around 560 nm with a more intense peak at 610 nm shifting the centre of its defect band. Work by Studenikin et al. [60] indicates that the green centered emission originates from oxygen vacancies within the crystal lattice, therefore it could be postulated that the metal cations interfere with the lattice creating interstitials and substitutionals (O_{Ni} and Ni_S), this being predominantly associated with nickel and its strong affinity for ZnO [61]. It has been shown in the literature that metal cations can interfere with hydrothermal ZnO crystal growth due to local reduction of OH^- precursor ions [62]. This variable will be examined further as it has been shown by Greene et al. [63] that scaling up hydrothermal recipes from test substrate size to whole wafers can have significant effects on nanowire morphology.

In conclusion it has been shown that a change in the morphology of the seed later likely caused by preferential nucleation during deposition and surface roughness governing the initial growth parameters of the nanostructures; and that it is the subtle differences between the grain size of the seed layers that lead marked changes in nanowire array density that lead to changes in length and alignment. While it is clear that metals maybe used to tailor the morphology of the nanowires there were detrimental consequences to the optical quality of the crystals with substantial changes in NBE / DLE intensity ratio with the addition of metals. However, it can still be seen that the volume of ZnO material per cm^2 grown on each substrate is independent of seed layer roughness with consistent volumes per cm^2 of 3.02E+7 μm^3, 3.30E+7 μm^3 and 3.60E+7 μm3 for Au, Ni and Si respectively; therefore the effect of solution concentration ideally needs to be investigated. Thus, 20 nm thick PVD seed layers with no underlying layer will be used exclusively from here on.

It should be noted that the PL spectra in Fig. 7.27. cannot be fairly compared to those in Fig. 7.24c. as different recipes were used in both sets of experiments. Though it is interesting to observe that one of the key differences, solution concentration (being 25 mM for Fig. 7.24c and 20 mM for Fig. 7.27) has such a profound effect on the

optical properties of the nanowires. Changes in solution concentration and precursor ratio will be discussed next.

7.6. Solution Experiments

In Fig. 7.2. an equimolar zinc nitrate and hexamine solution with a concentration of 2.5 mM and growth temperature of 95 °C were chosen after finding encouraging observations reported by Xu et al. [4]. It was quickly determined that the amount of ZnO nanowires produced was insufficient so the experiment was repeated using a solution concentration an order of magnitude higher; this became the norm as 25 mM yielded a much higher density of ZnO nanowires. Other than the solution volume in sub-section 7.4.1. a detailed investigation of the precursor solution has yet to be conducted, this section contains the most important set of experiments and findings that lead to the use of the 2 main recipes used and extensively characterised in the cell-nanowire interaction phase of the work next chapter. This section will cover the role of Hexamine, optimum solution concentration and precursor ratio, as well as smaller variables such as the effect of stirring and preheating the solution.

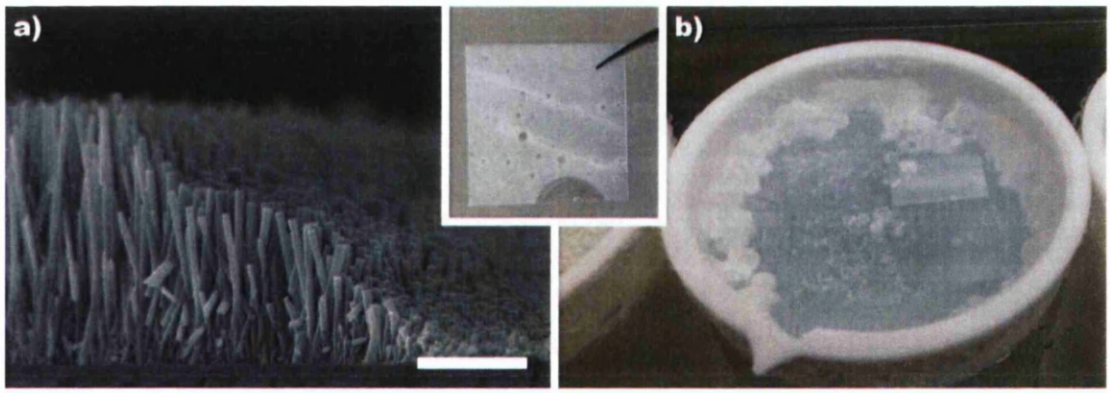

Figure 7.28. Shows the effect of not preheating the solution prior to adding the substrates, b) bubbles often form on the underside of the floated substrate, shown inset that caused regions of no growth. The cross-sectional SEM image a) shows that the bubbles appear to decrease in volume over time, Scale bar is 1µm. *[90°C for 9hrs in 500ml 25mM 1:1 sol. – 35min stir (2min hot) – Glass coverslip with 20nm ZnO PVD either annealed or not]*

Fig. 7.28a. is a cross-sectional SEM image showing the effect of bubbles that form underneath the substrate on the growth on nanowires in that region, where it can been seen that the bubble either shrinks or expands over time inhibiting the contained

seed layers interaction with the solution. The inset shows the substrate post growth with circular areas of limited nanowire growth clearly present. The photograph shows the formation of bubbles under the substrate. It was found early on in the work to optimize the hydrothermal growth method that if the water was not pre-warmed (i.e. used from RT) then two negative events often occurred, firstly the substrate being cooler than the surrounding water vapour provided the ideal surface and conditions for condensation, with this additional weight often leading to a floating failure rate of more than 80 %. Secondly bubbles covered in colloidal growth would often form within the growth solution nucleated on the PTFE beaker and as the solution warmed dislodge and float to surface producing a scum layer on the surface, as seen in Fig. 7.28b. It has been reported by Wang et al. [31] that the formation of this scum layer is due to the release of ammonia when the vapour pressure of the water bath is altered, such as in the instance of removing the lid during growth. Additionally any bubbles caught under the substrates would severely inhibit growth, destroying uniformity across the substrate. It should be noted that the two parallel lines seen running diagonally across the substrate are caused by the original technique of lowering substrates with a paperclip to support them. This however leads to alteration of seed layer thickness and subsequent changes in nanowire morphology; this was one of the earliest indications of the importance of seed layer thickness.

7.6.1. Precursor Concentration

The following set of experiments was conducted to obtain the most suitable precursor concentration to produce high aspect ratio, well aligned, mono-disperse ZnO nanowires of excellent crystal quality. The experiment explored the concentration range from 5 to 45 mM to confirm reports from the literature. Vayssieres et al. [30] suggests that by decreasing the precursor concentration by one order of magnitude the diameter of the nanowires shall also decrease by an order of magnitude, due to the critical diffusion of the monomers and subsequent limited growth. The original range of the experiment was from 5 to 50 mM, unfortunately the 50 mM sample dropped to the bottom of the beaker during growth making it unreliable for comparison to the other samples; so it was discarded. However, this comparison can be crudely made with 5 and 45 mM instead, where it can be seen in Table 7.3 that Vayssieres et al.'s order of magnitude change does not occur.

This could however be due to a difference in measurement, as in this work all width measurements are taken from the length's midpoint (as is often reported in the literature [64]) for consistency as all ZnO nanowires grown via the hydrothermal method are generally tapered and pyramid-like. It has been suggested by Wang et al. [15] that the formation of pyramid-like nanowires is due to the limited supply of growth units from Zinc Nitrate solutions of concentration lower than 25 mM. Table 7.3. also shows the average angular spread / alignment of the nanowires with respect to the substrate, where the value is the amount of divergence plus or minus from alignment perpendicular to the substrate. Therefore, nanowires grown at 5 mM solution concentration were aligned on average between 70.2 – 109.8° with respect to the substrate, whereas those grown at 45 mM were aligned on average between 84.7 – 95.3° with respect to the substrate. The largest improvement in angular spread distribution is from 15 to 25 mM, which is easily observable in Fig. 7.29. Fig. 7.29. compares cross-sectional SEM images for concentrations from 5 to 45 mM, where significant differences in morphology with changing precursor concentration can be observed. Other than the drastic change from 5 to 15 mM the length there after doesn't seem to alter much and only changes in density and substantial differences in width are observed with precursor concentration change.

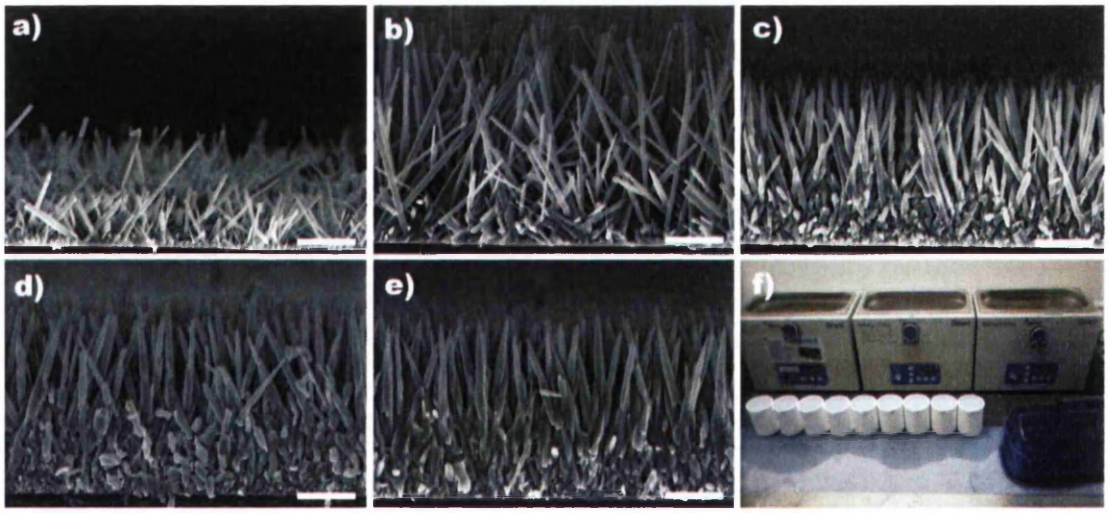

Figure 7.29. Shows cross-sectional SEM images depicting the effect of precursor concentration on nanowire morphology, where a) is 5 mM, b) 15 mM, c) 25 mM, d) 35 mM and e) 45 mM. Scale bars are all 1 µm. The photograph in f) shows the layout of the experiment. *[90°C for 9hrs in 250ml 5-45mM 1:1 sol. – 0min stir (1min hot) – Glass coverslip with 20nm ZnO PVD]*

Table 7.3: Effect of precursor solution on ZnO nanowire length, width, density and alignment.

Concentration (mM)	Length (μm)	Width (nm)	Density (NWs/cm^2)	Aspect Ratio	Alignment (°)
5	1.2 ±0.3	47 ±14	1.6 x10^9	25.5	19.8
15	3.5 ±0.4	81 ±20	2.1 x10^9	43.5	15.0
25	3.0 ±0.1	104 ±12	3.5 x10^9	28.4	8.4
35	3.4 ±0.1	124 ±28	3.6 x10^9	27.1	6.7
45	3.2 ±0.1	143 ±28	3.2 x10^9	22.4	5.3

It should be noted that although the precursor concentration changes significantly, the pH of the solution is unaffected, remaining at around 6.75 for all solutions at the start of the experiment. This is likely because (as discussed in chapter 3) HMTA is an OH^- producing buffer that maintains the pH of each solution after a critical concentration is exceeded (see the following sub-section 7.7.2). Govender et al. [34] found a similar starting pH of 6.81 and examined the kinetics of crystal growth with respect to the concentration of HMTA, reporting that solutions containing Ammonia and/or formaldehyde (both byproducts of thermal decomposition of HMTA) were supersaturated with respect to zinc hydroxide at pH 6.81. They go on to hypothesize that ZnO nanowire morphology may be affected during growth due to the influence of these counter-ions; either through weak electrostatic forces or more significant physi- or chemisorption behaviour. Where electro statistic forces are likely to result in specific adsorption of ions resulting in change in point zero charge or f-potential, etc... PL results will be paramount to understanding if solution concentration has forced substantial changes in growth kinetics such that surface adsorption is affected.

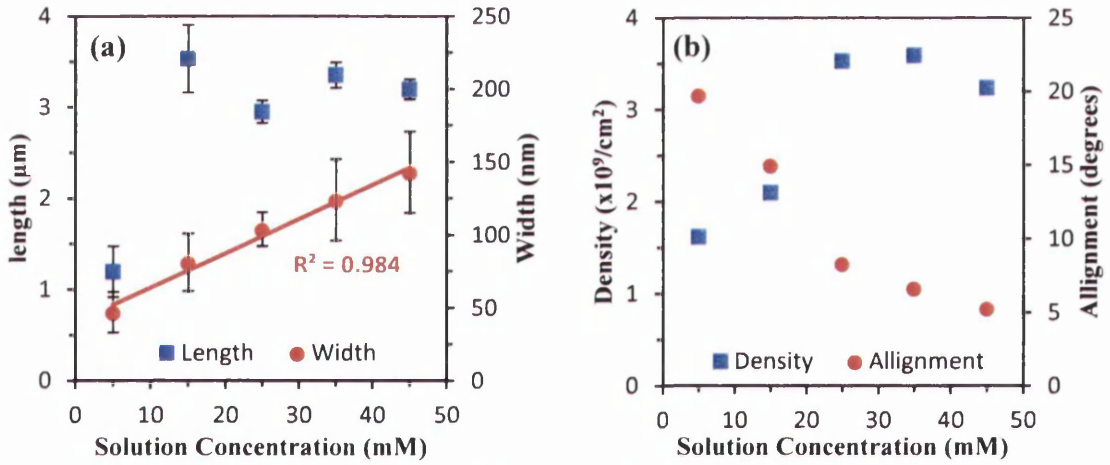

Figure 7.30. Graphs show effect of precursor concentration on a) length and width and b) aspect ratio and density of ZnO nanowires. For a) data was taken from 90 measurements for each concentration across 3 different areas and error bars represent ±SD of the 3 areas.

Fig. 7.30a. shows the significant change in ZnO nanowire morphology with increasing solution concentration, where the width of the nanowires increases linearly with increasing concentration in an almost perfect (R^2 = 0.984) linear relationship. This is in agreement with work by Shin et al. [65] who observe the diameter and length of their ZnO nanowires increase from 89 to 446 nm and from 1.3 to 3.7 μm, respectively, with increasing precursor concentration from 25 to 125 mM. It can be said that the result for 15 mM is questionable, given the large standard deviation of length and erratic alignment, but all substrates were PVD deposited at the same time so that the seed layers will be identical, and the solution was made up at the same time, and stirred for the same time for each beaker. For these reasons the observed 195 % increase in nanowire length from 5 to 15 mM and subsequent 17 % decrease from 15 to 25 mM is most likely due to the super saturation level of the solution. Where it can be assumed that the 5 mM solution is not sufficiently supersaturated and therefore the precipitation of the zinc hydroxide intermediate doesn't occur as readily as it does for the 15 mM solution. The 25 mM solution is already above this assumed supersaturation level and so the additional precursors instead evoke a higher zinc chemical potential (a larger shift towards the right of equation 3.7) and so more nucleation sites form on the substrate surface, increasing the density and slightly reducing the length.

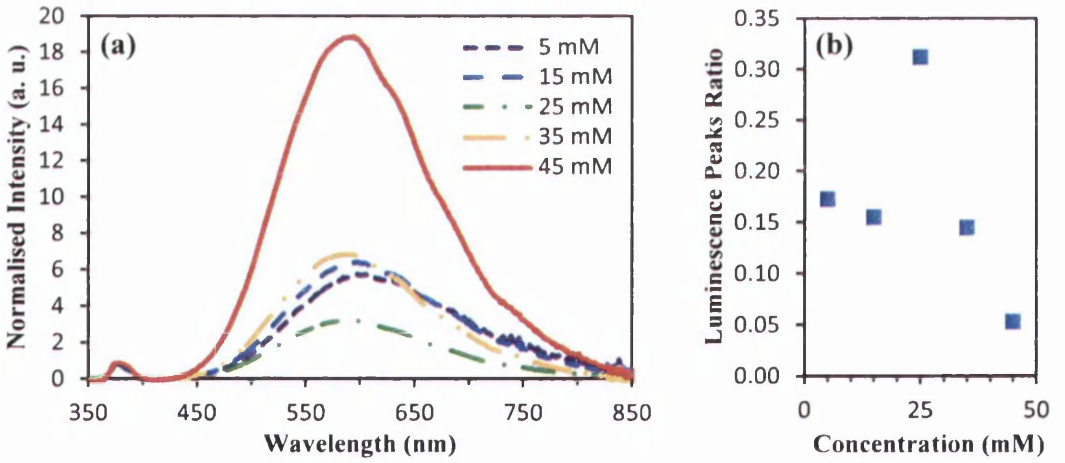

Figure 7.31. Graphs show effect of precursor concentration on a) the photoluminescence spectra for each sample, and b) the NBE/DLE peak ratio for each concentration. PL data is normalized to NBE.

Fig. 7.30b. shows the increase in density with increasing solution concentration, which plateaus above 30 mM and decreases thereafter. This trend is well established in the literature, where Peng et al. [66] has hypothesized that due to surface energy

minimization the ZnO crystallites that nucleate along the c-axis will aggregate together due to excess saturation of the zinc hydroxyl intermediate precipitate. While Pacholski et al. [67] say that the increase in crystal width with increasing solution concentration is undoubtedly an Ostwald ripening process, whereby dissolution of seed layer particulate increases with decreasing particle size leading to the growth of larger particles at the cost of the smaller ones. Jeong et al. [68] also report that Ostwald ripening as the mechanism behind the increase in nanowire width with increasing solution concentration, but only for concentrations greater than 50 mM. Xu et al. [69] observe a similar trend to this work, finding that density increases with increasing solution concentration but also has a tendency to plateau and decrease for concentrations >20 mM. Xu et al. hypothesise that the arrival of more ions to the substrate will not initiate new nuclei as the critical size required for a nucleus to grow into a crystal is less energetically favourable than attaching to an existing nanowire. This interpretation of the data would explain why after a critical solution concentration (25 mM) the other concentrations yield fairly uniform height. Additionally, although higher concentrations appear to not add additional length to the nanowire, and the density remains steady at higher precursor concentration levels the increase in nanowire width does indicate that more material is being produced. These findings show concentrations higher than 25 mM to be unfavourable for this work, where high aspect ratio nanowires are required to more easily observe cell-nanowire interaction.

Fig. 7.31. shows the change in optical quality with increasing solution concentration, where interestingly it can be seen that the DLE peak intensity decreases from 5 to 25 mM then increases again from 25 to 45 mM; giving 25 mM the most ideal NBE/DLE peak ratio. This trend has also been reported by Lee et al. [70] where precursor concentrations from 10 to 70 mM in increments of 10 were used to profile the effect of solution concentration on morphology and optical properties of ZnO nanowires. They found that both 10 and 70 mM yielded the highest DLE peak intensity in photoluminescence spectra, while 30 mM gave the lowest DLE peak intensity and high NBE/DLE peak ratio. Instead the precursor solution concentration can be seen to directly affect the density of defects within the crystal lattice. Recent work by Penn and Banfield [71] have found that particles that coalesce on substrate may do so not by a dissolution and regrowth mechanism (i.e. Ostwald ripening) but also by a mechanism called orientated attachment. Orientated attachment involves spontaneous self-organisation of adjacent nanoparticles such that a common crystallographic orientation

is shared. If interface between two planes is not perfectly aligned then screw and edge dislocations at the contact areas can arise leading to significant defects within the crystal lattice. Penn and Banfield suggest that orientated attachment is more energetically favourable as it reduces the overall energy by removing surface energy associated with dangling bonds. This mechanism could well explain the trend in Fig. 7.31. as a 25 mM precursor concentration has been shown in Fig. 7.30a. to yield the most mono-disperse and well aligned ZnO nanowires, as shown by the tiny standard deviation. However, without extensive investigation with XPS and XRD etc... it is extremely difficult to prove this mechanism is occurring in this work and therefore this is only speculation. Regardless, all future experiments unless otherwise stated shall use 25 mM as precursor solution concentration at a 1:1 equimolar ratio, next the ratio is explored.

7.6.2. Precursor ratio

The results from the concentration experiments yielded 25 mM as a concentration that gave the best balance between morphology and density, and the most ideal photoluminescence spectra. However since this was an equimolar value, and the following sections explore the effect of altering the ratio of $ZnNO_3$ to HMTA on the morphology on ZnO nanowires. First we shall explore the effect of HMTA concentration while $ZnNO_3$ is maintained at 25 mM for all data, as HMTA is often the main topic of conversation in the literature with its mechanism often hotly debated. It has been reported by Sugunan et al. [72] that the zinc hydroxide ($Zn(OH)_4$) intermediate (discussed in chapter 3) created during the intermediate stage of the growth process can lead to a differing of the growth rate of the different crystal facets; with growth of non-polar planes being inhibited by the chelating agent HMTA improving aspect ratio. Although this additional function for HMTA is commonly mentioned in the literature, it has been proposed by McPeak et al. [73] to be unlikely as they obtained similar morphology without the presence of HMTA, and used in situ attenuated total reflection Fourier transform infrared spectroscopy to determine that no HMTA is absorbed onto the surface of ZnO from solution.

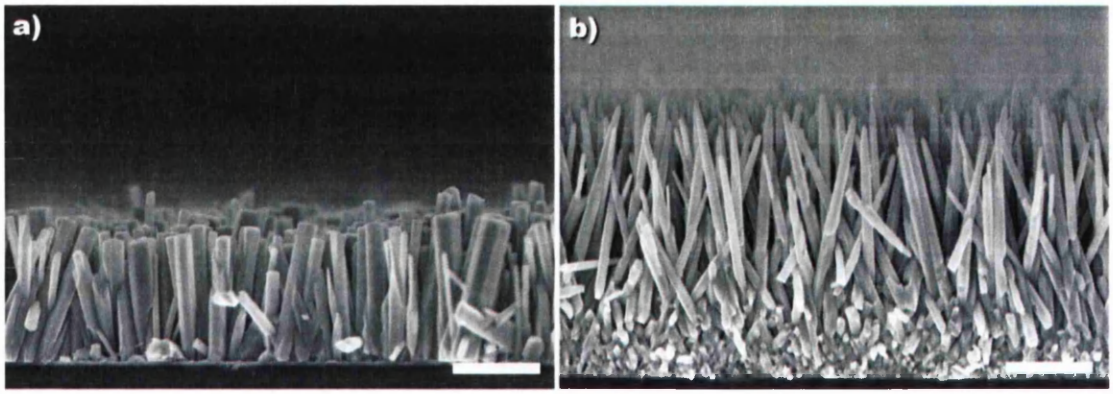

Figure 7.32. Cross-sectional SEM images comparing two different concentrations of HMTA when $ZnNO_3$ is held at 25 mM, where a) is the zinc nitrate to HMTA ratios of 5:1 (25 mM : 5 mM) and b) is the ratio 1:1. All scale bars are 1µm. Notice the difference in non-polar facet growth in hibition between the two images. *[90°C for 9hrs in 250ml sol. Where $ZnNO_3$ held at 25mM and HMTA varied between 5-45mM – 10min stir – Glass coverslip with 50nm ZnO PVD]*

Five 250 ml beakers were used to provide ample data to profile the effect of HMTA concentration on nanowire morphology by raising HMTA concentration from 5 to 45 mM in 10 mM increments while $ZnNO_3$ was held at 25 mM. Fig. 7.32. compares the typical 1:1 equimolar (listed as 5:5 for clarity in graphs) zinc nitrate to HMTA ratio to a 5:1 ratio of (25 : 5 mM), showing the drastic effect that HMTA has on inhibiting the growth of non-polar facets. Notice the improved aspect ratio as width is decreased by 45 % and length increased by 95 % from 25 : 5 mM (5:1) and 25 : 25 mM (5:5 or 1:1) precursor ratios, highlighting the importance of HMTA.

Fig. 7.33a. shows that HMTA is a good chelating agent as a reduction in HMTA concentration from 25 mM to 5 mM severely increases the growth rate of the non-polar facets from 11 ±2 nm/hour to 21 ±4 nm/hour for 1:1 and 5:1, respectively. The reduction of HMTA almost doubles the growth rate with an 82 % increase, highlighting how well the buffer perfoms as a non-polar facet ZnO crystal growth inhibitor, as discussed in the literature [72]. The data also confirms that the 1:1 eqimolar 25 mM ratio and concentration yields the most ideal aspect ratio and a reasonable density that should allow for ample bending of the nanowires. Note that a 50nm PVD coated seed layer was used in these experiments as they were conducted before the experiments in section 7.5.2. revealed the importance of seed layer thickness, therefore the alignment seen in Fig. 7.32 is not representative of the final recipe. Fig. 7.33c. shows the photoluminesence spectra for 5:1 and 5:5 where it can be seen that the increased growth rate of the non-polar facets is detrimental to the overal quality of the ZnO crystals. Deenathayalan et al. [74] show a similar trend by altering the $ZnNO_3$ to HMTA ratio

from 1:5 to 1:15 (where 1 is 20 mM), here they show a drastic increase in optical absorbance with increasing HMTA, using the data to calculate the band gap decrease from 3.4 to 3.1 eV. However, no such change is observed in Fig. 7.33c. and a 0.3 eV change would equate to a 35.29 nm shift. Although a slight 1.09 nm blue shift is observed from 5:5 to 5:9, it is likely this observation was overlooked as our upper HMTA concentration was only 45 mM.

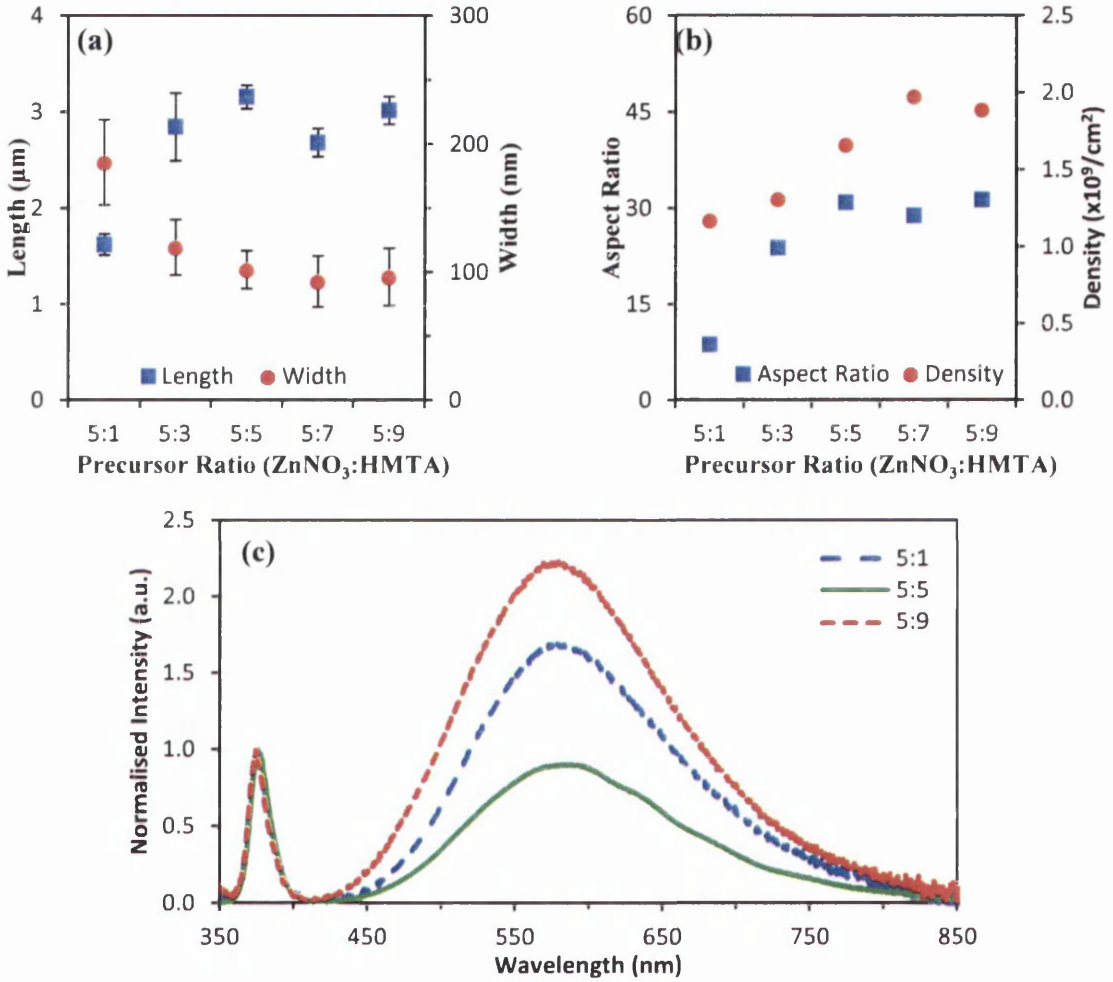

Figure 7.33. Graphs showing the effect of varying concentration of HMTA on nanowire a) length and width, b) aspect ratio and density. Data taken from 90 measurements for each thickness across 3 different areas and error bars represent ±SD of the 3 areas. The numbers represent the ratio, i.e 5:3 = 25 mM : 15 mM. c) shows photoluminescence spectra of ZnO nanowires grown with 5, 25 and 45 mM of HMTA. 325nm HeCd excitation source used and results are mean of 3 acquisitions from 3 areas. Data is normalized to the near band edge.

We have previously discussed Demianets et al. [21] and their work on growth kinetics and defect incorporation, where it was shown that an increased crystal growth rate can introduce substantial defects within the lattice, affecting the photoluminesence

spectra of the ZnO nanowire array. This is especially noticable for both 5:1 and 5:9, where an increase in the DLE band area compared to 1:1 of a 46 and 61 %, respectively can be observed. It is believed that this is due to the increased non polar lateral growth rate in 5:1, with a 82 % width decrease from 5:1 to 1:1. However, for 5:9 both axial and lateral growth rates are similar to 1:1, being only 6.0 and 5.8 % slower than 1:1 for length and width, respectively. Govender et al. [34] suggest that by increasing HMTA concentration the solubility of the product increases while the thermodynamic stability constants of the metal ligands (see chapter 3) decrease, thus highlighting the difficulty of making casual observations with interrelated parameters. By calculating the thermodynamic stability constants of solutions with different concentrations of HMTA they observed a difference in the precipitation point of the zinc hydroxide intermediate solute. Reporting $Zn(OH)_2$ precipitation points for solutions containing Zn : HMTA in the ratios, 2:1, 1:1, 1:2, 1:4, 1:8 (where 1 = 25 mM) occur at pH values of 6.8, 6.8, 6.9, 7.04 and 7.16 respectively. Where these small changes in supersaturation at a given pH yield explain why as HMTA concentration increases, lateral growth rate decreases. But since no real change is observed until HMTA concentration exceeds 100 mM this effect should not be present here. Therefore it can be concluded that a 1:1 ratio yields the most favourable nanowire morphology and optical properties.

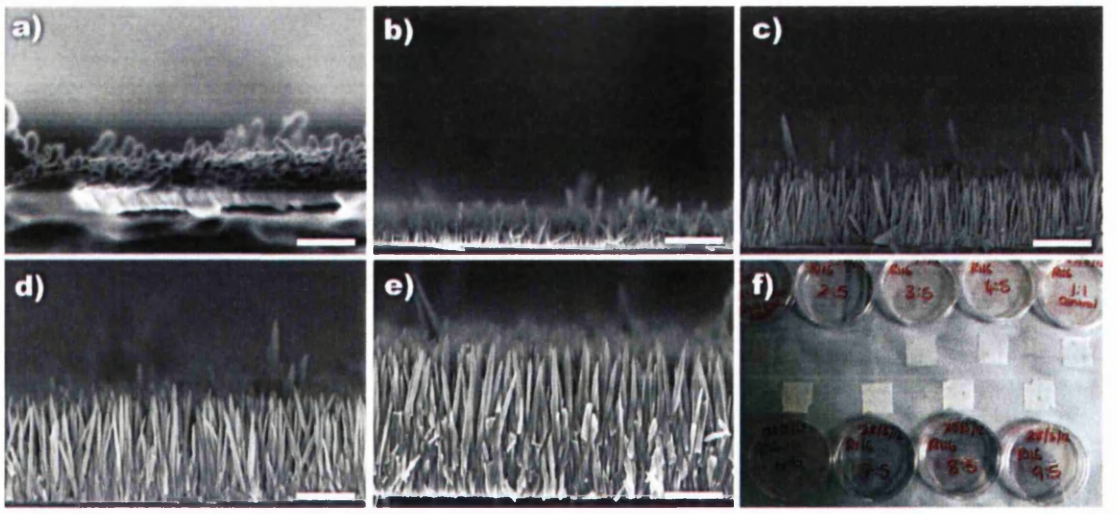

Figure 7.34. Cross-sectional SEM images of ZnO NWs on glass substrates grown with the following Zinc Nitrate to HMTA ratios, a) 1:5, b) 3:5, c) 5:5, d) 7:5, e) 9:5, f) photograph of substrates post growth. Scale bars are 150 nm for a) and 1 µm for b-e). Notice the substantial increase in crystal growth rate as the amount of $ZnNO_3$ is increased, most notabliy shown by the gradient change in f). *[90°C for 9hrs in 250ml sol. Where HMTA was held at 25mM and $ZnNO_3$ varied between 5-45mM in 5mM increments across 9 beakers – 5min stir (2min hot) – Glass coverslip with 50nm ZnO PVD]*

Next the effect of zinc nitrate concentration on the morphology of ZnO nanowires was investigated, where this time HMTA was held at 25 mM while $ZnNO_3$ was varied between 5 to 45 mM in 10 mM increments. Fig. 7.34. shows the drastic change in morphology due to to increased concentration of zinc nitrate precursor in the solution. This observed increase in nanowire length is likely due to the additional zinc nitrate precursor providing more Zn^{2+} ions in the solution allowing the supersaturation of Zn^{2+} to be maintained for longer period of time; as it was previously discussed that Baruah and Dutta [29] suggested a significant reduction in growth rate after 5 hours. Since it was shown in section 7.3 that the supersaturation of Zn^{2+} ions is crucial to maintaining uniform crystal growth rate for the full duration of growth time by avoiding the dissolution and regrowth mechanism proposed by Qiu et al. [35]. However, the trendlines in Fig. 7.35a show a 875 nm increase in nanowire length per 5 mM of $ZnNO_3$ which comes at a significant cost to aspect ratio, as the width also increases by 29 nm per 5 mM; yielding the best two aspect ratios of 14.2 and 10.2 at 3:5 and 1:1, respectively.

Fig. 7.35b shows that the inverse relationship between nanowire aspect ratio and density witnessed in several previous sections remains for these experiments. This relationship was previosuly atributed to lateral growth rate and the 'fourling' structure created from each nuclei during the first hour of growth, discussed in section 7.3. It can be clearly seen in Fig. 7.35b that the precursor ratio determines the morphology of the nanowires within the first hour of growth as the density is not consistent for each sample with the lowest $ZnNO_3$ concentration producing the densist nanowire array, even though all seed layers were deposited simultaneously. This is interesting as this observation further supports the dissolution and regrowth mechanism hypothised by Qiu et al. [35], where a decrease in width and aspect ratio with the reduction of the zinc precursor concentration was reportedly due to nanowire widths <100 nm. Where such small diameters cause the dissolution rate of the (0001) polar facet to be decelerated due to insufficient exposed area, further increasing the aspect ratio as the six non polar facets are dissolved more quickly. This results in a decrease of the diameter and a quick increase in the length and aspect ratio, as recently decomposed zinc ions interact with the (0001) polar facet due to higher catalytical activity [75].

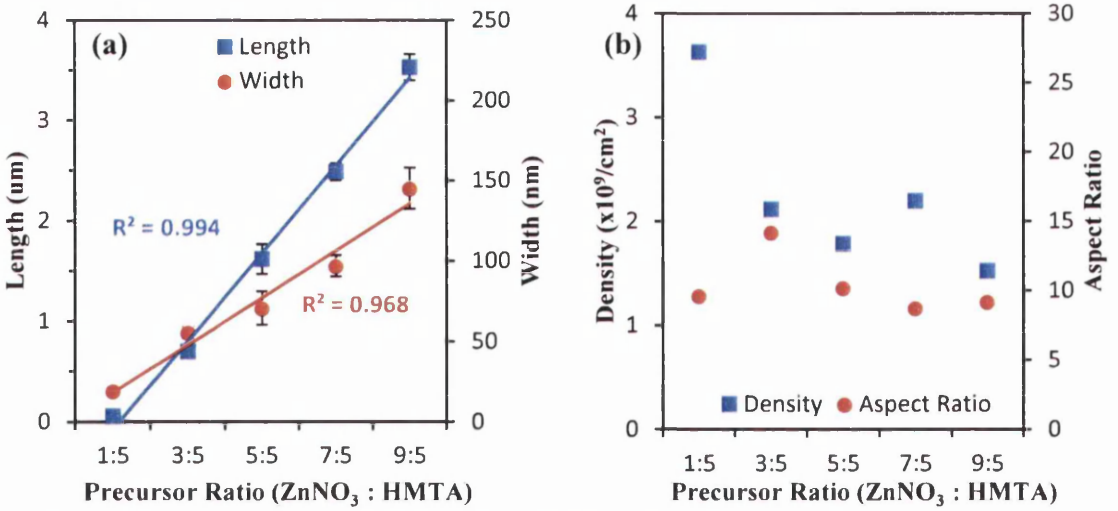

Figure 7.35. Graphs showing the effect of varying concentration of HMTA on nanowire a) length and width, b) aspect ratio and density. The numbers represent the ratio, i.e 3 : 5 = 15 : 25 mM.

Fig. 7.36a shows the photoluminesence spectra of all samples from 1:5 to 9:5 ratios, where significant deviation from the equimolar 1:1 solution is shown to negatively affect the optical properties of the ZnO nanowires. It can be seen in Fig. 7.36b that the equimolar 1:1 25 mM concentration yields the most ideal nanowires in terms of optical properties and crystal quality, with 1:1 giving the greatest luminesence peak ratio of 1.3. Fig. 7.36a shows that 1:5 yields most unideal spectra with the visible defect band being 1103 % larger than 1:1. This significant change in DLE emission is most likely due to a change in surface area to volume ratio with the width of the nanowires being drastically reduced for 1:5 at 19 ±3 nm compared to 71 ±13 nm for 1:1.

It can be seen that the visible band defect emission peak for 1:5 is blue shifted by 4 nm from 588.20 to 584.77 nm for 1:1 and 1:5, respectively. There is also substantial emission between the NBE and DLE peaks which is uncharacteristic for ZnO or its related defects which typically range between 0.8 - 2.8 eV [25]. However, due to the low intensity (remember that Fig. 7.36a. has been normalised to NBE peak) the integration time was five times larger for 1:5 than all other concentrations being 1000 seconds for 1:5 compared to 200 seconds for all other samples (in this work). It has been reported by D. Ehrt [76] that willemite (Zn_2SiO_4) can yield 485 nm centred emission. It could be the case that such large integration times and such poor emission from the tiny ZnO nanowires has enhanced the appearance of an emission that would normally go unnoticed under normally circumstances. Also due to the small size of the nanowires for 1:5, then the Surface Area to Volume Ratio (SAVR) would likely have a

greater effect on the PL spectra, such that the results maybe surface sensitive and this is also contributing to the uncharacteristic PL spectra for 1:5.

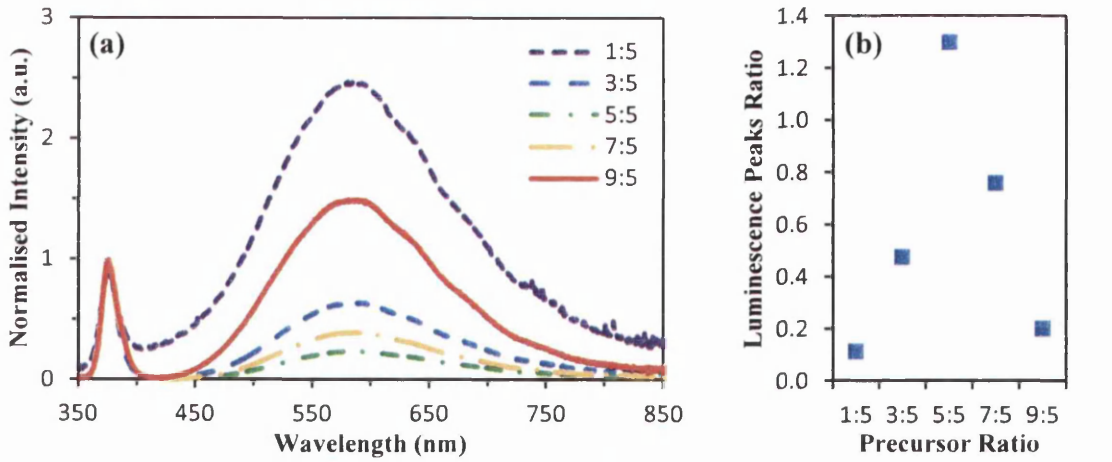

Figure 7.36. Graphs showing the effect of varying concentration of HMTA on nanowire on a) the photoluminescence spectra for each sample, and b) the NBE/DLE peak ratio for each concentration.

Least mean squares linear regression trend lines in Fig. 7.35a. show that both nanowire length and width are effected linearly with the amount on zinc nitrate precursor added to the growth solution. This is a crucial finding as a linear relationship allows for predictable growth at higher concentrations, with the data suggesting nanowires grown at around 2:1 will be of larger width and higher density; both these changes are likely to provide a more ideal surface for cell culture as observed by Canoifi et al. [77]. However as the photoluminescence data indicates, nanowires grown at precursor ratios with $ZnNO_3$ not equimolar to HMTA result in an increase of defects and surface states within the array. It was discussed earlier that an increased density could be detrimental to AFM force measurements. It has been shown by ter Brugges et al. [78] that cells are more viable on surfaces with less 'no adhesive' gaps; it would therefore be wise to take a 2:1 based recipe as well as the more ideal 1:1 based recipe to the cell culture phase of this work to ensure that the nanowires are fully biocompatible. Before these two recipes are explored further the reproducibility will be investigated, highlighting the importance of scientific diligence.

7.7. Significance of minor variables on reproducibility

Before recipes can be taken to the cell culture phase of the work it is important to confirm that an adequate level of reproducibility has been obtained. The following section will explore the importance of accounting for every variable as small variables such as relative humidity, stirring time, beaker immersion depth and substrate surface area can all play a significant role determining nanowire morphology. For example although the nanowires grown in Fig. 7.32. and Fig. 7.34. both have a 1:1 precursor ratio and 25 mM concentration the morphology and optical properties of these two samples differs drastically! Therefore the effect of minor variables needs to be explored. The HMTA experiment yielded nanowires 3.2 ± 0.1 μm long and 102 ± 15 nm wide, while zinc nitrate experiment yielding nanowires 1.6 ± 0.1 μm long and 71 ± 13 nm wide, yielding an increase of 95 and 44 % for length and width, respectively. These nanowires are significantly different in morphology and optical properties and yet the major variables have been reported as being identical (time, temperature, seed layer thickness, solution concentration and ratio etc...).

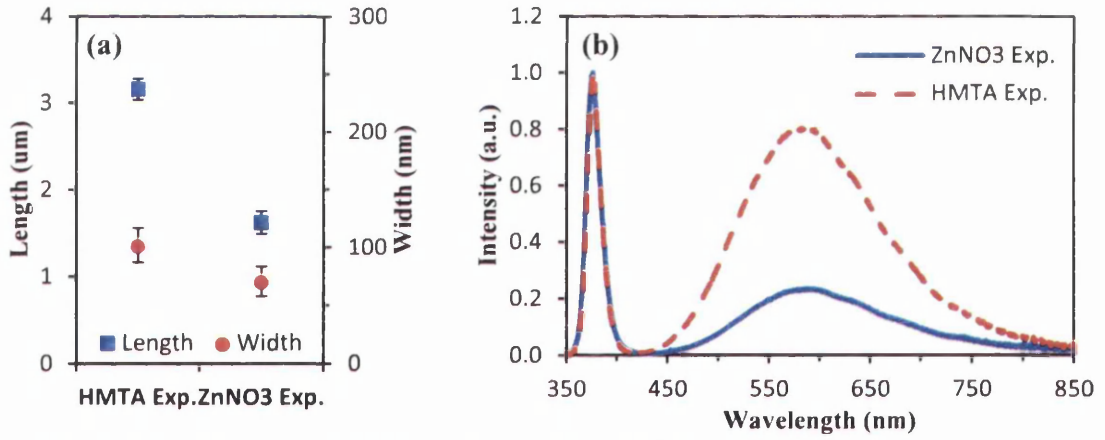

Figure 7.37. Comparison of same recipe from two separate experiment sets, where a) shows length and width, and b) their optical properties. Data taken from 90 measurements for each thickness across 3 different areas and error bars represent ±SD of the 3 areas. 325nm HeCd excitation source used and results are mean of 3 acquisitions from 3 areas. Data is normalized to the near band edge. In both cases the major variable were listed as: *[90°C for 9hrs in 250ml 25mM 1:1 sol. Glass coverslip with 50nm ZnO PVD]*

Fig. 7.37. shows quite a significant difference between the morphology yielded from the two experiments, with one length being almost double the other. Given the laboratory has a closed circuit air-conditioning system (no interference from outside air) then contributions from outside ambient temperature and relative humidity can be

neglected and are unlikely to have effected growth. These are suggested as it has been shown by Lee et al. [46] that relative humidity can have a significant effect on the formation of ZnO seed layers, however this is applicable to spin coated seed layers only so only PVD coated sample have been considered for comparison. Besides relative humidity was typically between 38 – 42 % and rarely fluctuated. However when the two recipes stirring times and size of substrates are compared differences appear, showing that the HMTA experiment was stirred for double the time of the $ZnNO_3$ experiment; surely something so subtle couldn't effect nanowire morphology so drastically?

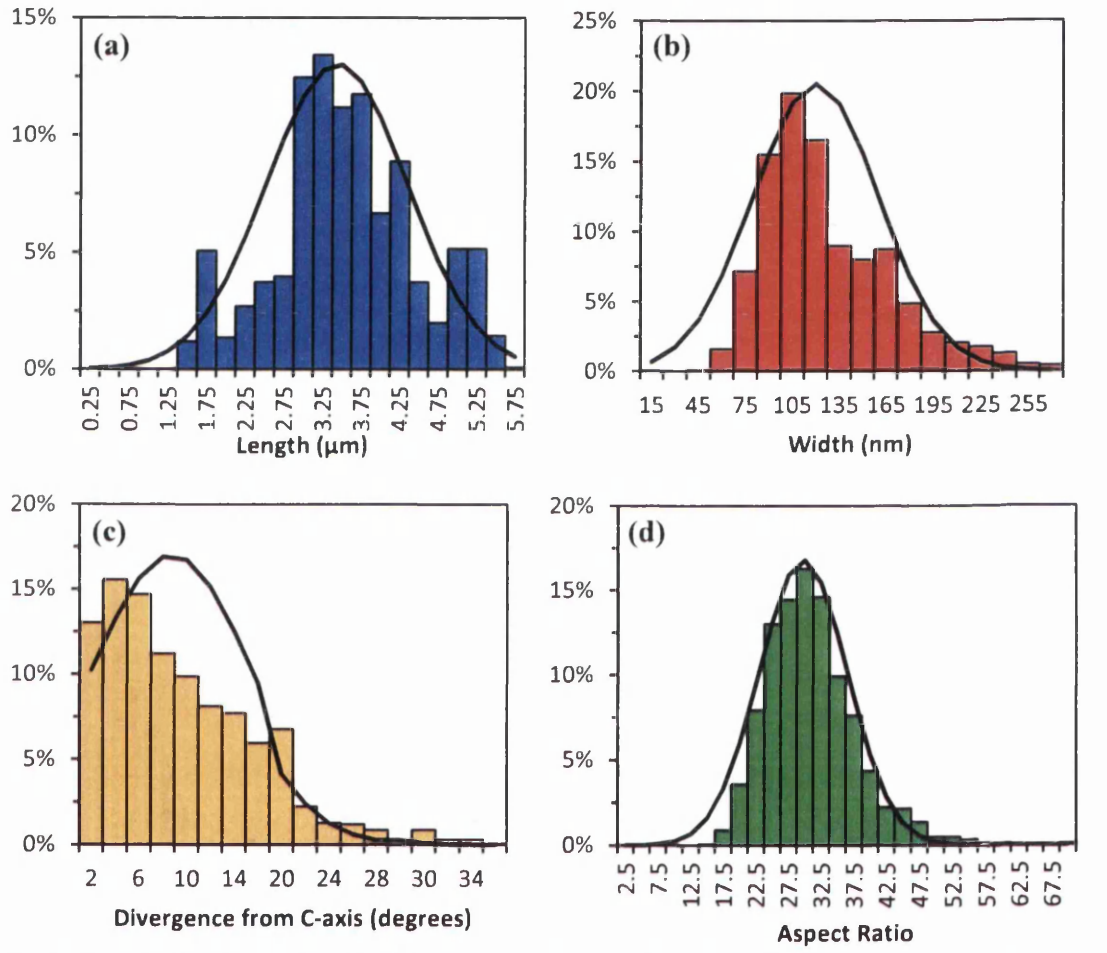

Figure 7.38. Histograms showing distribution of measurements for all PVD only 1:1 25 mM experiments with a seed layer thickness of 20nm, where a) is length, b) diameter, c) divergence from c-axis (angle/alignment) and d) aspect ratio. Black lines show the normal distribution of data.

Fig. 7.38. Compares the morphology of all nanowires fabricated using the 90 °C for 9 hours in 500 ml 25 mM equimolar solution with 20 nm PVD coated glass cover slips recipe refined throughout the course of this chapter. The histograms comprise of data from 1260 individually measured nanowires, and as such the normal distribution

curves (overlayed as black lines) provide the mean value for each attribute measured across all 1260 nanowires that should be (hypothetically) identical; highlighting that although key variables already investigated are maintained significant differences appear. Table 7.4. shows the most dominant 'bins' for the histrograms in Fig. 7.38, which disagree with the means shown in Table 7.5. This is because the measurements are not perfectly mono-disperse with distribution curves having substantial tails in all but the aspect ratio, which has yielded a mean that correlates with the dominant bin, as shown by a Gaussian distribution curve.

Table 7.4: Dominant morphology from all PVD 25 mM 1:1 experiments, from Fig. 7.38.

Highest %	*Bin*	*Frequency*	*%*
Length (μm)	3 - 3.25	169	13.4
Width (nm)	90 - 105	250	19.8
Angle (degrees)	2 - 4	196	15.6
Aspect Ratio	27.5 - 30	205	16.3

Table 7.5: Mean morphology from all PVD 25 mM 1:1 experiments, from Fig. 7.38.

	Length (μm)	Width (nm)	Angle (degrees)	Aspect Ratio	Density (NWs/cm^2)
Min	1.3	40	0.0	22.9	7.2×10^8
Max	5.5	268	34.3	34.3	1.8×10^9
Mean	3.4	120	8.8	28.9	1.8×10^8
SD	0.9	41	6.7	3.8	4.8×10^8

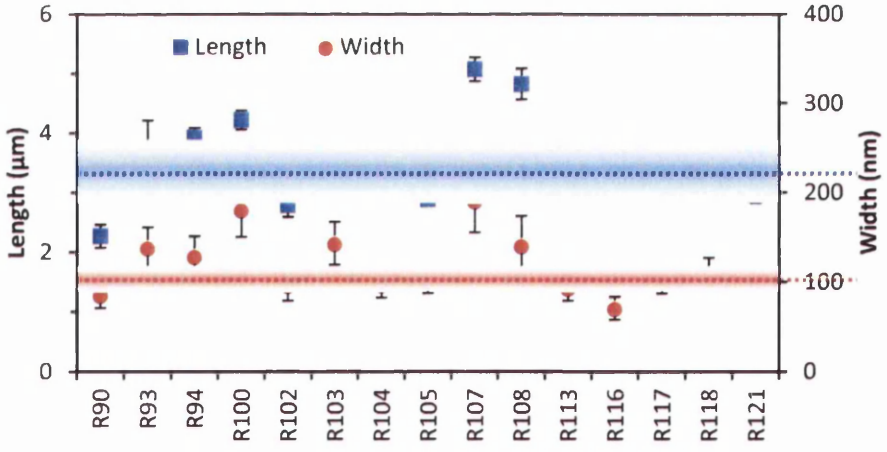

Figure 7.39. Morphology of all PVD only 1:1 experiments with a seed layer thickness of 20nm is shown and organized chronologically by experiment number.

Fig. 7.39. shows that several experiments deviate significantly from the average nanowire morphology of 3.4 ± 0.9 µm and 120 ± 41 nm (indicated by dashed lines and colour bars for SD). For example it is very interesting to observe that Runs 90, 102 and 116 that yieled the smallest nanowires also have the three shortest stirring times of 0, 5 and 5 minutes respectively; this cannot be a coinsidence. Nor can it be coinsidence that Runs 107 and 108 that produced the largst nanowires were stirred for a significantly longer period of 35 minutes each. Replotting Fig. 7.39. As a function of stirring time bears witness to a trend that may have otherwise been overlooked had reproducibility not been examined.

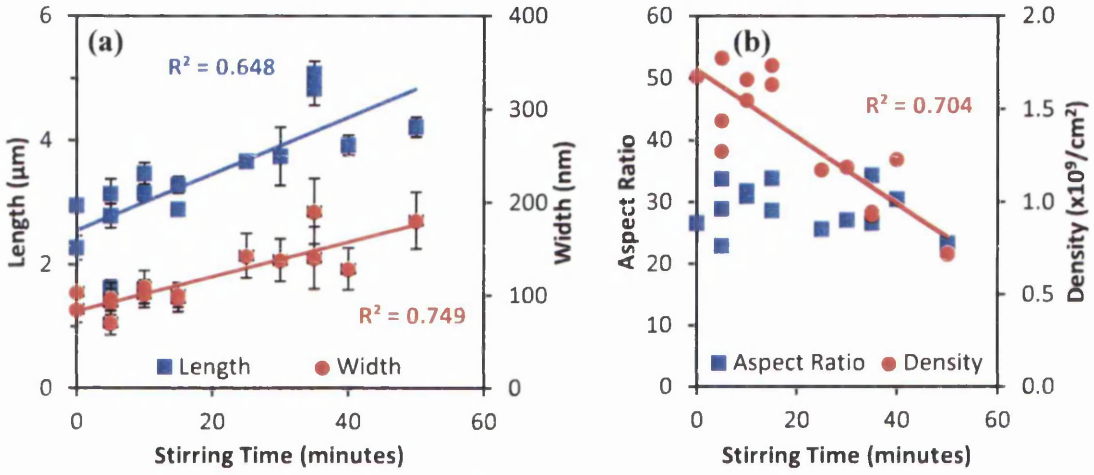

Figure 7.40. Morphology of all PVD only 1:1 experiments with a seed layer thickness of 20nm is shown and organized chronologically by experiment number. Error bars represent ±SD of the 3 areas.

Fig. 7.40. shows when length and width are plotted as a function of stirring time that a least means squared interpretation of the results leads to a R^2 coefficient of determination values of 0.65 and 0.75 for length and width respectively. This data shows how extremely diligent one must be while using the hydrothermal growth technique to fabricate nanowires of the same morphology for use in other experiments where consistency is key, such as cell cultivation and viability assays. Fig. 7.40b shows again that density is shown to be inversely proportional to nanowire width, even from data sourced for separate experiments! As previously discussed, Qiu et al. [35] attribute their observed increase in nanowire length when the growth solution is preheated for 7 hours prior to adding the substrate for nanowire growth, to the linearly decreasing zinc concentration during preheating. However in this work the solutions are stirred in room temperature water (21 °C), and so the change cannot be due to preheating unless we

assume that the kinetic energy put into the system (from the stir bar) is sufficent enough to allow (at least) precipitation of the $Zn(OH)_2$ intermediate. Which was often evident for longer stir times as the solution would go slightly cloudy, indicating a precipitate had formed. It is unfortunate that the starting pH of the solution was not always measured as it has been suggested by Ashfold et al. [79] that when the zinc ion concentration decreases the formation of $Zn(OH)_2$ eventually becomes thermodynamically unfavourable. Such that any $Zn(OH)_2$ formed will dissolve and contribute to the growth of nanowires by direct deposition of ZnO. If stirring leads to more rapid precipitation of the $Zn(OH)_2$ intermediate, then it could be assumed that solutions that are stirred longer stockpile $Zn(OH)_2$ allowing for more rapid deposition of ZnO compared to non stirred solutions.

After reviewing the earlier results (before run 107) it was decided that run 104 would be used for all surface analysis and tissue culture work, as the experiments 104 and 118 are the two closest batches to the mean of all 15 (20 nm PVD only) 1:1 experiments. Run 104 also included nanowires grown at the 2:1 ($ZnNO_3$:HTMA) ratio.

7.7.1. Effect of DI water temperature during stirring

Since it has been discussed that preheating the precursor solution can yield large increase in nanowire length and aspect ratio [35] then the effect of solution temperature during stirring (as indicated under all SEM images throughout the chapter) should also be considered, as this would significantly increase the rate of the reaction as the release of OH^- from HMTA predominantly relies on thermal decomposition.

In all previous experiments the solution has been mixed with 10 % of the total DI water while the other 90 % was pre heated to growth temperature to allow the reaction sufficient energy to begin as soon as the two solutions are added. Obviously this is not the case as the energy from stirring has been shown to significantly alter results, leading the author to believe that dissolution of precursors into separate solutions (as sometimes mentioned in the literature) would have been a more reliable way to obtain much improved reproducibility and tighter distribution in Fig. 7.39. Typically the preheated DI water is mixed with the 10 % stirred precursor solution and stirred for 1 minute before splitting into separate beakers when the experiment consisted of multiple beakers ~(most were). It was observed that the solution could often become cloudy when stirred with solutions exceeding room temperature, literature suggests that

the precipitate is the hydroxide ($Zn(OH_2)$) intermediate stage in the growth process [14], see equation 3.7. Therefore an experiment was conducted to compare the difference between dissolving precursors at room temperature (21 °C) and growth temperature (90 °C), where the precursor chemicals would be stirred for 15 minutes.

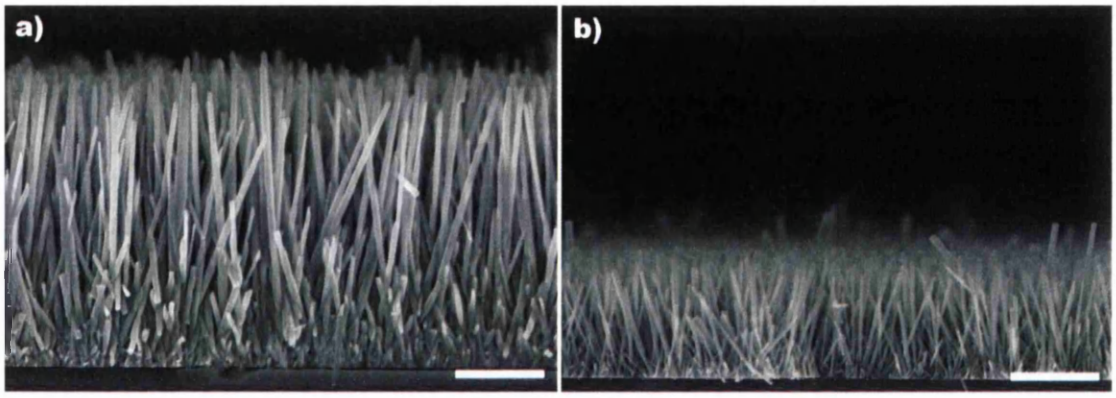

Figure 7.41. Cross-sectional SEM images of ZnO nanowires on glass substrates grown with different stirring temperatures, where chemicals were stirred for 15 minutes at a) room temperature (20°C) and b) 90°C. All scale bars are 1µm. *[90°C for 9hrs in 500ml 25mM 1:1 sol. – 15min stir for one beaker at room and the other at preheat temperature – Glass coverslip with 37nm ZnO PVD]*

Fig. 7.41. shows the difference in nanowire morphology due to stirring for 15 minutes at either room temperature or the growth solution temperature. It can clearly be seen that dissolving the precursors in DI water at elevated temperatures significantly affects the growth rate of the ZnO crystals. It could be rashly concluded that stirring the precursors at 90 °C must inhibit growth by reducing the availability of Zn^{2+} once the substrate is added post stirring by promoting homogeneous nucleation during stirring; as the solution after 15 minutes was as opaque as milk. However, this cannot be caused by the zinc hydroxide intermediate stage as the growth has been inhibited which is contrary to findings in the previous sub-section and literature which observed a growth rate increase. Therefore, the solution must be so super saturated due to the dissolution of precursors at elevated temperature that homogeneous nucleation of ZnO dominates, as per observations by Govender et al. [34]. This hypothesis can be further supported by Degen et al. [80] who report that Zn^{2+} dominates at pH 6 – 7, whereas $Zn(OH)_2$ dominates at pH 9 – 11; solution pH will be discussed in further in the next sub-section.

Fig. 7.42a shows the measured nanowire morphology comparing the difference between elevated and room temperature stirring, where stirring for 15 minutes at room temperature yielded nanowires of 3.4 ± 0.1 µm and 77 ± 9 nm while stirring for 15

minutes at 90 °C yielded nanowires of 1.4 ± 0.1 µm and 42 ± 4 nm, for length and width respectively. These values show an astounding decrease in crystal growth rate of 59 % and 46 % for length and width respectively from cold to hot stirring. This finding is similar to that observed in Table 7.3 and Fig. 7.30. for 5 and 15 mM. Again an inverse relationship in maintained between nanowire width and density. Notice that this data though not included in Fig. 7.39 due to it 37 nm thick PVD ZnO seed layer would at 3.4 µm after 15 minutes stirring be in good agreement with the trend line. This experiment further highlights the complex nature of the hydrothermal method.

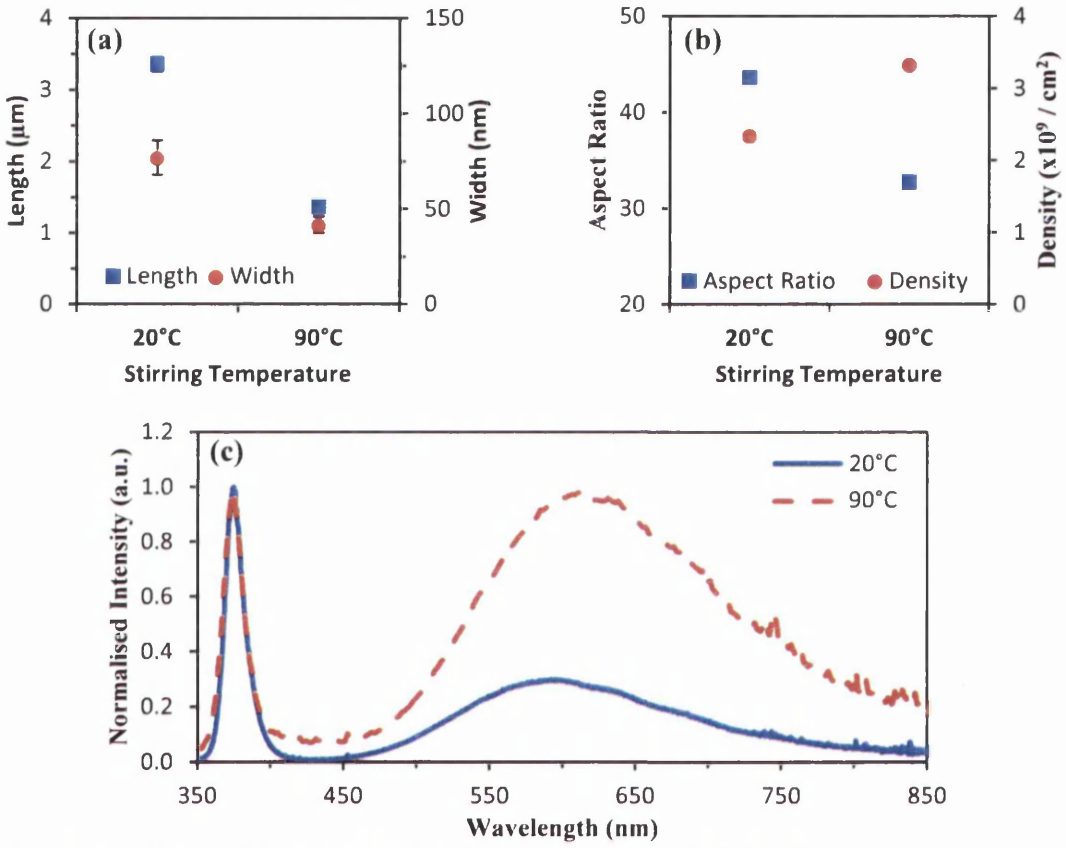

Figure 7.42. Graphs show effect of stirring temperature on a) length and width and b) aspect ratio and density, and c) shows photoluminescence spectra comparing stirring temperature, data is normalized to the NBE for both cold and hot solutions.

Although the data suggests discontinuing any form of stirring at elevated temperature this step is crucial to making sure that the 10 % solution stirred at room temperature and 90 % preheated solution are thoroughly mixed so that the precursor chemicals are evenly distributed. Therefore a 1 minute stirring using preheated DI water will always occur, regardless of the time the solution is stirred at room temperature.

Also following the analysis of 25 mM 1:1 stirring data it can be said that although stirring for longer yields a longer nanowire it also produces a wider one, as Fig. 7.40b shows that the aspect ratio barely affected. Therefore there is no reason to stir for extended durations from here on as there is no benefit to nanowire morphology with respect to bending and cell analysis. Also, as Fig. 7.42c shows that the optical properties are affected by stirring temperature, with solutions stirred at elevated temperature yielding poor quality nanowires; likely due to increased defect incorporation due to decrease in zinc ion concentration (as shown in as Fig. 7.31).

The effect of substrate surface area (i.e. nucleation area) on nanowire morphology is not accounted for in either stirring sub-sections and could be accountable from some of the observed variation from the mean. It could be argued that the solution should be treated as having an infinite supply of precursor ions (Zn^{2+} and OH^-) given its large volume (500 ml) and high concentration (25 mM). However, it is has been discussed in section 7.4. that work by Baruah and Dutta [29] reported the need to replenish the solution to avoid decreased growth rate and a dissolution and regrowth mechanism dominating. Such observations could not be made if the solution were infinite; therefore the total surface area available for heterogeneous nucleation could have significant effects on the long term availability of precursor ions as a change in surface area will alter the time point at which dissolution and regrowth dominate.

7.7.2. Solution pH and Homogeneous Nucleation

During this work some key initial experiments were repeated and samples of solution taken at 30 minute intervals, with the intention to check the Zn^{2+} content of the samples using Atomic Absorbance Spectroscopy (AAS). Although analysis with AAS did not occur as planned (sample volume sizes were too small) the collection of samples allowed solution pH to be tested and changes in pH during the experiments to be observed. This prompted the repeat of several experiments using a pH probe during the experiment to obtain pH results in real time. It should be noted that for each 30 minute measurement of solution pH the pH probe was cleaned between measurements and pH reading allowed to stabilise for 10 minutes.

The observed change in solution pH over time is not unexpected as it is understood that the finite amount of HMTA will expire, with Burah and Dutta [29] suggesting a 5 – 6 hour limit per solution until precursors are exhausted. Burah and

Dutta derive this time limit irrespective of volume or concentration as HTMA can only be considered a buffer if it thermally decomposes **slowly**, as if it spontaneously hydrolysed quickly producing a large quantity of OH^- then the Zn^{2+} ions in solution would precipitate out rapidly due to the high pH environment; resulting in depletion of precursor solution and subsequently prohibited growth of ZnO nanowires [79]. Therefore, the pH change was reinvestigated, however given the size of the pH probe it became impossible to measure the pH for for beakers with more than two 22 x 22 mm substrates (at this point in the work four would be used).

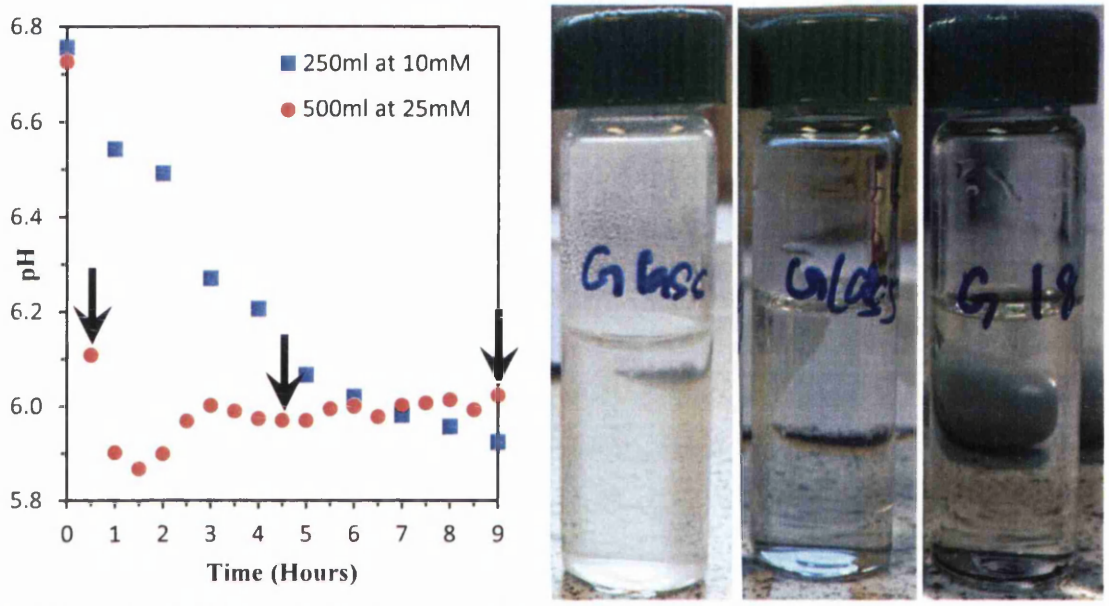

Figure 7.43. Change in pH over time comparing the previous recipe (250ml of 10mM 1:1 growth solution stirred for 40 minutes) and current recipe (500ml of 25 mM 1:1 growth solution stirred for 15 minutes) . Where the black arrows highlight the datums corresponding to the vials in the photographs, from left to right, 30 minutes, 4 hours 30 minutes and 9 hours. The graph compares a low volume low concentration and high volume high concentration, see how the high concentration has a rapid reduction in OH^- likely due to substantial homogeneous nucleation within the first 2 hours as indicated by the glass vial at 30 minutes.

Fig. 7.43a. shows two sets of pH measurements, one recorded in a 10 mM 250 ml solution and the other in a 25 mM 500 ml solution; the latter being the expected recipe this far into the work. The 10 mM solution gradually decreases it pH over the 9 hour period of nanowire growth, whereas the 25 mM solution starts with an initial rapid decrease in pH from 0 – 1.5 hours, then a slight increase to pH 6.0 as the solution stabilises. Since the OH^- concentration decreases (increases) by one order of magnitude for every unit decrease (increase) in pH [18], then a high volume of homogeneous nucleation and formation of colloidal ZnO must take place within the first 2 hours in the

25 mM solution. This is most likely due to the overly super saturated solution dropping to a less super saturated state after 2 hours making homogeneous nucleation unfavourable, as indicated by the lack of precipitate visible in the solution at 4.5 hours compared to 30 minutes, in Fig 7.43b. However, Hodes [18] has pointed out that although an excess of OH^- should increase the production of the zinc hydroxide intermediate, there is also another intermediate stage (discussed in chapter 3), where OH^- can form a complex with Zn^{2+} called the zincate ion ($Zn(OH)_4^{2-}$).

This observation is also supported by Jacobs et al. [14] who report that the addition of base to the zinc salt solution causes pure hexaqua zinc ion complexes to precipitate zinc hydroxide forming the soluble zincate anionic complex. Since zinc hydroxide is an amphoteric metal hydroxide then it can be assumed that it can act as a Bronsted base [18] causing more zinc hydroxide to be formed. However, pH on its own makes any kind of hypothesis on chemical interactions difficult to prove, ideally AAS (Atomic Absorbance Spectroscopy – which yields the concentration of a specific ion in a solution) needs to be incorporated into this work to further understand the chemical mechanism behind the reaction. Ashfold et al. [79] have conducted an AAS and pH investigation in situ and find that while the Zn^{2+} concentration steadily decreases over 9 hours the pH only changes for the first 2.5 hours. They postulate that this is due to the removal of the zinc hydroxide intermediate, which becomes thermodynamically unstable and dissolves at lower Zn^{2+} concentrations.

Govender et al. [34] suggest that the point of introduction of the substrate to the growth solution has a significant impact on the morphology of the ZnO nanowires. Stating that if the seeded substrate is inserted in the solution 15 minutes after 90 °C is reached, the bath produces no homogeneous precipitation during the reaction period and a dense white film is obtained. More importantly Govender et al. also support the growth of ZnO nanowires at the unadjusted pH of 6.8 (such as in this work), reporting that precipitation occurred rapidly in baths in which no pH adjustment was made, by using both ZnO seeded substrates and lower solution pH, good quality films can be deposited. This is because the rate of HMTA hydrolysis decreases with increasing pH reducing the availability of precursor ions.

pH was initially investigated and the results showed previously in Fig 7.11d. where the pH of the solution over the course of the 9 hour growth time was shown to drop by 0.2 pH from 0 to 5 hours, gradually falling after that. This trend followed colloidal growth observations where after 3 - 4 hours the colloids were witnessed to

have settled and formed a sediment at the bottom of the beaker; indicating that colloidal growth formation had likely ceased. It was hypothesised that this was likely due the pH falling outside of the optimum for colloidal growth, as similar results had been reported in the literature [81]. However Fig 7.11d. showed the change in pH for Experiment 73 whos recipe was 90 °C for 9 hours in 250 ml 10 mM 1:1 solution with a 40 minute room temperature stir (2 minute hot) and a single floated glass coverslip with a zinc acetate spin coating seed layer. Therefore Fig 7.43. represents an update now the the recipe has been almost finalised; and what a significant difference it displays! It is worth noting that the starting and finishing pH are similar for both experiments and that the main differences are, concentration, volume, subtrate surface area and stirring time. It would appear that the increased volume and concentration yields a higher volume of colliodal nanostructures due to the concentration; and therefore supersaturation as discussed in section 7.6.

7.8. Characterisation of Final Recipe

Fig. 7.44. shows multiple techniques used to prove that the nanowires grown using the final recipe are indeed ZnO, and of good crystal quality. These techniques include high resolution transmission electron microscopy (HRTEM), selected area electron diffraction (SAED), energy dispersive x-ray spectroscopy (EDX) and x-ray diffraction (XRD).

Fig. 7.44a shows a HRTEM image of a single ZnO nanowire, where the lattice spacing's for both a_0 and c_0 are clearly visible and match with the properties of ZnO discussed in Table 2.1; where a_0 and c_0 are reported to be 0.325 nm and 0.521 nm, respectively for bulk ZnO at 300 K [82]. It can also observed that the lattice of this nanowire is highly ordered with no point defects (such as vacancies or dislocations close to (1010) etc...) visible in the image. Fig. 7.44b shows the selected area electron diffraction (SAED) pattern for the nanowire in the HRTEM image, where is can be seen from the discrete spots that the nanowire is single-crystal, and is preferentially grown along the c-axis (0001). Fig. 7.44c shows the energy dispersive x-ray spectroscopy (EDX) spectra for an array of hydrothermally grown ZnO nanowires, where only Zn and O elements can be seen indicating no contaminants are introduced via the hydrothermal method. It should be noted that the EDX has a detection limit of 200 ppm,

so trace amount of contaminants may exist [83]. EDX can be used to determine the amount of Zn and O elements are present within the nanowire array, where Fig. 7.44c yielded atomic percentages of 51.34 and 48.66 % (SD ± 0.17%) for Zn and O, respectively. This result is in good agreement with observations by Xue et al. [84], and indicates the nanowires have close to ideal stoichiometry.

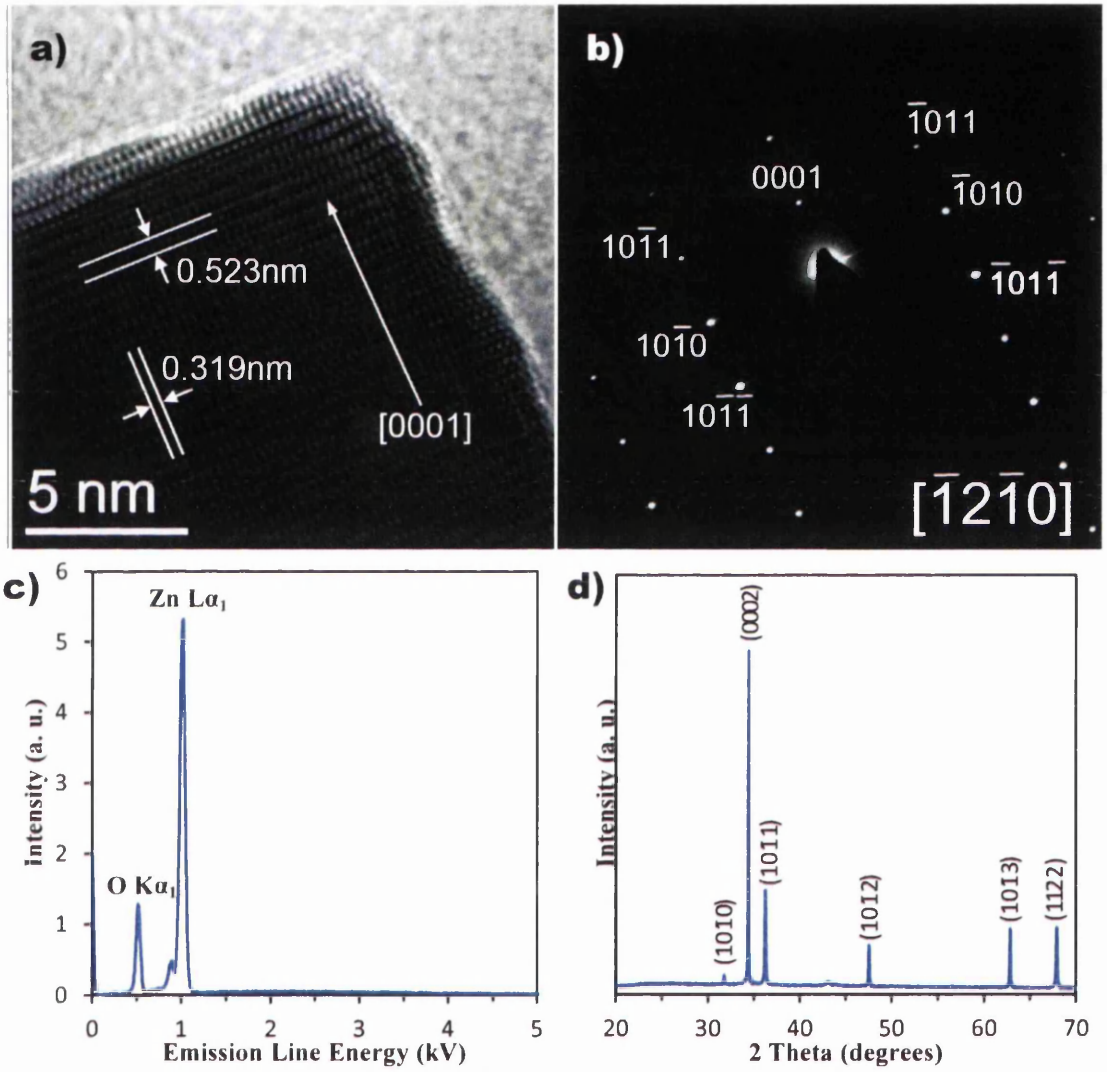

Figure 7.44. HRTEM images of a single ZnO nanowire fabricated using the hydrothermal method, where a) is a HRTEM image with c and a axes measured and the c-axis growth direction [0001] labeled. Also, b) shows the SAED pattern, c) the EDX spectra and d) the XRD spectra with orientations labeled. *[90°C for 9hrs in 500ml 25mM 1:1 sol. – 10min stir (1min Hot) – Glass coverslip with 20nm ZnO PVD]*

Although it is difficult to tell from Fig. 7.44d the (0002) peak exhibits the lowest full width at half maximum (FWHM) and highest intensity compared to the other diffraction peaks, see Table 7.6. This indicates that the [0001] growth direction is the preferred direction of growth for these hydrothermally grown ZnO nanowires. It has

also been reported that narrow diffraction peaks show that the material is of good crystal quality [57]. Fig. 7.44d certainly has peaks with very small FWHM, with the planes $(10\bar{1}0)$, (0002) and $(10\bar{1}1)$ yielding FHWM of 0.067 °, 0.063 ° and 0.113 °, respectively. The degree of c-axis orientation can be accessed via the relative texture coefficient (TC), which was calculated to be 0.8 for Fig. 7.45d using the following equation from [85].

$$TC_{0002} = \frac{\left(I_{0002}/I^{o}_{0002}\right)}{\left[\left(I_{0002}/I^{o}_{0002}\right)+\left(I_{10\bar{1}1}/I^{o}_{10\bar{1}1}\right)\right]} \tag{7.1}$$

Where I_{0002} and I_{1011} are the measured diffraction intensities due to (0002) and $(10\bar{1}1)$ planes of as grown ZnO nanowires, respectively. I^{o}_{0002} and I^{o}_{1011} are the values taken from reference card 96-230-0113 [86], freely available online from the Crystallography Open Database [87]. Peak values from reference card 96-230-0113 are shown in Table 7.6. for comparison to peak values obtained from nanowires fabricated using the final recipe in this work. Kajikawa et al. [85] has shown that for equation 7.1 TC_{0002} = 0, 0.5 and 1 correspond to preferred orientations that are $(10\bar{1}1)$, random and (0002), respectively. Using data from Fig. 7.44d, (0002) yielded the highest relative texture coefficient value of 0.8, which was significantly larger than other values, therefore, the (0002) plane must dominate in our hydrothermally grown ZnO nanowires. Also, the XRD results show the nanowires to be free from impurities as no non ZnO diffraction peaks were detected within the measured region. As well as being free from substantial internal strain, as Ando et al. [88] has shown that such strain results in a shift of the (0002) peak to lower diffraction angles; not witnessed in Fig. 7.44d. These techniques have proven that the final recipe used in this work to fabricate ZnO nanowire arrays for cell viability (chapter 8) are made of ZnO and of high crystal quality.

Table 7.6: FWHM of peaks in Fig. 7.44d, highlighting (0002) is the preferred orientation with the lowest FWHM. Peak positions from Crystallography Open Database reference card 96-230-0113 are also shown.

Plane	$(10\bar{1}0)$	(0002)	$(10\bar{1}1)$	$(10\bar{1}2)$	$(10\bar{1}3)$	$(11\bar{2}2)$
Peak Position (°)	31.788	34.458	36.282	47.566	62.884	67.970
FWHM	0.074	0.059	0.133	0.104	0.069	0.133
96-230-0113	31.773	34.430	36.260	47.549	62.873	67.961

7.9. Summary

This chapter has taken the reader on a journey though the thought process of the author and the decisions made profile the hydrothermal growth method to finalise a recipe for use in subsequent microbiology experiments. From this point onward two recipes will be used, firstly both will be grown at 90 °C for 9 hours in 500 ml however the precursor ratio will be altered with one a 25 mM 1:1 solution and the other a 50 mM : 25mM ($ZnNO_3$: HMTA) solution both stirred at room temperature with 10% of the total volume (50 ml) for 15 minute followed by stirring for 1 minute after the preheated Di water has been added to the solution. This desision was made to just alter a single varable to maintain a low level of human error to improve reproduciblity of the recipes as the majority of micro biology experiments need to be run in triplicate to ensure differences in data are significant – this requires a lot of samples! The reason for picking the 2:1 (50 mM : 25 mM) recipe was the substantial increase in nanowire width and reduction in aspect ratio, which could improve biocompatibility as suggested in the literature. The following chapter will look at the two recipes in more detail explaining the literature that lead to the decision then looking at the surface properties of the wires, their biocompatibility and finally their effect on cell behavior.

7.10. References

[1] T. G. G. Maffeis, M. W. Penny, A. Castaing, O. J. Guy, and S. P. Wilks, "XPS investigation of vacuum annealed vertically aligned ultralong ZnO nanowires," *Surf. Sci.*, pp. 5–9, Sep. 2011.

[2] M. H. Huang, Y. Wu, H. Feick, N. Tran, E. Weber, and P. Yang, "Catalytic Growth of Zinc Oxide Nanowires by Vapor Transport," *Adv. Mater.*, vol. 13, no. 2, pp. 113–116, Jan. 2001.

[3] Y. Qin, R. Yang, and Z. L. Wang, "Growth of Horizonatal ZnO Nanowire Arrays on Any Substrate," *J. Phys. Chem. C*, vol. 112, no. 2, pp. 18734–18736, Nov. 2008.

[4] S. Xu, Y. Wei, M. Kirkham, J. Liu, W. Mai, D. Davidovic, R. L. Snyder, and Z. L. Wang, "Patterned Growth of Vertically Aligned ZnO Nanowire Arrays on Inorganic Substrates at Low Temperature without Catalyst," *J. Am. Chem. Soc.*, vol. 130, no. 45, pp. 14958–9, Nov. 2008.

[5] M. A. Verges, A. Mifsud, and C. J. Serna, "Formation of rod like zinc oxide microcrystals in homogeneous solutions," *J. Chem. Soc. Faraday Trans.*, vol. 86, no. 6, pp. 959–963, 1990.

[6] S.-N. Bai, "Growth and properties of ZnO nanowires synthesized by a simple hydrothermal method," *J. Mater. Sci. Mater. Electron.*, vol. 23, no. 2, pp. 398–402, Jun. 2011.

[7] C. E. Wilkes, J. W. Summers, C. A. Daniels, and M. T. Berard, *PVC Handbook*. Hanser Verlag, 2005, p. 723.

[8] S. Yamabi and H. Imai, "Growth conditions for wurtzite zinc oxide films in aqueous solutions," *J. Mater. Chem.*, vol. 12, no. 12, pp. 3773–3778, Nov. 2002.

[9] B. A. Laudise, E. D. Kolb, and A. J. Caporaso, "Hydro-thermal Growth of Large Sound Crystals of Zinc Oxide," *J. Am. Ceram. Soc.*, vol. 47, pp. 9–12, 1960.

[10] Y. Yoshino, K. Inoue, M. Takeuchi, T. Makino, Y. Katayama, and T. Hata, "Effect of substrate surface morphology and interface microstructure in ZnO thin films formed on various substrates," *Vacuum*, vol. 59, pp. 403–410, 2000.

[11] R. A. Brown, J. E. Evans, N. A. Smith, A. Tarat, D. R. Jones, C. J. Barnett, and T. G. G. Maffeis, "The effect of metal layers on the morphology and optical properties of hydrothermally grown zinc oxide nanowires," *J. Mater. Sci.*, vol. 48, no. 14, pp. 4908–4913, Mar. 2013.

[12] X. Shen, J. Sun, G. Zhu, Z. Ji, Z. Chen, and N. Li, "Morphological syntheses of ZnO nanostructures under microwave irradiation," *J. Mater. Sci.*, vol. 48, no. 6, pp. 2358–2364, Nov. 2012.

[13] R.-C. Wang, H.-Y. Lin, S.-J. Chen, Y.-F. Lai, and M. R. S. Huang, "Boundary layer-assisted chemical bath deposition of well-aligned ZnO rods on Si by a one-step method," *Appl. Phys. A*, vol. 96, no. 3, pp. 775–781, May 2009.

[14] K. Jacobs, D. Balitsky, P. Armand, and P. Papet, "Low-temperature chemical bath deposition of crystalline ZnO," *Solid State Sci.*, vol. 12, no. 3, pp. 333–338, Mar. 2010.

[15] H. Wang, J. Xie, K. Yan, and M. Duan, "Growth Mechanism of Different Morphologies of ZnO Crystals Prepared by Hydrothermal Method," *J. Mater. Sci. Technol.*, vol. 27, no. 2, pp. 153–158, Feb. 2011.

[16] C. Q. Chen, Y. Shi, Y. S. Zhang, J. Zhu, and Y. J. Yan, "Size Dependence of Young's Modulus in ZnO Nanowires," *Phys. Rev. Lett.*, vol. 96, p. 075505, 2006.

[17] C.-H. Ku, H.-H. Yang, G.-R. Chen, and J.-J. Wu, "Wet-Chemical Route to ZnO Nanowire-Layered Basic Zinc Acetate/ ZnO Nanoparticle Composite Film," *Cryst. Growth Des.*, vol. 8, no. 1, pp. 12–19, 2008.

[18] G. Hodes, *Chemical Solution Deposition Of Semiconductor Films*. CRC Press, 2002, p. 388.

[19] H. Zhang, J. Feng, J. Wang, and M. Zhang, "Preparation of ZnO nanorods through wet chemical method," *Mater. Lett.*, vol. 61, no. 30, pp. 5202–5205, Dec. 2007.

[20] C. J. Barnett, R. A. Brown, D. R. Jones, A. Tarat, R. J. Cobley, and T. G. G. Maffeis, "Investigation into the initial growth parameters of hydrothermally grown zinc oxide nanowires," in *Nanotechnology (IEEE-NANO), 2012 12th IEEE Conference*, 2012, pp. 297–300.

[21] L. N. Demianets, D. V. Kostomarov, I. P. Kuz'mina, and S. V. Pushko, "Mechanism of growth of ZnO single crystals from hydrothermal alkali solutions," *Crystallogr. Reports*, vol. 47, no. S1, pp. S86–S98, Jan. 2002.

[22] J. . Sans, A. Segura, M. Mollar, and B. Marí, "Optical properties of thin films of ZnO prepared by pulsed laser deposition," *Thin Solid Films*, vol. 453–454, pp. 251–255, Apr. 2004.

[23] P. Sundara Venkatesh, V. Ramakrishnan, and K. Jeganathan, "Vertically aligned indium doped zinc oxide nanorods for the application of nanostructured anodes by radio frequency magnetron sputtering," *Cryst. Eng. Comm*, vol. 14, no. 11, p. 3907, 2012.

[24] D. W. Lynch and W. R. Hunter, "Comments on the optical constrants of the metal and an introduction to the data for several metals," in *Handbook of Optical Constants of Solids*, E. D. Palik, Ed. London: Academic Press, 1998, p. 804.

[25] K. H. Tam, C. K. Cheung, Y. H. Leung, A. B. Djurišić, C. C. Ling, C. D. Beling, S. Fung, W. M. Kwok, W. K. Chan, D. L. Phillips, L. Ding, and W. K. Ge, "Defects in ZnO nanorods prepared by a hydrothermal method.," *J. Phys. Chem. B*, vol. 110, no. 42, pp. 20865–71, Oct. 2006.

[26] X. Wang, J. Zhou, J. Song, J. Liu, N. Xu, and Z. L. Wang, "Piezoelectric field effect transistor and nanoforce sensor based on a single ZnO nanowire.," *Nano Lett.*, vol. 6, no. 12, pp. 2768–72, Dec. 2006.

[27] R. Agrawal, B. Peng, E. E. Gdoutos, and H. D. Espinosa, "Elasticity size effects in ZnO nanowires--a combined experimental-computational approach.," *Nano Lett.*, vol. 8, no. 11, pp. 3668–74, Nov. 2008.

[28] W.-J. Lee, J.-G. Chang, S.-P. Ju, M.-H. Weng, and C.-H. Lee, "Structure-dependent mechanical properties of ultrathin zinc oxide nanowires.," *Nanoscale Res. Lett.*, vol. 6, no. 1, p. 352, Jan. 2011.

[29] S. Baruah and J. Dutta, "pH-dependent growth of zinc oxide nanorods," *J. Cryst. Growth*, vol. 311, no. 8, pp. 2549–2554, Apr. 2009.

[30] L. Vayssieres, "Growth of Arrayed Nanorods and Nanowires of ZnO from Aqueous Solutions," *Adv. Mater.*, vol. 15, no. 5, pp. 464–466, Mar. 2003.

[31] L. Wang, D. Tsan, B. Stoeber, and K. Walus, "Substrate-free fabrication of self-supporting ZnO nanowire arrays.," *Adv. Mater.*, vol. 24, no. 29, pp. 3999–4004, Aug. 2012.

[32] N. S. Ramgir, M. Kaur, P. K. Sharma, N. Datta, S. Kailasaganapathi, S. Bhattacharya, a. K. Debnath, D. K. Aswal, and S. K. Gupta, "Ethanol sensing properties of pure and Au modified ZnO nanowires," *Sensors Actuators B Chem.*, Nov. 2012.

[33] L.-W. Ji, S.-M. Peng, J.-S. Wu, W.-S. Shih, C.-Z. Wu, and I.-T. Tang, "Effect of seed layer on the growth of well-aligned ZnO nanowires," *J. Phys. Chem. Solids*, vol. 70, no. 10, pp. 1359–1362, Oct. 2009.

[34] K. Govender, D. S. Boyle, P. B. Kenway, P. O'Brien, and P. O. Brien, "Understanding the factors that govern the deposition and morphology of thin films of ZnO from aqueous solution," *J. Mater. Chem.*, vol. 14, no. 16, pp. 2575–2591, 2004.

[35] J. Qiu, X. Li, W. He, S.-J. Park, H.-K. Kim, Y.-H. Hwang, J.-H. Lee, and Y.-D. Kim, "The growth mechanism and optical properties of ultralong ZnO nanorod arrays with a high aspect ratio by a preheating hydrothermal method.," *Nanotechnology*, vol. 20, no. 15, p. 155603, Apr. 2009.

[36] B. Postels, H.-H. Wehmann, a Bakin, M. Kreye, D. Fuhrmann, J. Blaesing, a Hangleiter, a Krost, and a Waag, "Controlled low-temperature fabrication of ZnO nanopillars with a wet-chemical approach," *Nanotechnology*, vol. 18, no. 19, p. 195602, May 2007.

[37] Y. Tak and K. Yong, "Controlled growth of well-aligned ZnO nanorod array using a novel solution method.," *J. Phys. Chem. B*, vol. 109, no. 41, pp. 19263–9, Oct. 2005.

[38] J. Joo, B. Y. Chow, M. Prakash, E. S. Boyden, and J. M. Jacobson, "Face-selective electrostatic control of hydrothermal zinc oxide nanowire synthesis.," *Nat. Mater.*, vol. 10, no. 8, pp. 596–601, Aug. 2011.

[39] Z. Yang, Z. Ye, Z. Xu, and B. Zhao, "Effect of the morphology on the optical properties of ZnO nanostructures," *Phys. E Low-dimensional Syst. Nanostructures*, vol. 42, no. 2, pp. 116–119, Dec. 2009.

[40] A. G. Emslie, F. T. Bonner, and L. G. Peck, "Flow of a Viscous Liquid on a Rotating Disk," *J. Appl. Phys.*, vol. 29, no. 5, pp. 858 – 862, 1958.

[41] L. E. Greene, M. Law, D. H. Tan, M. Montano, J. Goldberger, G. Somorjai, and P. Yang, "General route to vertical ZnO nanowire arrays using textured ZnO seeds.," *Nano Lett.*, vol. 5, no. 7, pp. 1231–6, Jul. 2005.

[42] G. Kenanakis, D. Vernardou, E. Koudoumas, and N. Katsarakis, "Growth of c-axis oriented ZnO nanowires from aqueous solution: The decisive role of a seed layer for controlling the wires' diameter," *J. Cryst. Growth*, vol. 311, no. 23–24, pp. 4799–4804, Dec. 2009.

[43] W. Wu, T. Chen, and J. Ting, "Effects of Seed Layer Precursor Type on the Synthesis of ZnO (A)," *Nanotechnology*, pp. 177–181, 2010.

[44] J. Bin, H. Joon, S. Gil, C. Seong, and S. Hong, "Deposition of ZnO thin films by magnetron sputtering for a film bulk acoustic resonator," *Thin Solid Films*, vol. 435, pp. 179–185, 2003.

[45] C. Xu and D. Gao, "Two-Stage Hydrothermal Growth of Long ZnO Nanowires for Efficient TiO 2 Nanotube-Based Dye-Sensitized Solar Cells," *J. Phys. Chem. C*, vol. 116, pp. 7236–7241, 2012.

[46] Y. Lee, T. Sounart, D. Scrymgeour, J. Voigt, and J. Hsu, "Control of ZnO nanorod array alignment synthesized via seeded solution growth," *J. Cryst. Growth*, vol. 304, no. 1, pp. 80–85, Jun. 2007.

[47] N. Neves, R. Barros, E. Antunes, I. Ferreira, J. Calado, E. Fortunato, and R. Martins, "Sintering Behavior of Nano- and Micro-Sized ZnO Powder Targets for rf Magnetron Sputtering Applications," *J. Am. Ceram. Soc.*, vol. 95, no. 1, pp. 204–210, Jan. 2012.

[48] D. Yoon, "Microstructure and CO gas sensing properties of porous ZnO produced by starch addition," *Sensors Actuators B Chem.*, vol. 45, no. 3, pp. 251–257, Dec. 1997.

[49] A. Tarat, C. J. Nettle, D. T. J. Bryant, D. R. Jones, M. W. Penny, R. a Brown, R. Majitha, K. E. Meissner, and T. G. G. Maffeis, "Microwave-assisted synthesis of layered basic zinc acetate nanosheets and their thermal decomposition into nanocrystalline ZnO.," *Nanoscale Res. Lett.*, vol. 9, no. 1, p. 11, Jan. 2014.

[50] J. Song and S. Lim, "Effect of Seed Layer on the Growth of ZnO Nanorods," *J. Phys. Chem. C*, vol. 111, no. 2, pp. 596–600, Jan. 2007.

[51] M. D. Abràmoff, P. J. Magalhães, and S. J. Ram, "Image Processing with ImageJ," *Biophotonics Int.*, vol. 11, no. 7, pp. 36–42, 2004.

[52] D. Sage, "Image J: Graylevel Watershed." [Online]. Available: http://bigwww.epfl.ch/sage/soft/watershed/.

[53] F. C. M. van de Pol, F. R. Blom, and T. J. A. Popma, "R. F. Planer Magnetron Sputtered ZnO Films I: Structural Properties," *Thin Solid Films*, vol. 204, pp. 349–364, 1991.

[54] G. A. Kumar, M. V. R. Reddy, and K. N. Reddy, "Effect of substrate temperature on structural and optical properties of nanostructured ZnO thin films grown by RF magnetron sputtering," *Int. Conf. Nanosci. Eng. Technol. (ICONSET 2011)*, pp. 56–60, Nov. 2011.

[55] O. Kluth, G. Schöpe, J. Hüpkes, C. Agashe, J. Müller, and B. Rech, "Modified Thornton model for magnetron sputtered zinc oxide: film structure and etching behaviour," *Thin Solid Films*, vol. 442, no. 1–2, pp. 80–85, Oct. 2003.

[56] Y. E. Lee, J. Bin Lee, and Y. J. Kim, "Microstructural evolution and preferred orientation change of radio-frequency-magnetron sputtered ZnO thin films," *J. Vac. Sci. Technol. A Vacuum, Surfaces, Film.*, vol. 14, no. 3, pp. 1943–1948, 1996.

[57] D. Polsongkram, P. Chamninok, S. Pukird, L. Chow, O. Lupan, G. Chai, H. Khallaf, S. Park, and A. Schulte, "Effect of synthesis conditions on the growth of ZnO nanorods via hydrothermal method," *Scan. Electron Microsc.*, vol. 403, pp. 3713–3717, 2008.

[58] S. Yamabi and H. Imai, "Growth conditions for wurtzite zinc oxide films in aqueous solutions," *J. Mater. Chem.*, vol. 12, no. 12, pp. 3773–3778, Nov. 2002.

[59] E. Shim, H. Kang, S. Pang, J. Kang, I. Yun, and S. Lee, "Annealing effect on the structural and optical properties of ZnO thin film on InP," *Mater. Sci. Eng. B*, vol. 102, no. 1–3, pp. 366–369, Sep. 2003.

[60] S. a. Studenikin, N. Golego, and M. Cocivera, "Fabrication of green and orange photoluminescent, undoped ZnO films using spray pyrolysis," *J. Appl. Phys.*, vol. 84, no. 4, p. 2287, 1998.

[61] J. Liu, C. Cheng, W. Zhou, H. Li, and H. J. Fan, "Ultrathin nickel hydroxidenitrate nanoflakes branched on nanowire arrays for high-rate pseudocapacitive energy storage.," *Chem. Commun. (Camb).*, vol. 47, no. 12, pp. 3436–8, Mar. 2011.

[62] Z. J. Chew, R. A. Brown, T. G. G. Maffeis, and L. Li, "Comparison of ZnO nanowires synthesized on various surfaces on a single substrate," *Mater. Lett.*, vol. 72, pp. 60–63, Apr. 2012.

[63] L. E. Greene, M. Law, J. Goldberger, F. Kim, J. C. Johnson, Y. Zhang, R. J. Saykally, and P. Yang, "Low-temperature wafer-scale production of ZnO nanowire arrays.," *Angew. Chem. Int. Ed. Engl.*, vol. 42, no. 26, pp. 3031–4, Jul. 2003.

[64] J. Joo, B. Y. Chow, M. Prakash, E. S. Boyden, and J. M. Jacobson, "Face-selective electrostatic control of hydrothermal zinc oxide nanowire synthesis: Supplimentary Information," *Nat. Mater.*, vol. 2, pp. 1–23, 2011.

[65] C. M. Shin, J.-T. Jang, C.-Y. Kim, H. Ryu, W.-J. Lee, J.-H. Chang, C.-S. Son, and H. Choi, "Structural and optical properties of ZnO rods hydrothermally formed on polyethersulfone substrates," *J. Korean Phys. Soc.*, vol. 60, no. 12, pp. 2043–2048, Jun. 2012.

[66] W. Peng, S. Qu, G. Cong, and Z. Wang, "Synthesis and Structures of Morphology-Controlled ZnO Nano- and Microcrystals," *Cryst. Growth Des.*, vol. 6, no. 6, pp. 1518 – 1522, 2006.

[67] C. Pacholski, A. Kornowski, and H. Weller, "Self-assembly of ZnO: from nanodots to nanorods.," *Angew. Chem. Int. Ed. Engl.*, vol. 41, no. 7, pp. 1188–91, Apr. 2002.

[68] I. J. Y., M. S. C., H. H. J., R. H., J. L. W., S. S. C., and C. H., "Effect of Reactant Concentration on the Structural Properties of Hydrothermally-grown ZnO Rods on Seed-layer ZnO/Polyethylene Terephthalate Substrates," *J. Korean Phys. Soc.*, vol. 59, no. 3, p. 2338, Sep. 2011.

[69] S. Xu, C. Lao, B. Weintraub, and Z. L. Wang, "Density-controlled growth of aligned ZnO nanowire arrays by seedless chemical approach on smooth surfaces," *J. Mater. Res.*, vol. 23, no. 08, pp. 2072–2077, Jan. 2011.

[70] K. M. Lee, K. H. Park, K. H. Koh, and S. Lee, "Synthesis of High Quality ZnO Nanorods by Low Temperature Wet Chemical Process," *2007 2nd IEEE Int. Conf. Nano/Micro Eng. Mol. Syst.*, pp. 775–778, Jan. 2007.

[71] R. L. Penn and J. F. Banfield, "Imperfect Oriented Attachment□: Dislocation Generation in Defect-Free Nanocrystals," *Science (80-.).*, vol. 281, no. August, pp. 969–971, 1998.

[72] A. Sugunan, H. C. Warad, M. Boman, and J. Dutta, "Zinc oxide nanowires in chemical bath on seeded substrates: Role of hexamine," *J. Sol-Gel Sci. Technol.*, vol. 39, no. 1, pp. 49–56, May 2006.

[73] K. M. McPeak, T. P. Le, N. G. Britton, Z. S. Nickolov, Y. a Elabd, and J. B. Baxter, "Chemical bath deposition of ZnO nanowires at near-neutral pH conditions without hexamethylenetetramine (HMTA): understanding the role of HMTA in ZnO nanowire growth.," *Langmuir*, vol. 27, no. 7, pp. 3672–7, Apr. 2011.

[74] J. Deenathayalan, M. Saroja, M. Venkatachalam, P. Gowthaman, and T. S. Senthil, "Effect of Growth Layer Solution Concentration on the Structural and Optical Properties of Hydrothermally Grown Zinc Oxide Nanorods," *Chalcogenide Lett.*, vol. 8, no. 9, pp. 549–554, 2011.

[75] S. E. Mavundla, G. F. Malgas, D. E. Motaung, and E. I. Iwuoha, "Fabrication of hybrid solar cells using poly(2,5-dimethoxyaniline) hexagonal structures and zinc oxide nanorods," *J. Mater. Sci.*, vol. 47, no. 14, pp. 5455–5460, Apr. 2012.

[76] D. Ehrt, "Photoluminescence in glasses and glass ceramics," *IOP Conf. Ser. Mater. Sci. Eng.*, vol. 2, p. 012001, Jul. 2009.

[77] G. Ciofani, G. G. Genchi, and V. Mattoli, "ZnO nanowire arrays as substrates for cell proliferation and differentiation," *Mater. Sci. Eng. C*, vol. 32, no. 2, pp. 341–347, Nov. 2011.

[78] P. J. ter Brugge, S. Dieudonne, J. a Jansen, and P. J. Brugge, "Initial interaction of U2OS cells with noncoated and calcium phosphate coated titanium substrates.," *J. Biomed. Mater. Res.*, vol. 61, no. 3, pp. 399–407, Sep. 2002.

[79] M. Ashfold, R. Doherty, N. Ndiforangwafor, D. Riley, and Y. Sun, "The kinetics of the hydrothermal growth of ZnO nanostructures," *Thin Solid Films*, vol. 515, no. 24, pp. 8679–8683, Oct. 2007.

[80] A. Degen and M. Kosec, "Effect of pH and impurities on the surface charge of zinc oxide in aqueous solution," *J. Euro. Ceram. Soc.*, vol. 20, pp. 667–673, 2000.

[81] T. Kawano and H. Imai, "Fabrication of ZnO Nanoparticles with Various Aspect Ratios through Acidic and Basic Routes," *Cryst. Growth Des.*, vol. 6, no. 4, pp. 1054–1056, Apr. 2006.

[82] S. Pearton, "Recent progress in processing and properties of ZnO," *Prog. Mater. Sci.*, vol. 50, no. 3, pp. 293–340, Mar. 2005.

[83] D. C. Bell and A. J. Garratt-Reed, "Energy Dispersive X-ray Analysis in the Electron Microscope," in *Volume 49 Microscopy Books*, Garland Science, 2003, p. 160.

[84] H. Xue, N. Pan, M. Li, Y. Wu, X. Wang, and J. G. Hou, "Probing the strain effect on near band edge emission of a curved ZnO nanowire via spatially resolved cathodoluminescence.," *Nanotechnology*, vol. 21, no. 21, p. 215701, May 2010.

[85] B. Y. Kajikawa, S. Noda, and H. Komiyama, "Preferred Orientation of Chemical Vapor Deposited Polycrystalline Silicon Carbide Films," *Chem. Vap. Depos.*, vol. 8, no. 3, pp. 99–104, 2002.

[86] H. Sowa and H. Ahsbahs, "High-pressure X-ray investigation of zincite ZnO single crystals using diamond anvils with an improved shape," *J. Appl. Crystallogr.*, vol. 39, no. 2, pp. 169–175, Apr. 2006.

[87] S. Gražulis, D. Chateigner, R. T. Downs, a F. T. Yokochi, M. Quirós, L. Lutterotti, E. Manakova, J. Butkus, P. Moeck, and A. Le Bail, "Crystallography Open Database - an open-access collection of crystal structures.," *J. Appl. Crystallogr.*, vol. 42, no. Pt 4, pp. 726–729, Aug. 2009.

[88] E. U. Ando and M. Miyazaki, "Moisture resistance of the low-emissivity coatings with a layer structure of Al-doped ZnO/Ag/Al-doped ZnO," *Thin Solid Films*, vol. 392, pp. 289–293, 2001.

Chapter 8. Cell Viability on Zinc Oxide Nanowires

8.1. Introduction

This chapter is the summation of the results of previous chapter, where the properties of the two recipes are more rigorously tested for use in life sciences. The recipes both used 500 ml of precursor solution at 90 °C for 9 hours with four 22 x 22 mm glass coverslips substrates coated in 20 nm ZnO seed layer via PVD. They were both stirred for 15 and 5 minutes in room temperature (cold) and 90 °C (hot) DI water, respectively. The only difference being their precursor ratios 2:1 and 1:1, where 1 = 25 mM and ratio is $Zn(NO)_3$: HMTA. 2:1 was also included for phase two (cell-substrata interaction and viability) as it was deemed necessary as it was shown in the literature by ter Brugge et al. [1] that gaps between surface structures are non-adhesive for U-2 OS cells and so substrata with large gaps yield a reduction in proliferation rate. The results were split this way as the author felt the reader may understand better the reasons behind observations with respect to the cell-substrata interaction if the properties of the two recipes were covered beforehand.

In this work U-2 OS (ATCC, USA) osteosarcoma cells were used due to their low level of chromosomal anomalies and fast proliferation rate, to build upon the limited quantity of cell types explored for biocompatibility with ZnO nanowires, which have (at the time of writing) only been investigated for viability with Hela [2], H9C2, PC12 [3] and SAOS-2 [4]; and a preliminary investigation presented by the author for U-2 OS [5]. Three substrata are used throughout the study to help determine the role of nanowire morphology on the viability of cells on nanowires; including a glass coverslip for control. This preliminary investigation is phase two of a larger project, the first being reproducible production of ZnO nanowires covered in the previous chapter.

This chapter will cover the interaction of zinc oxide nanowires with an osteosarcoma cell line, specifically how different substratum surface properties affect both the viability and behaviour of the cells. The following areas have been investigated and will be discussed:

- Properties of ZnO Nanowire post Immersion in Cell Medium.

- Comparison of Nanowire Properties.
- Biocompatibility with MTS and LIVE DEAD Assays.
- Cell-Substratum Interaction with ImmunoGold SEM of α-vinculin.
- Substratum Surface Properties

The above will show how simple properties such as surface charge can have an astonishing impact on cell behaviour and proliferation.

Throughout the majority of data presented in the chapter the statistically derived relevance of the data will frequently be shown using Student's Ttest. In this chapter, if a Ttest line and asterisk encompasses multiple data groups then they all possess the same significant difference between each other; unless otherwise indicated by another Ttest bar and asterisk below. The majority of the data will show a groups significance versus the control, deviation from this will be explained in the figure caption. The significance will be shown in the following convention, * indicates $p < 0.005$ and ** $p < 0.05$.

8.2. Zinc Oxide nanowires in solution

Before it was decided that two recipes would be used to optimize data from cell-substrata interaction analysis, 1:1 was tested for its compatibility in solution for extended periods of time (up to 72 days for tissue culture). However, because the 2:1 nanowires are much wider than the 1:1 nanowires the surface to volume ratio will be significantly higher for 1:1 nanowires possibly leading to increased differential loss of ions from the lattice. Therefore if the structure of 1:1 remains intact for 72 hours there is a high probability that 2:1 will also.

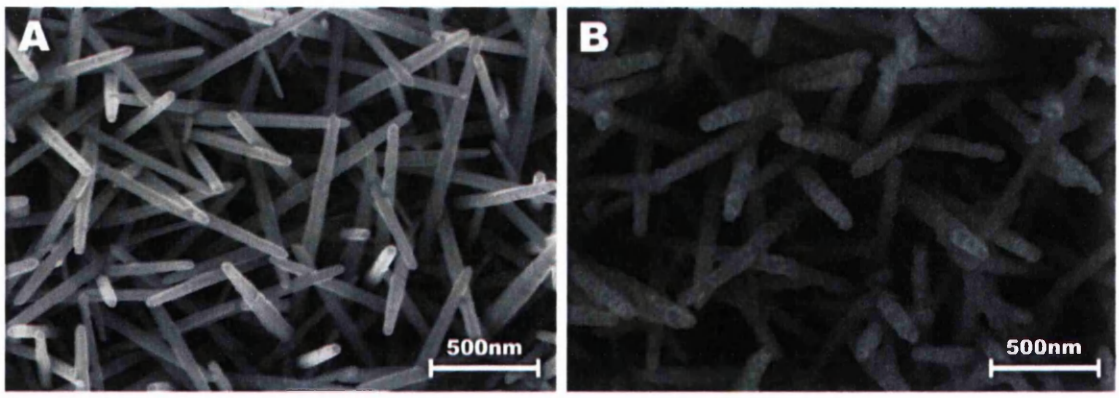

Figure 8.1. Scanning electron micrographs showing the changes in the appearance of zinc oxide nanowires (A) before and (B) after Ishikawa cells cultured for 2 days in DMEM medium at 37 °C 5 % CO_2 and subsequent fixation in 3 % Glutaraldehyde. It should be noted that cells were stored in PBS at 4 °C for 2 weeks prior to drying via ethanol series and imaging with SEM.

Normally in life sciences plates/experiments containing cells are fixed and stored in PBS at 4 °C for long term storage. However, it was found that this leads to significant degradation of nanowires, as seen in Figure 8.1., where the time-frame is as follows. The substratum was fabricated on the 29/03/2011 and promptly characterized with Scanning Electron microscopy (SEM) after removal from solution in the early hours of 30/03/2011, to allow Ishikawa cells to be seeded later that day on the 30/03/2011. After 2 days incubation in DMEM medium at 37 °C 5 % CO_2 the sample was fixed in 3 % glutaraldehye on the 01/04/2011, stored in PBS at 4 °C then imaged using SEM on the 13/04/2011. Fig. 8.1. shows that 2 weeks storage in PBS at 4 °C is sufficient enough to significantly degrade the nanowires, and therefore from this point onwards all experiments were run through an ethanol series and blotted for storage in an ambient environment at room temperature, unless otherwise stated.

Fig. 8.2. shows the changes in zinc oxide nanowire morphology after immersion in HBSS, McCoy's 5A medium and PBS at 37 °C 5 % CO_2 for 168 hours (7 days). Scanning Electron Micrographs acquired at 100,000x magnification highlight the extent of morphology change of the zinc oxide nanowires. Exposure to McCoy's 5A medium and PBS affects the surface and morphology of the nanowires more than HBSS.

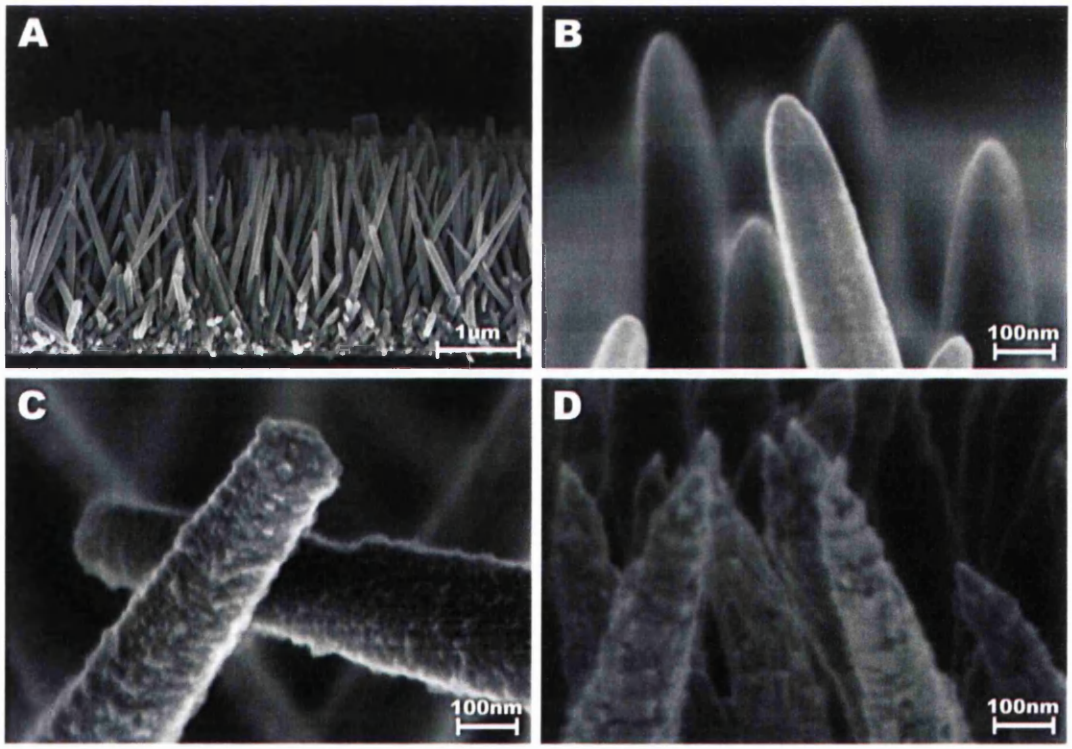

Figure 8.2. Scanning electron micrographs showing the changes in the appearance of (A) zinc oxide nanowires after immersion for 7 days at 37 °C 5 % CO_2 in (B) HBSS, (C) McCoy's 5A medium (supplemented with 10 % FBS) and (D) PBS.

The measured pH values for McCoys 5A media, PBS and HBSS were found to be 6.9, 7.4 and 7.2 respectively, using a VWR pHenomenal 221 pH meter. It has been reported by Zhou et al. [6] that ZnO nanowires are biodegradable in horse blood serum (pH = 8.5), with a single nanowire being dissolved completely within a few hours. Muller et al. [7] exposed ZnO nanowires to two different simulated body fluids (SBFs) in vitro, the first SBF was similar in ionic composition and pH to extracellular fluid (pH 7.4) and the second SBF similar to lysosomal fluid (pH 5.2) with human macrophage viability also observed. It was found that ZnO nanowires were stable at extracellular pH but readily dissolved at intracellular pH. But more importantly Muller concluded that the cause of macrophage necrosis was primarily the concentration of ionic Zn^{2+} rather than the substratum topography, as when the solutions were filtered to remove non-dissolved ZnO nanowires and the amount of dissolved Zn quantified (using Inductively coupled plasma mass spectrometry) it was found that the extracellular pH 7.4 SBF contained only 4.5 % of Zn added, compared to 99.3 % for intracellular pH 5.2 SBF. Therefore Muller concluded that the major cause of cell necrosis is via toxicity not phagocytosis. It should also be noted that T. Arnett [8] reported that osteoclasts are sensitive to extracellular H^+ is such that pH changes of 0.1 unit can be sufficient to cause changes in cell behaviour. Degen and Kosec [9] report that water molecules are chemically adsorbed onto the zinc oxide surface, where hydroxyl surface coatings adsorb protons at low pH (< 7.2) and lose them at high pH (> 12); creating a surface that changes charge with changing pH. A change to the surface coating of the nanowires is likely to alter the photoluminescence spectra obtained as it has been shown by Wang et al. [10] by using XPS and annealing their nanowires that the green centred DLE peak intensity is most likely controlled by multiple defects or defect complexes originating from centres at the nanostructures surface.

Fig. 8.3a shows the measurements taken from Scanning Electron Micrographs in Fig. 8.2, where it can be seen that in each solution nanowire width increases with increasing immersion time. Fig. 8.2 implies that the nanowires width decreases, however all width measurements are taken at the midpoint of length therefore it is more likely that the (0001) facet is more highly affected due to the higher reactively or charge of the that crystal plane. Otherwise, the 18, 63 and 93 % increase in nanowire width for HBSS, PBS and Media respectively, would be observable at the tip of the nanowire. However, the observed change in nanowire tip appearance is in line with observations by Sugunan et al. [11] who report that the (0001) polar facet will preferentially dissolve

in solutions with low Zn^{2+} concentration; therefore some dissociation of Zn ions is to be expected in all solutions. However given the small quantity (~1.22 μg/ml)* of ZnO nanowires used per well toxicology will likely not be due to mass of Zn ions as this should never exceed (if nanowires completely dissolved) 490 μg per well. Furthermore, Franklin et al. [12] investigated the effect of Zn in the water supply and reported an IC_{50} value for Zn ions at 72 hours incubation for freshwater alga (Pseudokirchneriella subcapitata) of 0.6 μg Zn/mL. However, Muller et al. [7] reports for human monocyte macrophages that an exposure to solutions of 6 μg /mL Zn concentration for 24 hours lead to cells loosing surface protrusions and nuclear chromatin became condensed. At 8 μg /mL, the cells started to show cell surface blebbing, indicative of apoptosis and at the highest concentration of 12 μg /mL, the cells were largely necrotic with leached out cell contents and highly condensed nuclear chromatin; with these values being more relavent. This is clearly not the case in this work as the cells show after 72 hours a nucleus that is well spread with distinct protrusions as seen throughout this chapter, a great example can be seen in sub-section 8.4.1. This is to be expected given the small quantity (~1.22 μg/ml)* of ZnO nanowires used per well. The aim of this work is not to prove that cells can withstand a certain amount of Zn ions, rather it is to prove that a nanowire array could be used to monitor cell mechanics; therefore this small quantity never needs to be exceeded. *Values based on 1:1 nanowires.

Only the nanowires immersed in McCoys 5A medium are observed to slightly increase their radius of curvature with the tip becoming more hexagonal compared to the original.. Since the medium is supplemented with 10 % FBS is can be assumed that this increase in width and radius of curvature is likely due to protein adsorption from the medium; creating the textured surface that appears as a heterogeneous collection of particles in Fig. 8.2c. Ideally a Sirius Red based assay should have been conducted as per work by Zhao et al. [13] to monitor the degree of protein adsorption to the substratum, to prove that observed morphological changes were indeed due to protein adsorption instead of some other unknown phenomena. However, EDX was conducted post immersion and will be discussed shortly, with Fig. 8.5.

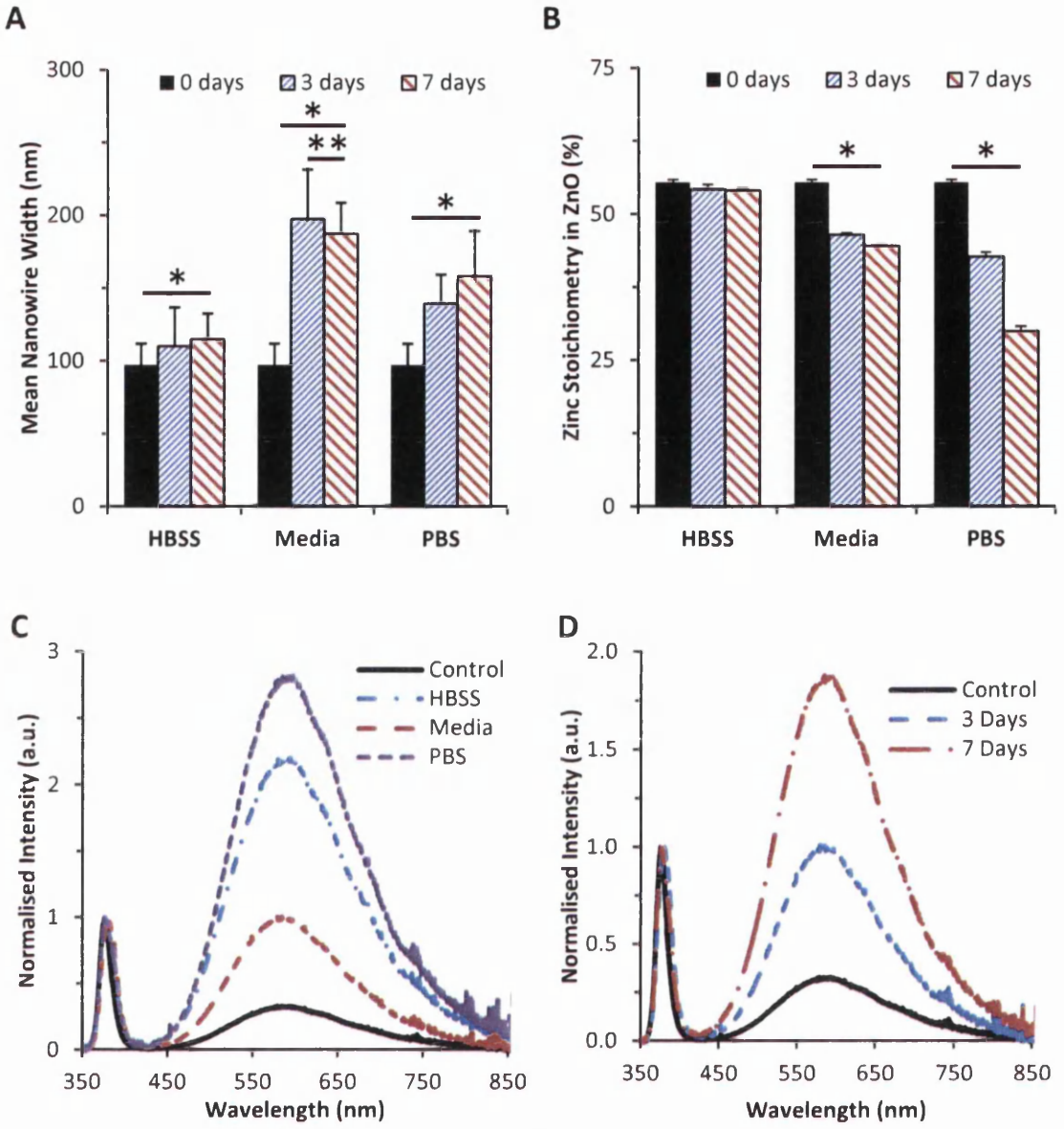

Figure 8.3. Changes in zinc oxide nanowire (A) width and (B) stoichiometry after immersion in HBSS, PBS and McCoy's 5A medium (supplemented with 10% FBS) for up to 7 days. Values represent the mean ± SD of 90 measurements, where * and ** indicate $p<0.005$ and $p<0.05$; respectively. (C) shows the change in photoluminescence spectra for nanowires immersed in all solutions for 3 days compared to initial (control) sample, while (D) shows the changes in DLE area due to immersion time for media only. A substantial increase in nanowire width for samples immersed in media can be seen in (A), this is likely due to significant protein adsorption within 24 hours as indicated by no change between 3 and 7 days.

Fig. 8.3c. compares the PL spectra of nanowires immersed in all solutions for 7 days, where it can be seen that the DLE band is greatly increased compared to the control. However, the two solutions are observed to negatively affect the morphology of the nanowires are also observed to yield the worst (highest) DLE peaks in Figure 8.3c; with DLE area increasing by 66, 85 and 89 % for Media, HBSS and PBS, respectively.

The slight increase in DLE peak intensity (compared to salt solutions) for nanowires immersed in media for 7 days further supports that the media is not as detrimental to nanowire morphology and that the observed 66 % increase in DLE area is likely due to the absorption of proteins. However literature shows that protein adsorption is typically detected using a more sensitive optical technique such as in situ ellipsometry and therefore it would be more likely that interaction with components within the medium has altered the surface properties of the nanowires, likely changing the amount of defect centres at the surface.

Fig. 8.3d. shows that the optical properties of the zinc oxide nanowires are significantly affected by immersion in medium for 3 days, where the DLE band is seen to increase in area with increasing immersion time. It is however unclear if this 83 % increase in DLE area from 0 to 7 days is due to a change in crystal quality or the inclusion of additional materials within the array, such as the coating in Figure 8.2c. It should be noted however that the PL spectra were obtained from dry samples post ethanol series and blotting, so there is no contribution from solution either. This is something that should have been investigated as obtaining spectra with live cells in solution may have substantially altered the optical properties of the nanowires; or even be impossible due to unknown refraction and excitation and emission properties of the liquid.

Fig. 8.4. shows the cross-section of a nanowire after immersion in McCoys 5A medium for 3 days at 37 °C 5 % CO_2. It can clearly been seen that the original hexagonal cross-section of the nanowire is mainly intact and that the coating that comprises of a heterogeneous collection of particles (between 5 - 15 nm in diameter) is most likely due to protein adsorption. EDX spectra acquired from the area shows elevated levels of carbon, calcium, magnesium and phosphorus (see figure 8.5.), thus indicating that the solution is reacting with the ZnO nanowires. Whether this is chemical or due to protein adsorption is unclear, however, Berlind et al. [14] have reported that adsorption of proteins on to implant surfaces strongly influences subsequent cellular response, where the cellular response determines if the implant is accepted by the body or not. Therefore investigating the cause of this reaction is crucial to further understanding biocompatibility findings later in this chapter.

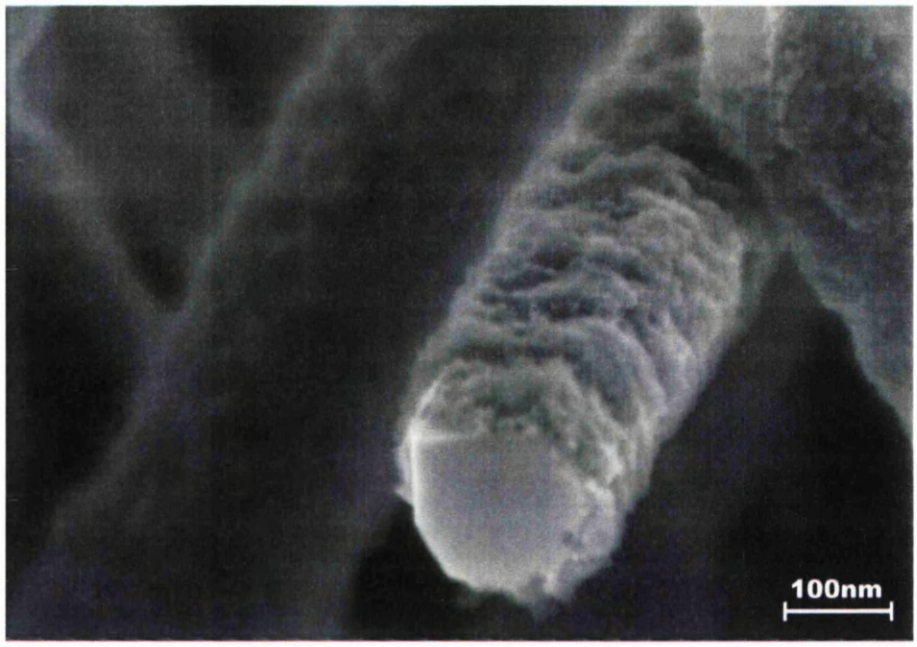

Figure 8.4. Scanning electron micrograph depicting the cross-section of a cleaved zinc oxide nanowire after 7 days immersion in McCoy's 5A medium at 37 °C 5 % CO_2. Notice how the medium has only affected the outside of the nanowire, with the hexagonal structure still intact. It appears the serum in the medium has allowed secretion of proteins for adsorption on to the surface to form an extra cellular matrix.

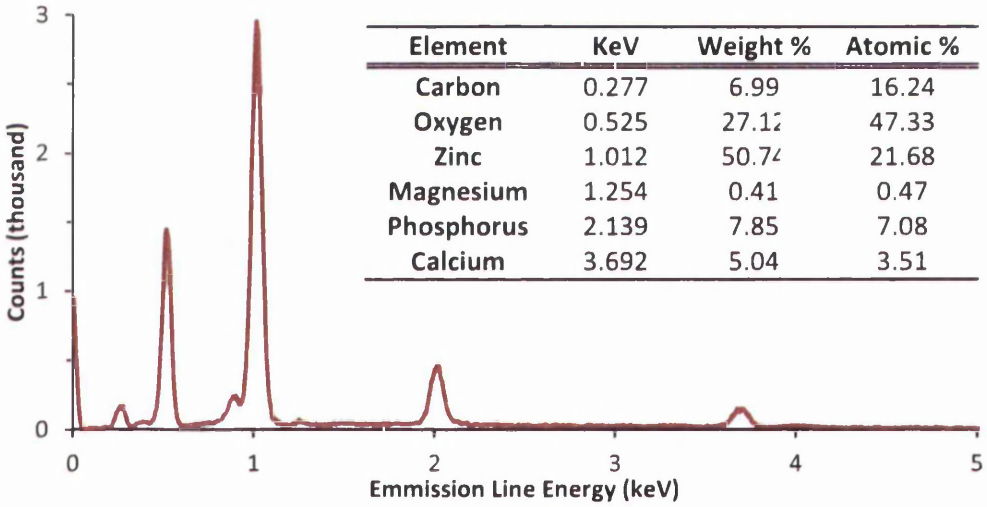

Element	KeV	Weight %	Atomic %
Carbon	0.277	6.99	16.24
Oxygen	0.525	27.1[illegible]	47.33
Zinc	1.012	50.7[illegible]	21.68
Magnesium	1.254	0.41	0.47
Phosphorus	2.139	7.85	7.08
Calcium	3.692	5.04	3.51

Figure 8.5. Energy dispersive x-ray (EDX) spectra of ZnO nanowires after immersion for 3 days in McCoy's 5A modified medium supplemented with 10 % FBS. Table (inset) shows peak labels and corresponding atomic percentages. The EDX spectrum shows magnesium, phosphorus and calcium; these are likely what makes up the surface coating on the non-polar facets.

The table within Fig. 8.5. shows the elements found and the quantity for ZnO nanowires immersed in medium for 3 days, rinsed in HBSS and run through an ethanol series to replace water before being allowed to dry in air. Any elements found in the scan will be securely attached to the nanowires rather than residue left behind from cell

culture due to the washing protocols. It is interesting that chlorine and sulphur are not present in the spectrum together with magnesium and calcium since both magnesium sulphate and calcium chloride were inorganic salts used in McCoy's 5A medium (see Table 8.1.). However this will likely be because chlorine and sulphur have formed bonds with zinc ions forming inorganic salts zinc chloride and zinc sulphide ($ZnCl_2$ and ZnS); in doing so the amount of free zinc ions in the solution will have been greatly reduced reducing the toxicology of ZnO nanowires in McCoy's 5A medium. EDX spectrum supports this hypothesis as chlorine and sulphur were not detected, as these elements will have been removed with the supernatant as salt solutes. Also the reduction in the zinc : oxygen ratio from (in Fig. 7.44c) 55 % zinc to 31 %, is highly indicative of preferential dissolution of Zn ions into the solution. It should be noted that even though the electron acceleration voltage was increased to obtain calcium at 3.6 KeV, the interaction volume can be seen from the data not to be sufficiently big enough to obtain information from the glass (SiO_2) substratum as silicon (1.74 KeV) is not present in the spectrum. It is also possible that the layer present in Fig. 8.4. is not a coating due to serum protein secretion but some other form zinc oxide – solution interaction. It has been reported by Govender et al. [15] that ZnO is susceptible to the influence of counter-ions during growth, this could also be the case during dissolution.

Table 8.1. Concentration* of Inorganic Salts in Solutions used for immersion experiment

	McCoys 5A (mM)	PBS (mM)	HBSS (mM)
Calcium Chloride	0.898	-	1.26
Magnesium Chloride	-	-	0.493
Magnesium Sulfate	0.813	-	0.407
Potassium Chloride	5.33	-	5.33
Potassium Phosphate monobasic	-	10.59	0.441
Sodium Bicarbonate	26.19	-	4.17
Sodium Chloride	111.38	1551.72	137.93
Sodium Phosphate dibasic	4.16	29.66	0.338

* Values taken from Invitrogen: http://www.invitrogen.com/site/us/en/home.html

To confirm that the observed heterogeneous collection of particles was indeed protein absorption ideally sodium dodecyl sulfate (SDS) could have been added to detach the proteins from the surface so that a MicroBCA protein assay kit could have been used to determine the amount of protein present. Using this method Zhao et al.

[13] were able to determine that protein adsorption is slightly enhanced on nanowire arrays compared to control substratum.

It is easier to understand the importance of these experiments when put in context. ZnO nanowires are being tested in this chapter for their biocompatibility, so they can (as in the brief) be used as a novel force sensor for cell mechanics. However, there is lots of work in the literature using ZnO for bio-sensing due to its unique properties (covered in chapter 2), and a key component of biocompatibility testing is consideration for effects of implantation of devices and their survival rate in vivo. In other words the activation of immune system response may be initiated when foreign materials (ZnO nanowires) are implanted in the body, where an uncontrolled inflammatory response may occur upon contact with blood leading to thrombus formation. The formation of fibrous capsule around an implant (because of prolonged inflammation) would certainly increase the probability of the bio-sensor not functioning correctly (depending on the application). Therefore to witness such successful protein adsorption (in Fig. 8.4.), though not confirmed by SDS assay or Null Ellipsometry* is an essential step in proving that ZnO nanowires could survive in vivo application. *Null Ellipsometry monitors changes in refractive index of substratum due to changes in surface properties, allowing detection of adhering proteins and lipids.

8.3. Comparison of selected Zinc Oxide nanowire recipes

In this work two different substrata were created by coating glass coverslips in the two different ZnO nanowires recipes used in this study (researched in chapter 7) are compared in Fig. 8.6, showing SEM images of the larger, sparser, better aligned 2:1 nanowires on the left hand side and the thinner, denser, less aligned 1:1 nanowires on the right hand side. After initial observations it was hypothesised that the cells would respond better to the environment provided by the 2:1 nanowires, likely maintaining a normal proliferation behaviour compared to the 1:1 nanowires due to the increased width and density of the 2:1 nanowires providing a more suitable surface; see Table 8.2. This hypothesis is further supported by ter Brugge et al. [1] who reported that changes in substratum roughness can alter cell function due to substrate induced cell shape changes affecting integrin formation, ultimately interfering with intracellular signaling events. Before exploring cell-substrata interaction the following sub-sections will

investigate and compare morphology using SEM, optical properties using PL, chemical composition using EDX and XRD and elasticity and susbtrata roughness using AFM.

8.3.1. Morphology (SEM & AFM)

Fig. 8.9. shows the difference in morphology for the nanowire arrays fabricated from the two recipes. In terms of cell growth, the available surface for attachment is substantially different both in morphology and charge. As briefly mentioned already, it has been shown by Joo et al. [16] that face sensitive electrostatics can alter chemical attachment of particles to the polar and non polar facets of zinc oxide nanowires, it could therefore by assumed even at this point that the significant difference in surface area of the (0001) plane could affect cell attachment, given that the U-2 OS cells may or may not like to adhere to the (0001) plane based on surface charge. Bodhak et al. [17] report that surface charge and wettability affect surface adhesion and proliferation of human fetal osteoblast cells (hFOB). Their results show that tailoring the wettability and surface charge of their substrata enabled differential binding of inorganic ions (Ca^{2+}, Cl^-, Na^+, HCO^{3-} etc ~as observed in Fig. 8.5.~) and organic cell adhesive proteins (fibronectin, vitronectin etc) with different surface properties, resulting in accelerated or decelerated proliferation depending on the surface charge and wettability. Both the taper and the radius of curvature or surface area of (0001) facets are different for the two recipes. The 1:1 nanowires are clearly much more tapered than the 2:1 nanowires with a small radius of curvature (26 nm) while the 2:1 nanowires have uniform widths and have a flat (0001) facet at the tip. This could therefore lead to substantial differences in terms of cell adhesion and biocompatibility between the two samples.

Wang et al. [18] suggest that Zn^{2+} precursor concentrations of less than 25 mM provides insufficient growth units, such that the seed layer is partially dissolved forming a concentration gradient between the substratum and the tip of the nanowires. This gives the nanowires their tapered shape, while precursor concentrations of more than 25 mM provide sufficient homogeneous distribution of growth units throughout the solution such that no gradient of concentration forms and nanowires are not tapered. However many researchers attribute tapering of nanowires to the amount of Ostwald ripening of the seed layer, as discussed in sub-section 7.5.2. Lee et al. [19] have attributed the tapered tip profile to the minute (0001) steps between layers, where they intentionally retard Ostwald ripening removing the tapered tip profile of their nanowires.

Equation 3.2. Indicates that solubility of the seed layer increases with decreasing grain size, therefore the smaller seed crystals tend to dissolve and deposit on larger particles. Since all seed layers are deposited at the same time this cannot be the mechanism for the taper, unless this argument is combined with Wang et al. [18] suggestion that < 25 mM Zn^{2+} precursor concentration provides insufficient growth units leading to dissolution of the seed layer. It could be that the lower $ZnNO_3$ concentration for the 1:1 recipe (compared to 2:1) leads to altering of the seed layer in the initial stages of growth.

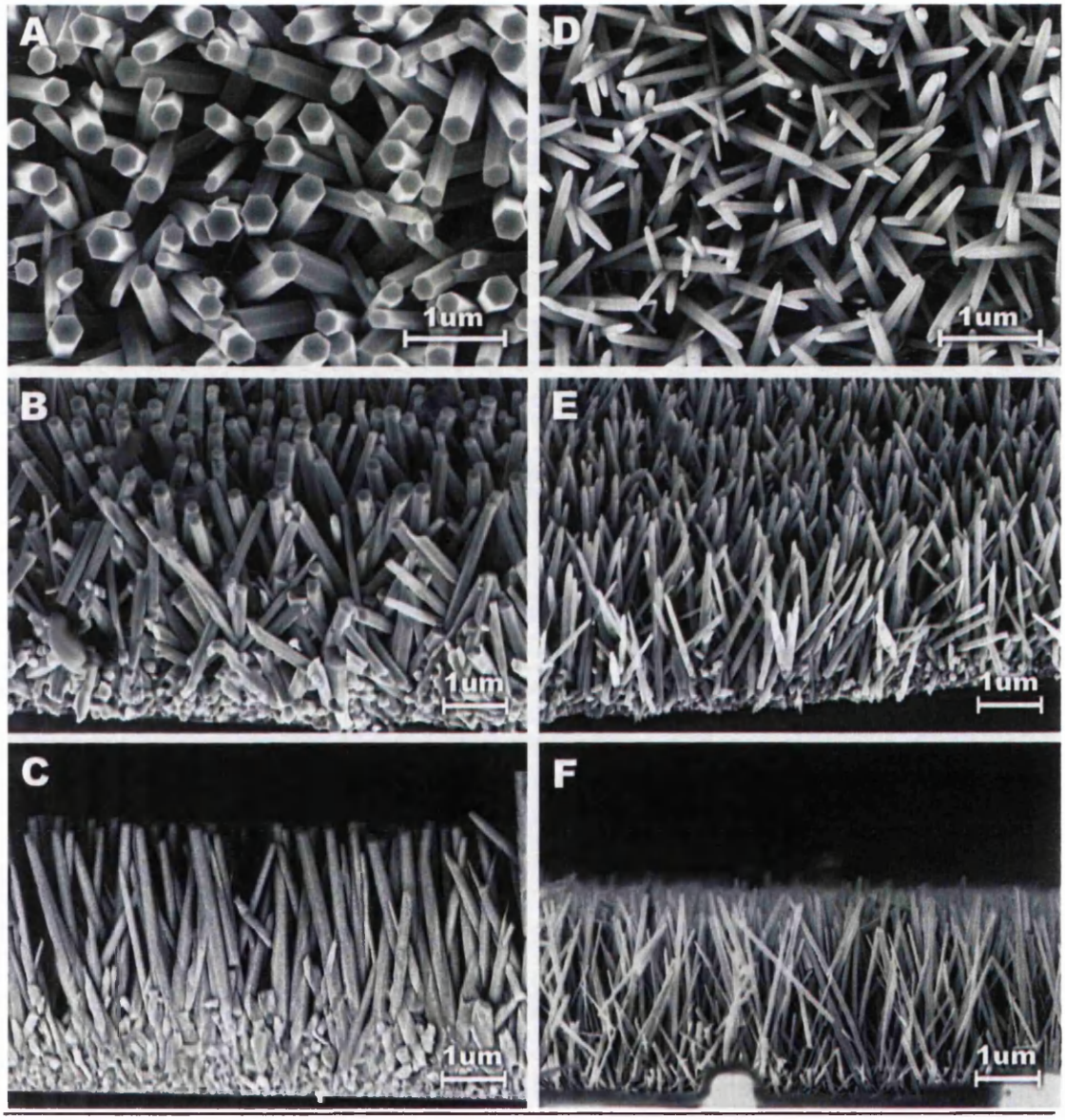

Figure 8.6. Scanning electron micrographs comparing the morphology of the two selected zinc oxide nanowire recipes, 2:1 (A-C) and 1:1 (D-F).

As discussed previously in sub-section 7.5.2. the mean angles shown in Table 8.2. show the angular spread distribution of the nanowires. For example, the Table 8.2. shows that nanowires growth using the 2:1 recipe may on average diverge from being orientated perpendicular to the substrate by ±6.7°. That is to say that the nanowires in the array grown at using the 2:1 precursor ratio recipe are on average aligned between 83.3 – 96.7° with respect to the substrate; in other words they're well aligned. This is a crucial value often over looked in literature with many researchers just merely stating their nanowires to be 'well aligned' as an evaluation of alignment or vertically of nanowires [20,21]. Obtaining a quantitative measurement of alignment can help explain several trends seen, for example when observing Fig. 8.6. it is apparent that the mean angle value holds true as 2:1 appears to be visually more well aligned than 1:1, but the angle supports this observation quantitatively. Alignment is extremely important as it controls the way in which the cells interact with the surface and more quantitative analyse improves understanding of how forces exerted by the cells bend the nanowires and even control cell behaviour.

Table 8.2. Comparison of nanowire properties for 2:1 and 1:1 recipes (n=90).

	2:1 NWs	**SD**	**1:1 NWs**	**SD**
Length (μm)	4.4	0.14	3.3	0.13
Width (nm)	176	25	97	15
Angular Spread (°)	6.7	±4.6	9.9	±6.6
Aspect Ratio	25.1	-	33.8	-
Density (/cm^2)	1.32×10^{10}	-	2.55×10^{10}	-

Data from Table 8.2. indicates that nanowire arrays fabricated using the 1:1 recipe are more likely to have larger gaps between nanowires due to their mean diameter, and although the density of 1:1 is higher the width is half of that yielded by the 2:1 recipe. Also the mean angle of divergence from the c-axis is larger, creating more gaps in the surface, as seen in Fig. 8.6. Chen et al. [22] have shown that non adhesive regions severely affect the formation of focal adhesions and therefore the overall shape of the cell; this would be the case here as a gap between nanowires is essentially a non-adhesive region, an area where the cell is unable to attach to the surface; thus affecting the cells shape and function [23]. This difference in density is more easily understood when compared over a much larger range, where Fig. 8.7. shows AFM images over 25x the area. AFM images were obtained in non-contact

tapping mode as to not blunt the tip, and allow collection of RMS roughness measurements in situ. Images were obtained using a Silicon tip of 8 nm radius (RTESP, Bruker) with a 'thermal tune' calibrated frequency of 334.65 kHz, assuming this was never blunted the image should not contain surface imaging tip artifacts as the nanowires are an order of magnitude larger in width. Also the scanning velocity was slow at 0.5μm/s to minimise dragging artifacts causing low gain values in feedback, the raster direction is indicated by the 'fast' axis label in Fig. 8.7. The images show how different the two substrata are with (B) or 1:1 yielding a surface with far more and larger gap regions with no nanowires, how this affect cell proliferation and behaviour will be investigated further in sub-section 8.4.2.

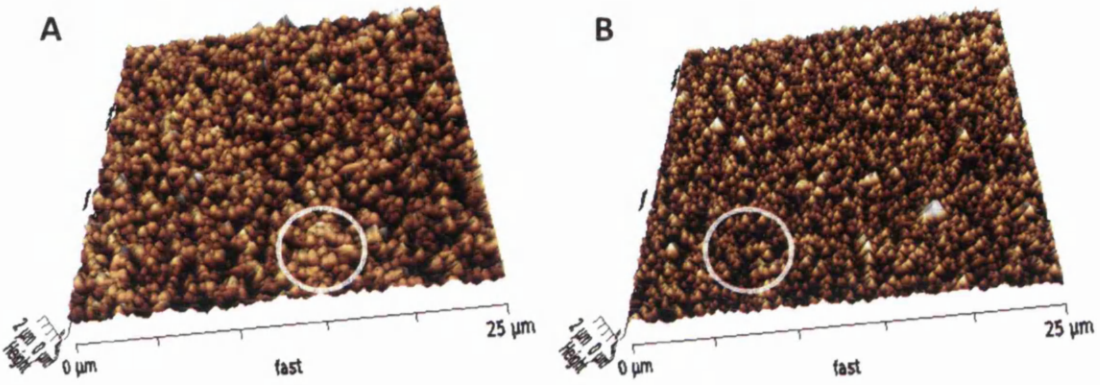

Figure 8.7. Atomic force micrographs showing the substrata available for the cells, where substratum (A) is comprised of an array of 2:1 zinc oxide nanowires and (B) 1:1 nanowires. It should be noted that the X Y ranges for the above AFM images are 5x larger than the SEM images in Fig. 8.6. White circles show regions on high density with little space between 2:1 nanowires and much larger space available between 1:1 nanowire tips for images (A) and (B), respectively.

8.3.2. Chemical properties (EDX & XRD)

The chemical properties of the two recipes were compared using both EDX and XRD, to confirm both recipes produce zinc oxide. Fig. 8.8. shows both EDX and XRD, where it can be seen that both 2:1 and 1:1 are almost identical in with only subtle differences. Fig. 8.8a shows the energy dispersive x-ray spectroscopy (EDX) spectra for both samples, where only zinc and oxygen can be seen indicating no contaminants are introduced via the hydrothermal method. 2:1 is offset by two thousand counts for clarity. Lα zinc (1.01 KeV) and Kα oxygen (0.52 KeV) peaks can be seen, however the zinc peaks (Kβ and Kα) at 8.63 and 9.57 keV are not shown here as the beam energy was only 5 kV to minimise the interaction volume within the sample and avoid

obtaining data from the glass substratum. EDX shows that both samples are ZnO, however it should be mentioned again that the EDX SSD (see chapter 4) detector has a detection limit of 200 ppm, so trace amount of contaminants may exist below this limit, as indicated in work by Bell and Garratt-Reed [24]. EDX can be used to determine stoichiometry allowing comparison between the two samples, where 2:1 yielded atomic percentages of 54.3 and 45.7 % while 1:1 yielded 51.5 and 48.5 % for zinc and oxygen, respectively. This result is in good agreement with observations by Xue et al. [25], and certainly indicates that the 1:1 nanowires have close to ideal stoichiometry.

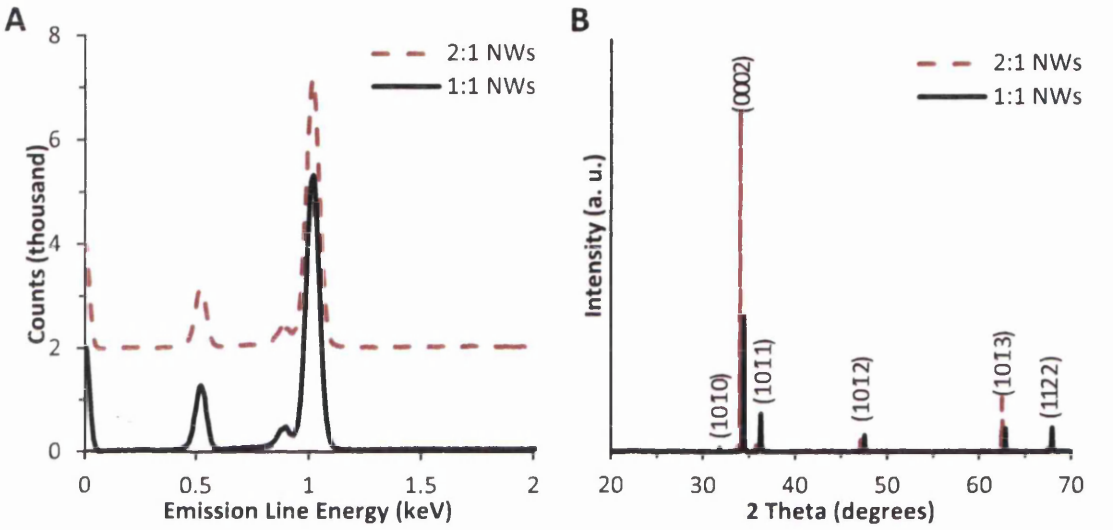

Figure 8.8. The graphs compare 2:1 and 1:1 ZnO nanowires, where (A)* shows the energy dispersive x-ray spectra and (B) the x-ray diffraction spectra, with key orientation peaks labelled for ZnO. *2:1 nanowires are offset by 2000 counts for clarity.

Fig. 8.8b shows the X-ray diffraction spectra (XRD) spectra for both samples, where both spectra have been matched to ZnO taken from reference card 96-230-0113 [26], freely available online from the Crystallography Open Database [27]. However, 2:1 had to be manually shifted by 0.372 ± 0.016 ° to match the reference card, the reasons for this will be discussed shortly. The (0002) peak for 1:1 (34.458 °) is similar to the (0002) peak position of ZnO powder (34.43 °) reported by Kumar et al. [28], meaning these wires are of extremely high crystal quality. Also, the (0002) peaks exhibit the lowest full width at half maximum (FWHM) and highest intensity compared to the other diffraction peaks for both samples, with a FWHM of 0.065 and 0.059 for 2:1 and 1:1, respectively; see Table 8.3. Thus, indicating the [0001] direction is the preferred growth direction for both samples. Both XRD results show the nanowires are free from impurities as no non ZnO diffraction peaks were detected within the measured

region, and such narrow diffraction peaks show that the material is of good crystallinity [29]. However, 2:1 is not free from internal strain due to the 0.372 ° shift in the spectra. Work by Ando and Miyazaki [30] has shown that shifts in peak position to lower diffraction angles are due to substantial internal strain. This supports the EDX findings nicely as such strain could be caused on an atomic level due to the imbalance of zinc to oxygen (as shown in Fig. 8.8a) ratio resulting in oxygen vacancies, zinc interstitials or zinc antisites. Photoluminescence spectra in Fig. 8.9. also supports this as is has been shown in the literature by Sans et al. [31] that many recombination mechanisms that compete with exciton-related luminescence are dependent on the stoichiometry of ZnO rather that the amount of defects present. As zinc is much larger than oxygen strain will develop and this has been detected by XRD, this finding ideally needs to be supported optically as oxygen vacancies are commonly reported in the literature to contribute to the DLE band emission [32]. However, a shift of 0.372 ° is seen throughout the spectra for each peak position so it is more likely that misalignment of goniometer is the cause of such a shift, as the literature predominantly mentions a (0002) peak shift only [33].

Table 8.3. FWHM of peaks in Figure 8.8b, highlighting (0002) is the preferred orientation.

Sample	Plane	$(10\bar{1}0)$	(0002)	$(10\bar{1}1)$	$(10\bar{1}2)$	$(10\bar{1}3)$	$(11\bar{2}2)$
1:1	**Peak Position (°)**	31.788	34.458	36.282	47.566	62.884	67.970
	FWHM	0.074	0.059	0.133	0.104	0.069	0.133
2:1	**Peak Position (°)**	31.399	34.076	35.898	47.196	62.531	67.617
	FWHM	0.097	0.065	0.136	0.0881	0.0906	0.130
Ref. Card:	**96-230-0113**	31.773	34.430	36.260	47.549	62.873	67.961

8.3.3. Optical Properties (PL)

EDX and XRD has shown that although nanowires grown using the 2:1 recipe are comprised of ZnO they appear to be of poor crystal quality with XRD showing a peak shift due to considerable internal strain. It was hypothesized that this strain detected by XRD was likely due to an imbalance in the zinc : oxygen ratio as shown by EDX where this could be due to heavy oxygen vacancies incorporation during growth. Fig. 8.9. shows that this is indeed likely to be a good hypothesis as 2:1 can be seen to have a much larger DLE peak intensity than 1:1, with a DLE area increase of 45 %. As with the previous chapter the typical spectra is obtained, showing the expected UV near band edge (NBE) emission for ZnO at 375.8 nm as well as the deep level emission

(DLE) centred at 588.9 nm normally attributed to defects in the material, such as oxygen vacancies [34].

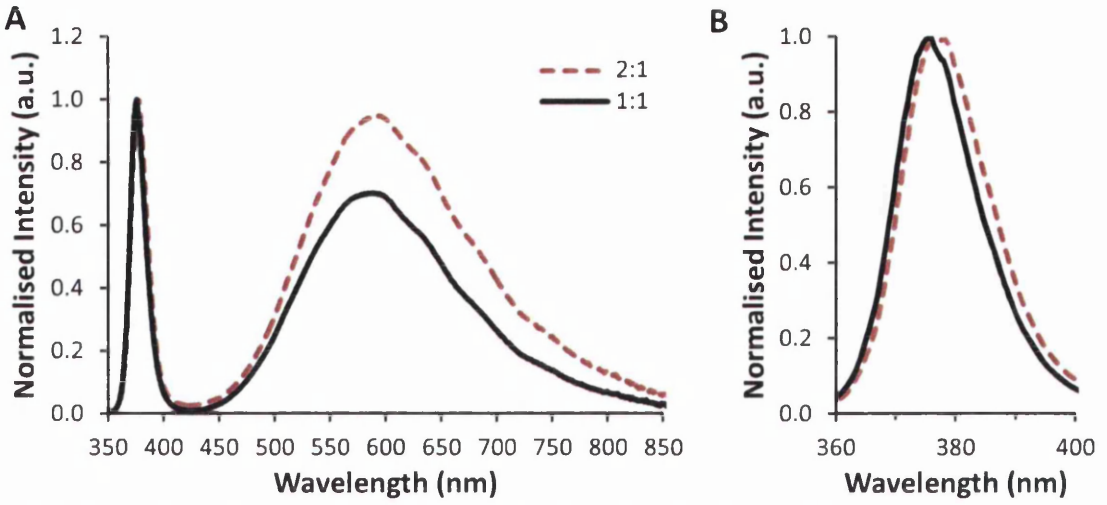

Figure 8.9. The photoluminescence spectra for 2:1 and 1:1 nanowires, where both spectra have been normalized to the near band edge and calibration for absolute irradiance. (B) shows the NBE peak, where a slight redshift of the 2:1 NBE peak can be observed.

Fig. 8.9b shows a subtle redshift of 2.2 nm from 375.8 to 378.0 nm for 2:1 and 1:1, respectively. It has been shown by Deenathayalan et al. [35] that optical absorption determines the optical band gap, with the band gap decreasing with solution concentration increase; further indicating a change in crystal quality. Srikant and Clarke [36] have reported a 0.1 eV (~11.3 nm) shift in band edge emission due to thermal mismatch strain in annealing experiments, with peak shift indicating a change from that of a perfect, unstrained single crystal to one containing point defects, dislocations, impurities and strain. Since only minor differences are observed in Fig. 8.9b it can be concluded that both samples contain some degree of defects and strain, clearly supported by their ample contribution from deep level emission. From Fig. 8.9a. both samples appear to have similar crystal, though the subtle difference in NBE peak position may affect the application of 2:1 to cell-substrata interaction studies, if changes are to be recorded via optical observation. This result is in line with observations by Reynolds [37] who report that the green emission in ZnO increases rapidly with increasing Zn concentration. This is shown with the reduction in NBE : DLE peak intensity ratio from 1.42 for 1:1 to 1.05 for 2:1 in Fig. 8.9b; these values are similar to the of 1.10 for an early 1:1 recipe from Fig. 7.9b.

However work by Ha et al. [34] has shown that the ZnO crystal lattice maybe 'healed' by thermal excitation in argon or oxygen. It was previously shown that the 0.3719 ° shift in XRD spectra for 2:1 was likely due to internal strain, with EDX showing excess zinc and PL showing excess defects, most likely oxygen vacancies. Several experiments were conducted to see if the crystal lattice could be 'healed' in this work with extremely favourable results witnessed, essentially showing that the DLE part of the spectra for both 2:1 and 1:1 could be substantially reduced. See section 4.4.2. Wang and Reynolds [38] revealed that post oxygen annealing their nanowires didn't have any significant change in stoichiometry, although they did gain a dramatic reduction in the UV-to-GL intensity ratio (from 0.4 to 0.023). With this information and the previously discussed breakdown of spectra it could be concluded that although the amount of oxygen hasn't changed within the nanowires the interstitials have been given sufficient energy to fill vacancies. A similar result was reported by Gupta and Mansingh [39] who reported that the improvement with annealing was due to a reduction of stress within the crystal lattice; which supports both this works results and spectra breakdown by Ha et al. [34]; see appendix I. It is worth noting that regardless of DLE shape/origin the NBE to DLE peak ratio has been improved significantly enough (with an order of magnitude improvement from 0.59 to 5.7) at this point to show that the 2:1 recipe with an additional annealing treatment can yield nanowires of the same optical quality as 1:1.

8.4. Biocompatibility of Zinc Oxide nanowires

This section will briefly cover the development of cell culture and problems that were overcome before moving onto biocompatibility, where results obtained from observation (SEM) as well test kits from both Promega (MTS) and Invitrogen (LIVE DEAD) are used to establish whether or not ZnO nanowires are biocompatible. This result is then supported with Cryo-SEM, giving the first insight into cell-substrata interaction ready for section 8.4. where surface properties such as charge, roughness, wettability, and adhesion of the two substrata are investigated.

Originally Ishikawa cells were used for cell-nanowire interaction studies while both the nanofabrication and microbiology aspects of the work were refined in tandem. Fig. 8.10. shows Ishikawa (or lack of) cells on ZnO nanowires after 48 hours incubation in DMEM medium at 37 °C 5 % CO_2, and represents the one of the initial findings before protocols were optimized through trial and error (and research). In these images the

Ishikawa cells have been removed, with only cell remnants remaining, as in Fig. 8.10b where the cell seems to have preferentially attached using the outer edge of its cytoplasm. As discussed in chapter 5 while a cell migrates across the substratum and is ruffling at the leading edge, the sections at the rear can remain adhered and get drawn into long retraction fibers, see Fig. 5.5e. These can often break suddenly leaving behind a fragment of adherent plasma membrane and cytoplasm [40]. However, given the amount of cytoplasm observed in Fig. 8.10b. and the removal of nanowires the cell has likely become necrotic and detached from the substratum. It is therefore unclear if the nanowires have been dissolved due to phagocytosis or removed with the cell during rinsing cycles.

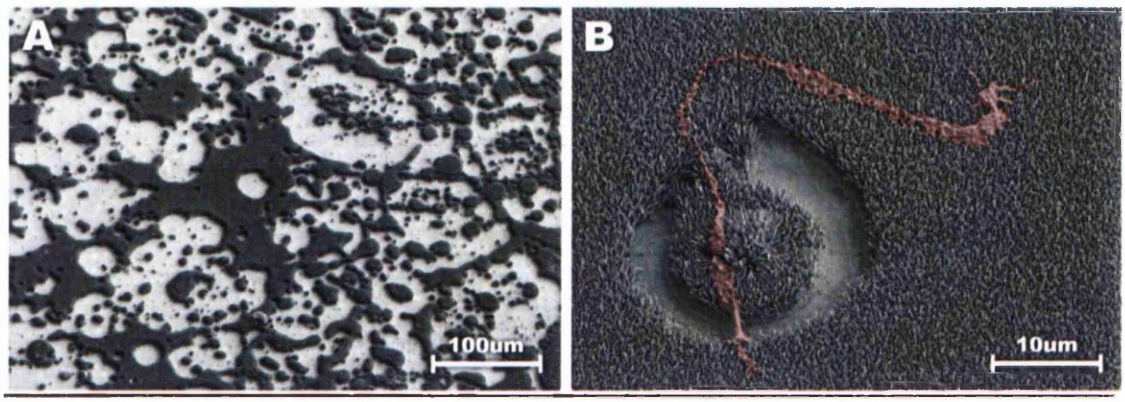

Figure 8.10. Scanning electron micrographs showing (A) destruction of zinc oxide nanowire substratum grown from a spin coated seed layer and (B) higher magnification image showing cell remnants adhered to substratum. It can be concluded from the images that the spin coated seed layers do not provide suitable attachment to glass substrate to withstand the substantial washing cycles in either cell culture or cell fixation. Samples fixed in 3% gluteraldehyde

The dissolving of ZnO nanowires due to phagocytosis is plausible as it has been reported by Muller et al. [7] that intercellular pH in lysosomes are acidic enough (pH 5.2) to break down ZnO, compared to extracellular simulated body fluid (pH 7.2) where nanowires remained unperturbed for 1 day. However, it is more likely that the cell-nanowire adhesion has remained intact and that aggressive rinsing cycles have broken the seed layer-glass substratum bond, reported as thin as 3.5 nm for spin coated samples [41]. Therefore spin coated substrata were phased out in favour of PVD coated substrata after findings like Fig. 8.10. were frequently observed. Fig. 8.11. shows the improvement yielded from transition from spin coated to PVD coated ZnO seed layers, where cells were always found to be well attached. However, the fine structures such as fillipodium were always perturbed and often damaged, as in Fig. 8.11b. This prompted

investigation into the fixative protocol to use, as well as use of U-2 OS instead of Ishikawa due to more favourable results during initial trials.

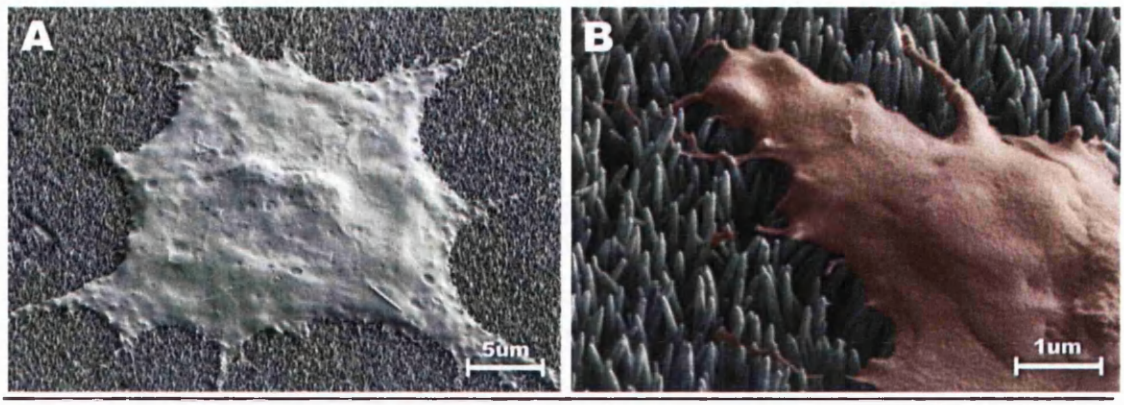

Figure 8.11. Scanning electron micrographs showing (A) typical arrangement of Ishikawa on substratum comprised of an array of zinc oxide nanowires and (B) lamellipodium attachment to substratum. Notice that the majority of fillipodia have been perturbed and even destroyed possibly during fixation. Cells were cultured for 2 days in DMEM medium at 37 °C 5 % CO_2, then fixed with 3 % glutaraldehyde. It should be noted that both images were acquired at 45 °.

8.4.1. U2-OS (Fixed cell SEM)

Due to the opaqueness of the ZnO nanowire array traditional optical microscopy techniques could often not be used, as they often involve an inverted microscope and rely on transparent samples. Therefore initially the cells were inspected using scanning electron microscopy after fixation to check cell shape and confluency after a 3 to 7 day culture. As explained in chapter 6 for a typical experiment whenever a new substratum was fabricated biocompatibility was initially inspected using SEM to check confluency and numbers as both light microscopy and confocal microscopy techniques were nearly impossible with an opaque substrata. More detailed explanation of the reasons for not conducting a quick DAPI / PI (or EthD-1) check on an inverted sample was discussed in sub-section 6.3.3. Generally, U-2 OS cells were cultured in M cCoy's modified 5A medium supplemented with 10 % fetal bovine serum (FBS), 1 % penicillin / streptomycin (pen/strep) and 1 % glutamine (Glut); incubated in a 5 % CO_2 environment at 37 °C in T75 culture flasks. At ~90 % confluency cells were trypsinized, re-suspended in media and 10 µl added to an automated cell counter (Bio-Rad TC10) to obtain cell concentration without use of equation 6.1. The 49 – 64 mm^2 glass control and ZnO nanowire substrata were washed twice in 100 % ethanol then PBS prior to being added to a 48-well plate. Cells were carefully pipetted on top of the substrate and given 2 minutes to attach before being supplemented with 500 µl fresh media as

suggested by Francis et al. [42]. Typically cell populations were always low (2000) and high (8000) cells seeded from often a 2.5 $x10^5$ /ml stock solution, and plates were incubated at 37 °C in 5 % CO_2 for as long as the experiment required.

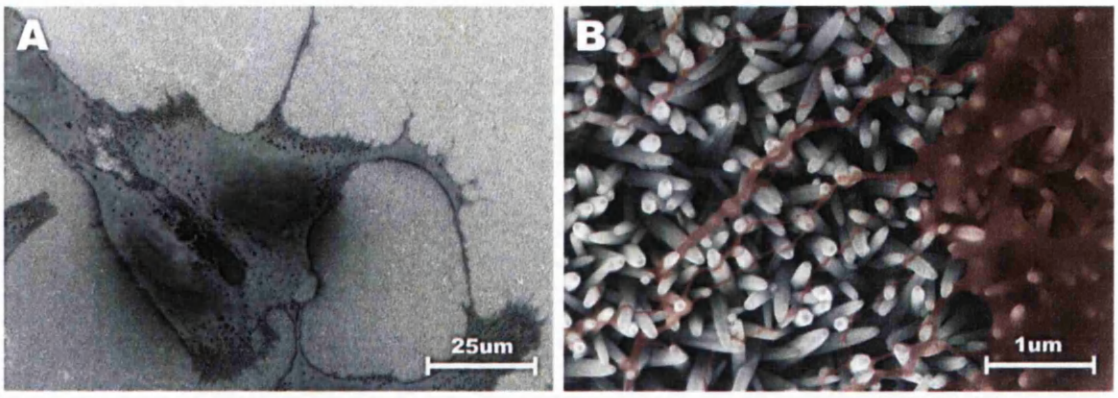

Figure 8.12. Scanning electron micrographs showing (A) typical arrangement of U2-OS on substratum comprised of an array of zinc oxide nanowires and (B) fillipodia attachment to substratum. It can be seen that the fillipodium appear to avoid the [0001] polar facet of the nanowires with preferential attachment to the non polar facets seen throughout the image in (B). Cells were cultured for 3 days in McCoy's 5A modified medium at 37 °C 5 % CO_2.

Fig. 8.12. shows a few U-2 OS cells on ZnO nanowires after 72 hours, where it can be seen that protocols have been sufficiently refined to the point that all the fine details are maintained post cell fixation and dehydration, as emphasized by Fig. 8.12b. Also from the shape of the cells and the extension of the lamillipodia it can be seen that the cells are healthy. Typically, adhesive cells exhibit a globular, bunched quasi-spherical shape when not pleased with the environment. Saravia et al. [43] promote such findings with HepG2 cells on positively and negatively charged surfaces, stating that the substratum yielding larger cell areas is more biocompatible. This will be covered later with observations from MTS (next) and cell spreading area (sub-section 8.5.1.), as it is commonly accepted in the literature that mitosis is completed halted when cell area falls below a critical value [44]. However, work by Bacáková et al. [45] has shown that although a cell with a large spreading area may appear healthy it may not be gearing up for mitosis / proliferation, instead it may be ready to differentiate.

8.4.2. Promega's MTS Assay

The effect of ZnO nanowires on cell proliferation was examined using the MTS assay, as discussed in section 6.3 knowing the proliferation rate of the cells is not always an indication of biocompatibility as the population doubling rate can slow for

any number of reasons, such as elevated $C0_2$ [46] or even if the cells are seeded at such a low concentration as to inhibit signalling [40]. For example, this could mean that two wells could not double within the doubling period yielding the same number of cells, yet the reason could be either proliferation inhabitation or cell necrosis. However even a change in cell proliferation rate indicates a change in cell behaviour that could be due to adverse conditions in the environment. Therefore, MTS results have also been confirmed using various other techniques that will be discussed within this chapter.

The response of U-2 OS cells to the addition of hydrothermally grown zinc oxide nanowires has been experimentally examined by observing the activity of the mitochondrial enzyme succinate dehydrogenase (SDH) in U-2 OS Cells. After a 72 hour incubation period 50 µl of Promega's MTS (3-(4,5-dimethylthiazol-2-yl)-5-(3-carboxy-methoxyphenyl)- 2-(4-sulfophenyl)-2H-tetrazolium) solution was added to each well, (except for media controls used for background removal) and then re-incubated for 4 hours. 50 µl was found after several assays to be sufficient for the amount of cells present in 48 well plate and deviates from Promega's suggested amount 20 µl / 100 ml, the reasons for this were explained in sub-section 6.3.1. 500 µl of medium was used in each well as this was the upper medium volume limit for a 48 well plate to still enable gaseous diffusion through the liquid, as per equation 6.2 [47].

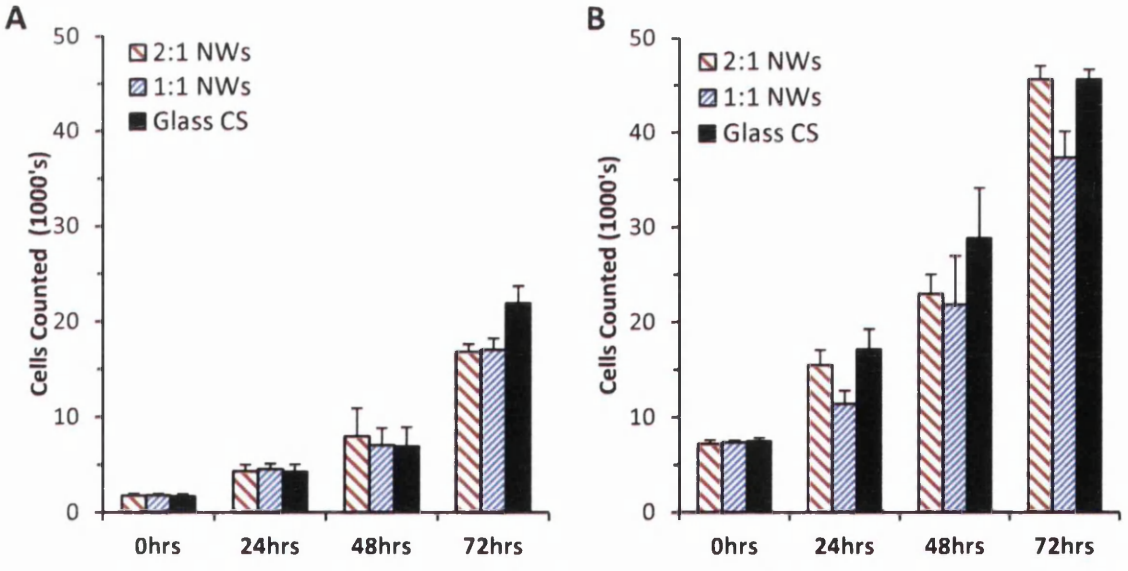

Figure 8.13. Graphs showing the amount of cells counted using MTS assay for different substrata at 0, 24, 48 and 72 hours; where (A) had an initial seeding of 2000 cells and (B) 8000 cells. It can be seen in (B) that after 3 days the cells hit confluency as the 2:1 nanowire based substratum has cell number equivalent to the glass cover slip control. Values represent the mean ± SD of 12 microplate readings taken from 2 separate experiments assayed in duplicate ($n \leq 4$). Student's Ttest p values are shown in Table 8.5.

The MTS solution was used as it is bio-reduced by cells into formazan dye that is soluble in tissue culture medium, whereas others variants (MTT or XTT) are typically non-soluble. Berridge and Tan [48] have reported that this conversion can only be accomplished by SDH enzymes in metabolically active cells, and therefore when the optical density of the formazan dye (absorbance peak ~492 nm) is measured it directly relates to the number of live cells in each well. The MTS solution is far superior to other tetrazolium based reagents as it yields soluble formazan dye after incubation reducing errors compared to MTT and XTT. This is because other tetrazolium based reagents produced formazan as a solute, increasing errors during a solubilizing step, as reported by Goodwin et al. [49]. Even though the formazan produced was a liquid the plate was still shaken softly for 1 minute at room temperature in a double orbital to assure formazan was uniformly distributed throughout the media. This yielded more accurate photon absorbance optical density plate readings with a FLUOstar OPTIMA (BMG Labtech) at 490 nm.

Fig. 8.13. shows the MTS results from 4 replicates. For the 'low' cell seeding density the difference between control and samples is insignificant for 48 hours, only becoming significant at 72 hours; yet the higher seeding density displays significant differences within a single day. This is due to reduced cell-cell interactions in the lower seeding density leading to an extension of time taken to progress from lag to log phase; for this reason comparisons will primarily focus on the 72 hour time point. For the high seeding density samples at 72 hours there is no difference in cell count between the glass and nanowire 2:1 substrates, this would normally be attributed to stationary phase growth due to limited space in the well. However this is not the case, as shown by the no substratum control run in tandem with the experiment. After 72 hours the mean amount of cells measured was 51.6 $x10^3$ for the well only control, compared to 45.6 $x10^3$, 45.7 $x10^3$ and 37.4 $x10^3$ for the glass control, 2:1 and 1:1 substrata respectively. The presence of a substratum in the well and frequent handling could lead to a certain amount of cell death, explaining the difference observed between the well only and glass substrate controls. This difference could also be attributed to the differing surface area as the substrates used were 49 – 64 mm^2 compared to the 95 mm^2 of the well, meaning that the adherent cells could be reaching the boundaries of the substrates by 72 hours and explaining why the cell numbers are similar for the glass and 2:1 substrata.

Table 8.5. p values obtained from 2 tailed paired-sample T-tests ($n \leq 12$)

Control vs.	2:1 (Low)	2:1 (High)	1:1 (Low)	1:1 (High)
0hrs	0.82631	0.05768	0.78048	0.01554
24hrs	0.72954	0.10841	0.10995	0.00001
48hrs	0.05987	0.01129	0.63111	0.00710
72hrs	0.00659	0.88551	0.00003	0.00035

There is no apparent trend for the low cell density samples until 72 hours, at which point the observations sit well with expectations and the trend set by high cell density samples. But what is very apparent is that at higher seeding densities the texture/shape/size of the substratum has a more substantial influence on the fate of cells residing upon it, as the highest, lowest and in between amount of cells are detected on glass, 1:1 and 2:1 substrata respectively for the majority of time points. Table 8.5. shows the statisitical analysis of Fig. 8.13. where values larger than 0.05 are not significantly different; therefore at 72 hours there is no statistical difference between samples and control for low seeding density samples, even given the high concentration (~1.22 μg/ml) of ZnO nanowires used per well. However, it has been shown by Muller et al. [7] that Macrophages after 24 hours incubation with 8 μg /mL Zn showed surface blebbing, indicative of start of apoptosis. From MTS data, at 72 hours the viability of cells on 2:1 substrata was found to be 88.4 % and 79.0 % for high and low cell seeding densities respectively. However for 1:1 substrates the high cell density value was much lower at 72.4 %, while the low cell density value was similar at 48 hours with 80.0 %. The viability percentage was obtained by comparing to a non substrate well control that yields the proliferation rate and amount of cells obtained in an unihibited controlled environment, see Table 8.6. Fellows et al. [50] similarly produce a relative cell count to determine toxicology.

Table 8.6. Viability of Glass, 2:1 and 1:1 compared to well only control.

Control vs.	Glass (Low)	Glass (High)	2:1 (Low)	2:1 (High)	1:1 (Low)	1:1 (High)
24hrs	99.7 %	106.6 %	101.2 %	96.4 %	106.5 %	71.2 %
48hrs	76.6 %	89.5 %	88.7 %	71.4 %	78.5 %	67.9 %
72hrs	102.9 %	88.3 %	79.0 %	88.4 %	80.0 %	72.4 %

Both Fig. 8.13. and Table 8.6. show that ZnO nanowires appear to be biocompatible with U-2 OS with there being no difference between the two controls

(well only and glass substratum) and two samples (nanowire types 2:1 and 1:1) up to 48 hours incubation. However, for incubation times greater than 48 hours it can be seen that a statistically significant difference emerges between the controls and the samples. Notice also that there is little difference between the two nanowire samples themselves at low seeding concentrations, these subtle differences only significantly appear in the highest concentration at 72 hours. Assuming that the well only control yields the maximum amount of cells obtainable in this experiment, and growth rate is inhibited by surface area at 72 hours for the higher seeding, then lowest viability in this case is still greater than 72 % for 1:1 nanowires at 72 hours, see Fig. 8.13b.

Table 8.5. shows statistical analysis between the well control and the samples with paired-sample student t-tests. The p values support the observations made highlighting statistical differences at lower seeding densities, which can be interpreted as the nanowires inhibit the growth rate (μ) of U-2 OS, with this only being observable at the lower seeding density due to well surface area not being an issue by 72 hours (i.e the higher seeding density cells are likely over confluent at 72 hours). This is certainly shown by comparing population doubling times derived from these results, using equation 5.1 the low seeding density yields 22.1 hours whereas high yields 25.8 hours, clearly indicating that the population curve is at its plateau (or growth is now stationary). Solly et al. [51] reported the doubling time of U-2 OS to be 23.7 ±0.5 hours so values here are clearly nothing to be concerned about.

Work by Wataha et al. [52] has shown that toxicology due to Zn^{2+} ions is very dependent on cell density, with higher cell density decreasing the sensitivity of cells to metal ions as shown by higher TC_{50} values at high cell density. Where TC_{50} is the concentration required for 50 % of the cells to become necrotic. However, if this were the case here then there would not be such discrepancy between 2:1 and 1:1's values for low and high seedings, with them being similar at low seeding and significantly different at high seeding. The data therefore suggests that U-2 OS cells are surface sensitive as the data shows only the 1:1 substrata inhibit proliferation of the cells compared to the glass control and 2:1 substrata at 72 hours and high cell seeding. Since Fig. 8.12b. showed preferential attachment to nonpolar facets, then it can be hypothesised that as 1:1 have a tapered tip, and therefore their surface charge is likely to be different this could be the cause of differences in viability results.

In conclusion it has been shown that ZnO nanowires are biocompatible with U-2 OS cells and are able to survive for 72 hours, yielding cell populations on par with glass

substratum control. MTS results yeilded survival rates of 71 – 96 and 68 – 72 % of cells counted for well only control for substrata with a precursor chemical ratio of 2:1 and 1:1, respectively. Therefore it is apparent from MTS results that ZnO nanowire biocompatibility is dependent on nanowire morphology or some other surface property otherwise 2:1 and 1:1 would yield similar survival values. If there were more time available then this would be repeated using detached nanowires to make up solutions of various concentrations, allowing the IC_{50} and TC_{50} values to be determined.

8.4.3. Invitrogen's LIVE DEAD Assay

It was previously shown via MTS assay that biocompatibility was different between the two nanowire samples, with 2:1 being on par with plain glass coverslip, whereas 1:1 nanowires yielded only 68 – 72 % of the well only controls cell count. Therefore, further investigation has been conducted using Invitrogen's LIVE DEAD assay, an immunocytochemical technique that uses CalcienAM and ethidium homodimer-1 (EthD-1) to label live and dead cells, respectively. The details of which were covered in chapter 6. However, concentration assays (used to determine optimum dye concentration) showed that EthD-1 reacted un-expectedly with ZnO nanowires creating non-specific background staining making dead cells hard to distinguish. The reason for this was never fully explored so the author is unsure if it was the move to propidium iodide or the inclusion of additional rinsing cycles that lead to elimination of non-specific background staining. However, the chlorine in EthD-1 [53] could make the stain more likely to react with ZnO. Fig. 8.14. shows DAPI and EthD-1 added to U-2 OS cells after 72 hours incubation, were the effect of such a large background emission can be observed. Note that DAPI concentration here is too high as although shutter opening / exposure time was slightly high at 500 msec the intensity reading was greater than the maximum recorded value of 125 % leading to overexposure / saturation of emission at 461 nm. This is obvious from the luminescent gradient apparent form centre to extremities of the image, leading to a blurring of cell nuclei in the centre of the image. But this is why concentration assays are conducted, to optimise staining protocols for the cell line. Fig. 8.14. shows a scratch (down to glass substratum) that yields the expected zero emission at 617 nm, meaning the background is likely due to ZnO-stain interaction rather than non-specific binding, assuming the scratch was made pre-staining.

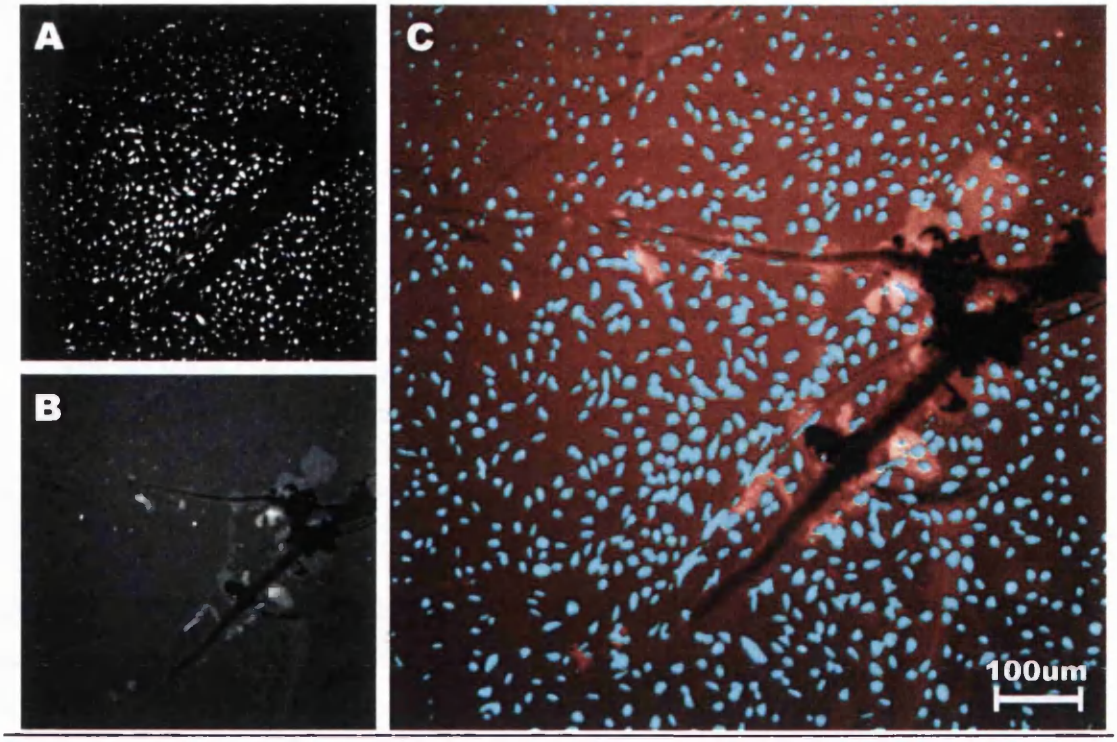

Figure 8.14. Immuno-fluorescence micrographs of U-2 OS on ZnO nanowires 72 hours after seeding, where (A) is DAPI, (B) ethidium homodimer-1 and (C) a merge of (A) and (B). Notice how DAPI appears heavily saturated in the image, this is because the exposure time was too long (at 500 msec) resulting in an intensity reading of 125 % (i.e. > limit).

All dye concentrations were determined individually before conducting simultaneous staining to further optimise dye concentration. Fig. 8.15. the effect of moving to propidium iodide (PI), with nanowires not effecting / reacting with PI as they were with EthD-1. Note that CalcienAM is also in this image, showing live and dead U-2 OS cells after 72 hours incubation on ZnO nanowires; were due to the blurred nature of some of the red sections cell deaths appears due to scratches most likely from substratum transferal during washing and staining cycles. However, a DAPI counter stain was not conducted in this experiment as certain problems were met at this stage with DAPI more readily interacting with dead cells, as discussed in sub-section 6.3.3. However, using program like ImageJ (see Appendix IIX) both live and dead contributions can be recorded manually without use of highlighting nucleic acid. For example, using ImageJ the live and dead percentages of the 7190 cells counted from Fig. 8.15. was 86.04 and 13.96 %, respectively.

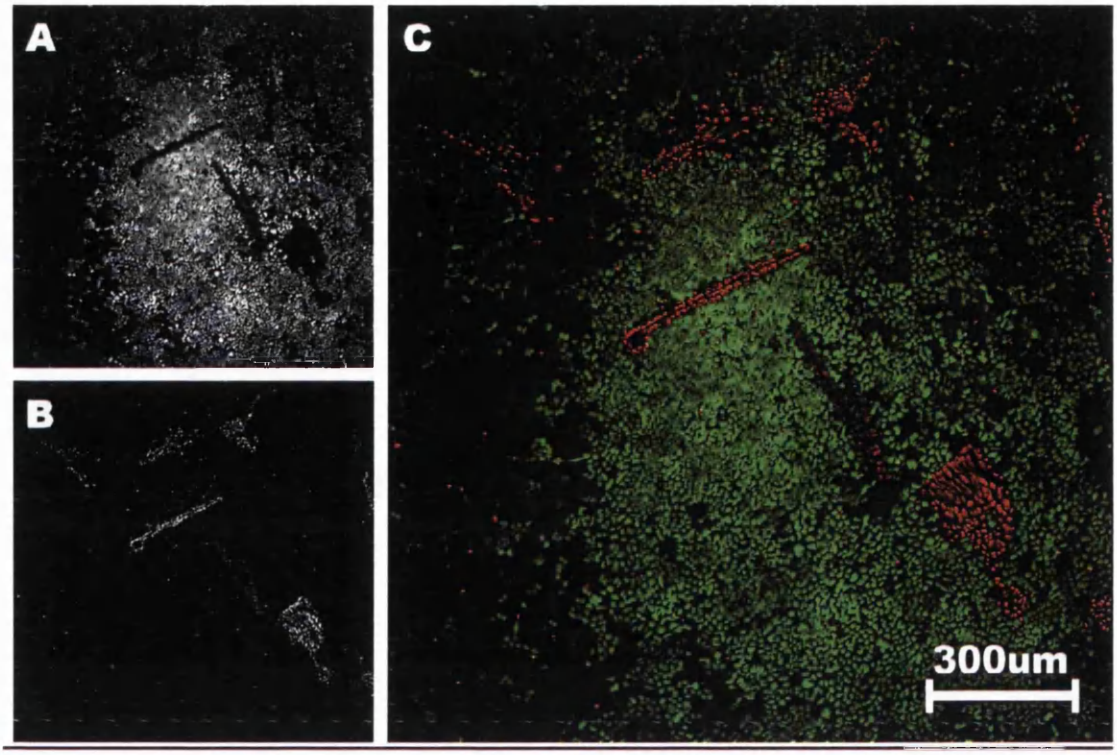

Figure 8.15. Immuno-fluorescence micrographs of a LIVE/DEAD assay showing U-2 OS on ZnO nanowires 72 hours after seeding, where (A) is CalcienAM, (B) prodidium iodide and (C) a merge of (A) and (B). Notice how PI appears heavily blurred in the bottom right, indicating the cells are likely dead due to tweezer scratch during experiment.

Note that the results in Fig. 8.16. are from images measured by ImageJ (as discussed in chapter 6) as uptake of DAPI showed major discrepancies between live and dead cells, likely due to the nature of cell death and membrane compromised samples. It was also often the case that the IN Cell 2000 would detect contribution from both stains within a cell, yielding scatter plots with non discrete distribution of data, see Fig. 8.17d. It should be known that confocal microscopy was used to observe cell mechanics, with work invested in coating the nanowires in a cell impermeable stain for z-stack analysis of cell-nanowire interaction. This was due to the limited information obtained with non-fluorescent nanowires, see Fig. 8.16. Here it was unknown if difference in CalceinAM concentration within the cell was due to mitochondria location or increases Z-depth of cell membrane due to topography change of nanowires. A zinc stain (FluoZin3, Invitrogen) was used to stain the wires, work on this can be found in future work (chapter 9). IN Cell 2000 images showed that cells often contained contribution from both CalcienAM and EthD-1, leading to the assumption that cells were membrane compromised but somehow also healthy enough for enzymatic conversion of non-

fluorescent cell-permeant, calcein AM, to the intensely fluorescent non-permeant calcein.

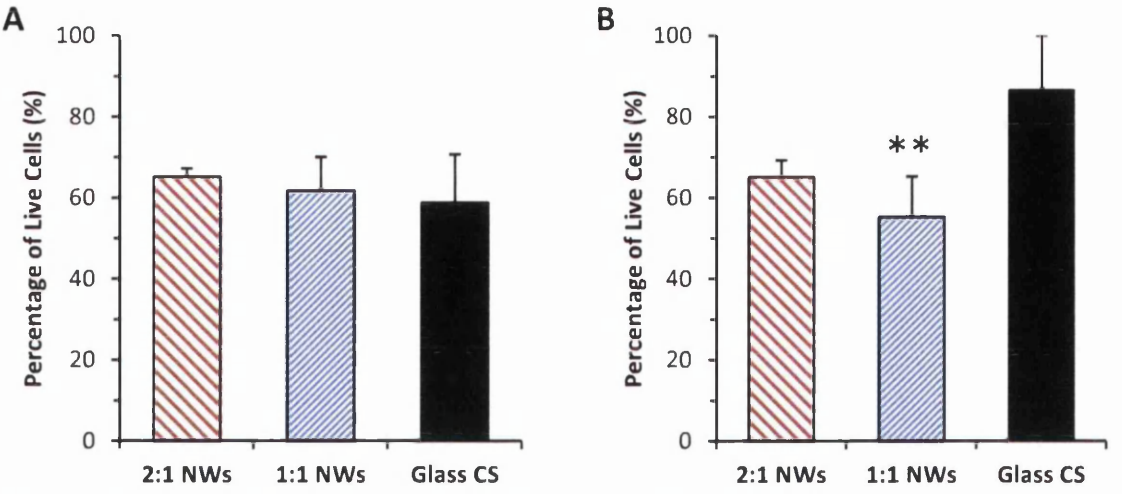

Figure 8.16. Results of cell count from LIVE DEAD assay after 72 hours incubation for (A) low (2000) and (B) high (8000) concentration of cells seeded at 0 hours. * indicates $p<0.005$ and ** $p<0.05$ compared to glass cover slip control.

Table 8.7. Viability of Glass, 2:1 and 1:1 compared to well only control*.

72 Hours	Glass (Low)	Glass (High)	2:1 (Low)	2:1 (High)	1:1 (Low)	1:1 (High)
Live (%)	58.9 %	86.6 %	65.2 %	65.2 %	61.8 %	55.4 %

* Well only control was 94.8 ±0.6 % across all replicates and seeding densities.

Fig. 8.17. shows scatter plots of LIVE (CalceinAM) vs DEAD (EthD-1) stain intensity as determined by IN Cell 2000 software. Here it can be seen that the well only substratum shows a distinct difference between LIVE and DEAD stain intensity, with minimal overlap. However, both the nanowire substrata have considerable overlap between the two stains with thousands of cells exhibiting contribution from both stains. This clearly shows that nanowire substrata are causing destruction of cell membrane as ethidium homodimer 1 is cell-impermeant, and undergoes a 40 fold enhancement of fluorescence intensity upon binding with nucleic acid [3]. It has been shown by Lane and Burka [54] that inclusion of cyanate ions leads to reduced cell survival due to reduction in metabolism of membrane lipid synthesis. This process took 30 days in their work so it is likely that if a similar mechanism was behind the results obtained in Fig. 8.17. then both graphs C and D (2:1 and 1:1) would yield similar overlap between LIVE and DEAD stain intensity. Therefore contribution from both stains in multiple

cells can only be due to perforation of the cell membrane via ZnO nanowires, as observed in Fig. 8.18.

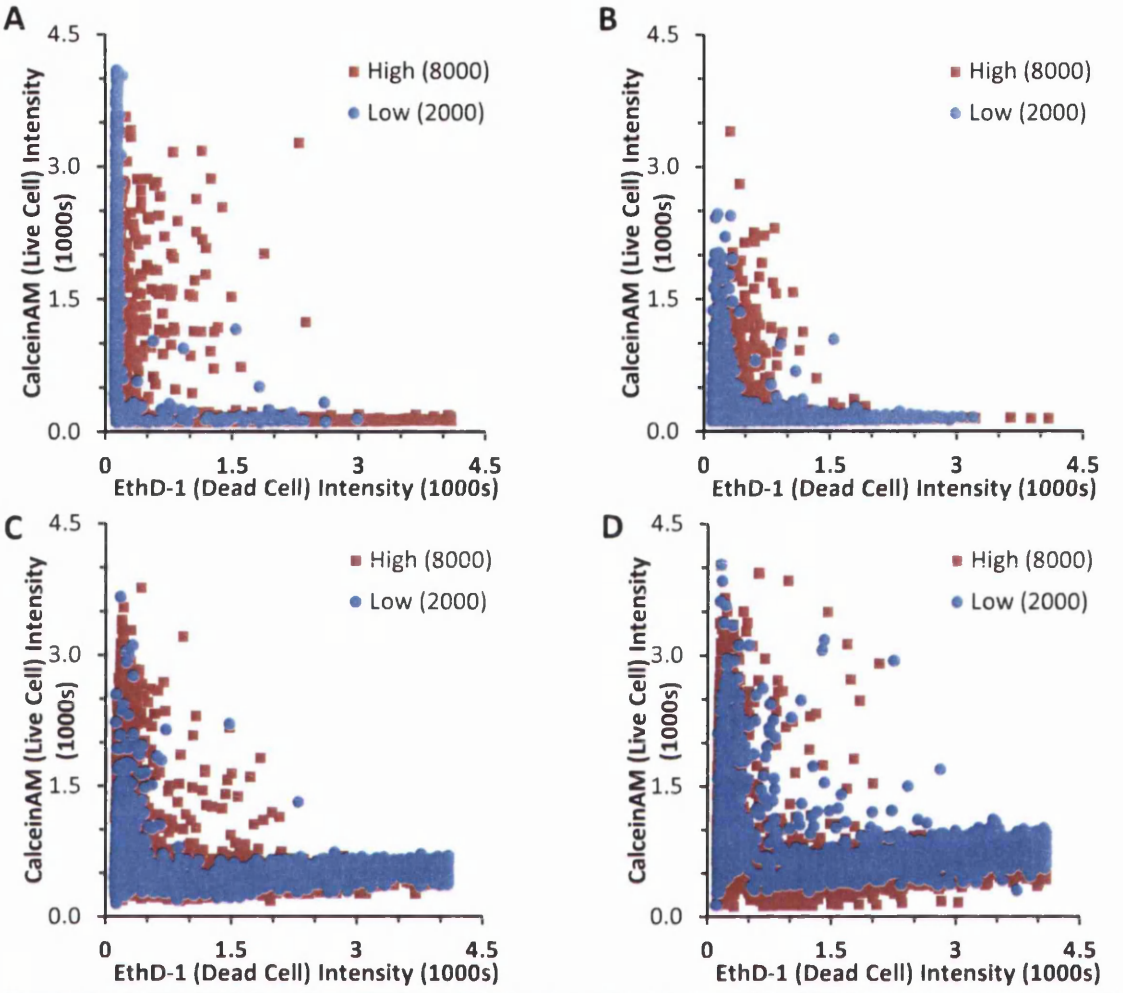

Figure 8.17. Distribution of cell intensity for CalceinAM (Live) and EthD-1 (Dead) stains in every cell for each of the 4 substrata after 72 hours incubation (A) is well only, (B) Glass coverslip, (C) 2:1 nanowires and (D) 1:1 nanowires.

Fig. 8.18. shows U-2 OS cells in cytokinesis post mitosis, as indicated by the compacted nature of the bottom left cell's nucleus [40]. Whether this is damage has occurred during fixation or cell culture is unknown, however it does imply that standard immunocytochemistry assays to check for necrotic cells could be redundant under these circumstances, as if the membrane is compromised cell-impermeant stains like PI and EthD-1 may enter yielding a false positive result. However this result also raises other concerns. It has been shown by Draeger et al. [55] that nucleated cells can reseal their injured plasmalemma by endocytosis of the permeabilized site. While Jahn and Fasshauer [56] have shown that a cell may direct secretory vesicles towards a damaged

area to provide membrane proteins and lipids to patch the damaged area. This process is called exocytosis, and is dependent on extracellular Ca^{2+} concentration as calcium signals the cell. Therefore why has the cell membrane not been patched in this cell, when the other cell appears intact post cytokinesis?

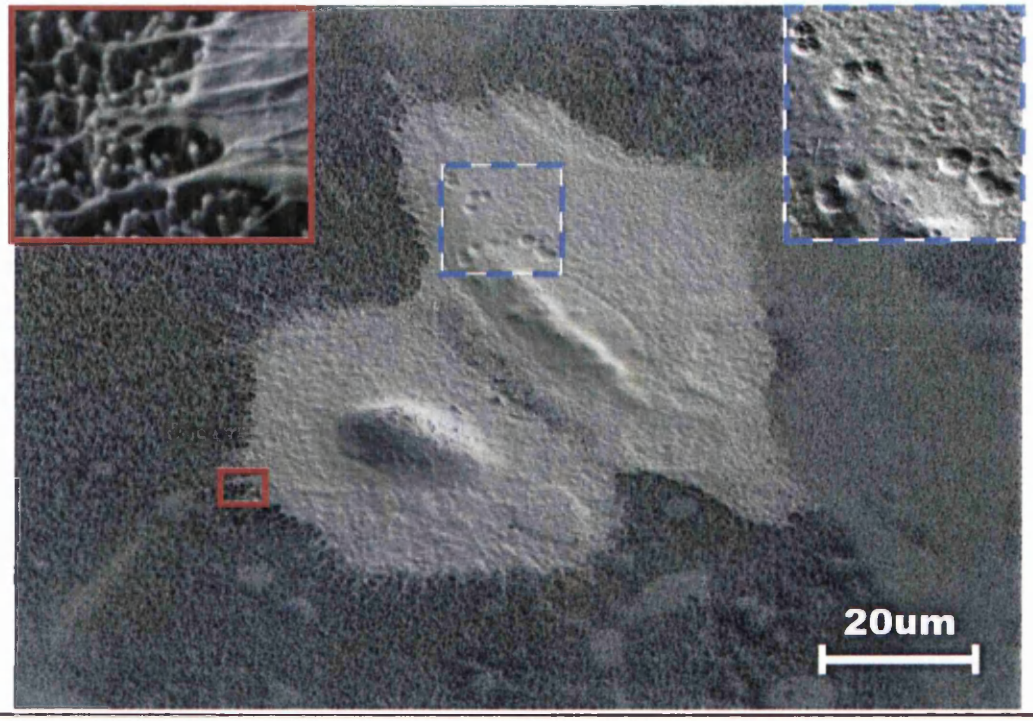

Figure 8.18. Scanning Electron Micrograph of two U-2 OS cells post mitosis, where it can be seen that north easterly cell has considerable damage to it's cell membrane. Insets show (Left) fillipodia attachment to ZnO nanowires and (Right) higher contrast zoom of damage to cytoplasm. Whether this damage has occurred during fixation or cell culture is unknown, however it does suggest that cell impermeable dyes contained in most necrosis assays maybe redundant. Cells were incubated for 48 hours in McCoy's 5A modified medium at 37 °C 5 % CO_2 and fixed with 3 % glutaraldehyde in PBS

It should be noted that Fig. 8.18. is not representative of the final nanowire morphology as show in Fig. 8.6., as the above image is from an early prototype substratum as both tissue culture and nanofabrication were researched in tandem once the hydrothermal process began to yield favourable results. It could therefore be that the observed cell membrane damage does not occur so extensively on more homogeneously distributed nanowire arrays. It is therefore only reasonable to conclude from MTS and LIVE DEAD assays that ZnO nanowires are biocompatible up to 72 hours. However, given the puzzling results from the LIVE DEAD assay experiments, biocompatibility was further investigated.

8.4.4. Result verification (Cryo-SEM)

The puzzling results from the LIVE DEAD assay and the reduction in cell proliferation for 1:1 substrata compared to 2:1 (that yielded values on par with glass substrata) prompted the cell-nanowire interaction to be investigated via cryo-SEM. Use of cryo-SEM abrogates the need to fix the cells as they're quickly flash frozen in liquid nitrogen and sublimated to remove excess ice, thus allowing observation of fine details normally perturbed or even destroyed due to fixation [57]. Fig. 8.19. shows cryo-SEM images of U-2 OS cells after 48 hours culture on 2:1, 1:1 and glass control substrata, where the difference in cell shape is clearly seen. Differences in 'apparent' confluency can be neglected as the images were taken from different locations and cell distribution was often non-homogeneous throughout the substratum. It can be seen that cryo-SEM is prone to charging artifacts (see Fig. 8.19) making detailed analysis more difficult as higher magnifications were often unsuccessful resulting in carbon deposition and charging lines as indicated by white arrows. Even though SEM yields no Z range use of the lower detector can be used to give 3D topographical information.

Fig. 8.19. show that both 2:1 nanowires and glass control substrata yield cells that are well spread with several protrusions / lamelliapodia and nuclei that are of larger height (Z) and contain distinct components. Unfortunately cells on 1:1 nanowires (although have lammeilipodia) are bunched to the point that a nucleus is indistinguishable from the rest of the cell, indicating that the cells are uncomfortable with their environment and supporting results from MTS and LIVE DEAD assays. Again it should be noted that the cells on 1:1 are not huddled due to the confluency observed in Fig. 8.19. as the cells were of similar elsewhere in less confluent areas. Cryo-SEM has shown the behaviour of U-2 OS cells on 2:1 nanowire arrays is similar to that of a glass coverslip control substratum; where differences in apparent Z height are due to changing artifacts in Fig. 8.19f. Therefore it is apparent that the surface properties between 2:1 and 1:1 must be substantially different, and that it is not solely a change in surface morphology that has lead to the reduction in cell proliferation on 1:1, else 2:1 would also be reduced compared to glass control whereas Table 8.6 shows it is not. It is assumed that the increased (0001) surface area of the 2:1 nanowire array provides an increased area for the interaction and formation of focal adhesions compared to the smaller and pointier 1:1 nanowire array that are thought to inhibit cell proliferation due to non adhesive gaps in the array, as per work by ter Brugge et al. [58].

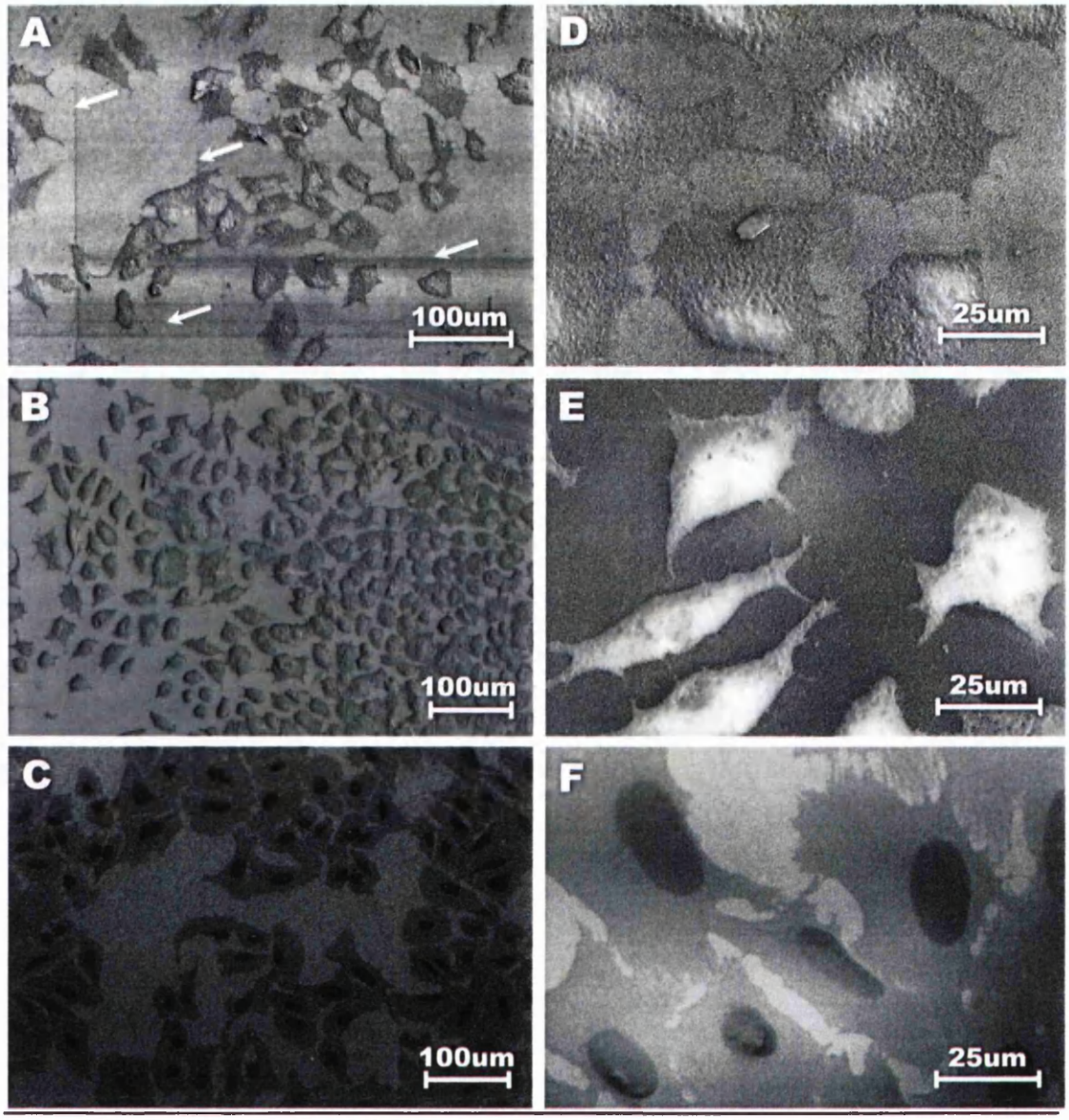

Figure 8.19. Cryo-SEM images of U-2 OS on (A,D) 2:1 nanowires, (B,E) 1:1 nanowires and (C,F) glass control substrata. Cells were incubated for 48 hours in McCoy's 5A modified medium at 37 °C 5 % CO_2, frozen with liquid nitrogen and sublimated at -90 °C until ice was removed.

Therefore the surface properties causing the observed differences in biocompatibility across multiple assays shall be investigated in the following section. Cell surface area will also be investigated using refined fixation protocols, allowing any doubt regarding cryo-SEM results to be negated. Also due to difficultly of obtaining high resolution images at < 1 kV acceleration voltage due to charging means that the cons of cryo-SEM out-weigh the benefits in this work. Work by Puliafito et al. [44] has shown that complete arrest of mitosis occurs when cell area falls below a critical value, explaining how the small size of cells on 1:1 nanowires in Fig. 8.19. could link in with reduced proliferation in MTS assay experiments.

8.5. Cell-Substratum Interaction

To date few papers exist that fully explore the surface science behind the observed changes in cell behaviour on substrata of different morphology, it is also equally as rare to find material profiling the interaction of cells with ZnO nanowires, which is unfortunate as nanowire morphology is highly tunable and could lead to some exciting avenues of research. To fully understand the mechanisms behind cell-substratum interactions it is important to first understand better their effect on cell behaviour. This section will investigate cell-nanowire interaction using SEM observation and immunofluorescence microscopy techniques.

Fig. 8.20. shows a confocal microscopy Z-stack of a single U-2 OS cell on an array of ZnO nanowires, where the gap between each image is ~600 nm. It can be seen in Fig. 8.20h. the point at which the cell meets the nanowire substratum that the distribution of CalceinAM appears heterogeneously distributed throughout the cell. Since the process by which the LIVE stain Calcein is processed from a cell-permeant non fluorescent dye to a cell-impermeant fluorescent dye is an enzyme based process, then it cannot be determined if areas of high CalceinAM density could be due to non-uniformly distributed enzyme or differences in cell membrane Z height due to substratum topography.

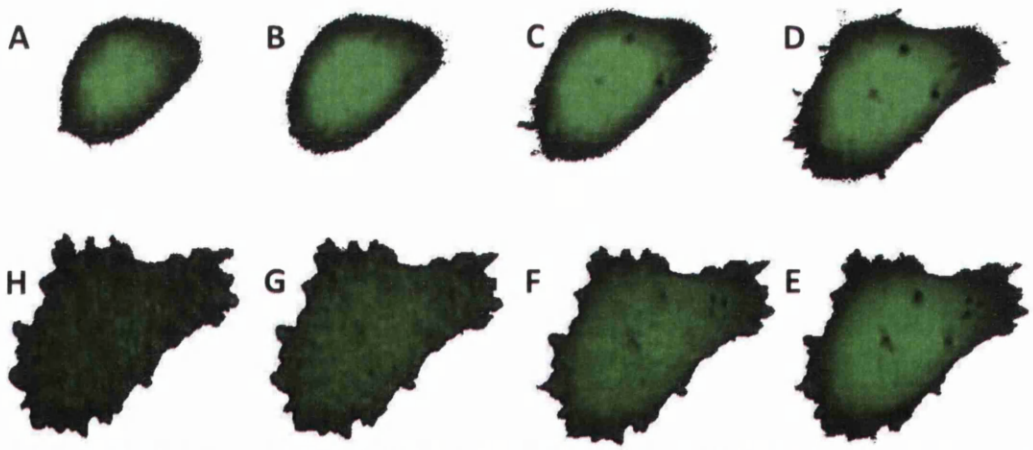

Figure 8.20. Confocol Microscopy Z-stack of single U-2 OS cell on ZnO nanowires after 72 hours incubation stained with CalceinAM, where (A) is top of stack which drops 600 nm towards (H) the cell-substrate interface in a clockwise direction. Notice how midway through the cell appears to contain lysosomes, possibly indicating that the cell has attempted phagocytosis or endocytosis of ZnO nanowires.

8.5.1. Fixed cell SEM observation of interaction

After cryo-SEM indicated that there was a difference in cell spreading area / behaviour between the three substrates but gave less than favourable images due to

problems with charging and low accelerating voltage the experiment was repeated using fixed cells. While this may seem like a step backwards, the fixing protocols by this point had been refined significantly enough that fine details are well preserved, see Fig. 8.21. Also the previously discussed cryo-SEM experiment used cultured cells for 48 hours only which is not in line with the 72 hours used in all other experiments investigating cell-substratum interaction.

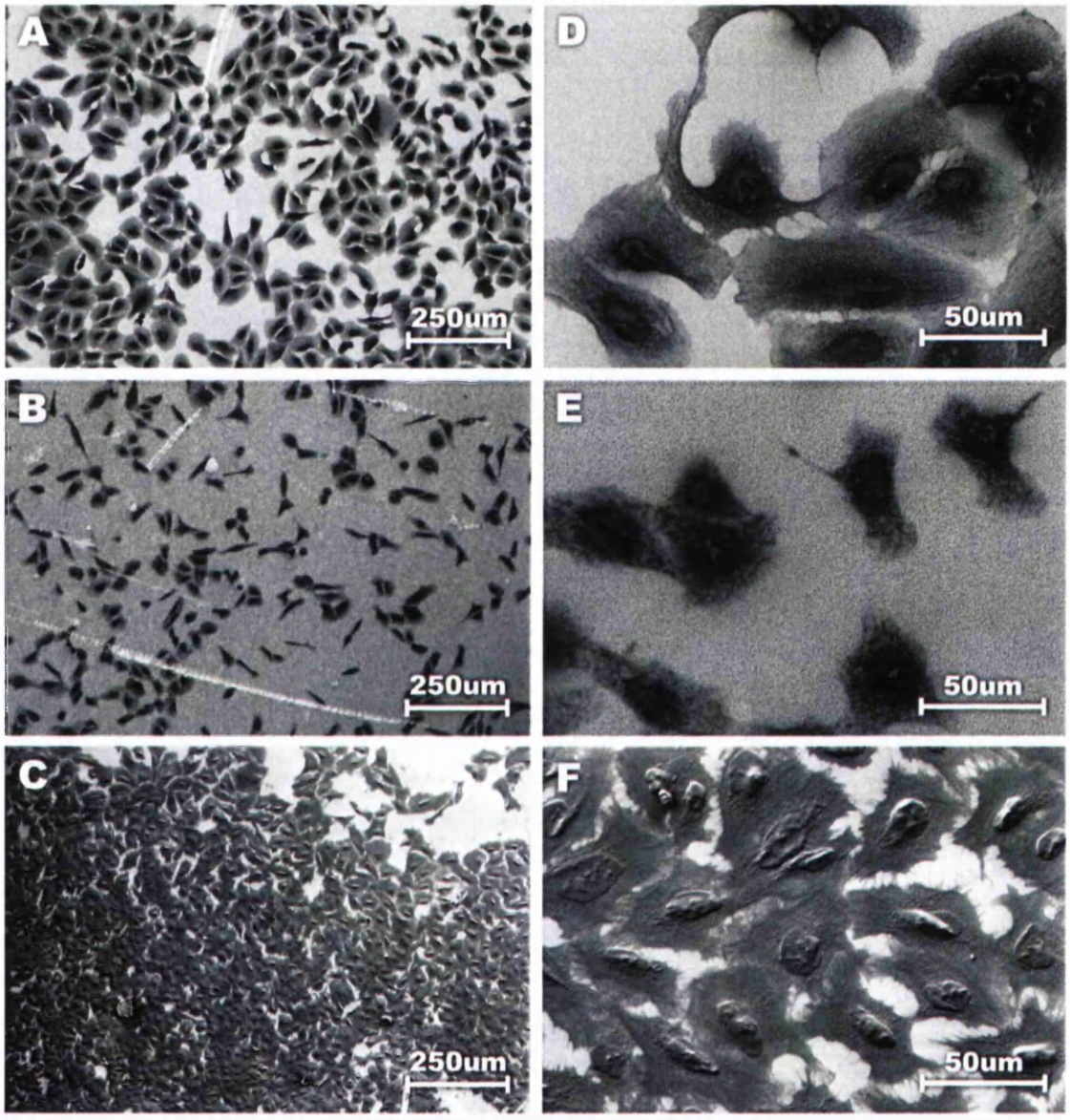

Figure 8.21. Scanning Electron Micrographs comparing the shape and distribution of U-2 OS cells on (A) 2:1 nanowires, (B) 1:1 nanowires and (C) glass control substrata at 200x magnification, images (D-F) correspond to (A-C) and are taken at 600x magnification. Cells were incubated for 72 hours in McCoy's 5A modified medium at 37 °C 5 % CO_2 and fixed with 4 % Paraformaldehyde. Notice how (B) and (E) clearly show U-2 OS's inability to proliferate and spread / create focal adhesions effectively on the 1:1 nanowire array surface.

Fig. 8.21. shows Scanning Electron Micrographs of U-2 OS cells on glass coverslip controls and the 2 different ZnO nanowire arrays taken at 200x and 600x magnification. Here both the 2:1 nanowire and glass control substrata yielded both a high confluency and higher cell spreading areas compared to the 1:1 nanowire substratum; supporting findings of both MTS and LIVE DEAD assays. Using fluorescent microscopy Lampin et al. [59] reported that U-2 OS cell size was clearly affected by surface characteristics, with cells on smooth surfaces spreading out to a larger cell area than cells on the rough substrates. Shah [23] suggests that the lack of apparent spreading on rough surface maybe because the three-dimensional structure of rough substrates provide large surface contact, without the need for extensive lateral spreading. However, for nanoscale topography their observation may not be applicable as this would be unable to explain how in Figs. 8.19-21. 2:1 nanowires and glass substrates yield similar cell spreading areas. It should be noted that the glass coverslip control have pronounced nucleui and topography as they have been coated with 17 nm of Gold to enhance conduction and allow imaging at 5 kV. It has been shown by Loosli et al. [60] that cell spreading behaviour is indicative of the amount of focal adhesions formed, and that spreading area determines signalling that affects various physiological functions such as cell migration.

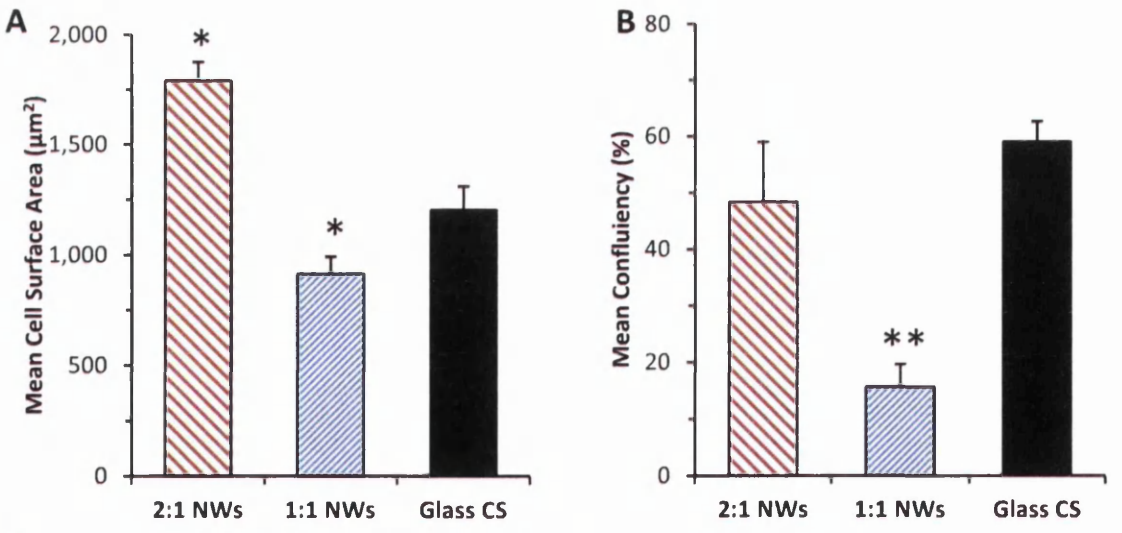

Figure 8.22. Graphs showing (A) the mean lateral spreading area and (B) the confluency of U-2 OS cells after 72 hours incubation on 2:1 amount of cells counted using Scanning Electron Micrographs. * indicates $p<0.005$ and ** $p<0.05$ compared to glass cover slip control.

Fig. 8.22. shows the cell spreading areas obtained using ImageJ [61] NIH image processing software on images from Fig. 8.21. (as well as several other areas). More

than 1400 measurements were taken per sample and the surface spreading area of cells was found to be 1203.9 μm^2, 915.1 μm^2, and 1791.1 μm^2 for 2:1 nanowires, 1:1 nanowires and glass coverslip control, respectively. The mean cell spreading area is likely larger for U-2 OS cells on 2:1 nanowires because of the additional width and orientation of the nanowires. It is also likely that due to 2:1's more flat hexagonally terminated [0001] plane that the cells are able to create adhesion points more readily on 2:1 than on 1:1's more pointy terminated nanowires; this will be investigated further in section 8.6. The differences observed in cell surface spreading area between glass and 2:1 nanowires are interesting given that both were 88 % viable at 72 hours compared to well only control and both have extremely different surface topography. It can be assumed that there are mechanisms affecting cell proliferation other than the topography of the substrate, such as surface charge or local pH; these will be subsequently investigated.

Table 8.8. Cell spreading area for 3 substrates (n≥500)

Substrate	Area (um^2)	SD	Perim. (um)	SD
Glass	1203.86	59.03	167.92	8.62
2:1 NWs	1791.09	85.27	178.65	2.71
1:1 NWs	915.11	77.61	129.70	5.48

Shelton et al. [62] has shown that focal adhesions are charge sensitive. They report that the shape of neonate rat calvarial osteoblasts was significantly different between cultures on a positively or negatively charged polymer substratum. It could also be the case that the main mechanism behind the observed change in cell shape is the density of the nanowires, more specifically the gap between the wires, as ter Brugge et al. [58] has reported that voids in a substratum are non-adhesive regions for cells, affecting their behavior. It has been reported recently the effect of altering substrate rigidity by Fu et al. [63], and wettability by Ayala et al. [64] on cell morphology and mesenchymal stem cell (MSC) differentiation. However to date only a few papers exist that explore the differentiation of cells using zinc oxide Nanowires, Ciofani et al. [3] report on differentiation of H9c2 myoblasts into myotubes, by adding a collagen layer to their nanowire array to act as an artificial extra cellular matrix (ECM) and added 1% insulin-transferrin-sodium selenite mixture (a growth factor) to induce the expression of a skeletal phenotype. It should be noted that confluency values don't match images as

contribution from cells touching the sides of the image were neglected to avoid biasing of cell spreading area results in Fig. 8.22a.

It is interesting that cell spreading area matches closely the MTS and LIVE DEAD results as Puliafito et al. [44] has shown that complete arrest of mitosis occurs when cell area falls below a critical value. U-2 OS cells cultured on 1:1 nanowires are likely below this critical value. Gronowicz and McCarthy [65] has reported that integrin properties are dependent on substratum surface characteristics, where initial interaction of the human osteoblasts SAOS-2 with orthopaedic implant materials showed SAOS-2 cells are capable of attaching directly to implant materials through integrins. As when a GRGDSP peptide was added to inhibit integrin receptors, cell adhesion was reduced by 28 – 40 %. They postulate that the type of substrate determines which integrins and extracellular matrix proteins are expressed by osteoblasts. If further time was available an in depth analysis of ECM formation on ZnO nanowires would be conducted, as well as an in depth analysis of cell migration as cell motility is inversely proportional to cell surface area [64].

8.5.2. Immunocytochemistry of Vinculin

An immunocytochemistry investigation of actin and vinculin was conducted to determine how and where focal adhesions form on each substrate, aiding understanding of cell shape and behaviour that leads to such drastic differences in proliferation rate (especially between 2:1 and 1:1). However, it was quickly found that the laboratory did not have the facilities to accommodate for an opaque substrate, as it was unknown in the beginning that the hydrothermal growth method would introduce so many defects. Therefore, the main system available was a General Electric's IN Cell 2000, (see chapter 6) which was used to obtain the images in Fig. 8.23.

Fig. 8.23. shows fluorescent micrographs of U-2 OS cells on glass coverslips and ZnO nanowires, where green fluorescence is due to anti-vinculin (raised in mouse) at 1:100 and anti-mouse (raised in goat) conjugated to FITC at 1:32; and blue fluorescence is due to DAPI counter-stain 1:1000 (57 μm). It should be noted that the 40x magnification objective was unable to focus correctly, as discussed in Chapter 6. α-vinculin was selected as it is part of the cross-linking and attachment mechanism joining actin filaments with integrin, where integrin forms adhesion points to the substratum [66], see Fig. 5.6. Spreading cells edge protrusions are connected to the underlying

extracellular matrix via integrin and cytoskeletal structures (called nascent adhesions) that are created at the same time as the lamellipodia protrusion extends [67]. Lawson et al. [68] has shown that talin binds vinculin and actin, at each integrin site, therefore knowing the location of vinculin allows determination of focal adhesion location.

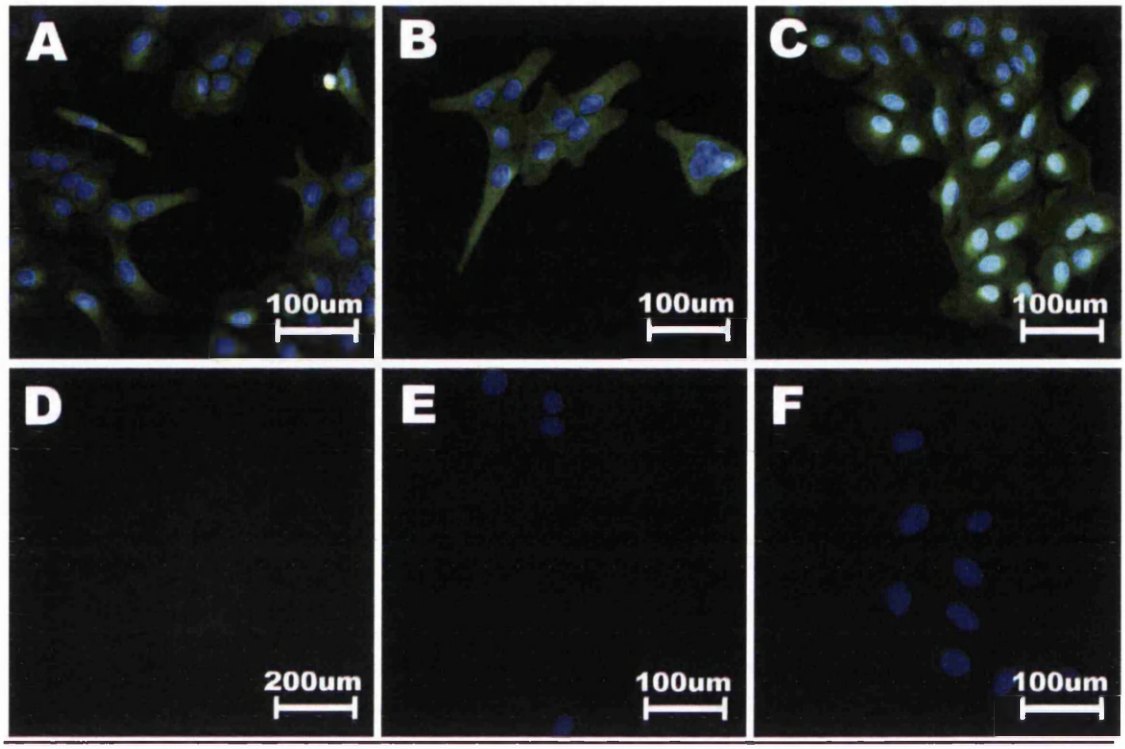

Figure 8.23. Fluorescent micrographs at 20x of U-2 OS cells after 72 hour incubation stained for Vinculin (green) and counter stained for nucleic acid (blue) adhered to (A) 2:1 nanowires, (B) 1:1 nanowires and (C) glass coverslip. Notice the difference between the two nanowire arrays, U-2 OS cells are clearly much more comfortable adhered to 2:1 nanowire arrays. Also, (D) shows minimal non-specific binding to substratum, (E) using just Primary with no Secondary and (F) using just Secondary with no Primary. All images have been counter stained with DAPI.

It is believed that differences in U-2 OS cell secretions and protein adsorption to the different substrata have led to the differences in cell proliferation and behaviour / migration observed so far. However, it is difficult to correlate individual surface properties to observed differences in cell behaviour as all properties appear inter-related. Berlind et al. [14] investigated protein adsorption on different substrata, stated that a complex situation occurs where results are subject to multiple microstructural properties, such as surface chemistry, isoelectric point, hydrophobic effects and surface charge. Even when a correlation is hypothesised unquantified effects such as photobleaching can have unknown effects on the obtained data, it has been shown by Lele et al. [69] that photobleaching can cause detachment of focal adhesions. Thus,

investigation of surface properties and cell behaviour is difficult to analyse due to the way several surface properties inter-relate. Therefore the work was repeated again using anti-Vinculin antibodies conjugated with 5 nm gold colloids, on dried samples in SEM for investigation at higher magnification.

8.5.3. ImmunoGold SEM of α-Vinculin

The previous sections investigation was re-conducted using anti-vinculin conjugated with 5 nm gold colloids, allowing SEM to be used to image at around 100,000x magnification. Fig. 8.24d. clearly shows the benefit of using SEM as backscattered electrons are used to observed cell-substratum interaction at 100,000x magnification, where white arrows indicate high contrast gold colloids that correlate with backscattered electron information. Here image contrast is derived from electron density and atomic weights rather than topographical information; allowing clear distinction between low contrast carbon 'background' of cell membrane, ZnO nanowires and high contrast gold colloids attached to vinculin. These colloids are definitely from within the cell membrane and not just sitting on top and several rinsing cycles were conducted and the samples were also looked at in cross-section.

As before primary antibody, anti-vinculin (from Mouse) concentration was 1:100 and secondary antibody, anti-mouse (from Goat) conjugated with 5 nm gold colloids with a concentration of 1:30. Cells were permeabilised with 0.05% Triton-X and blocked with 1 % bovine serum albumin in PBST (0.05 % Triton-X), to allow for Gold conjugates as per Bozzola and Russell's protocol [70]. However, this time substantially more information can be obtained from cell behaviour. 1:1 and glass are not shown as colloid distribution was random, for 2:1 though it appears that the nanowire dictated where focal adhesions could be made. Just like SEM images of fillipodia (in Fig. 8.11.) where [0001] facets were avoided, there must be some property of 2:1 nanowires that causes this kind of behaviour. This is imperative for understanding of cell-nanowire interaction and more importantly use of ZnO nanowire coatings for in vivo application. However the real challenge for in vivo work will be to observe ZnO interaction with macrophages, to observe if implantable devices are viable or not due to encapsulation. Zavedri et al. [71] investigated the influence of nanotopography on macrophage-substratum adhesion and viability on ZnO nanowires compared to flat sputtered ZnO controls and glass coverslips. They found that

macrophages initially adhere and spread well on ZnO nanowire arrays but that the number of adherent macrophages was reduced compared to flat ZnO and glass substrata. In this work it should be noted that unfortunately imaging of fillipodia was impossible due to beam interaction and charging, a metal coating could not be used as it would mask the fine details and hide 5 nm gold colloids; therefore SEM does have its limitations for life sciences.

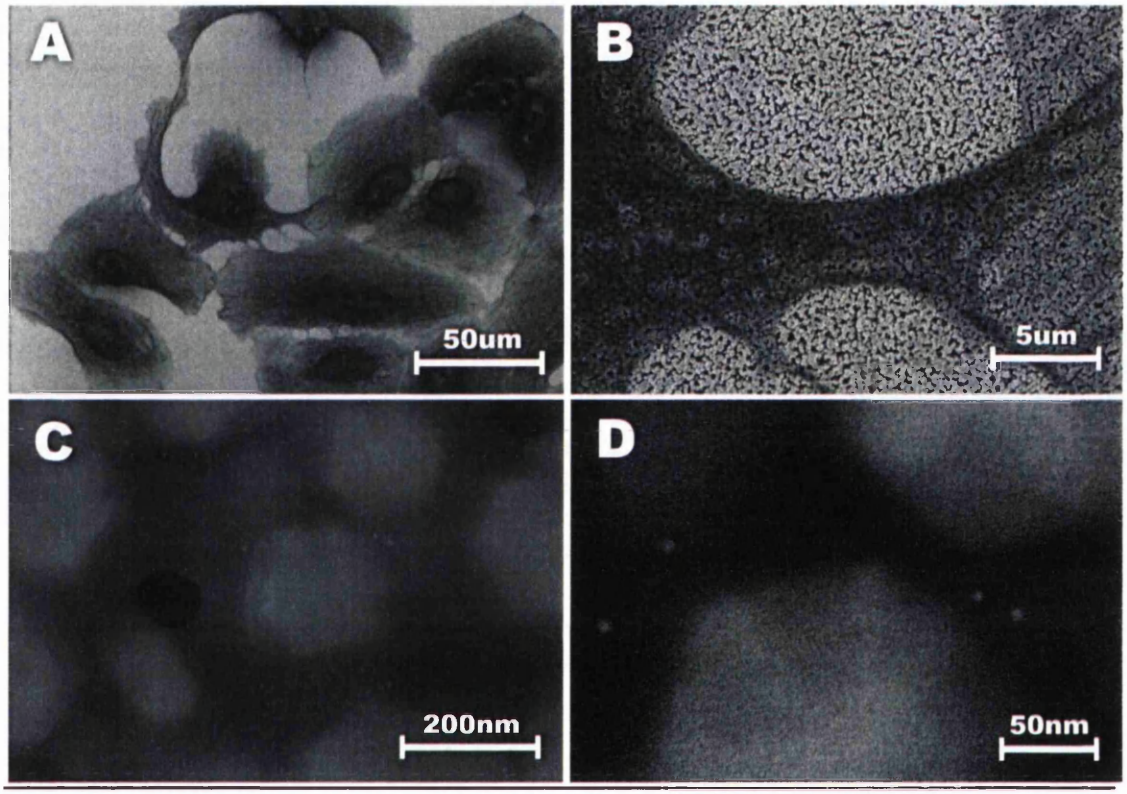

Figure 8.24. Scanning Electron Micrographs of U-2 OS cell on 2:1 nanowires after 72 hours incubation in McCoy's 5A modified medium at 37 °C 5 % CO_2, fixed with 4 % Para-formaldehyde, Permeablised with 0.05% Triton-X and stained. (A) shows that the cells are happy and well spread on 2:1 nanowires, (B) zoom of cell, (C) zoom of cell's leading edge and (D) Back scattered electron image of [0001] facet of 2:1 nanowire with cells lammilipodium and preferential attachment to non-polar facets as indicated by 5nm Gold colloids around edges of nanowires.

8.6. Surface Properties of Substrata

To fully understand the mechanisms behind cell-substratum interactions it is important to characterise the surfaces used as extensively as possible. In this work the substrates were characterised using, Scanning Electron Microscopy (SEM), Atomic Force Microscopy (AFM), Zeta potential and contact angle measurements; yielding substrate morphology, surface roughness, adhesion force, elasticity, surface charge and

wettability. Such an extensive array of techniques allows for more in depth observation and hypothesis. Scanning Electron Microscopy (SEM, Hitachi S-4800) was used to determine the nanowire morphology and cell shape post fixation; Atomic Force Microscopy (AFM, JPK Nanowizard II) was used to determine the arrays adhesiveness and roughness. Zeta Potential (ZP, Malvern Zetasizer 2000) was used to determine the substrates surface charge in PBS; also contact angles were acquired of 1 µl water droplets in air using a (Hitachi Denshi Ltd., Colour CCD) to determine surface wettability. As previously discussed Lampin et al. [59] has shown that substratum surface characteristics affected U-2 OS cell spreading area. Similarly it has been shown by Martin et al. [72] that surface roughness affected cell shape, proliferation, differentiation, and protein synthesis of human osteoblasts (MG63) on Titanium disks. Könönen et al. [73] conducted similar research with human gingival fibroblasts, conducting immmunofluoresence microscopy and reporting that appearance of stress-fiber type actin bundles and vinculin-containing focal adhesions were dependent on the texture of the Titanium surface. Therefore it can be seen that substrate roughness is likely to be a key variable for examination of cell behaviour witnessed so far and it will be investigated next.

8.6.1. Surface roughness and Adhesion (AFM)

It is well documented in the literature that surface roughness can have a major effect on cell-substrata interaction that may lead to cell behavioural changes, changes in motility and proliferation rate or even necrosis. It has been shown by Lampin et al. [59] that chick embryo explants are susceptible to surface roughness and wettability, with surface roughness substantially altering cell behaviour (shape), migration (motility) and proliferation on PMMA substrata of different roughness. Chung et al. [74] have reported that nanometer scale roughness can improve the adhesion and proliferation of human endothelial cells (HUVECs) on a biomaterial surface. Conducting an MTT assay they found that increased surface roughness of 10 – 100 nm scale enhances proliferation of HUVECs on polyethylene glycol (PEG) on polyurethane (PU) substrata. AFM measurements were performed in contact and tapping modes to acquire force curves and images for RMS roughness, see Fig. 8.25.

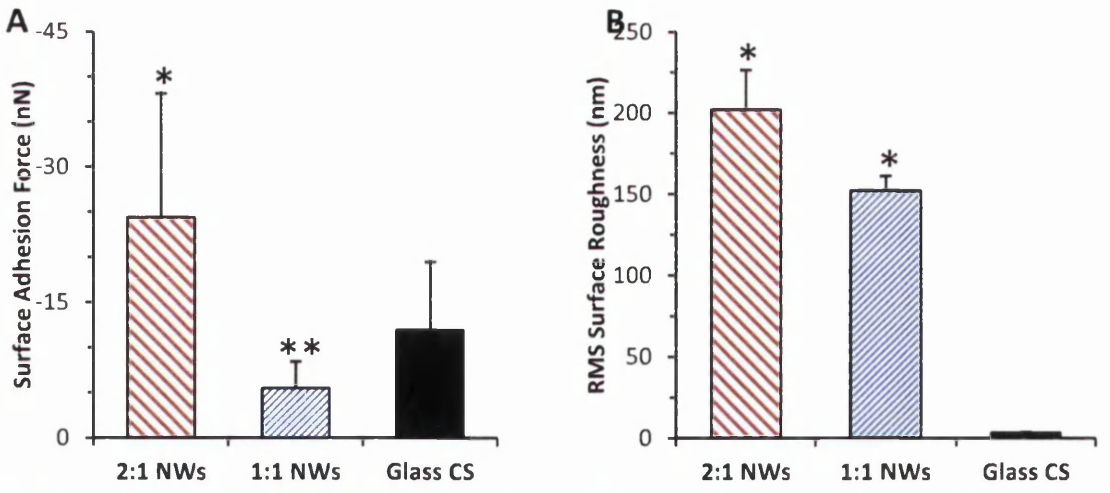

Figure 8.25. Graphs' comparing the surface properties for the two different ZnO nanowire recipes compared to a glass cover slip control, where (A) shows Surface Adhesion and (B) Surface Roughness; where N = (A) 300 force curves, and (B) 15 locations. * indicates $p<0.005$ and ** $p<0.05$ compared to glass cover slip control.

Fig. 8.25a. shows the adhesion properties of the 3 different substrates, where it can be seen that the 2:1 nanowire arrays yields the 'stickiest' surface for U-2 OS to adhere to. 300 force curves were taken per sample and the surface adhesion force with a 8 μm latex sphere was found to be -24.40, -5.52 and -11.92 nN for 2:1 nanowires, 1:1 nanowires and glass coverslip control, respectively. It is most likely that the increased (0001) facet surface area of 2:1 nanowires provides additional contact for van der walls forces yielding increased adhesion force in AFM force curves compared to pointy 1:1 nanowires and flat glass coverslips. Zaveri et al. [71] made a similar discovery with mouse macrophages in vivo, where they subcutaneously implanted ZnO nanowire coated and a ZnO-layer coated substrata in mice for 14 days and found that cell adhesion and viability correlate to both topography and toxicity of ionic zinc. They also conducted a similar study in vitro where the ZnO nanowire and ZnO layer substrata were suspended above the cells and observed a 30 % reduction in cell adhesion compared to a glass control indicating that viability was independent of topography. However, it has already been hypothesised that ionic zinc is likely removed via reaction with chlorine and sulphur forming inorganic salts zinc chloride and zinc sulphide as shown by the EDX findings in Fig. 8.5.

Fig. 8.25b. shows the surface roughness properties of the 3 different substrates, where it can be seen that the 2:1 nanowire arrays yields the most textured surface for U-2 OS to adhere too. 15 locations were randomly selected from 3 substrata per sample and the RMS surface roughness was found to be 202, 152 and 3 nm for 2:1 nanowires,

1:1 nanowires and glass coverslip control, respectively. Chung et al. [74] reports that the viability of HUVECs on substrata with increased surface roughness significantly improved, evaluated by MTT assay. Similarly, Martin et al. [72] has found increased MG63 cell numbers on rough Titanium substrates compared to smooth controls. It has been reported by ter Brugge et al. [1] that substrate characteristics can affect cell function due to surface roughness altering the cell's shape, leading to changes in integrin formation and so they hypothesise that this leads to interference with intracellular signaling events. It is commonly mentioned in the literature that substrata with greater surface area will have greater protein adsorption. Specifically, Mora et al. [75] have shown that pore size and surface area of carbon biomaterials had a substantial effect on the amount of protein adsorption. Such differences in protein adsorption due to surface roughness could greatly affect cell proliferation as integrin requires a robust ECM for creating cell-substratum focal adhesions. Therefore the AFM analysis provides a possible explanation for the difference in cell viability between the two types of wires.

8.6.2. Surface charge and wettability

It is often reported in the literature that cell-substratum adhesion is highly dependent on surface charge and hydrophobicity of the substratum. This is predominately due to the protein adsorption process being hydrophobicity sensitive, where hydrophobic surfaces are often shown to adsorb more proteins than hydrophilic surfaces [76]. Also Lopes et al. [77] have reported that substratum surface charge affects the formation of the proteinaceous layer absorbed onto the surface. Where Saravia and Toca-Herrera [43] have reviewed cell-substratum interaction and report that mechanical tension between the cytoskeleton and ECM has an effect on cell shape and behaviour, leading to complex signaling cascades.

Fig. 8.26a. shows the surface charge properties of the 3 different substrates, where it can be seen that the glass coverslip control yields the most highly charged surface for U-2 OS to adhere to. 11 measurements were taken per solution and the surface charge was found to be -25.1, -17.5 and -35.8 mV for 2:1 nanowires, 1:1 nanowires and glass coverslip control, respectively. Chen et al. [78] reported that the cellular uptake of hydroxyapatite (HAP) nanoparticles and effect on cell viability and proliferation of MC3T3-E1 cell lines (osteoblast) in vitro was surface charge dependent. They report that MC3T3-E1's negatively charged cell membrane lead to more uptake of

positively charged HAP nanoparticles compared to those with negative charge, which they attribute to either attractive or repulsive cell-nanoparticle interaction. Degen and Kosec [9] report that water molecules are chemically adsorbed onto the zinc oxide surface, where hydroxyl surface coating leads to a change in surface charge with changing pH. They report a similar zeta potential value of – 30 mV for ZnO nanoparticles when sulphate ions are added to their solution and the pH is in the region of 6.5 – 12. They hypothesize that sulphate ions form high valency conjugate bases of sulphuric acid, where the significant reduction in zeta potential may be due to strong surface adsorption due to high negative charge density of this polyvalent acid. As Fig. 8.5. indicated, sulphate ions will be in the solution, so this explanation for the obtained surface charge is highly probable.

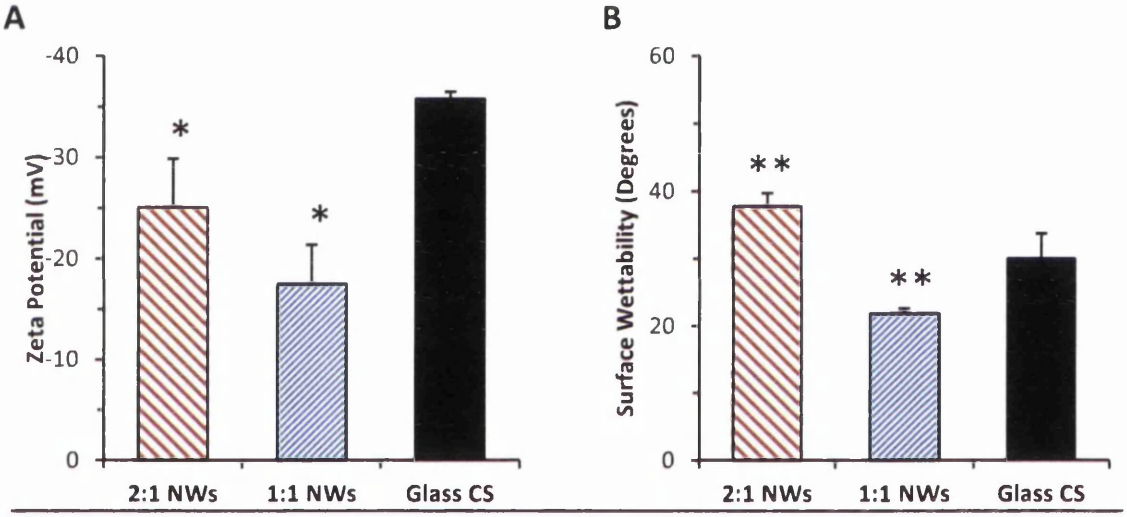

Figure 8.26. Graphs' comparing the surface properties for the two different ZnO nanowire recipes compared to a glass cover slip control, where (A) shows Surface Charge and (B) Surface Wettability. For each graph n= (A) 11 measurements and (B) 4 droplets. * indicates $p<0.005$ and ** $p<0.05$ compared to glass cover slip control.

It is well established in the literature that negatively charged osteoblasts prefer to adhere to a negatively charged substratum, typically because negatively charged substrata promote additional protein adsorption [79]. It has been reported by Bodhak et al. [17] that human fetal osteoblast cells assumed a flattened and spread morphology on negatively charged HAP substrata after 5 days incubated. They postulate that the mechanism for increased cell spreading area and proliferation on negatively charged substrates is due to their preferential adsorption of Ca^{2+} ions and cell adhesive proteins

(e.g. fibronectin), providing more sites for osteoblast cell adhesion and therefore a more spread and happy cell. Therefore the increased negative charge of 2:1 nanowires compared to other substrata could well be the cause behind previously observed large cell spreading area. Chen et al. [80] has shown for bacteria that substrata zeta potentials lead to difference in cell-substratum adhesion due to surface charge and there is an interplay between long-range Lifshitz - Van der Waals, electrical double layer and short-range Lewis acid-base interaction forces. It is often reported in the literature that titanium is the best biomaterial for orthopedic implants and is widely used for bone-implant application due to its hydrophilic and negatively charged surface [14].

Fig. 8.26b. shows the surface wettability of the 3 different substrates, where it can be seen that the 2:1 nanowire arrays yields the least hydrophobic surface for U-2 OS to adhere too. 8 measurements were taken from 4 droplets per substratum and the surface wettability determined to be 37.8, 21.9 and 30.0 ° for 2:1 nanowires, 1:1 nanowires and glass coverslip control, respectively. It should be noted that although 2:1 nanowires yielded the least hydrophobic surfaces that all Student's Ttest p values in Table 8.9. exceeded 0.005 and so while still being significantly different they're more similar than other findings in this section [81]. Bacáková et al. [45] report that hydrophobic surfaces also have anti adhesive properties, and that adsorption of proteins on to a hydrophobic surface results in a rigid, reorganization resistant ECM. The correlation between hydrophobicity and surface adhesion is similar to findings in this work, where the most hydrophobic surface (1:1 nanowire array) also yielded the lowest adhesion force for the 8 μm latex colloid. García et al. [82] have shown that rigid ECM results in amino acid sequence inaccessibility for the cells integrin receptors, therefore reducing adhesion.

Table 8.9. Matched pair 2 tailed Student's ttests values for Figures 8.31-2.

Experiment	(Fig)	2:1 vs. 1:1	2:1 vs. Glass	1:1 vs. Glass
Adhesion	8.25a	5.49E-67	0.000914	0.034866
Roughness	8.25b	3.57E-06	2.14E-14	1.03E-18
Charge	8.26a	6.58E-08	6.81E-13	1.35E-17
Wettability	8.26b	0.000672	0.006407	0.029429

It is somewhat difficult to separate the influence of wettability from the influence of surface roughness as well as topography and adhesion force, since all parameters differ among the 3 substrata. This problem has been best described by Vitte

et al. [83] where they explain that when a cell has just adhered to a surface it has several decisions to make. The cell may undergo apoptosis, or remain alive and proliferate, it may remain on the site of adhesion or may start migrating; essentially the reason for this decision is the focus of the biological research community. While several of these decisions have been investigated in this work, it has been difficult to efficiently manage to pursue two areas of research in tandem, this is why cell-substratum interaction became the focus of the work as it is an essential piece in the puzzle that is cell mechanics.

8.7. Summary

It has been shown that ZnO nanowire arrays are biocompatible with U-2 OS with little difference between the glass coverslip control and both the ZnO nanowire substrata up to 48 hours. However for incubation times greater than 48 hours it has been observed that a statistical difference emerges between the glass coverslip control and one of the ZnO nanowire arrays; specifically the 1:1 recipe. The viability still remains at 88.4 % for 2:1 nanowire arrays and drops to 72.4 % for 1:1 nanowire arrays. Although MTS only gives an indication of cell health via proliferation it doesn't yield any information about the death of cells, and therefore it has often been suggested in literature that a lactose dehydrogenase assay should be conducted in tandem to confirm if necrosis is reducing proliferation or just adverse conditions inhibiting mitosis keeping cells in their lag phase. Smith et al. [84] present a thorough MTS/LDH based protocol to determine if reduced proliferation is due to growth inhibition or cell death , and this should be conducted if the work were repeated. A LIVE DEAD assay was also conducted supporting the findings of the MTS assay, where at the highest cell seeding concentration after 72 hours it was found that 86.6, 65.2 and 55.4 % of the U-2 OS cells were alive on glass control, 2:1 and 1:1 nanowires, respectively.

The main mechanism behind the observed change in cell shape witnessed during the study is attributed to surface charge, hydrophobicity and surface roughness of the nanowires. However, exciting results using immuno-gold SEM of α-vinculin to determine integrin focal adhesion points indicated that the cells preferentially attached to the non-polar facets, where 1:1 nanowires pointy ends would not allow such attachment. It is also likely that (0001) facets provide more support and apply less

pressure on the cell's cytoplasm. Specifically the gap between the wires are encouraging a change in cell shape due to a change in global surface roughness [1]. The viability percentages obtained during the study undoubtedly directly relate to the observations present on the surface spreading area of the the cells. Work on observing the interface between the cells and nanowires has already been started by the author and this research is ongoing (discussed in chapter 9). Preliminary immunocytochemisty work to study focal adhesions with confocal microscopy is also underway.

It is believed that further work should be conducted and the differentiation of human mesenchymal stem cells (hMSCs) using ZnO NWs should be investigated. McBeath et al. [85] have observed the switching of stem cells lineage commitment by introducing the cells to different micro-patterned surfaces, reporting that cells that flatten and spread underwent osteogenesis while unspread round cells became adipocytes. If this idea is combined with the solubility of ZnO nanowires then some novel device coatings could be brought to market. Zhou et al. [6] have reported ZnO nanowires dissolving in horse serum within 14 days, this creates a great deal of potential for coating implantable devices such as (for example) replacement joints that can inhibit immune system response and negate osteoimmunology response. Imagine a hip-joint that can reduce post-operation inflammation and encourage wound healing via differentiation of the own patients hMSCs harvested during the the operation. The ZnO nanowires would dissolve harmlessly by which time plenty of oseteopontin and hydroxyapatite will have been created due to the high number of osteoblasts from promotion of osteogenic differentiation. The possibilites with this material are endless now that it has been proven biocompatible, however the logical next step in work would be investigate cytotoxicology and in vivo application initally with micronucleas assay and in vitro assesment with macrophages, as per work by Zaveri et al. [71]. Also, Hu et al. [86] say that the perfect bone implant should actively recruit osteoblasts and promote cell adhesion as well as release appropriate bioactive signals (growth factors or cytokines) to promote cell proliferaion for rapid new bone formation.

This work has proven ZnO nanowires grown by chemical bath deposition provide good cell adhesion and the next step would be to investigate bioactive signals and differentiation. The majority of literature consentrates on the viability and biocompatabily of ZnO nanowires, therefore research into differentiation of cells, as well as other areas such as gene expression, phenotypes etc... would likely be well received by the Academic commmunity.

8.8. References

[1] P. J. ter Brugge, S. Dieudonne, J. a Jansen, and P. J. Brugge, "Initial interaction of U2OS cells with noncoated and calcium phosphate coated titanium substrates.," *J. Biomed. Mater. Res.*, vol. 61, no. 3, pp. 399–407, Sep. 2002.

[2] Z. Li, R. Yang, M. Yu, F. Bai, C. Li, and Z. L. Wang, "Cellular Level Biocompatibility and Biosafety of ZnO Nanowires," *J. Phys. Chem. C*, vol. 112, no. 51, pp. 20114–20117, Dec. 2008.

[3] G. Ciofani, G. G. Genchi, and V. Mattoli, "ZnO nanowire arrays as substrates for cell proliferation and differentiation," *Mater. Sci. Eng. C*, vol. 32, no. 2, pp. 341–347, Nov. 2011.

[4] N. Neykova, A. Brož, Z. Remeš, K. Hruška, M. Kalbáčová, A. Kromka, and M. Vaněček, "ZnO hedgehog-like structures for control cell cultivation," *Appl. Surf. Sci.*, vol. 258, no. 8, pp. 3485–3489, Feb. 2012.

[5] R. A. Brown, C. J. Barnett, A. Tarat, D. R. Jones, L. W. Francis, S. Conlan, and T. G. G. Maffeis, "The viability of U-2 OS cells on Zinc Oxide nanowires observed via MTS assay in vitro," in *Nanotechnology (IEEE-NANO), 2012 12th IEEE Conference*, 2012, pp. 190–193.

[6] J. Zhou, N. S. Xu, and Z. L. Wang, "Dissolving Behavior and Stability of ZnO Wires in Biofluids: A Study on Biodegradability and Biocompatibility of ZnO Nanostructures," *Adv. Mater.*, vol. 18, no. 18, pp. 2432–2435, Sep. 2006.

[7] K. H. Muller, J. Kulkarni, M. Motskin, A. Goode, P. Winship, J. N. Skepper, M. P. Ryan, and A. E. Porter, "pH-Dependent Toxicity of High Aspect Ratio ZnO Nanowires in Macrophages Due to Intracellular Dissolution," *ACS Nano*, vol. 4, no. 11, pp. 6767–6779, 2010.

[8] T. R. Arnett, "Extracellular pH regulates bone cell function.," *J. Nutr.*, vol. 138, no. 2, p. 415S–418S, Feb. 2008.

[9] A. Degen and M. Kosec, "Effect of pH and impurities on the surface charge of zinc oxide in aqueous solution," *J. Euro. Ceram. Soc.*, vol. 20, pp. 667–673, 2000.

[10] Z. Wang, X. Zu, S. Zhu, and L. Wang, "Green luminescence originates from surface defects in ZnO nanoparticles," *Phys. E Low-dimensional Syst. Nanostructures*, vol. 35, no. 1, pp. 199–202, Oct. 2006.

[11] A. Sugunan, H. C. Warad, M. Boman, and J. Dutta, "Zinc oxide nanowires in chemical bath on seeded substrates: Role of hexamine," *J. Sol-Gel Sci. Technol.*, vol. 39, no. 1, pp. 49–56, May 2006.

[12] N. M. Franklin, N. J. Rogers, S. C. Apte, G. E. Batley, G. E. Gadd, and P. S. Casey, "Comparative Toxicity of Nanoparticulate ZnO, Bulk ZnO, and ZnCl2 to a Freshwater Microalga (Pseudokirchneriella subcapitata): The Importance of Particle Solubility," *Environ. Sci. Technol.*, vol. 41, no. 24, pp. 8484–8490, 2007.

[13] L. Zhao, L. Hu, K. Huo, Y. Zhang, Z. Wu, and P. K. Chu, "Mechanism of cell repellence on quasi-aligned nanowire arrays on Ti alloy.," *Biomaterials*, vol. 31, no. 32, pp. 8341–9, Nov. 2010.

[14] T. Berlind, P. Tengvall, L. Hultman, and H. Arwin, "Protein adsorption on thin films of carbon and carbon nitride monitored with in situ ellipsometry.," *Acta Biomater.*, vol. 7, no. 3, pp. 1369–78, Mar. 2011.

[15] K. Govender, D. S. Boyle, P. B. Kenway, P. O'Brien, and P. O. Brien, "Understanding the factors that govern the deposition and morphology of thin films of ZnO from aqueous solution," *J. Mater. Chem.*, vol. 14, no. 16, pp. 2575–2591, 2004.

[16] J. Joo, B. Y. Chow, M. Prakash, E. S. Boyden, and J. M. Jacobson, "Face-selective electrostatic control of hydrothermal zinc oxide nanowire synthesis.," *Nat. Mater.*, vol. 10, no. 8, pp. 596–601, Aug. 2011.

[17] S. Bodhak, S. Bose, and A. Bandyopadhyay, "Role of surface charge and wettability on early stage mineralization and bone cell-materials interactions of polarized hydroxyapatite.," *Acta Biomater.*, vol. 5, no. 6, pp. 2178–88, Jul. 2009.

[18] H. Wang, J. Xie, K. Yan, and M. Duan, "Growth Mechanism of Different Morphologies of ZnO Crystals Prepared by Hydrothermal Method," *J. Mater. Sci. Technol.*, vol. 27, no. 2, pp. 153–158, Feb. 2011.

[19] Y. Lee, T. L. Sounart, J. Liu, E. D. Spoerke, B. B. Mckenzie, J. W. P. Hsu, and J. A. Voigt, "Tunable Arrays of ZnO Nanorods and Nanoneedles via Seed Layer and Solution Chemistry," *Cryst. Growth Des.*, vol. 8, no. 6, pp. 2036 – 2040, 2008.

[20] M. Wang, C.-H. Ye, Y. Zhang, H. Wang, X.-Y. Zeng, L.-D. Zhang, and L.-D. Zhsng, "Seed-layer controlled synthesis of well-aligned ZnO nanowire arrays via a low temperature aqueous solution method," *J. Mater. Sci. Mater. Electron.*, vol. 19, no. 3, pp. 211–216, Jul. 2007.

[21] C.-C. Lin, S.-Y. Chen, and S.-Y. Cheng, "Nucleation and growth behavior of well-aligned ZnO nanorods on organic substrates in aqueous solutions," *J. Cryst. Growth*, vol. 283, no. 1–2, pp. 141–146, Sep. 2005.

[22] C. S. Chen, J. L. Alonso, E. Ostuni, G. M. Whitesides, and D. E. Ingber, "Cell shape provides global control of focal adhesion assembly," *Biochem. Biophys. Res. Commun.*, vol. 307, no. 2, pp. 355–361, Jul. 2003.

[23] J. V Shah, "Cells in tight spaces□: the role of cell shape in cell function," *J. Cell Biol.*, vol. 191, no. 2, pp. 233–236, Oct. 2010.

[24] D. C. Bell and A. J. Garratt-Reed, "Energy Dispersive X-ray Analysis in the Electron Microscope," in *Volume 49 Microscopy Books*, Garland Science, 2003, p. 160.

[25] H. Xue, N. Pan, M. Li, Y. Wu, X. Wang, and J. G. Hou, "Probing the strain effect on near band edge emission of a curved ZnO nanowire via spatially resolved cathodoluminescence.," *Nanotechnology*, vol. 21, no. 21, p. 215701, May 2010.

[26] H. Sowa and H. Ahsbahs, "High-pressure X-ray investigation of zincite ZnO single crystals using diamond anvils with an improved shape," *J. Appl. Crystallogr.*, vol. 39, no. 2, pp. 169–175, Apr. 2006.

[27] S. Gražulis, D. Chateigner, R. T. Downs, a F. T. Yokochi, M. Quirós, L. Lutterotti, E. Manakova, J. Butkus, P. Moeck, and A. Le Bail, "Crystallography Open Database - an open-access collection of crystal structures.," *J. Appl. Crystallogr.*, vol. 42, no. Pt 4, pp. 726–729, Aug. 2009.

[28] G. A. Kumar, M. V. R. Reddy, and K. N. Reddy, "Effect of substrate temperature on structural and optical properties of nanostructured ZnO thin films grown by RF magnetron sputtering," *Int. Conf. Nanosci. Eng. Technol. (ICONSET 2011)*, pp. 56–60, Nov. 2011.

[29] D. Polsongkram, P. Chamninok, S. Pukird, L. Chow, O. Lupan, G. Chai, H. Khallaf, S. Park, and A. Schulte, "Effect of synthesis conditions on the growth of ZnO nanorods via hydrothermal method," *Scan. Electron Microsc.*, vol. 403, pp. 3713–3717, 2008.

[30] E. U. Ando and M. Miyazaki, "Moisture resistance of the low-emissivity coatings with a layer structure of Al-doped ZnO/Ag/Al-doped ZnO," *Thin Solid Films*, vol. 392, pp. 289–293, 2001.

[31] J. . Sans, A. Segura, M. Mollar, and B. Marí, "Optical properties of thin films of ZnO prepared by pulsed laser deposition," *Thin Solid Films*, vol. 453–454, pp. 251–255, Apr. 2004.

[32] K. H. Tam, C. K. Cheung, Y. H. Leung, A. B. Djurišić, C. C. Ling, C. D. Beling, S. Fung, W. M. Kwok, W. K. Chan, D. L. Phillips, L. Ding, and W. K. Ge, "Defects in ZnO nanorods prepared by a hydrothermal method.," *J. Phys. Chem. B*, vol. 110, no. 42, pp. 20865–71, Oct. 2006.

[33] I. Özen, M. A. Gülgün, and M. Özcan, "Self-induced Crystallinity in RF Magnetron Sputtered ZnO Thin Films," *Key Eng. Mater.*, vol. 268, pp. 1225–1228, 2004.

[34] B. Ha, H. Ham, and C. J. Lee, "Photoluminescence of ZnO nanowires dependent on O2 and Ar annealing," *J. Phys. Chem. Solids*, vol. 69, no. 10, pp. 2453–2456, Oct. 2008.

[35] J. Deenathayalan, M. Saroja, M. Venkatachalam, P. Gowthaman, and T. S. Senthil, "Effect of Growth Layer Solution Concentration on the Structural and Optical Properties of Hydrothermally Grown Zinc Oxide Nanorods," *Chalcogenide Lett.*, vol. 8, no. 9, pp. 549–554, 2011.

[36] V. Srikant and D. R. Clarke, "Optical absorption edge of ZnO thin films: The effect of substrate," *J. Appl. Phys.*, vol. 81, no. 9, p. 6357, 1997.

[37] D. Reynolds, "Optical properties of ZnO crystals containing internal strains," *J. Lumin.*, vol. 82, no. 2, pp. 173–176, Aug. 1999.

[38] D. Wang and N. Reynolds, "Photoluminescence of Zinc Oxide Nanowires: The Effect of Surface Band Bending," *ISRN Condens. Matter Phys.*, vol. 2012, pp. 1–6, 2012.

[39] V. Gupta and A. Mansingh, "Influence of postdeposition annealing on the structural and optical properties of sputtered zinc oxide film," *J. Appl. Phys.*, vol. 80, no. 2, p. 1063, Jul. 1996.

[40] B. Alberts, A. Johnson, J. Lewis, M. Raff, K. Roberts, and P. Walter, *Molecular Biology of the Cell*. Garland Science, 2002, p. 1146.

[41] J. Liu, J. She, S. Deng, J. Chen, and N. Xu, "Ultrathin Seed-Layer for Tuning Density of ZnO Nanowire Arrays and Their Field Emission Characteristics," *J. Phys. Chem. C*, vol. 112, pp. 11685–11690, 2008.

[42] L. W. Francis, D. Gonzalez, T. Ryder, K. Baer, M. Rees, J. O. White, R. S. Conlan, and C. J. Wright, "Optimized sample preparation for high-resolution AFM characterization of fixed human cells.," *J. Microsc.*, vol. 240, no. 2, pp. 111–21, Nov. 2010.

[43] V. Saravia and J. L. Toca-Herrera, "Substrate Influence on Cell Shape and Cell Mechanics□: HepG2 Cells Spread on Positively Charged Surfaces," *Microsc. Res. Tech.*, vol. 964, no. May, pp. 957–964, 2009.

[44] A. Puliafito, L. Hufnagel, P. Neveu, S. Streichan, A. Sigal, D. K. Fygenson, and B. I. Shraiman, "Collective and single cell behavior in epithelial contact inhibition.," *Proc. Natl. Acad. Sci. U. S. A.*, vol. 109, no. 3, pp. 739–44, Jan. 2012.

[45] L. Bacáková, E. Filová, F. Rypácek, V. Svorcík, and V. Starý, "Cell adhesion on artificial materials for tissue engineering.," *Physiol. Res.*, vol. 53, pp. S35–45, Jan. 2004.

[46] C. U. Vohwinkel, E. Lecuona, H. Sun, N. Sommer, I. Vadász, N. S. Chandel, and J. I. Sznajder, "Elevated CO(2) levels cause mitochondrial dysfunction and impair cell proliferation.," *J. Biol. Chem.*, vol. 286, no. 43, pp. 37067–76, Oct. 2011.

[47] R. I. Freshney, *Culture of Animal Cells: A Manual of Basic Technique*, 5th ed. Wiley-Blackwell, 2005, p. 672.

[48] M. V. Berridge and A. S. Tan, "Characterization of the Cellular Reduction of 3-(4,5-dimethylthiazol-2-yl)-2,5-diphenyltetrazolium bromide (MTT): Subcellular Localization, Substrate Dependence, and Involvement of Mitochondrial Electron Transport in MTT Reduction," *Arch. Biochem. Biophys.*, vol. 303, no. 2, pp. 474–482, 1993.

[49] C. J. Goodwin, S. J. Holt, S. Downes, and N. J. Marshall, "Microculture tetrazolium assays: a comparison between two new tetrazolium salts, XTT and MTS.," *J. Immunol. Methods*, vol. 179, no. 1, pp. 95–103, Feb. 1995.

[50] M. D. Fellows, M. R. O'Donovan, E. Lorge, and D. Kirkland, "Comparison of different methods for an accurate assessment of cytotoxicity in the in vitro micronucleus test. II: Practical aspects with toxic agents.," *Mutat. Res.*, vol. 655, no. 1–2, pp. 4–21, 2008.

[51] K. Solly, X. Wang, X. Xu, B. Strulovici, and W. Zheng, "Application of Real-Time Cell Electronic Sensing (RT-CES) Technology to Cell-Based Assays," *Assay Drug Dev. Technol.*, vol. 2, no. 4, pp. 363–372, Aug. 2004.

[52] J. C. Wataha, R. G. Craig, and C. T. Hanks, "Precision of and new methods for testing in vitro alloy cytotoxicity.," *Dent. Mater.*, vol. 8, no. 1, pp. 65–70, Jan. 1992.

[53] A. N. Glazer, K. Peck, and R. A. Mathies, "A stable double-stranded DNA-ethidium homodimer complex: application to picogram fluorescence detection of DNA in agarose gels," *Proc. Natl. Acad. Sci. U. S. A.*, vol. 87, no. 10, pp. 3851–5, May 1990.

[54] T. a Lane and E. R. Burka, "Decreased life span and membrane damage of carbamylated erythrocytes in vitro.," *Blood*, vol. 47, no. 6, pp. 909–17, Jun. 1976.

[55] A. Draeger, K. Monastyrskaya, and E. B. Babiychuk, "Plasma membrane repair and cellular damage control: the annexin survival kit.," *Biochem. Pharmacol.*, vol. 81, no. 6, pp. 703–12, Mar. 2011.

[56] R. Jahn and D. Fasshauer, "Molecular machines governing exocytosis of synaptic vesicles.," *Nature*, vol. 490, no. 7419, pp. 201–7, Oct. 2012.

[57] M. Hagedorn, E. M. Neuhaus, and T. Soldati, "Optimized fixation and immunofluorescence staining methods for Dictyostelium cells.," *Methods Mol. Biol.*, vol. 346, no. 1, pp. 327–38, Jan. 2006.

[58] P. J. ter Brugge, S. Dieudonne, and J. a Jansen, "Initial interaction of U2OS cells with noncoated and calcium phosphate coated titanium substrates.," *J. Biomed. Mater. Res.*, vol. 61, no. 3, pp. 399–407, Sep. 2002.

[59] M. Lampin, Warocquier-Clérout, C. Legris, M. Degrange, and M. F. Sigot-Luizard, "Correlation between substratum roughness and wettability, cell adhesion, and cell migration.," *J. Biomed. Mater. Res.*, vol. 36, no. 1, pp. 99–108, Jul. 1997.

[60] Y. Loosli, R. Luginbuehl, and J. G. Snedeker, "Cytoskeleton reorganization of spreading cells on micro-patterned islands: a functional model.," *Philos. Trans. A. Math. Phys. Eng. Sci.*, vol. 368, no. 1920, pp. 2629–52, Jun. 2010.

[61] M. D. Abràmoff, P. J. Magalhães, and S. J. Ram, "Image Processing with ImageJ," *Biophotonics Int.*, vol. 11, no. 7, pp. 36–42, 2004.

[62] R. M. Shelton, A. C. Rasmussen, and J. E. Davies, "Protein adsorption at the interface between charged polymer substrata and migrating osteoblasts," *Biomaterials*, vol. 9, no. 1, pp. 24–29, Jan. 1988.

[63] J. Fu, Y.-K. Wang, M. T. Yang, R. a Desai, X. Yu, Z. Liu, and C. S. Chen, "Mechanical regulation of cell function with geometrically modulated elastomeric substrates," *Nat. Methods*, vol. 7, no. 9, pp. 733–736, Aug. 2010.

[64] R. Ayala, C. Zhang, D. Yang, Y. Hwang, A. Aung, S. S. Shroff, F. T. Arce, R. Lal, G. Arya, and S. Varghese, "Engineering the cell-material interface for controlling stem cell adhesion, migration, and differentiation.," *Biomaterials*, vol. 32, no. 15, pp. 3700–11, May 2011.

[65] G. Gronowicz and M. B. McCarthy, "Response of human osteoblasts to implant materials: integrin-mediated adhesion.," *J. Orthop. Res.*, vol. 14, no. 6, pp. 878–87, Nov. 1996.

[66] R. Ananthakrishnan and A. Ehrlicher, "The forces behind cell movement.," *Int. J. Biol. Sci.*, vol. 3, no. 5, pp. 303–17, Jan. 2007.

[67] M. L. Gardel, I. C. Schneider, Y. Aratyn-Schaus, and C. M. Waterman, "Mechanical integration of actin and adhesion dynamics in cell migration.," *Annu. Rev. Cell Dev. Biol.*, vol. 26, pp. 315–33, Jan. 2010.

[68] C. Lawson, S.-T. Lim, S. Uryu, X. L. Chen, D. a Calderwood, and D. D. Schlaepfer, "FAK promotes recruitment of talin to nascent adhesions to control cell motility.," *J. Cell Biol.*, vol. 196, no. 2, pp. 223–32, Jan. 2012.

[69] T. P. Lele, C. K. Thodeti, J. Pendse, and D. E. Ingber, "Investigating complexity of protein-protein interactions in focal adhesions.," *Biochem. Biophys. Res. Commun.*, vol. 369, no. 3, pp. 929–34, May 2008.

[70] J. J. Bozzola and L. D. Russell, *Electron Microscopy: Principles and Techniques for Biologists*. Jones and Bartlett, 1992, p. 542.

[71] T. D. Zaveri, N. V Dolgova, B. H. Chu, J. Lee, J. Wong, T. P. Lele, F. Ren, and B. G. Keselowsky, "Contributions of surface topography and cytotoxicity to the macrophage response to zinc oxide nanorods.," *Biomaterials*, vol. 31, no. 11, pp. 2999–3007, Apr. 2010.

[72] J. Y. Martin, Z. Schwartz, T. W. Hummert, D. M. Schraub, J. Simpson, J. Lankford, D. D. Dean, D. L. Cochran, and B. D. Boyan, "Effect of titanium surface roughness on proliferation, differentiation, and protein synthesis of human osteoblast-like cells (MG63).," *J. Biomed. Mater. Res.*, vol. 29, no. 3, pp. 389–401, Mar. 1995.

[73] M. Könönen, M. Hormia, J. Kivilahti, J. Hautaniemi, and I. Thesleff, "Effect of surface processing on the attachment, orientation, and proliferation of human gingival fibroblasts on titanium.," *J. Biomed. Mater. Res.*, vol. 26, no. 10, pp. 1325–41, Oct. 1992.

[74] T.-W. Chung, D.-Z. Liu, S.-Y. Wang, and S.-S. Wang, "Enhancement of the growth of human endothelial cells by surface roughness at nanometer scale," *Biomaterials*, vol. 24, no. 25, pp. 4655–4661, Nov. 2003.

[75] E. Mora, V. Ruiz, R. Santamaría, C. Blanco, M. Granda, R. Menéndez, J. M. Juarez-Galán, and F. Rodríguez-Reinoso, "Influence of mesophase activation conditions on the specific capacitance of the resulting carbons," *J. Power Sources*, vol. 156, no. 2, pp. 719–724, Jun. 2006.

[76] J. Benesch, A. Askendal, and P. Tengvall, "Quantification of adsorbed human serum albumin at solid interfaces: a comparison between radioimmunoassay (RIA) and simple null ellipsometry," *Colloids Surfaces B Biointerfaces*, vol. 18, no. 2, pp. 71–81, Aug. 2000.

[77] M. a Lopes, F. J. Monteiro, J. D. Santos, A. P. Serro, and B. Saramago, "Hydrophobicity, surface tension, and zeta potential measurements of glass-reinforced hydroxyapatite composites.," *J. Biomed. Mater. Res.*, vol. 45, no. 4, pp. 370–5, Jun. 1999.

[78] L. Chen, J. M. Mccrate, J. C.-M. Lee, and H. Li, "The role of surface charge on the uptake and biocompatibility of hydroxyapatite nanoparticles with osteoblast cells.," *Nanotechnology*, vol. 22, no. 10, p. 105708, Mar. 2011.

[79] E. Gongadze, D. Kabaso, S. Bauer, T. Slivnik, P. Schmuki, U. van Rienen, and A. Iglič, "Adhesion of osteoblasts to a nanorough titanium implant surface.," *Int. J. Nanomedicine*, vol. 6, pp. 1801–16, Jan. 2011.

[80] Y. Chen, H. J. Busscher, H. C. van der Mei, and W. Norde, "Statistical analysis of long- and short-range forces involved in bacterial adhesion to substratum surfaces as measured using atomic force microscopy.," *Appl. Environ. Microbiol.*, vol. 77, no. 15, pp. 5065–70, Aug. 2011.

[81] R. C. Campbell, *Statistics for Biologists*. Cambridge: Cambridge University Press, 1967, p. 242.

[82] A. J. García, M. D. Vega, and D. Boettiger, "Modulation of cell proliferation and differentiation through substrate-dependent changes in fibronectin conformation.," *Mol. Biol. Cell*, vol. 10, no. 3, pp. 785–98, Mar. 1999.

[83] J. Vitte, a M. M. Benoliel, a Pierres, and P. Bongrand, "Is there a predictable relationship between surface physical-chemical properties and cell behaviour at the interface?," *Eur. Cells Mater.*, vol. 7, pp. 52–63, 2004.

[84] S. M. Smith, M. B. Wunder, D. A. Norris, and Y. G. Shellman, "A Simple Protocol for Using a LDH-Based Cytotoxicity Assay to Assess the Effects of Death and Growth Inhibition at the Same Time.," *PLoS One*, vol. 6, no. 11, p. e26908, Jan. 2011.

[85] R. McBeath, D. M. Pirone, C. M. Nelson, K. Bhadriraju, and C. S. Chen, "Cell shape, cytoskeletal tension, and RhoA regulate stem cell lineage commitment.," *Dev. Cell*, vol. 6, no. 4, pp. 483–95, Apr. 2004.

[86] Y. Hu, K. Cai, Z. Luo, Y. Zhang, L. Li, M. Lai, Y. Hou, Y. Huang, J. Li, X. Ding, B. Zhang, and K. L. P. Sung, "Biomaterials Regulation of the differentiation of mesenchymal stem cells in vitro and osteogenesis in vivo by microenvironmental modification of titanium alloy surfaces," *Biomaterials*, vol. 33, no. 13, pp. 3515–3528, 2012.

Chapter 9. Conclusions and Future Work

9.1. Introduction

Over the past 8 chapters this thesis has shown and discussed the properties of zinc oxide, the methods of its fabrication and the techniques used to characterize the vast arrays of zinc oxide nanowires created by hydrothermal method of chemical bath deposition. It has been shown that once a recipe that was reasonably reproducible was obtained and its properties explored the application of cells to zinc oxide nanowires and the effect this had on their behavior and proliferation was investigated. But what conclusions can be made from the observations made in this work and how does this help promote the research and development of zinc oxide as a viable biomaterial within the Academic community? This chapter will summarize the milestones that have been reached and those that are yet to be achieved.

9.2. Conclusions

In chapter 7 All the major variables for the hydrothermal growth of zinc oxide nanowires were explored, solution temperature, concentration, growth time, seed layer thickness and method, substrate position, ratio of precursors, yet initially reproducible crystal growth could not be obtained. Tolerances were too high when comparing the morphology results from two nanowire arrays using the same recipe; a significant variable was clearly being overlooked. By collating all the quantitative data and compiling it against all recorded variables it was promptly determined how the solution was stirred and for how long had an astonishingly high impact on the final morphology and optical properties of the obtained ZnO nanowires. This was postulated to be due to its effect on the formation of the $ZnOH_2$ intermediate, a source of Zn^{2+} ions. Once reproducibility was obtained a single variable was selected, precursor ratio, as it yielded the most significantly different nanowire arrays compared to all other variable changes.

$ZnNO_3$: HMTA at 2:1 and 1:1 where 1 = 25 mM, these were the finalized recipes taken into phase 2 of this work.

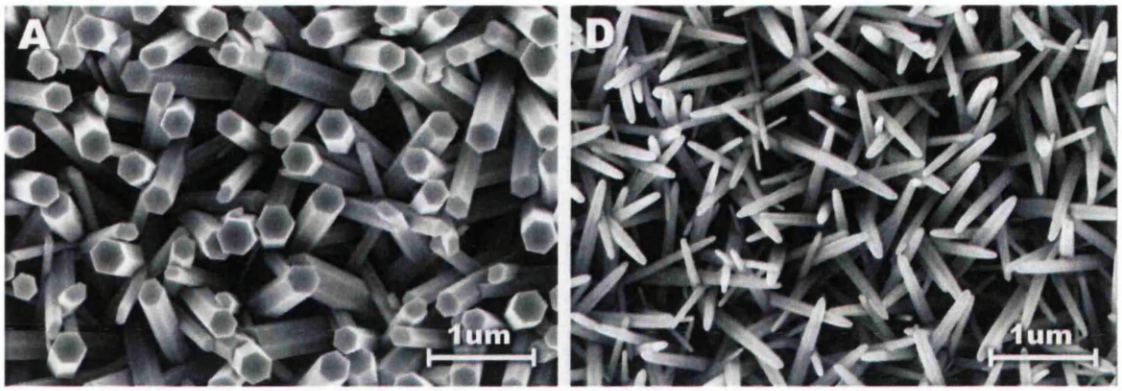

Figure 9.1. SEM images comparing the two final recipes, a) 2:1 and d) 1:1 that were used to investigate the biocompatibility and behaviour of cells on zinc oxide nanowires.

It has been shown in this work that ZnO nanowires are stable in media for 7 days, that U-2 OS cells adhere and proliferate as normal for 3 days. MTS assay results showed that at 3 days both 2:1 nanowires and the glass control had 88 % the number of cells of a no substrate (well only) control. It was also shown with LIVE DEAD assay that 2:1 nanowires obtained results similar to the glass control, with the results at low seeding after 3 days being 59, 65 and 62 % live cells for glass control, 2:1 and 1:1 nanowires, respectively. It should be noted that less emphasis was placed on LIVE DEAD results since there was a substantial difference between no substrate and glass controls, at 95 and 59 % live cells, respectively. This difference was likely due to the handling of the samples of the course of the 3 day experiments, where substrate samples would need to be frequently moved with tweezers in and out of new plates to complete the rinsing cycles and application of the LIVE DEAD assay.

After a few preliminary biocompatibility assays it become apparent that the nanowire arrays were having an effect on cellular behavior, the difference in cell spreading area was easily noticeable and so this was discussed. The author is unsure of the implications of a force sensor that alters the behavior of the specimen to be measured, but unless the effect can be minimized the ZnO nanowire arrays have little future for force sensing applications. However, they do have a future as surface coatings for implants, a future as a biomaterial as they are both biocompatible and easy to grow on any substrate (that is seeded with a layer of ZnO) using the hydrothermal chemical

bath deposition process. Therefore their future application as a surface coating for application in vivo will be discussed next.

9.3. Direction of Future Work

From above statements it cannot be argued that these nanowires are as biocompatible and safe as glass, but this work did not look into the long term effects of additional extracellular Zn^{2+}. If there was more time a micro-nucleus (genotoxicity) assay would have been conducted to confirm that U-2 OS cells were dividing correctly. The micro-nucleus assay just confirms the appearance of micronuclei, which are small cytoplasmic bodies containing parts or whole chromosomes not shared corrected during the anaphase (mitosis). Their formation essentially means that the cells are damaged at a genetic level and the chemical or substrate that was added is a carcinogen. Evaluation of cytotoxicology is an essential next step in ensuring that ZnO nanowires may be used for in vivo applications, or using macrophages for in vitro assessment.

A detailed plan of what to do and where to go next was discussed in section 8.7. and shall be summarised here. Phase 3 of the work should avoid force sensing application as cells are too easily perturbed, instead the influence the ZnO nanowire array has on the cells should be exploited to control the behavior of the cells. Sub-section 8.5.1 and 8.5.3. reported that the cell spreading area was altered depending on substrate topography, roughness and wettability. This phenomenon should be reinvestigated using human mesenchymal stem cells (hMSCs) to see if differentiation can be achieved, forming osteoblasts via osteogenesis. If this is achievable then ZnO nanowires would be a more ideal biomaterial for bone repair, where they could be used to coat titanium plates and screws to inhibit immune system response and negate osteoimmunology response. When the solubility of ZnO nanowires is considered then coating the osteo-implant could promote the formation of a thick layer of oseteopontin and hydroxyapatite from the osteoblasts, before dissolving.

Alternatively if observation of cell-substrate interaction is to be continued then the next logical step would be to conduct confocal microscopy for detailed information of this interface. Fig. 8.26. showed the cell-substratum interface of a single U-2 OS cell, however without emission from the ZnO nanowires determination of the exact cell-substrate interface is difficult as the emission from the dye used to stain the cell simply attenuates with Z-height from the cell-substrate interface. Therefore, research was

conducted to find a suitable ZnO stain / coating to provide more information from confocal microscopy. FluoZin-3 is a fluorescent marker (Excitation at 494 nm / Emission at 516 nm)[1] which targets Zn^{2+} and yields a 50-fold increase in fluorescence in response to saturating levels of Zn^{2+}. It was found that by using the cell-impermeant form of the dye that the ZnO nanowires in this work could be made to be fluorescent, with emission at 516 nm; see Fig. 9.2. Unfortunately this work did not go past the preliminary stages as there was insufficient time. However, it can be seen that continuation of work with FluoZin-3 could lead to some very interesting observations on cell-substrate interaction with ZnO nanowires. It is suggested to pursue ZnO nanowire staining in tandem with an investigation into the manipulation of differentiation of hMSCs due to ZnO nanowire surface properties providing a potentially fruitful avenue for future research.

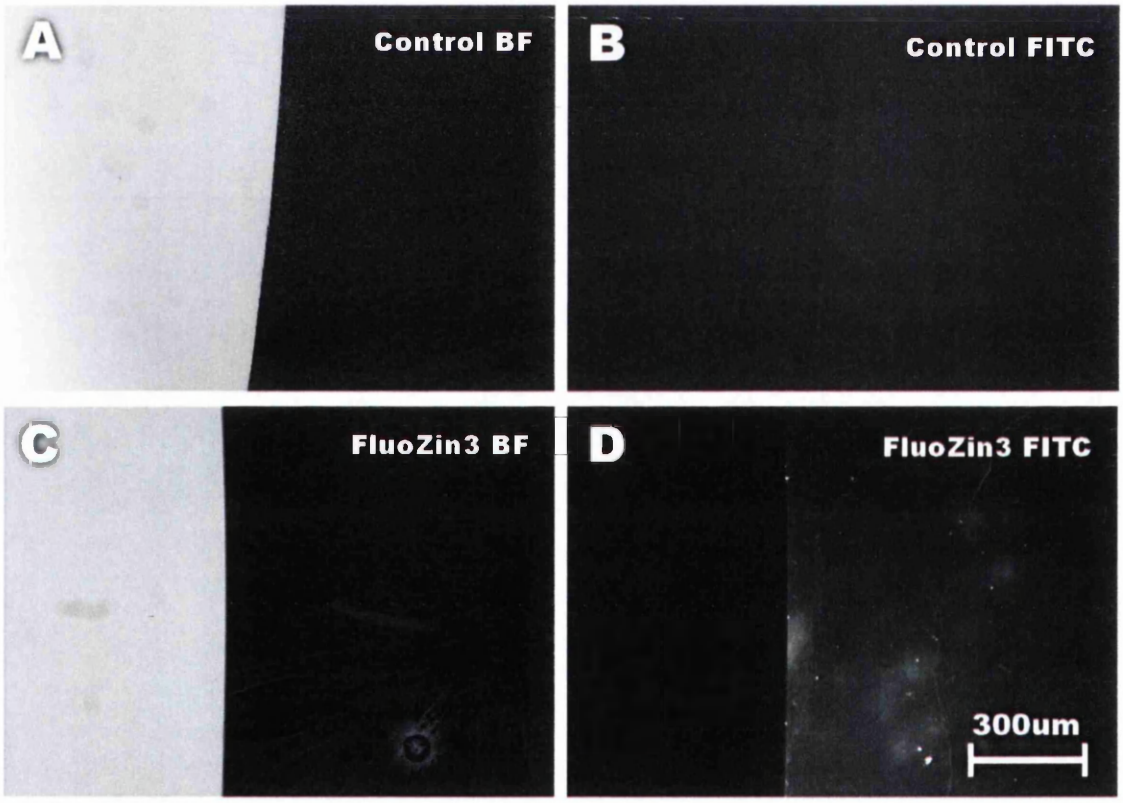

Figure 9.2. Immunofluorescence image of ZnO nanowire arrays that have (A and B) and have not (C and D) been treated with FluoZin3, where (A and C) are Brightfield images to show where the substrate is (on right) and (B and D) are FITC images. (D) shows emission from ZnO nanowires coated with FluoZin3 (emission at 516 nm).

[1] http://www.lifetechnologies.com/order/catalog/product/F24195

Appendix I. Lattice Defects, Planes and Doping

I.1. Defect Levels within the Band-gap

When planning to use a semiconductor for any electrical, optical or mechanical based sensing systems then the amount and types of point defects are an essential element to be both understood and considered in material selection as they can drastically alter the properties of their host material. In chapter 2 the majority of point defects that can exist in the crystal lattice were discussed and shown in Fig. 2.4., it was not however explained how much vacancies, interstitials, substitutionals and antisites may affect the optical properties of ZnO nanowires, by creating levels within the band-gap on a band diagram. It is well known that semiconductors are formed (in our case) when group II and VI (*2 and 6 electrons available respectively*) elements coalesce forming a neutral compound. However, as discussed elements from other groups can often be incorporated, or atoms can be in locations they shouldn't changing the properties of the material system. Fig. AI.1 uses band diagrams and crystal lattice diagrams to explain how the (for example) substitutionals can create additional levels within the band-gap, changing the electronic properties of the semiconductor material.

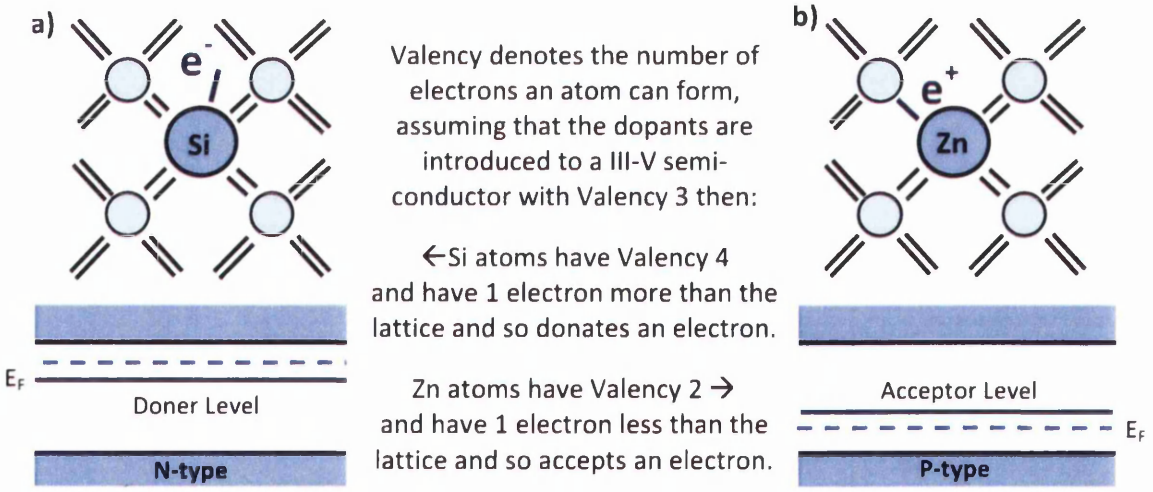

Figure AI.1. Diagrams shows two different substitutionals in a III-V semiconductor crystal lattice, where (a) shows electron donors, Si leads to electrons in the conduction band and an n type semiconductor material system (b) shows electron acceptors, Zn leads to holes in the conduction band and a p type semiconductor material system.

However, these point defects often manifest concurrently, that is to say it is not unlikely to find that three or more defect levels within the band-gap can be contributing to the deep level emission (DLE) peak so often observed in photoluminescence spectra throughout this work. For example in Fig. 4.23. and Table 4.4. it was shown that the NBE and DLE peaks often consist of the point defects within the band-gap, and that these are commonly accepted in the literature [1–4]; Fig. AI.2. takes these DLE 's and shows within a band diagram for perspective.

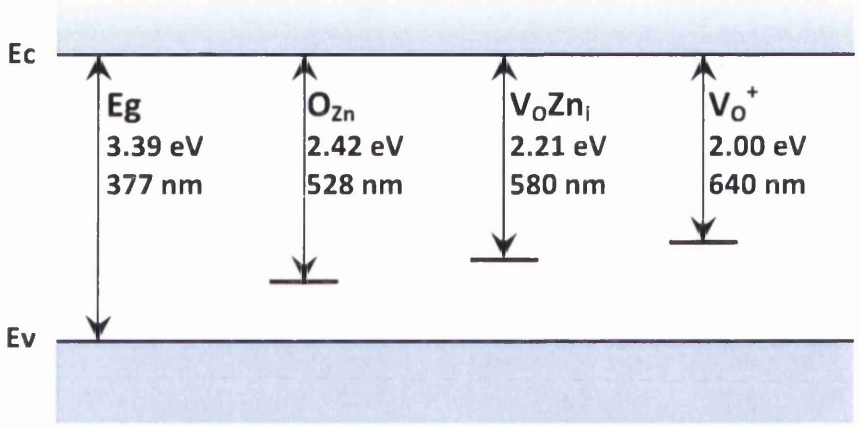

Figure AI.2. Energy band diagram shows how the addition of deep energy levels within the band-gap due to numerous point defects contributes to the photoluminescence signature seen throughout this work.

I.2. Miller-Bravais Indices

Miller Indices are notation to describe growth directions and groups of parallel planes in crystal lattices, where the unit cell is used to determine the index; see Fig. AI.1. Directions are expressed in terms of unit vector ratios in integers in the form [uvw], whereas planes are expressed as integers in the form (hkl), where h, k and l the axes of the unit cell. Planes are obtained by dividing the intercept points of the plane on each axis by their respective cell dimension yielding fractional intercept points; with their reciprocal generating the plane's miller indices, see Table AI.1. However (hkl) primarily applies to Face and Body Centered Cubic (FCC/BCC) Bravais lattices, but zinc oxide is a Hexagonal Close Packed (HCP) Bravais lattice and therefore it is useful to use the four index Miller-Bravais system instead to limit ambiguity between similar

planes. That is because HCP crystal lattices have six-fold symmetry, where planes parallel to the I axis will yield miller indices that suggest the planes are dissimilar they are actually identical with all planes through the 'long' diagonal of the unit cell being equivalent [5]. Therefore Miller-Bravais indices are used to eliminate confusion between crystallographically similar planes and directions, as axes on the basal plane are selected along the axes of symmetry ensuring similar planes yield similar indices. Table AI.1 shows how four index Miller-Bravais indices are obtained from observation of diagrams in Fig. AI.3a.

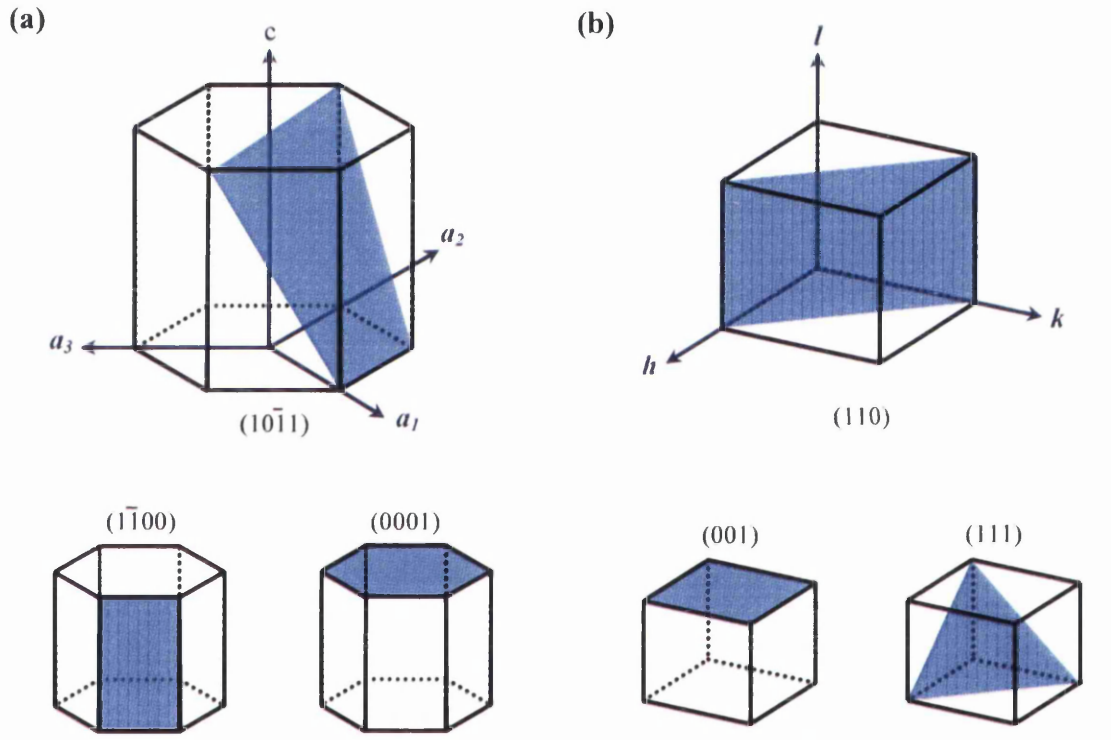

Figure AI.3. Examples of Miller-Bravais and Miller indices labeling crystal planes in a) HCP and b) FCC crystal structures; typical of zinc oxide and silicon respectively.

Table AI.1. Obtaining Miller-Bravais indices - (using $10\bar{1}1$) as an example

	$a_1(h)$	$a_2(k)$	$a_3(i)$	$C(l)$
Plane intersect	A_1	∞	A_3	1
Intersect Length	1	∞	-1	1
Reciprocal	1	0	-1	1
Miller Indices	1	0	$\bar{1}$	1

I.3. Conversion of Miller (*hkl*) to Miller-Bravais (*hkil*) indices

Since the interception point of the a_1 and a_2 axes also determines the point of interception on the a_3 axis, then one can easily convert between Miller-Bravais (*hkil*) and Miller (*hkl*) indices, using Equation A1. Fig. AI.4. shows how the FCC unit cell may be placed within the HCP unit cell to visually explain how Equation A1 yields the correct conversion from three index Miller indices to four index Miller-Bravais indices. The main advantage of the Miller-Bravias system is that similar planes have similar indices, therefore the four index system shall be used as the standard in this thesis.

$$i = -(h + k) \tag{A1}$$

Fig. AI.4. shows the overlay and comparison of FCC and HCP unit cells for (110) and (11$\bar{1}$0), respectively. It can be seen that conversion from three to four or from four to three index indices is quite straight forward when either visualized or calculated. For example, the follow conversions of common zinc oxide XRD peaks can be made:

Miller plane (100) is equivalent to the Miller-Bravais plane (10$\bar{1}$0)
Miller plane (002) is equivalent to the Miller-Bravais plane (0002)
Miller plane (101) is equivalent to the Miller-Bravais plane (10$\bar{1}$1)
Miller plane (102) is equivalent to the Miller-Bravais plane (10$\bar{1}$2)
Miller plane (103) is equivalent to the Miller-Bravais plane (10$\bar{1}$3)
Miller plane (112) is equivalent to the Miller-Bravais plane (11$\bar{2}$2)

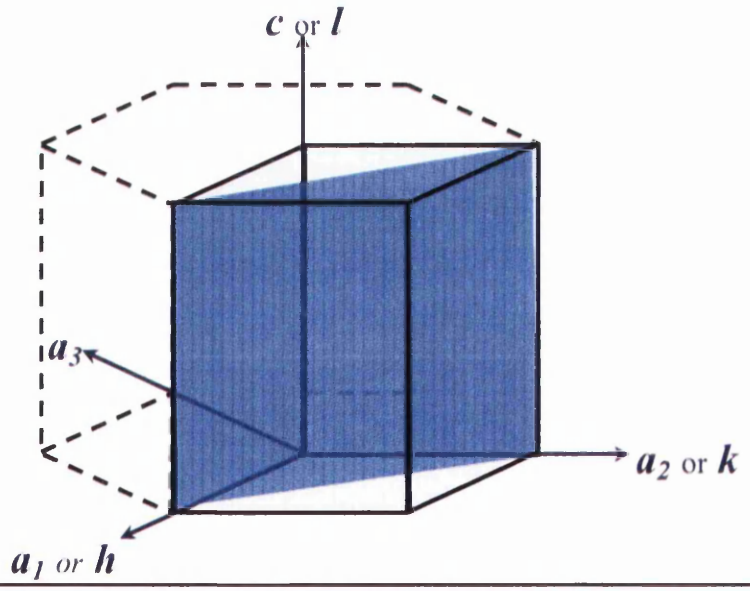

Figure AI.4. Diagram showing how Miller-Bravais four index indices may be obtained from three index Miller indices by visual comparison of the FCC and HCP unit cells.

Appendix II. List of Experiments

This section was originally intended to allow the reader to see the full range of experiments conducted throughout this work, to highlight how the methodical recording of minor experimental variables can often be key to find a correlation within the data. However, this would have required 54 sides of A3 so instead a representation of the details recorded from select experiments is presented, see Table AII.1. below.

Date	Name	Samples	N° - Name	Substrate	Size (mm)	Cleaning Method	Seed Layer	Seed Layer Method	Seed Sol
06/04/10	**Run 1**	2	1 - 2.5mM	Si(111)	?	Ace 10min> IPA 10min> N2	Spin	2x (1 drop> 3krpm 20sec> heat 7)	0.1M ZnA in Ethanol
			2 - 25mM	Si(111)	?	Ace 10min> IPA 10min> N2	Spin	2x (1 drop> 3krpm 20sec> heat 7)	0.1M ZnA in Ethanol
25/04/10	**Run 7**	4	Spin HP 2.5mM	Si(100)	10x10	10mins: Ace, Eth, IPA, DI> N2> 15min Plasma (80W 40mm O2)	Spin	2x (3 drops> 4krpm 30sec> heat 6)	0.1M ZnA in Ethanol
			Spin Furn 2.5mM	Si(100)	10x15	10mins: Ace, Eth, IPA, DI> N2> 15min Plasma (80W 40mm O2)	Spin	2x (3 drops> 4krpm 30sec> heat 6)	0.1M ZnA in Ethanol
			Spin HP 25mM	Si(100)	10x10	10mins: Ace, Eth, IPA, DI> N2> 15min Plasma (80W 40mm O2)	Spin	2x (3 drops> 4krpm 30sec> heat 6)	0.1M ZnA in Ethanol
			Spin Furn 25mM	Si(100)	10x15	10mins: Ace, Eth, IPA, DI> N2> 15min Plasma (80W 40mm O2)	Spin	2x (3 drops> 4krpm 30sec> heat 6)	0.1M ZnA in Ethanol
21/06/10	**Run 23**	4	1 - Si 25mM	Si(100)	10x10	10mins: Ace, Eth, IPA, DI> N2 & 5min Heat	PVD	20nm @ no heat - 100% Ar	-
			2 - Si 50mM	Si(100)	10x10	10mins: Ace, Eth, IPA, DI> N2 & 5min Heat	PVD	20nm @ no heat - 100% Ar	-
			3 - Glass 25mM	Glass	18x18	10mins: Ace, Eth, IPA, DI> N2 & 5min Heat	Spin	2x (3 drops> 3krpm 30sec> heat 6)	0.1M ZnA in Ethanol
			4 - Glass 50mM	Glass	18x18	10mins: Ace, Eth, IPA, DI> N2 & 5min Heat	Spin	2x (3 drops> 3krpm 30sec> heat 6)	0.1M ZnA in Ethanol
18/08/10	**Run 37**	2	glass spin	Glass	18x18	Ace 10mins> 15min Plasma Ash (80watt 20mm O2)	Spin	2x (3 drops> 3krpm 30sec> dry)	0.1M ZnA in Ethanol
			si pvd	Si(111)	6x6	10mins: Acetone, Ethanol, IPA, DIST. and 5min HP heat 5	PVD	37nm @ 230C - gas unknown	-
07/10/10	**Run 41Z**	2	MEMS	MEMS	15x15	Ace 30min> N2	Spin	2x (25ul> 3krpm 30sec> dry)	0.1M ZnA in Ethanol
13/10/10	**Run 44**	6	Glass Float	Glass	24x24	Ace Rub> N2	Spin	2x (25ul> 3krpm 30sec> dry)	0.1M ZnA in Ethanol
			Glass Mount	Glass	18x18	Ace 30min> N2	Spin	2x (25ul> 3krpm 30sec> dry)	0.1M ZnA in Ethanol
			Si Float	Si(111)	10x10	Ace 30min> N2	Spin	2x (25ul> 3krpm 30sec> dry)	0.1M ZnA in Ethanol
			Si Mount	Si(111)	10x10	Ace 30min> N2	Spin	2x (25ul> 3krpm 30sec> dry)	0.1M ZnA in Ethanol
13/10/10	**Run 44+**	2	Same	Same	Same	Same	Same	Same	Same
22/12/10	**Run 63**	2	1 - Oxygen+	Glass	24x24	Ace 10min> 15min Plasma Ash (80W 20mm O2)	Spin	2x (25ul> 3krpm 30sec> no heat dry)	0.1M ZnA in Ethanol
			2 - Normal	Glass	24x24	Ace 10min> 15min Plasma Ash (80W 20mm O2)	Spin	2x (25ul> 3krpm 30sec> no heat dry)	0.1M ZnA in Ethanol
11/02/11	**Run 73**	9	1hr	Glass	24x24	Ace 5min> IPA 5min> N2	Spin	2x (25ul> 3krpm 30sec> dry)	0.1M ZnA in DI
			2hrs	Glass	24x24	Ace 5min> IPA 5min> N2	Spin	2x (25ul> 3krpm 30sec> dry)	0.1M ZnA in DI
			3hrs	Glass	24x24	Ace 5min> IPA 5min> N2	Spin	2x (25ul> 3krpm 30sec> dry)	0.1M ZnA in DI
			4hrs	Glass	24x24	Ace 5min> IPA 5min> N2	Spin	2x (25ul> 3krpm 30sec> dry)	0.1M ZnA in DI
			5hrs	Glass	24x24	Ace 5min> IPA 5min> N2	Spin	2x (25ul> 3krpm 30sec> dry)	0.1M ZnA in DI
			6hrs	Glass	24x24	Ace 5min> IPA 5min> N2	Spin	2x (25ul> 3krpm 30sec> dry)	0.1M ZnA in DI
			7hrs	Glass	24x24	Ace 5min> IPA 5min> N2	Spin	2x (25ul> 3krpm 30sec> dry)	0.1M ZnA in DI
			8hrs	Glass	24x24	Ace 5min> IPA 5min> N2	Spin	2x (25ul> 3krpm 30sec> dry)	0.1M ZnA in DI
			9hrs	Glass	24x24	Ace 5min> IPA 5min> N2	Spin	2x (25ul> 3krpm 30sec> dry)	0.1M ZnA in DI
18/08/11	**Run 90**	9	1 - 5:1	Glass	22x22	Ace 10min> IPA 10min> N2	PVD	50nm @ no heat - Ar 9:1 O2	-
			2 - 5:2	Glass	22x22	Ace 10min> IPA 10min> N2	PVD	50nm @ no heat - Ar 9:1 O2	-
			3 - 5:3	Glass	22x22	Ace 10min> IPA 10min> N2	PVD	50nm @ no heat - Ar 9:1 O2	-
			4 - 5:4	Glass	22x22	Ace 10min> IPA 10min> N2	PVD	50nm @ no heat - Ar 9:1 O2	-
			5 - 1:1	Glass	22x22	Ace 10min> IPA 10min> N2	PVD	50nm @ no heat - Ar 9:1 O2	-
			6 - 5:6	Glass	22x22	Ace 10min> IPA 10min> N2	PVD	50nm @ no heat - Ar 9:1 O2	-
			7 - 5:7	Glass	22x22	Ace 10min> IPA 10min> N2	PVD	50nm @ no heat - Ar 9:1 O2	-
			8 - 5:8	Glass	22x22	Ace 10min> IPA 10min> N2	PVD	50nm @ no heat - Ar 9:1 O2	-
			9 - 5:9	Glass	22x22	Ace 10min> IPA 10min> N2	PVD	50nm @ no heat - Ar 9:1 O2	-
17/02/12	**R112Z**	4	Gold	Si(100)	10x10	Zheng Prepared Substrates...	PVD	Au: 35nm @ 20mA 2kV 5x10-3 60Secs > ZnO	-
			Nickel	Si(100)	10x10	Zheng Prepared Substrates...	PVD	Ni: 35nm @ 1.4A/s - 80W - 139 Ar > ZnO	-
			Silicon	Si(100)	10x10	Zheng Prepared Substrates...	PVD	20nm @ 0.4A/s - 70W - 45 Ar - 5 O2	-
			Glass	Glass	13diam	Ace 10min> IPA 10min> N2	PVD	20nm @ 0.4A/s - 70W - 45 Ar - 5 O2	-
28/03/12	**R116**	9	1.5	Glass	18x18	Ace 10min> Rub> IPA 10min> N2	PVD	50nm @ 0.4A/s - 60W - 45 Ar - 5 O2	-
			2.5	Glass	18x18	Ace 10min> Rub> IPA 10min> N2	PVD	50nm @ 0.4A/s - 60W - 45 Ar - 5 O2	-
			3.5	Glass	18x18	Ace 10min> Rub> IPA 10min> N2	PVD	50nm @ 0.4A/s - 60W - 45 Ar - 5 O2	-
			4.5	Glass	18x18	Ace 10min> Rub> IPA 10min> N2	PVD	50nm @ 0.4A/s - 60W - 45 Ar - 5 O2	-
			5.5	Glass	18x18	Ace 10min> Rub> IPA 10min> N2	PVD	50nm @ 0.4A/s - 60W - 45 Ar - 5 O2	-
			6.5	Glass	18x18	Ace 10min> Rub> IPA 10min> N2	PVD	50nm @ 0.4A/s - 60W - 45 Ar - 5 O2	-
			7.5	Glass	18x18	Ace 10min> Rub> IPA 10min> N2	PVD	50nm @ 0.4A/s - 60W - 45 Ar - 5 O2	-
			8.5	Glass	18x18	Ace 10min> Rub> IPA 10min> N2	PVD	50nm @ 0.4A/s - 60W - 45 Ar - 5 O2	-
			9.5	Glass	18x18	Ace 10min> Rub> IPA 10min> N2	PVD	50nm @ 0.4A/s - 60W - 45 Ar - 5 O2	-

Name	Bake Time (min)	Bake Temp (°C)	ZnNO3 (mM)	HMTA (mM)	Preheat?	Stir (min)	Hot Stir	Stir Speed	Volume (ml)	Temp (°C)	Time (hrs)	Orientation	Additional Growth Info
Run 1	5	heat 7	2.5	2.5	No	-	-	-	250	95	3	Float	
	5	heat 7	25	25	No	-	-	-	250	95	3	Float	
Run 7	5	heat 9	2.5	2.5	Yes	-	-	-	250	95	3	Float	photos confusing... Clearly have two separate runs muddled
	20	360	2.5	2.5	Yes	-	-	-	250	95	3	Float	Update, decided the one with 2x square and 2x rectangle
	5	heat 9	25	25	Yes	-	-	-	250	95	3	Float	must be this due to run from information in lab notes
	20	360	25	25	Yes	-	-	-	250	95	3	Float	in other lab book
Run 23	-	-	25	25	Yes	-	-	-	500	80	12	Float	sample allowed to cool naturally - not abruptly removed
	-	-	50	50	Yes	-	-	-	500	80	12	Float	and showed signs of dissolution and regrowth
	10	heat 10	25	25	Yes	-	-	-	500	80	12	Float	
	10	heat 10	50	50	Yes	-	-	-	500	80	12	Float	
Run 37	12	heat 10	25	25	Yes	0	15	8	500	90	8.5	Float	same as 36 but hot stir only
	-	-	25	25	Yes	0	15	8	500	90	8.5	Float	
Run 41Z	10	heat 7	25	25	Yes	?	?	?	250	80	2	Float	Had to use **6th floor DI water**, due to cartridge failure!
Run 44	20	heat 5	25	25	Yes	55	5	8	500	90	9	Float	It was noted that one stirrer produced more of a 'milky'
	20	heat 5	25	25	Yes	55	5	8	500	90	9	Mount	solution compared to the other - speed likely cause?
	20	heat 5	25	25	Yes	55	5	8	500	90	9	Float	**Investigate this further!**
	20	heat 5	25	25	Yes	55	5	8	500	90	9	Mount	
Run 44+	Same	Same	25	25	Yes	?	?	?	?	60	2	Both	
Run 63	15	heat 10	25	25	Yes	15	-	7	250	90	5	Float	Bubbled oxygen in preheating beaker
	15	heat 10	25	25	Yes	15	-	7	250	90	5	Float	
Run 73	15	360	10	10	Yes	40	2	8	250	90	1	Float	5 hour sample left on hotplate to dry for hour accidentally!
	15	360	10	10	Yes	40	2	8	250	90	2	Float	at 2hrs check revealed 3 dropped samples, refloated them
	15	360	10	10	Yes	40	2	8	250	90	3	Float	at 3hrs it is noted that the sample is far too white
	15	360	10	10	Yes	40	2	8	250	90	4	Float	i.e must be non linear growth due to drops
	15	360	10	10	Yes	40	2	8	250	90	5	Float	Must have been the first run to use the 2L beaker
	15	360	10	10	Yes	40	2	8	250	90	6	Float	no heat between spin coats
	15	360	10	10	Yes	40	2	8	250	90	7	Float	
	15	360	10	10	Yes	40	2	8	250	90	8	Float	
	15	360	10	10	Yes	40	2	8	250	90	9	Float	
Run 90	0	-	25	5	Yes	0	5	8	250	90	9	Float	5x 1cm2 argus samples added to 1:1
	0	-	25	10	Yes	0	5	8	250	90	9	Float	as this data can be easily replaced
	0	-	25	15	Yes	0	5	8	250	90	9	Float	
	0	-	25	20	Yes	0	5	8	250	90	9	Float	Big 2250ml beaker of 1:1 made up
	0	-	25	25	Yes	0	5	8	250	90	9	Float	and stirred with chemicals added to
	0	-	25	30	Yes	0	5	8	250	90	9	Float	other beakers...
	0	-	25	35	Yes	0	5	8	250	90	9	Float	
	0	-	25	40	Yes	0	5	8	250	90	9	Float	
	0	-	25	45	Yes	0	5	8	250	90	9	Float	
R112Z	-	-	20	20	Yes	5	1	8	500	90	9	Float	20 nm PVD of ZnO done at same time for all samples
	-	-	20	20	Yes	5	1	8	500	90	9	Float	2 litres of precursor solution made up in one beaker
	-	-	20	20	Yes	5	1	8	500	90	9	Float	
	-	-	20	20	Yes	5	1	8	500	90	9	Float	'scum' layer observed, someone must have opened WB lid?
R116	-	-	5	25	Yes	5	2	4	250	90	9	Float	**!!!CHANGE OF BUILDING!!! CNH Prep room**
	-	-	10	25	Yes	5	2	4	250	90	9	Float	**NEW DI USED from Millipore Elix 3, gave ~ 14MΩ DI**
	-	-	15	25	Yes	5	2	4	250	90	9	Float	**NEW Balance used - 3DP!**
	-	-	20	25	Yes	5	2	4	250	90	9	Float	
	-	-	25	25	Yes	5	2	4	250	90	9	Float	Used a conical flask previously used for NaOH,
	-	-	30	25	Yes	5	2	4	250	90	9	Float	it was rinsed thoroughly multiple times
	-	-	35	25	Yes	5	2	4	250	90	9	Float	2250ml of 5mM ZnNO3 made up and stirred
	-	-	40	25	Yes	5	2	4	250	90	9	Float	additional $ZnNO_3$ added to beakers to allow pouring
	-	-	45	25	Yes	5	2	4	250	90	9	Float	to aid mixing but were stirred by hand by glass rod

Appendix III. Tailoring Surface Properties (PEI)

III.1. Introduction

It is well known from the literature that cells are surface sensitive, and this has been heavily discussed in the chapter 8 of this work. However, the works investigations into the application of Polyethyleneimine (PEI) have not been discussed, and is done so here. PEI is an organic polymer containing a large amount of amino groups that may be protonated. In physiological pH (such as that in simulated body fluid, SBF) PEI is an effective DNA binding agent, and has been shown to led to fast cell attachment and further spreading [6]. In chemical bath deposition it has been shown that PEI inhibits lateral growth, promoting lateral growth only (much like HMTA) and can yield extremely long zinc oxide nanowires with concentrations added to the precursor solution as low as 5 mM [7]. Fig. AIII.1. shows the changes in nanowire morphology obtained from adding 5 mM of PEI to the 1:1 recipe in this work.

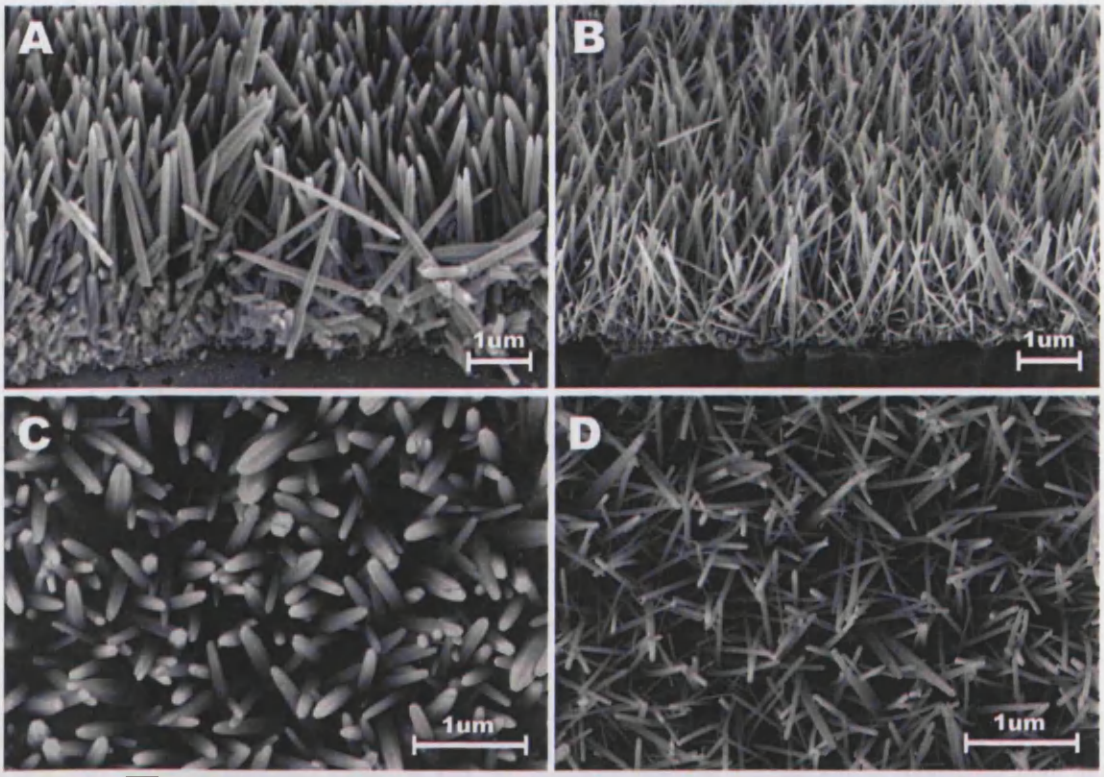

Figure AIII.1. SEM images of ZnO NWs on glass substrates, where a) and b) indicate solutions with and without 5mM PEI added respectively. Note images a) and b) were obtained at 45° therefore NWs are longer than they appear. Images c) and d) cleary show the difference in density and morphology.

III.2. Morphology (SEM)

Fig. AIII.1 shows that nanowire morphology is drastically altered by the addition of 5 mM PEI, which was expected from the literature. Qiu et al. [8] suggest that PEI can preferentially adsorb to different crystal faces allowing the additive to alter the surface free energy and growth rate of the nanowires, while also maintaining a relatively high nanowire density. It can be seen that in this work, in Fig. AIII.1b. that the density of the nanowire array between the control (1:1) and PEI samples doesn't vary significantly being 1.2 and 1.5 x 10^9 nanowires per cm^2 for control and PEI samples, respectively. The length and width however are severely affected with length dropping from 4.0 to 2.2 μm for control and PEI, respectively.

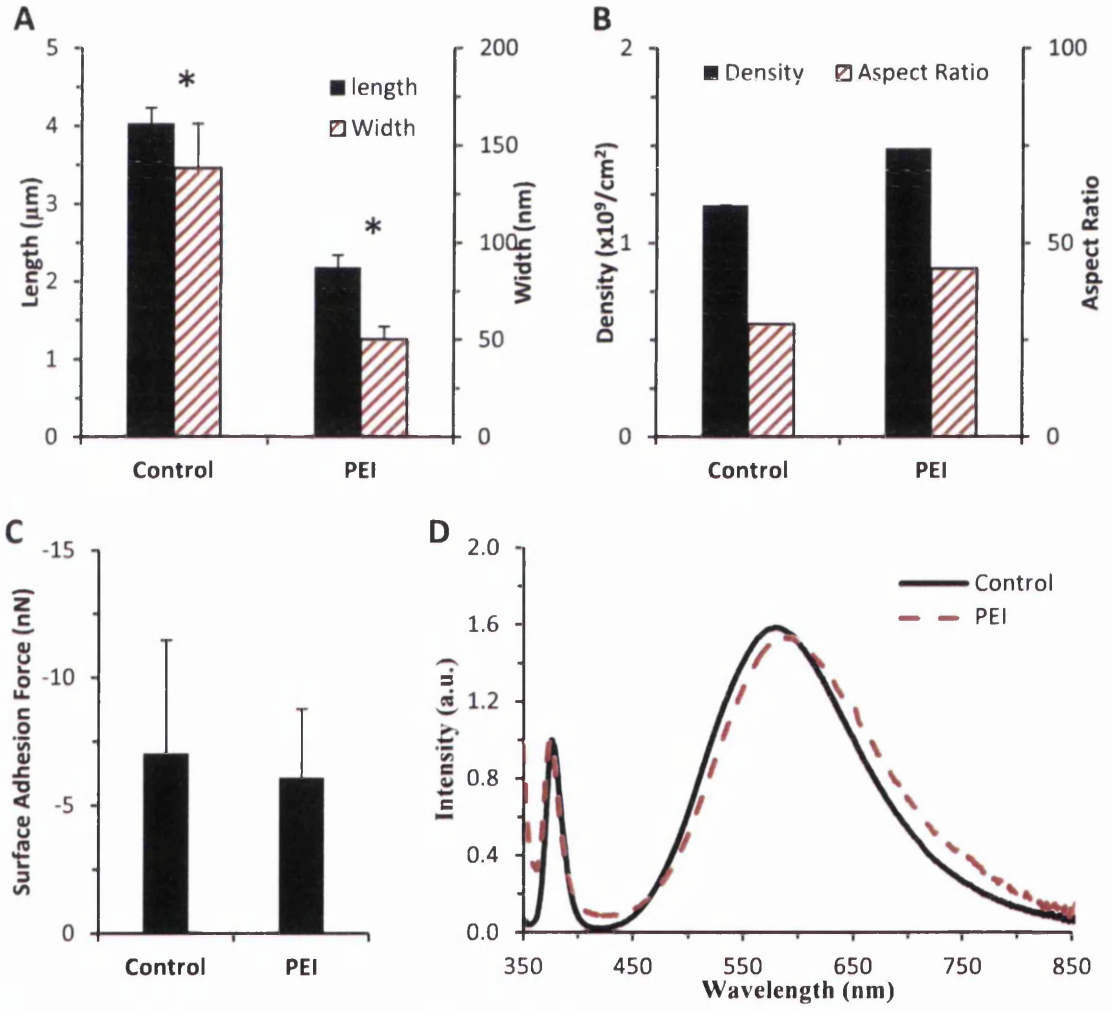

Figure AIII.2. Graphs showing mean of measurements taken from Figure AIII.1, where (A) shows length, (B) width, (C) Surface adhesion and (D) optical properties of Zinc Oxide nanowires with and without inclusive of PEI during hydrothermal growth. Morphology values obtained from 90 measurements for each dimension across 3 discrete areas. Error bars represent ±SD of 3 areas. * indicates $p<0.005$ and ** $p<0.05$ compared to each substratum

As the application of PEI has its roots firmly in microbiology, with researchers such as Vancha et al. [9] exploring the application of PEI for transfection of eukaryotic cells as the polycations are very effective in binding to DNA. They show that their PEI-based protocol was successfully used for transfections with HEK-293 (human embryonic kidney) and PC-12 (rat pheochromocytoma) cells. Similarly, Saravia and Toca-Herrera [10] use atomic force microscopy (AFM) to investigate the influence of cell shape on its mechanical properties, between control and PEI substrates. They find that if the cells were considered as a homogenous solid material then the Hertz model could be used to determine the elastic modulus of the cell. They report that the mean elastic modulus the central part of the cell was 191 ±14 Pa and 941 ±58 Pa for cells adsorbed on poly(sodium-4-styrenesulfonate) and PEI substrates, respectively. In this work, surface adhesion was investigated using AFM and the results are shown in Fig.AIII.2c. were it can be observed that PEI actually yields a less adhesive surface with a surface adhesion force of 6 nN compared to the controls 7 nN. No significant differences in optical properties of control or PEI ZnO nanowires were observed.

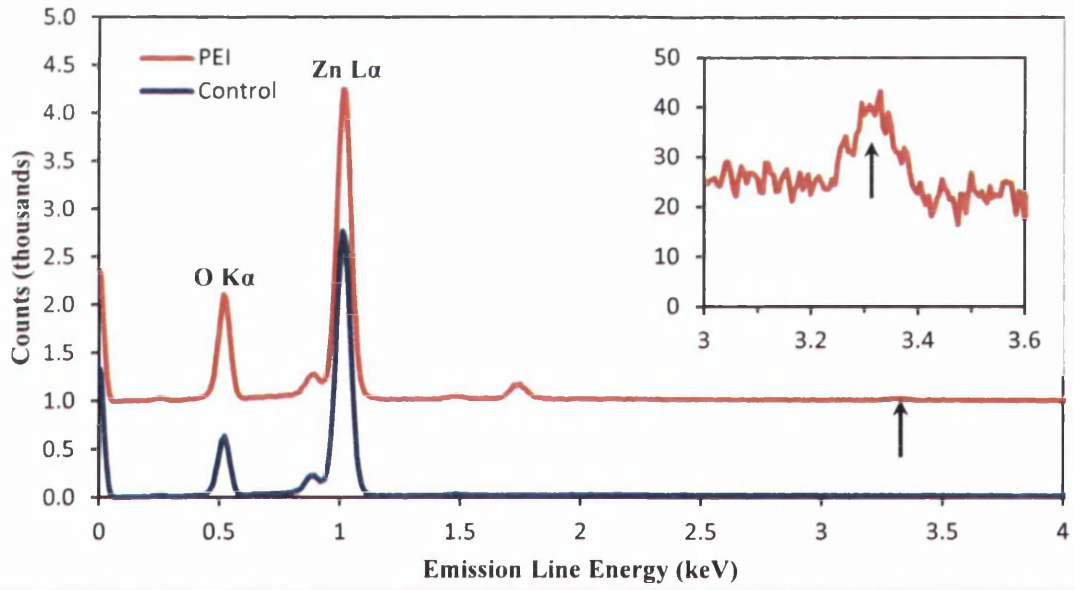

Figure AIII.3. EDX spectra from a normal (control) ZnO nanowire array grown with the 1:1 recipe, and an array grown with 5 mM Polyethyleneimine (PEI) added during chemical bath deposition. The control and PEI spectrums have been offset by 1000 counts for clarity. The spectrum shown inset corresponds to the low intensity peak shown by the arrow on the PEI spectrum, which is Potassium.

EDX was also conducted to confirm incorporation of PEI into the nanowire given the high 5 mM concentration of PEI used during chemical bath deposition. Fig. AIII.3 shows that PEI was indeed incorporated within the nanowire. It was discussed in

chapter 4 that chemical characterization techniques such as EDX can yield an understanding of the causes behind trends seen in other characterisation techniques. This is because while techniques such as PL can be surface sensitive EDX yields information from the bulk. EDX can be used to produce results revealing the atomic percentage of all the elements within the material; this can be useful for detailed quantitative analysis of samples.

Table AIII.1. Quantitative information obtained from EDX spectrum, comparing control and PEI.

Sample	Element	Line	App. Conc.	k ratio	Intensity Corrn.	Weight %	Weight % SD	Atomic %
Control	Carbon	K	0.57	0.00265	0.5473	1.35	0.55	4.57
	Oxygen	K	25.38	0.09110	1.8353	17.88	0.36	45.33
	Potassium	K	0.00	0.00000	1.2101	0.00	0.00	0.00
	Zinc	L	53.94	0.53937	0.8635	80.76	0.56	50.10
PEI	Carbon	K	1.03	0.00476	0.5732	1.74	0.47	5.27
	Oxygen	K	43.96	0.15778	1.8406	23.17	0.35	52.67
	Potassium	K	0.92	0.00754	1.1936	0.75	0.14	0.69
	Zinc	L	63.23	0.63235	0.8249	74.35	0.50	41.37

Table AIII.1. shows the atomic % data obtained from control and PEI samples shown in Fig, AIII.1. proving that potassium is incorporated in ZnO nanowires during growth due to inclusion of 5 mM PEI. Overall the addition of PEI to the final 1:1 recipe revealed in Fig. 7.45. has neither increased aspect ratio nor improved surface adhesion, and so the samples were never taken to tissue culture and the work not pursued further.

Appendix IV. Cross-sectional IEM of U-2 OS

It was discussed in chapter 8, sub-section 8.5.3 and shown in Fig. 8.24. that the focal adhesion points of the U-2 OS cells may preferentially adhere to the side of the ZnO nanowires during proliferation. This was achieved by showing the distribution of anti-vinculin conjugated with 5 nm gold colloids within the cell membrane with respect to the location of the nanowires in several IEM BSE (immuno-electron microscopy and back scattered electron) images. In chapter 8 it was mentioned that; these colloids are definitely from within the cell membrane and not just sitting on top as several rinsing cycles were conducted and the samples were also looked at in cross-section. This appendix shows that although extremely difficult to focus due to vibration noise at such high magnifications the 5 nm gold colloids were observable in cross-section using the PDBSE backscattered electron detector; see Fig. AIV.1.

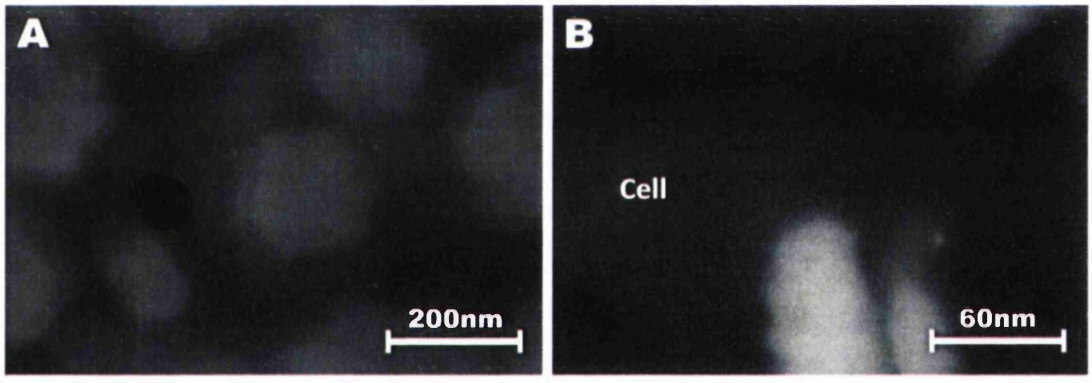

Figure AIV.1. Images show (A) scanning Electron Micrograph of U-2 OS cell on 2:1 nanowires, and (B) a backscattered electron image taken in cross-section of a U-2 OS cell fillpodium above and around two nanowires with a focal adhesion shown by high contrast 5 nm gold colloid. The sample was prepared after 72 hours incubation in McCoy's 5A modified medium at 37 °C 5 % CO_2, fixed with 4 % Para-formaldehyde, Permeablised with 0.05% Triton-X and stained.

In Fig. AIV.1. image contrast is derived from electron density and atomic weights rather than topographical information; allowing clear distinction between low contrast carbon 'background' of cell membrane, ZnO nanowires and high contrast gold colloids attached to vinculin. The location of the cell fillipodium is shown by the label 'cell' in Fig.AIV.1b., therefore it can be confirmed that the 5 nm gold colloids observed in Fig. 8.24. are from within the cell.

Appendix V. Quantifying Nanowire Alignment

It was discussed in chapter 7, multiple times but most substantially in sub-section 8.5.3 that the alignment of nanowires, or rather their angular spread distribution with respect to the substrate should be characterised and categorised into a value rather than (as many do in the literature) just reported the nanowires are 'well aligned'. Ideally his would mean that all nanowires were aligned 90° to the substrate, or perpendicular to it. This 'ideal' nanowire array is unlikely to be produced but even fabricating an array with an angular spread distribution of say 10 ° (i.e. all nanowires are aligned between 85 - 95° with respect to the substrate) would be more beneficial for monitoring of cell-substrate interaction. Fig. AV.1 explains how the angle with respect to the substrate was measured using ImageJ, qualitative data analysis program used in this work. In Fig. AV.1b. angle 1 is the divergence of the nanowire from the intended angle of alignment, where ideally the c-axis should be aligned perpendicular to the substrate. Angle 2 orientation of the nanowire with respect to the substrate, using this value angle 1 may be obtained yielding the angular spread distribution of the nanowire array.

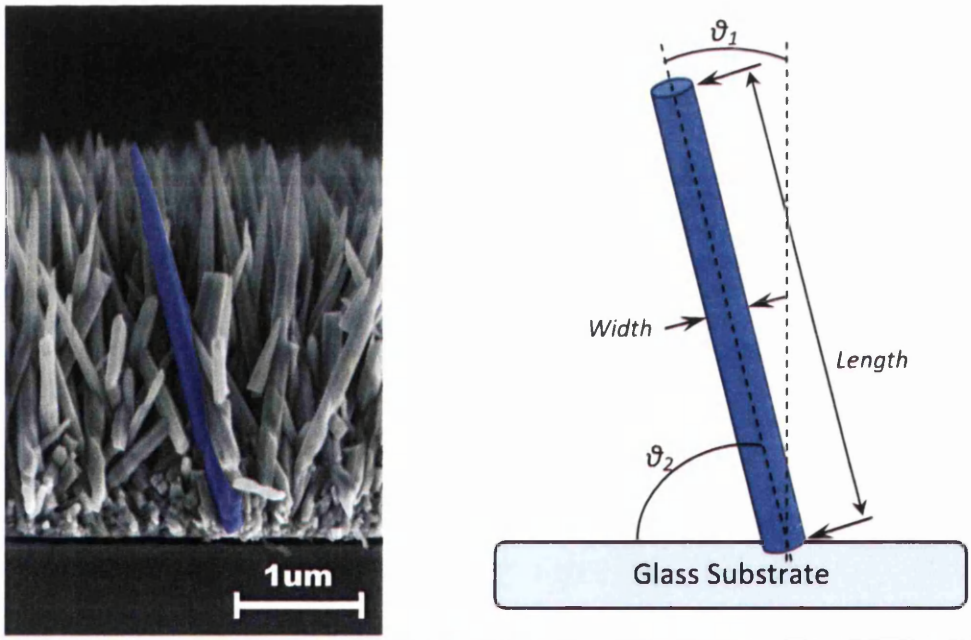

Figure AV.1. Scanning Electron Micrograph of ZnO nanowires with a single nanowire highlighted in blue and a diagram showing this nanowire and the measurements that are obtained from it in this work.

Appendix VI. Using Image J Image Editing Software

VI.1. Introduction

ImageJ is a freely available image processing program that uses Java and can display, edit, analyze, process, save and print binary to 32-bit images. ImageJ t supports importing and editing "stacks", a series of images that share a single window, useful for confocal microscopists. It ultalises multiple core computer processors so that time-consuming operations such as image file reading can be performed in parallel with other operations [11]. ImageJ was used in the majority of tasks of retrieving quantitative data from qualitative SEM images; and performed extremely well.

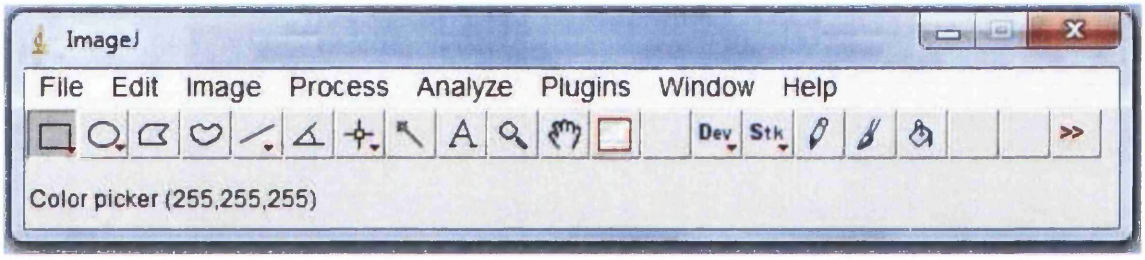

Figure AVI.1: Main window of the ImageJ image processing program.

VI.2. Measuring Density of Zinc Oxide Nanowires

ImageJ is able to import plugins written by the community and provide tools to allow the user to write their own programs to address any problem. It has already been discussed in chapter 4 that SEM imaging of insulating samples can lead to many charging artifacts appearing in the image. These artifacts can interfere with many of the measuring plugins available for ImageJ, such as the 'line by line' charging artifacts in Fig. AVI.2a. That would results in poor data. Artifacts like these can be removed by conducting a normalization of all grey levels in the image globally using 'Contrast-limited adaptive histogram equalization' method. CLAHE works by sectioning the image into multiple tiles and applies histogram equalization to each one evening out the distribution of used grey levels, see Fig. AVI.2b.

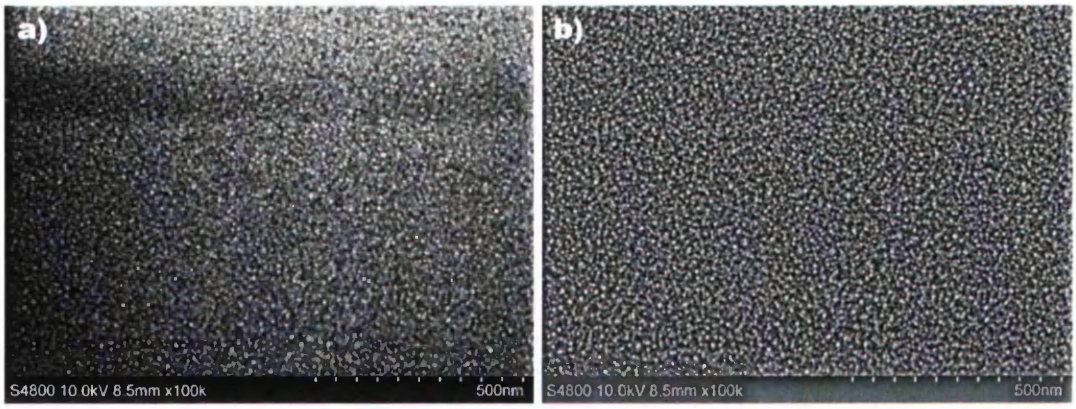

Figure AVI.2: CLAHE normalisation plugin run of ZnO nanowire array, where a) is before and b) is after process.

VI.3. Measuring cell surface area

In chapter 8 it was shown the affect of ZnO nanowire morphology on the shape of U-2 OS cells; however quantitative data was needed to fairly compare the change shown in Fig. AVI.3. The following method developed by the author was used to measure the surface area:

1) Open Image [File>Open]
2) Resize to a more workable resolution, 1280x960 [Image>Adjust>Size...]
3) Gaussian Smooth [Process>Smooth]
4) Eliminate background with Brightness and Contrast [Image>Adjust>Brightness/Contrast]
5) Check amount of pixels in scale bar, remember or write this down! [Analyse>Set Scale]
6) Remove the SEM Data bar [Click Rectangle Tool, Select Data Bar>Edit>Clear]
7) Run Greyscale Watershed Plugin [Plugins>Watershed>Watershed Segmentation] (http://bigwww.epfl.ch/sage/soft/watershed/index.html)
    a. It is important to smooth the image further, apply Gaussian Smooth, Radius 3
    b. Select Colourised basins as the output, yield our membrane boundaries
8) Return the image to greyscale [Image>Type>8bit]
9) Threshold the image to obtain either 0 or 255 [Image>Adjust>Threshold]
10) Compare the this image with the original and repair any obvious watershed errors (i.e. two cells not being split) using the pencil tool [Image>Colour>Colour Picker, select white]
    a. This step is only needed for large errors as others will be neglected during counting
11) Apply the remember scale from step 5

12) Using the Magic Wand tool check 20 cells for area spread to get an idea of range
13) Using this range count particles! [Analyze>Analyze Particles...]
    a. Set the range, typically 800-5000um^2 and tick show outlines
14) Finished, now overlay outlines on original to confirm good fit, Fig. AVI.3.

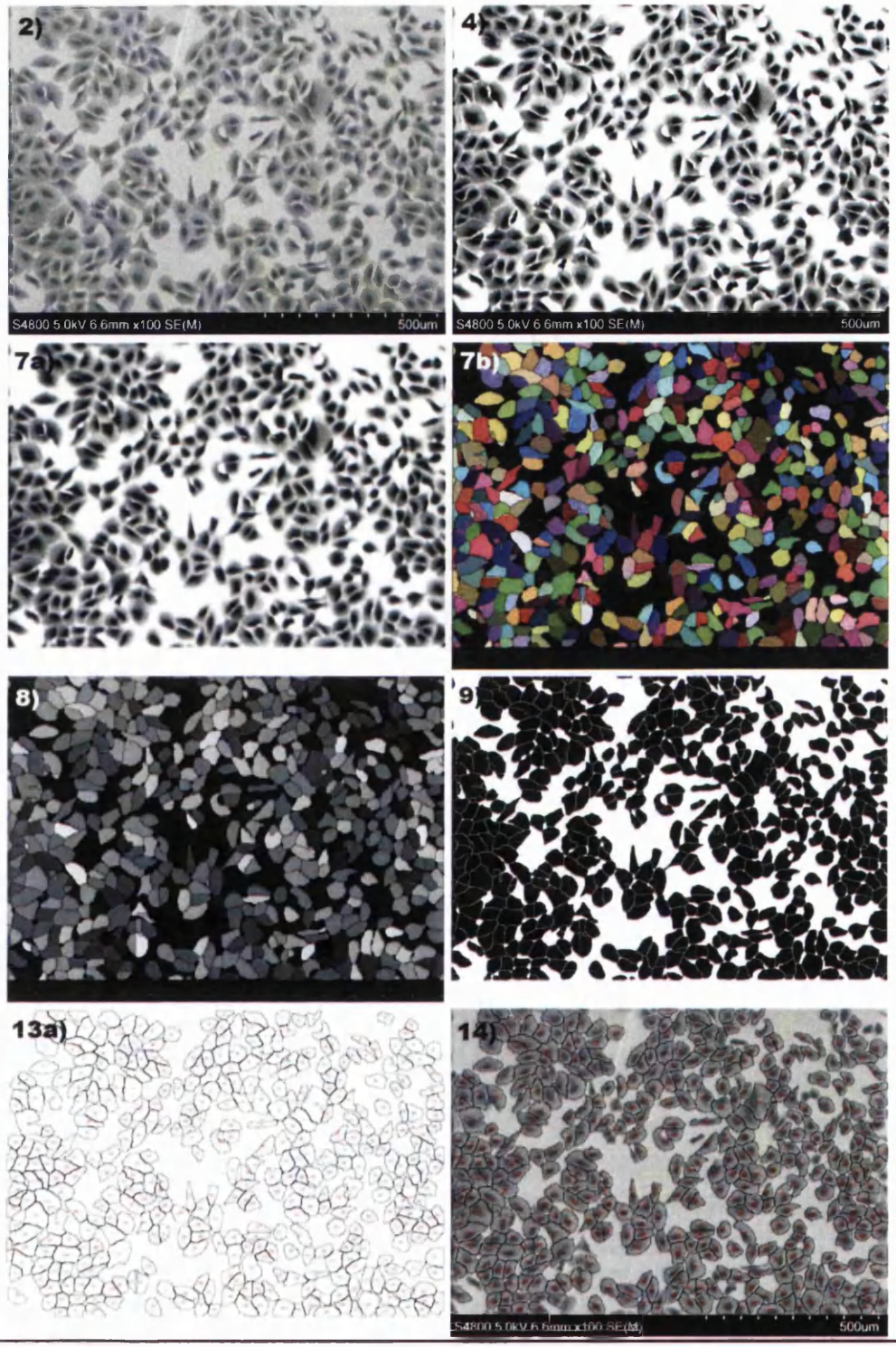

Figure AVI.3: Using the greyscale watershed algorithim to accurately determine the surface area of cells.

Appendix VII. References

[1] B. Ha, H. Ham, and C. J. Lee, "Photoluminescence of ZnO nanowires dependent on O2 and Ar annealing," *J. Phys. Chem. Solids*, vol. 69, no. 10, pp. 2453–2456, Oct. 2008.

[2] P. Xu, "The electronic structure and spectral properties of ZnO and its defects," *Nucl. Instruments Methods Phys. Res. Sect. B Beam Interact. with Mater. Atoms*, vol. 199, pp. 286–290, Jan. 2003.

[3] S. Lima, "Luminescent properties and lattice defects correlation on zinc oxide," *Int. J. Inorg. Mater.*, vol. 3, no. 7, pp. 749–754, Nov. 2001.

[4] B. Lin, Z. Fu, and Y. Jia, "Green luminescent center in undoped zinc oxide films deposited on silicon substrates," *Appl. Phys. Lett.*, vol. 79, no. 7, p. 943, 2001.

[5] R. J. D. Tilley, *Crystals an Crystal Structures*. Joh Wiley & Sons Ltd, 2006, p. 270.

[6] V. Saravia and J. L. Toca-Herrera, "Substrate influence on cell shape and cell mechanics: HepG2 cells spread on positively charged surfaces.," *Microsc. Res. Tech.*, vol. 72, no. 12, pp. 957–64, Dec. 2009.

[7] L. Wang, D. Tsan, B. Stoeber, and K. Walus, "Substrate-free fabrication of self-supporting ZnO nanowire arrays.," *Adv. Mater.*, vol. 24, no. 29, pp. 3999–4004, Aug. 2012.

[8] J. Qiu, X. Li, W. He, S.-J. Park, H.-K. Kim, Y.-H. Hwang, J.-H. Lee, and Y.-D. Kim, "The growth mechanism and optical properties of ultralong ZnO nanorod arrays with a high aspect ratio by a preheating hydrothermal method.," *Nanotechnology*, vol. 20, no. 15, p. 155603, Apr. 2009.

[9] A. R. Vancha, S. Govindaraju, K. V. L. Parsa, M. Jasti, M. González-García, and R. P. Ballestero, "Use of polyethyleneimine polymer in cell culture as attachment factor and lipofection enhancer.," *BMC Biotechnol.*, vol. 4, p. 23, Oct. 2004.

[10] V. Saravia and J. L. Toca-Herrera, "Substrate Influence on Cell Shape and Cell Mechanics : HepG2 Cells Spread on Positively Charged Surfaces," *Microsc. Res. Tech.*, vol. 964, no. May, pp. 957–964, 2009.

[11] C. A. Schneider, W. S. Rasband, and K. W. Eliceiri, "NIH Image to ImageJ: 25 years of image analysis," *Nat. Methods*, vol. 9, no. 7, pp. 671–675, Jun. 2012.